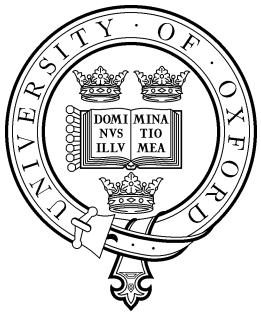
Mechanical and geometric cues guiding early mammalian tissue development



Karolis Leonavicius
St Edmund Hall
University of Oxford

A thesis submitted for the degree of
Doctor of Philosophy

Trinity 2016

Dedicated to my wonderful mother Nijole Leonaviciene.

Acknowledgements

Foremost, I would like to thank my programme director Dr. Gail Preston, without whom my interdisciplinary doctoral training programme would not exist. I would like to thank Prof. Shankar Srinivas, Prof. Fritz Vollrath and Dr. Christophe Royer - my supervisors, without whom the work in this thesis would not have been possible. Also, I would like to thank my two summer students Annemarie Kip and Deborah Fortin, who have helped a great deal with manual image outlining.

Abstract

Mammalian development is one of the most complex biological processes, that is responsible for converting a single cell into a whole organism. Although, mechanical forces are expected to play profound roles during development, proving the role of mechanical and geometric cues has been difficult due to the lack of suitable experimental techniques. The thesis investigates the hypothesis, that mechanical and geometric cues are driving the first two cell fate decision events. In order to test them and create a robust experimental framework, the first three chapters are dedicated to developing methodology based on three dimensional patterned hydrogels. The hydrogels were mechanically and biochemically characterised in high detail and then used as three dimensional moulds to shape developing tissues. This technique also made it possible to calculate mechanical forces, which could be estimated from hydrogel deformation and known elastic properties. Finally, to characterise the biological outcomes of mechanical tissue deformation a heuristic confocal image analysis technique has been developed and used to investigate developing mammalian tissues. Using the techniques it was possible to demonstrate, that the first cell fate decision is controlled by embryo geometry and the molecular mechanism involved a complex combination of Hippo pathway signalling and a sequence of cell polarisation. Similarly, the second cell fate decision was also found to be driven by tissue geometry and Hippo pathway signalling, although the precise biochemical pathway was less clear.

Contents

1 Introduction **3**

1.1 Cellular-level mechanical sensing 5

1.2 Methods for investigating single cell geometry and mechanics 6

1.3 Tissue-level geometry sensing 9

1.4 Defining 3D tissue shape 10

1.5 Measuring tissue-level forces 13

1.6 Analysing tissue-level biochemical responses 15

1.7 The Hippo pathway 17

1.7.1 Mouse pre-implantation development 21

1.8 Early stem cell organoid development 22

1.9 Thesis aims 24

2 Hydrogel tools for tissue micromanipulation **26**

2.1 Introduction 26

2.2 Materials and methods 30

2.2.1 HEK293 and LS180 cell culture 30

2.2.2 CGR8 cell culture 31

2.2.3 Synthesis of gelatin methacrylate 31

2.2.4 Synthesis of hyaluronic acid methacrylate 31

2.2.5 Synthesis of Lithium acyl phosphinate photoinitiator (405nm) 32

2.2.6 Hydrogel fabrication for cell culture 32

2.2.7 Mechanical hydrogel testing . . . 33
2.2.8 Biocompatibility testing . . . 34
2.2.9 Biodegradability measurements . . . 35
2.2.10 Cell viability testing . . . 35
2.2.11 Laser based direct-write hydrogel patterning . . . 35
2.2.12 Using hydrogels to change tissue shape . . . 36
2.3 Results and discussion . . . 37
2.3.1 Hydrogel stiffness . . . 37
2.3.2 Cell attachment . . . 37
2.3.3 Biodegradability . . . 39
2.3.4 Hydrogel toxicity and micro patterning . . . 41
2.3.5 3D tissue micromanipulation . . . 43
2.3.6 Defining embryoid body shape . . . 43
2.3.7 Studying the origin of tissue stiffness . . . 45
2.4 Conclusions . . . 47

3 Measuring tissue mechanics with deformable hydrogels 49

3.1 Introduction . . . 49
3.2 Materials and methods . . . 52
3.2.1 Animal experiments . . . 52
3.2.2 Preparing cylindrical hydrogels . . . 52
3.2.3 Inhibitor experiments . . . 53
3.2.4 Imaging setup and Image analysis . . . 53
3.2.5 Calibrating the pressure exerted by cylindrical cavities . . . 54
3.2.6 Mathematical model derivation . . . 54
3.3 Results and Discussion . . . 57
3.3.1 Pressure evolution during blastocyst development . . . 57
3.3.2 Descriptive statistics . . . 61

3.3.3 Perturbing media osmolarity 65
3.3.4 Epithelial integrity during cell divisions 68
3.3.5 Blastocyst hatching 68
3.3.6 Investigating the mechanism of embryo hatching 69
3.4 Conclusions 71

4 Microscopy based biochemical tissue characterisation 73
4.1 Introduction 73
4.2 Materials and Methods 77
4.2.1 Stem cell culture 78
4.2.2 Immunohistochemistry 78
4.2.3 Post-implantation embryos 78
4.2.4 Software and statistics 79
4.3 Results and discussion 79
4.3.1 Nuclei detection 79
4.3.2 Cell fluorescence sampling from detected nuclei 80
4.3.3 Membrane element detection 81
4.3.4 Cell fluorescence sampling from detected membranes 83
4.3.5 Method validation with CAD images 83
4.3.6 Method validation with pre-implantation embryos 84
4.3.7 Method validation with embryonic hearts 86
4.3.8 Development of 'SilentMark' 87
4.3.9 Using scRNA-seq data to extend spatial protein quantification 89
4.4 Conclusions 94

5 The role of tissue geometry during the first mammalian cell fate decision 95
5.1 Introduction 95

5.2 Materials and Methods 98
5.2.1 Mouse strains, husbandry and embryo collection 98
5.2.2 Hydrogel compression experiments 99
5.2.3 Embryo immunostaining 100
5.2.4 Live imaging of LifeAct embryos 100
5.3 Results and discussion 101
5.3.1 Analysis of transcriptional basis of the first cell fate decision . 101
5.3.2 Protein level embryo patterning during the first cell fate decision 105
5.3.3 Analysis of protein level patterning 108
5.3.4 The first cell fate decision is actively regulated by tissue geometry 111
5.3.5 The role of individual cell geometry 113
5.3.6 The process of outer cell polarisation 115
5.3.7 The role of polarised cell divisions 116
5.4 Conclusions 119

6 The role of tissue geometry during the second mammalian cell fate decision 122

6.1 Introduction 122
6.2 Materials and Methods 124
6.2.1 CGR8 cell culture 125
6.2.2 CCE cell culture and differentiation 125
6.2.3 Hydrogel compression experiments 126
6.2.4 Tissue immunostaining 126
6.2.5 FRAP experiments with YAP-GFP fusion protein 127
6.3 Results and discussion 127
6.3.1 Transcriptional control of the second cell fate decision 128
6.3.2 Inside/outside protein patterning during the second cell fate decision 130

6.3.3 Hippo pathway activity during tissue deformation 134
6.3.4 Investigating nuclear Yap transport rates 137
6.3.5 Hippo pathway link to G-protein coupled receptors 140
6.3.6 Actin/myosin inhibitor effects on Yap localisation 142
6.4 Conclusions 151

7 Conclusions **154**

Bibliography **158**

List of Figures

1.1 Summary of known geometry sensing mechanisms 4

1.2 Summary of mechanical experimental techniques 8

1.3 Commercial mechanotransduction research tools 10

1.4 Creating semi-synthetic hydrogels 12

1.5 Measuring forces generated during tissue growth 14

1.6 Overview of the context dependent Hippo pathway 19

1.7 Summary of early mouse development 21

1.8 The second cell fate decision 24

2.1 The common hydrogel cross-linking mechanisms 28

2.2 Device for measuring microscopic tissue stiffness 34

2.3 Laser based photolithography 36

2.4 Stiffness of methacrylated hydrogels and soft tissues 38

2.5 Stiffness dependence on light exposure and photo initiator concentration 39

2.6 Cell attachment as a function of GelMA content 40

2.7 Tuning gel biodegradability 41

2.8 Summary of cell encapsulation 42

2.9 Comparison of different photolithography approaches 43

2.10 Examples of 3D tissue micromanipulation 44

2.11 Defining 3D organoid shape 45

2.12 Studying mechanical embryoid body properties 46

2.13 Using chemical inhibitors to probe the molecular mechanism responsible for maintaining tissue stiffness 48

3.1 Modelling spherical droplet deformation 55
3.2 Agreement between the model and pressure data 57
3.3 Key components responsible for blastocyst pressure development . . . 58
3.4 A representative internal pressure 59
3.5 The rates of ion and water transport 59
3.6 A mathematical model for blastocyst expansion 62
3.7 Changes during blastocyst expansion 62
3.8 Embryo pressure and cavity osmolarity 64
3.9 The flux of water and ions 64
3.10 Ion transport inhibition by Ouabain 65
3.11 Zona Pellucida mechanical properties 66
3.12 Corellogram exploring relationships between embryo micro physiology variables 67
3.13 A transient pressure and volume response to changing media osmolarity 67
3.14 The pressure drop during cell divisions 68
3.15 Hatching types 69
3.16 Summary of hatching probability with varying embryo pressure and Zona Pellucida thickness. After shell thickness decreases beyond 2μm embryo hatching approaches certainty. 70
3.17 Embryo hatching modelled as a survival study 71

4.1 MorphographX, developed by the Max Planck institute 74
4.2 Embryo cell segmentation by manual outlining 75
4.3 Automated tissue segmentation by the RACE 76
4.4 Probabilistic image segmentation 76

4.5 Image analysis strategy for detecting nuclear positions 80
4.6 The algorithm for extracting cell nuclear and cytoplasmic fluorescence 81
4.7 A combined algorithm 82
4.8 Membrane fragment detection algorithm 82
4.9 Analysis of membrane and cytoplasmic fluorescence 83
4.10 Accuracy of sampling based image segmentation 84
4.11 Agreement between manual and automatic analysis approaches 85
4.12 Fluorescence sampling masks 86
4.13 Segmentation masks for embryonic heart tissue 87
4.14 Image analysis of SRF and NKX2 localisation 88
4.15 SilentMark graphical user interface 89
4.16 Combining geometric protein distribution analysis 90
4.17 Creating a standard score 91
4.18 Cdx2 expression variation with distance from embryo surface 92
4.19 Integrating distance measurements 93

5.1 The two geometric niches in the pre-implantation embryos 96
5.2 The Hippo pathway specific to pre-implantation development 98
5.3 Transcription of known trophectoderm factors 102
5.4 Transcription of known inner cell mass factors 103
5.5 Correlations between selected transcription factors 103
5.6 Transcription of core Hippo pathway components 104
5.7 Transcription of various cell polarity components 104
5.8 Cdx2 and Yap patterning 106
5.9 Cdx2 and Yap protein distribution analysis 107
5.10 Cdx2 and Yap protein distribution analysis 109
5.11 Emergence of two geometrically distinct cell populations 110
5.12 Population emergence based on actin levels 111

5.13 Changing embryo shape with hydrogels 112
5.14 A summary of changes in embryo patterning 113
5.15 Emergence of geometric cell differences 115
5.16 Development of apico-basal cell polarity 116
5.17 Cell polarity development 117
5.18 Live imaging of dividing LifeAct blastomeres 118
5.19 Immunostainings of 16 cell embryo blastomeres 119
5.20 The proposed mechanism of the first cell fate decision 121

6.1 The second cell fate decision 123
6.2 Transcriptional profiles Hippo pathway components 129
6.3 Correlation of transcriptional profiles 130
6.4 Immunostaining of key signalling components. A) CGR8 cell embryoid bodies before differentiation (images representative of 15 embryoid bodies), B) and C) CCE embryoid bodies after outer cell layer differentiation (images representative of 6 and 7 embryoid bodies). Scale bars represent 50μm 133
6.5 Differential localisation of various proteins 134
6.6 Correlations of several signalling components 135
6.7 Hippo pathway after the second cell fate decision 136
6.8 Hippo pathway activity in confined embryoid bodies 137
6.9 Analysis of Yap and Gata6 localisation during tissue shape change . . 138
6.10 FRAP experiments 140
6.11 Summary of FRAP experiments 141
6.12 Dobutamine effects on Hippo signalling 143
6.13 Immunostaining of Cytochalasin D treated embryoid bodies 144
6.14 Analysis of Cytochalasin D treated embryoid bodies 144
6.15 Effects of blebbistatin on Hippo pathway activity 145

6.16 The role of embryoid body compression timing 146
6.17 The effects of tissue compression 147
6.18 The effects of blebbistatin treatment. 147
6.19 Blebbistatin effects on differentiated CCE cells 148
6.20 Blebbistatin effects on differentiating CCE cells 149
6.21 Quantification of blebbistatin effects on CCE cell differentiation . . . 150

Nomenclature

AFM Atomic force microscopy

DMSO Dimethyl sulphoxide

DNA Deoxyribonucleic acid

dpc days post coitum

EB Embryoid body

Fgf Fibroblast growth factor

Fgfr Fibroblast growth factor receptor

FISH fluorescent *in situ* hybridization

FRET Frster resonance energy transfer

*Gata*6 GATA Binding Protein 6

GelMA Gelatin methacrylate

HAMA Hyaluronic acid methacrylate

ICM Inner cell mass

LAP Lithium acyl phosphinate

LATS Large tumor suppressor kinase

LIF Leukaemia inducible factor

LSM Laser scanning microscope

MAL Megakaryocytic acute leukaemia protein (also known as MRTF)

$MRTF$ Myocardin related transcription factor

MW Molecular weight

$MWCO$ Molecular weight cut-off

$Nanog$ ES cell-associated homeobox protein 4

$NF-kB$ nuclear factor kappa-light-chain-enhancer of activated B cells

PBS Phosphate buffered saline

$PEGDA$ Polyethylene glycol diacrylate

RGD L-arginine, glycine, and L-aspartic acid

RNA Ribonucleic acid

$RPKM$ Reads Per Kilobase of transcript per Million mapped reads

$scRNA-seq$ Single cell RNA sequencing

SRF Serum response factor

TAZ WW domain-containing transcription regulator protein 1

TE Trophectoderm

TEM Transmission electron microscopy

YAP Yes associated protein

ZP Zona Pellucida

Chapter 1

Introduction

Mammalian tissues are composed of a large variety of individual cells, each having a distinct lineage and contributing to the overall tissue functionality. The complexity of tissue architecture is achieved consistently throughout development, which demonstrates existence of tight cell fate regulation. Understanding these regulatory mechanisms is crucial for understanding diseases stemming from cell fate dysregulation and applications of tissue engineering to regenerative medicine.

So far much focus has been given to identifying and characterizing the chemical and genetic components of the molecular pathways responsible for tissue development [1, 2, 3, 4, 5]. While tissue geometry has also been shown to play important roles in these pathways, very little is known about the actual mechanisms that allow cells and tissues sense their mechanical properties. This gap in knowledge is due to the lack of suitable tools to manipulate and characterize the mechanical properties of a tissue.

The first decade of the 21st century saw a proliferation of experimental techniques to study mechanotransduction at the cell level. Most have focused on investigating fast events at a cellular resolution, which revealed the role of cytoskeleton and other upstream signalling elements. The subsequent rise of high throughput hydrogel based tools made it possible to study tissues on a developmental timescale and investigate signalling cascades involved in geometric sensing. Despite these advances and the move towards single molecule and single cell techniques, we still lack the information

on how geometric signalling integrates information at the different levels (Figure 1.1).

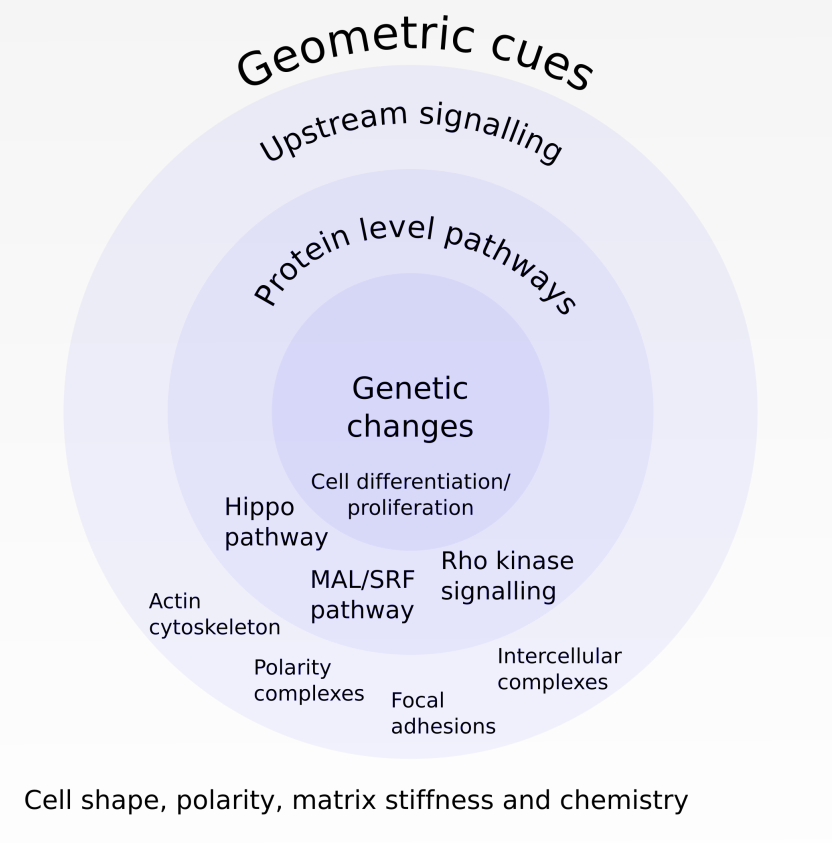


Figure 1.1: Summary of known geometry sensing mechanisms. Geometry is translated to genetic changes via several signalling levels involving structural proteins (upstream signals), kinases and then transcription factors acting on genes downstream of the signal. It is difficult to integrate different elements into a generalised understanding.

The motivation behind this thesis is to understand how developing tissue geometry generates feedback for cell fate control. The work focuses on the first cell fate decisions, which form the foundation of mammalian development. The first three experimental chapters are dedicated to developing tissue micromanipulation and characterisation techniques and the final two - investigating the role of geometry in the first and second cell fate decision events occurring in mouse pre-implantation embryos and stem cell organoids. This introductory chapter is organised to familiarise with existing work in the field of cell geometry sensing, the recent shift towards tissue-level

experimental systems and the most important transcription factor level signalling components.

1.1 Cellular-level mechanical sensing

Fundamentally, all cells are chemical systems and mechanical information ultimately has to be effectively converted into meaningful biochemical changes. This process is termed mechanotransduction and is most commonly investigated in the single cell context. Although sub-cellular mechanical sensing is not the focus of this thesis, it does form the foundation for hypotheses about tissue geometry sensing at the systematic level.

Historically, there have been multiple hypotheses about cellular mechanical sensing [4], even prior to robust evidence, that cell fate can be determined by matrix stiffness alone [6]. Such discoveries created the modern trend of mechanotransduction and led to development of new micromanipulation [7, 8, 9], measurement [10, 11, 12, 13, 14] and analysis techniques. The trend yielded multiple theories about how physical cues transform into biochemical changes [15], most of which focused on cellular cytoskeleton [16], actin/myosin based contractile machinery [17] and adaptor proteins [18], such as Integrins [19], Vinculin [20] and Cadherins [21]. These high temporal resolution techniques were particularly suitable for revealing details of cellular deformation events. Short timescale experiments on single cells made it possible to discover a lot of information on mechanosensitive channels [22], Rho kinases [23], MRTF/SRF [24] and YAP/TAZ [25] signalling. One challenge that has not attracted enough attention so far is integrating all of the information on different cell lines and pathways into a more complete picture of how mechanical information translates to transcriptional control [26].

Although we now know many protein candidates involved in mechanotransduction, there is much less information on how they act together. For example, it still is not

understood how matrix stiffness sensing works on a molecular level [27, 28, 29, 30]. One of the most popular theories describes cortical cytoskeleton as a collection of myosin motors acting on focal adhesion clutches via constantly polymerising actin fibers [31]. The rate of myosin pulling and phosphorylation becomes dependent on the rate of actin binding to focal adhesions, which provides a biochemical link between substrate rigidity and cell biochemistry. Other theories consider the changing rates of actin polymerisation [32] and capping protein processing [33]. Overall, despite the known details, there is still very little understanding of how mechanical information is perceived, however cytoskeleton is likely to be involved.

1.2 Methods for investigating single cell geometry and mechanics

Development of modern biomechanical experimental techniques has been crucial for uncovering the previously mentioned biochemical pathways. The technologies aimed at single cell experimentation usually have excellent temporal and spatial resolution, as in the case of atomic force microscopy. This enables high resolution measurement of cell stiffness and involved forces [34, 35, 36, 37]. Atomic force microscopy allowed to demonstrate various responses of single cells exposed to mechanical stimuli [38] and form hypotheses on mechanisms for stem cell differentiation [23, 36]. In addition to atomic force microscopy, micropipette aspiration has also become a popular tool for probing tissues at a cellular resolution. In addition to probing mechanical properties [39], the advantage of this technique is in studying cell adhesion forces and testing mechanical cell signalling hypotheses [7].

Atomic force microscopy and micropipette aspiration have traditionally been specialist techniques requiring a complex set up, that is often incompatible with the requirements for developmental biology experiments. This makes it difficult to study cells over longer timescales and investigate developmental changes resulting from

cellular deformation. As a result, several indirect mechanical micromanipulation techniques have been developed for more biocompatible experimentation. Magnetic micro-rheology is one option, which requires an adhesive magnetic bead and a high power electromagnet. This technique does not generate as large force range, as atomic force microscopy, but allows to apply deformation to cells for longer periods of time without a direct mechanical contact. It has been used for studying viscoelastic properties of cell membranes and cytoplasm [40, 41, 42], especially in relation to external cues [43]. Similarly to magnetic tweezers, optical tweezers produce similar levels of deforming forces [44] and have also been used to investigate cells [45, 46], position them to create unnatural tissue geometries [47, 48] or sort [49, 50] using microfluidics. Microfluidic techniques have also been used to deform tissues using shear flows and measure their responses during mechanotransduction experiments [51].

In general, less invasive mechanical deformation methods rely heavily on mathematical models to explain experimental observations and extract measurable parameters. Traction field microscopy is the most famous technique, where cell-level mechanics are characterised by a measured displacement of elastic hydrogels [13, 52, 53, 14]. Another commonly used technique for indirect mechanical measurements is based on FRET force sensors [54, 55]. These rely on well-characterised proteins bearing fluorescent markers (FRET pairs) with a known distance between them. Despite the mathematical complexity, these tewchniques offer the advantage of measuring mechanical properties during minimally invasive live experiments.

Single cell measurements have built an approximate picture of mechanical properties at various biological environments and scales (Figure 1.2). However, as different measurement methods work on different principles and have fundamentally different underlying physics, it is unsurprising, that reported stiffness values, viscosity and tension measurements often disagree between methods and even laboratories. Stiffness of Zona Pellucida has been reported to be around 80kPa by AFM measurements

[56] and 2-14kPa by micropipette aspiration [39], depending on the used mechanical models. Cell mechanical property measurements also vary from a few 100Pa [57, 58] to 5kPa [59]. These are some of the examples demonstrating the importance of context and instrumental setup, when comparing different reports. The reason behind these inconsistencies lies in the intrinsic mechanical complexity of biological systems, which means that reporting a single value, such as stiffness, requires making assumptions about the timescale and spatial scale of the measurement. Although this can be partially solved by building mechanical models [58], there are no standardised or widely accepted strategies. Therefore, in order to form comparative and representable mechanical observations it is crucial to maintain experimental consistency.

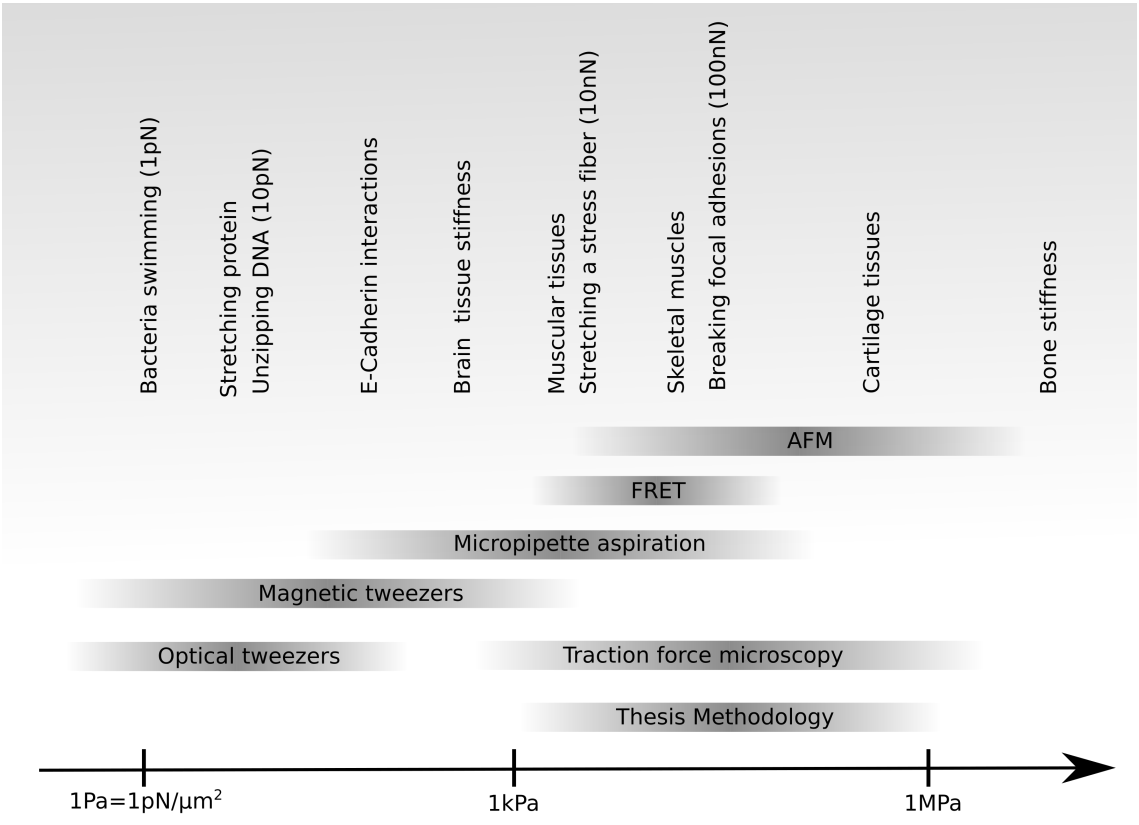


Figure 1.2: Summary of mechanical experimental techniques [15]. The figure combines multiple reports on the use of different techniques for measuring mechanical forces in different contexts.

The effects seen at the single cell level eventually translate to system level changes

seen in overall tissues. Integrating cell-level knowledge has proven particularly challenging, not just because of the variability seen in different reports, but also measurements themselves, which by design do not usually reveal intercellular mechanics. As a result, modern methodology has been moving towards more integrative measurements and automated higher-throughput, longer timescale experimental platforms.

1.3 Tissue-level geometry sensing

Studying the role of geometry (the shape and arrangement of cells within a tissue) at a systematic level is crucial for understanding tissue development. In comparison to single-cell techniques, three dimensional tissue studies pose additional problems with sample heterogeneity, sample handling and imaging. The first step towards integrative whole tissue experiments was investigating behaviour of 2D cell cultures grown on different gels and confinements [4]. Although this work predates most of single cell mechanotransduction, only recent technical developments [60] (Figure 1.3) allowed robust experimentation and high-throughput screening. The advances in material science were used by the bioscience community to discover potential target genes and transcription factors, which are involved in sensing and responding to mechanical changes in cellular environment [25].

The high-throughput nature and biological compatibility can be attributed to the ability to create well defined adhesion patterns and tuneable stiffness [24, 61] (Figure 1.3). Hydrogel transparency and biocompatibility due to high water content made it possible to use such systems for longer timescales with microscopic imaging. Using such geometrically defined hydrogel culture it was possible to identify some of the most fundamental tissue geometry sensing pathways including the Hippo pathway based on YAP/TAZ [25, 62], as well as MAL/SRF pathway [63, 64] and many others based on cell polarity [65, 66, 67, 68]. While these experiments revealed previously unseen mechanisms, they were still confined to 2D environments, which lack the

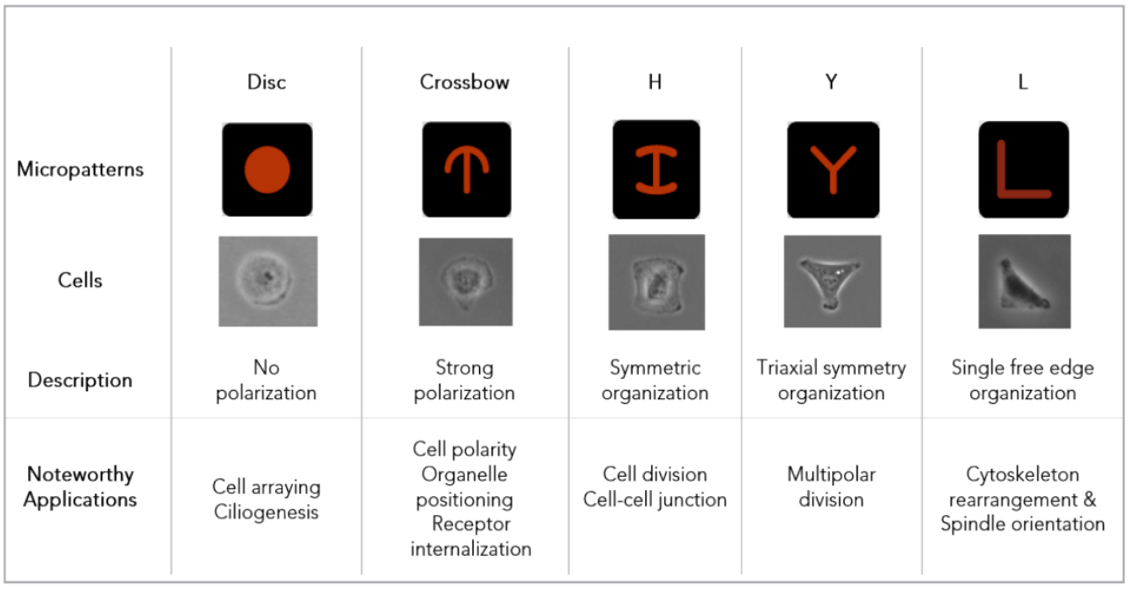


Figure 1.3: Commercial mechanotransduction research tools by Cytoo, image source: product catalogue

physiological relevance, except for planar epithelial tissues. In order to recreate the complexity seen in three dimensional environments, it is necessary to add another dimension to these patterned hydrogel substrates.

1.4 Defining 3D tissue shape

The shift towards growing tissues in three dimensional environments is quite recent despite the availability of matrices such as collagen, fibronectin and Matrigel [69, 70]. The trend towards recreating biological 3D model systems was largely driven by the increasing number of report stating that cells behave differently whether they are grown on 2D plastic or more representative three dimensional environments [5, 71, 72, 73, 74]. Cells generally require engagement with ECM, and one of the major challenges in the field is recreating chemical and mechanical environments that mimic the natural counterparts.In 2D culture this is achieved by coating plastic with gelatin and 3D cultures often employ collagen and Matrigel, as chosen biomaterials containing RGD amino acid fragments required for integrin engagement. Although such cell

derived materials are superior in supporting *ex vivo* tissue development, hydrogels such as collagen or matrigel are difficult to form into microscopically defined shapes. Furthermore, issues with variability and immunogenicity prohibit their use in clinical settings [75, 76]. As a result, synthetic hydrogels gained popularity due to well defined material properties, despite requiring more complex preparation.

Commonly used hydrogel materials can be classified into two broad categories based on their natural or synthetic polymer origins [77]. Synthetic materials generally benefit from better defined chemical and mechanical properties, while their biological counterparts usually offer better and more relevant cell culture environments [78]. Semi-synthetic materials have been recently emerging to create a third hydrogel type, which has both well defined chemical/mechanical properties and an optimum biocompatibility profile. This is achieved by using chemical modifications [79, 80] of relevant biological polymers to convert them into cross-linkable materials and form mechanically stable and defined gels.

Semi-synthetic hydrogels are created via several available modification strategies to introduce cross-linking capabilities (Figure 1.4). The reactions may involve Chemistry ranging from Click-type [81], Diels-alder [82] and Michael [83] chemistry to basic amine cross-linking [84] and mechanically interpenetrating networks [85]. The most popular strategy so far, has been to use methacrylate chemistry. This is due to the simple and scaleable preparation of starting materials and most importantly, the use of photochemistry, which is not only biocompatible, but also allows to create three-dimensional structures via photolithography [86, 87, 88] and 3D printing [89]. Using this modification strategy, virtually any biological polymer can be converted into hydrogels including gelatin [90], hyaluronic acid [91], chitosan [92], agarose [93], alginate [94] and keratin (chicken feathers) [95].

Among the methacrylated polymers, two materials in particular - gelatin and hyaluronic acid, have gained popularity due to the advantages of being able to mimic

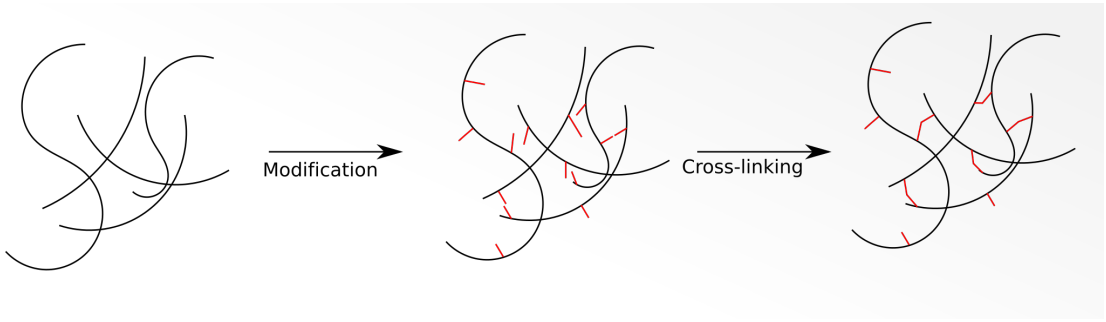


Figure 1.4: Creating semi-synthetic hydrogels by chemically introducing new functional groups to enable cross-linking

the natural extracellular environment. Gelatin is a polymer mixture based on collagen, which can support cell adhesion through integrins and RGD amino acid motifs. It is a readily available material, which is also routinely used for *in vitro* cell culture and clinical applications. Methacrylate modification makes it possible to create gelatin based hydrogels, with mechanical properties mimicking natural tissues [96]. Hence, it has become a popular bioengineering tool with *in vitro* and *in vivo* [97] applications. Hyaluronic acid is another naturally occurring extracellular matrix component, that is commonly used in the clinic. However, as it is a polysaccharide and does not contain integrin binding domains, it has to be chemically modified for *in vitro* cell culture [98, 52]. Compared to gelatin, hyaluronic acid is a hydrophilic polymer, which forms gels at low concentrations, making it possible to tune gel chemistry without significantly affecting overall hydrogel composition.

Most hydrogels are well characterised in terms of mechanical and biochemical properties in their original publications. However, as mentioned previously, different methods and experimental setups make it difficult to compare mechanical properties of different gels and particularly, living tissues. This creates a problem for creating biomimetic mechanical environments. Therefore, to create a mechanically well-defined experimental system it crucial to use the same characterisation techniques for various hydrogels and living tissues, which is the subject of the second chapter. Furthermore, knowing accurate stiffness can be used to model a relationship between

observed deformation and acting force [99, 100], which is discussed more widely in the next section. The overall combination of these advantages led to an increasing use of 3D patterned hydrogels [101, 47, 102, 103] for organoid culture [104, 105, 106, 107] and 3D force measurement [108].

1.5 Measuring tissue-level forces

Defining tissue shape and mechanical environment is the key requirement for researching mechanotransduction. In order to make it possible to put the observations into perspective and use this information for mathematical modelling, it is necessary to measure mechanical forces involved in tissue shape changes. Since hydrogels are elastic, it becomes possible to estimate mechanical forces by measuring observed gel deformations. Similar ideas have already been used in a 2D context in the form of deformable pillars [109, 21, 61] and traction force microscopy [14, 108]. Also, other deformable objects, such as modified oil droplets have recently been used for measuring tissue-level mechanical responses [110] inside developing tissues. In comparison to oil droplets, hydrogel stiffness does not scale with object dimensions, which makes it more practical to measure smaller tissue dimensions and small involved mechanical forces. The only remaining challenge then becomes mathematical modelling, which would translate observed deformations to physically relevant force values.

Calculating elastic body shape changes is the focus for the field of contact mechanics [111]. There has been several analytical solutions for simplified contact models, which are used for working with objects like ball bearings, bullet impacts and atomic force microscopy contacts [112]. With growing object complexity, it becomes impossible to develop analytical solutions and in these cases finite element modelling software is used to predict forces involved in deforming hydrogel objects [113].

To measure forces arising due to tissue growth, the simplest possible system can be created by using cylindrical channels to confine spherical tissues. As the tissue grows,

the cylindrical cavity becomes increasingly deformed and from the level of deformation it is possible to calculate involved forces, provided that hydrogel stiffness is known (Figure 1.5). The radial symmetry also makes it possible to avoid using confocal microscopy, which would otherwise be required for capturing complete 3D shapes, because cylindrical symmetry allows to recreate and approximate 3D shape from tissue profile.

The pressure measurements are then useful for understanding tissue-level forces generated in growing spheroids [71, 114, 115, 116, 117] and pressurised cavities [117, 118, 119, 120]. These are fundamental developmental biology elements found in various of contexts, including embryo [118, 120], organoid development [71, 121] as well as cancer [122, 116]. As a result, the role of mechanics in matrix remodelling is becoming increasingly recognised and it is becoming an interdisciplinary subject, involving physics and mathematics. Measuring forces is the foundation of quantitative understanding of developmental dynamics and hydrogel tools developed here (Figure 1.5) provide a biocompatible and a long term mechanical characterisation platform in addition to existing high spatial and temporal resolution techniques, such as AFM, FRET sensors and micropipette aspiration (Figure 1.2).

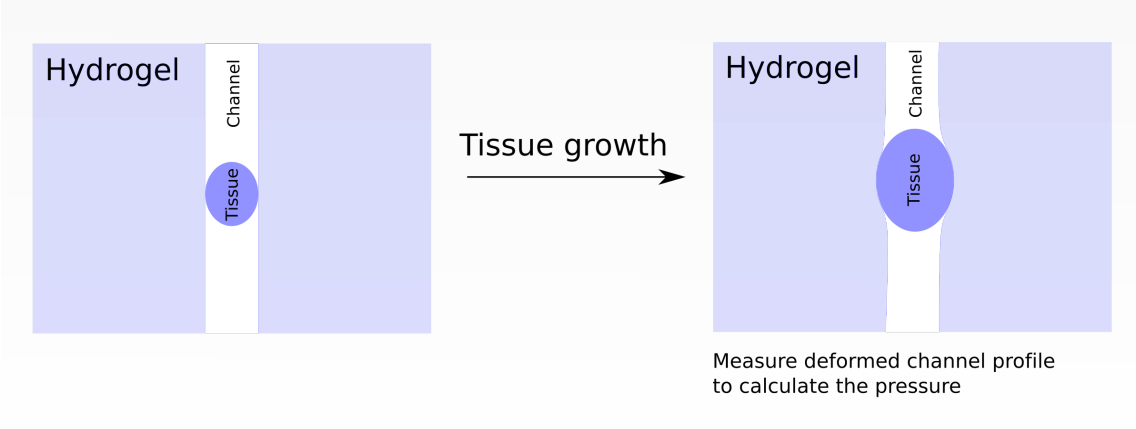


Figure 1.5: Measuring forces generated during tissue growth by hydrogel deformation. Developing tissues are inserted inside hydrogel cavities and the extent of hydrogel deformation can be used to calculate the forces exerted by tissues.

1.6 Analysing tissue-level biochemical responses

Just as measuring forces is important for understanding mechanical implications of tissue development, quantifying changes in cell biochemistry is crucial for understanding the biological outcomes. There are already many available molecular biology tools for protein (western blotting, mass spectrometry), DNA and RNA analysis, even at the single-cell level [123]. However, most quantitative techniques require destroying or disaggregating the sample, which ultimately results in loosing the information of relative cell position within the tissue. The methods looking at average protein and RNA levels are also difficult to interpret, because the readings do not represent cell heterogeneity in the samples. Therefore, to investigate tissue differentiation, it becomes critical to look at changes at the individual cell-level, rather than whole tissues.

There are several methods, which can probe tissue biochemistry at cellular resolution (*in situ* hybridisation [124] and fluorescent *in situ* hybridization (FISH), immunofluorescence, and TEM [125]). The most established of these techniques, which can also provide geometric information relies on confocal microscopy [126] and having either fluorescent protein reporters or specific antibodies binding to proteins of interest (immunostaining). There are two major experimental difficulties (apart from high price) why microscopy-based protein measurement tools have not reached widespread use.

Although several software tools are available for segmenting tissues into single cells, most are developed for specific cases or organisms. Mammalian tissues being particularly problematic due to high optical and experimental noise levels and tight cell packing. In addition to the problem of tissue segmentation, there has been little progress in developing robust analytical approaches, which would allow to internally normalise fluorescence levels making the measurements robust to experimental settings and optical tissue heterogeneity. In order to solve these issues new approaches

to 3D image analysis are required, which forms the basis of one of the chapters.

In order to remove bias from fluorescence measurements, previous 2D analyses used ratios of nuclear and cytoplasmic fluorescence intensities [25, 33]. Taking a ratio of two nearby cellular compartments provides an effective internal normalisation, which helps to overcome experimental variability and optical tissue heterogeneity. However, it requires cell sub-segmentation into compartments. While such 2D segmentation is possible manually, manual 3D outlining is extremely time consuming. Furthermore, images obtained from routine confocal microscopy of mammalian tissue samples often suffer from high noise to signal ratio, which makes it difficult to determine cell outlines, even during manual processing [127]. This requires a different strategy, which would be possible to automate and accept relatively noisy samples.

There are several existing tissue segmentation strategies ranging from basic thresholding, seed growing [128], watershedding [129], geodesic image segmentation [130] and tensor based voting [127]. Watershedding is one of the most commonly used techniques for separating 3D objects, because it does not make assumptions about object geometry. One of the main weaknesses is separating touching objects, which is sometimes solved by assuming, that segmented objects are round. Watershedding is also prone to noise, but that can be overcome by filtering objects by volume or area. In contrast, tensor based voting techniques, such as Hough Transform [131], are the most robust to noise, because they make a lot of assumptions about the searching object. The drawback however, is computational time, which rapidly increases with increasing shape complexity. Exceptions are Hough line and circle detection, both of which can be described by two parameters and are usually faster than watershedding feature extraction techniques.

Cell nuclei are the simplest features to detect due to availability of high signal-to-noise ratio DNA stains and relatively large internuclear separations. As a result, there are several existing available commercial tools including Imaris (Bitplane) and

Volocity (Perkin Elmer), as well as open source platforms such as MINS [130] and Fiji/ImageJ [132]. However, estimating protein concentrations from raw fluorescence readings is complicated by several factors. To begin with, fluorescence is determined by the image acquisition settings, such as laser intensity or detector gains. Fluorescence is also influenced by tissue optical properties, as regions further away from the objective appear dimmer and some of tissue regions may also be naturally more opaque. Finally, the relationship between observed fluorescence levels and protein concentration is dependent on the antibodies and experimental protocol. These factors make it difficult to quantitatively compare immunofluorescence images between different measurements or users.

In order to overcome these problems (segmenting mammalian cells and using fluorescence to estimate protein concentration), I have developed a software tool enables to look for protein level variations within different tissue regions. The main ideas behind the algorithm and its development are outlined in chapter 4. I have relied on this technique to investigate embryonic stem cell development, particularly in relation to the Hippo pathway (Figure 1.6).

1.7 The Hippo pathway

Hippo pathway was originally discovered during Drosophila knockout experiments to control tissue overgrowth [133, 134]. The same mechanism was also later discovered in mammals and also shown to respond to basic changes in *in vitro* tissue shapes [25]. Mechanotransduction experiments revealed that a pair of proteins (YAP and TAZ) localise differently within the cell in response to tissue stiffness and size sensing [25]. This sparked broader interest because of their ubiquitous and context dependent roles (Table 1.1). It provided the first robust link between tissue mechanics and other well established pathways [135, 136, 137, 138]. However, it is still largely unclear what are the upstream mechanisms, which directly respond to mechanical changes and

control phosphorylation of these proteins. It is worth mentioning, that in addition to these two essential Hippo pathway proteins, screens also revealed involvement of NF-kB and MAL/SRF actin sensing networks [25]. However, the latter received less attention due to their less widespread expression.

Hippo signalling pathway consists of a cascade of phosphorylation events, which converge on YAP and TAZ proteins, shuttling between the nucleus and cytoplasm depending on their phosphorylation status [136]. In the nucleus these components act as transcriptional co-activators for a variety of genes and their effects depend on context. Three notable cases, where this pathway has been investigated in great detail include intestinal crypts [139], mammary epithelial cells [25, 33] and mouse pre-implantation embryos [140, 141, 142]. Stem cell field has also received substantial attention, however there are conflicting reports about the roles of YAP/TAZ proteins. One view reports YAP activity as being a sign of cell pluripotency and progenitor expansion [143], while other reports suggest, that nuclear YAP is required for differentiation from the pluripotent state [144].

By comparison, the actin sensing MAL/SRF system [64] has received less attention than the YAP/TAZ pathway. However, it still presents another important mechanical sensing mechanism [26]. In comparison MAL has a better defined upstream mechanical sensing mechanism, as it has been demonstrated to bind actin monomers directly [64] thereby sensing actin dynamics, which depend on geometric environment and kinase activity. Identification of these geometry sensing pathways became possible due to the availability of reproducible 2D tissue deformation platforms. In order to make the next step to look at the whole tissue level and more relevant timescales it is necessary to move towards 3D experimental systems [110, 108] due to higher biological relevance and the fact, that many geometric cues do not exist at all in two dimensions. Cell density cannot be investigated without neighbouring cells and the role of cell position cannot be tested without considering the tissue as a whole.

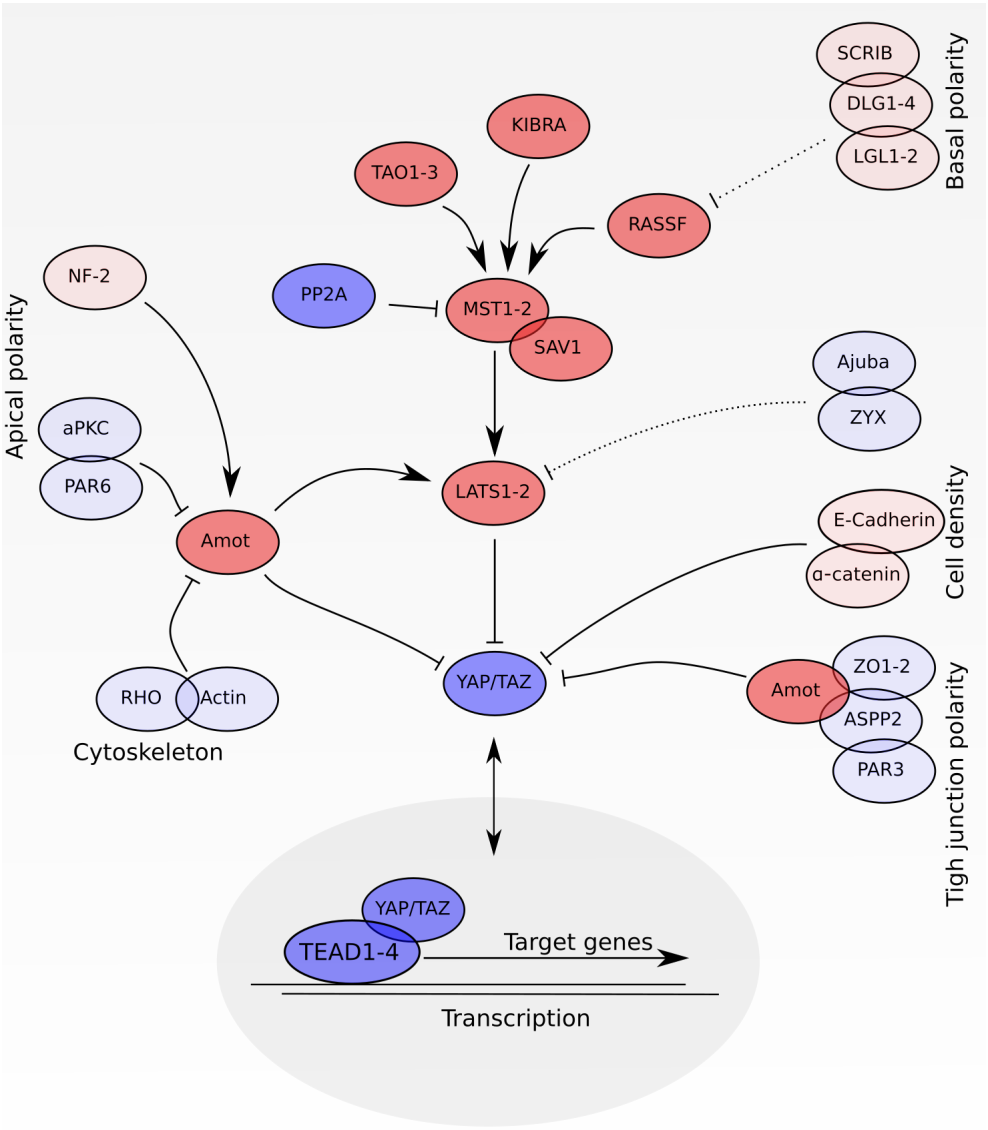


Figure 1.6: Overview of the context dependent Hippo pathway. Components, whose phosphorylation is responsible for pathway up-regulation are marked in red and components whose phosphorylation is responsible for down-regulation are marked in blue. The pathway is described in more detail in table 1.1.

To look at the role of geometric cues in three dimensional tissues, I have chosen two biological model systems: mouse pre-implantation embryos and embryonic stem cells. Working with embryos has three major advantages:

- Existing knowledge. While developing new methods it is important to have a framework of existing information, which would allow to validate the techniques.

Table 1.1: Context dependent Hippo signaling

Hippo components	Relationship	Context
TEAD1-4	Transcription factors	Pathway core
YAP/TAZ	TEAD1-4 coactivators	Pathway core
LATS1-2	Kinases	Pathway core
MST1-2	Kinases	Pathway core
SAV1	Scaffolding protein, Downregulation	Mesothelioma [145]
KIBRA	Scaffolding protein, Downregulation	HEK293 cells [146]
AMOT	Scaffolding protein, Downregulation	Multiple [147, 148, 149]
TAO1-3	Kinase, Downregulation	Drosophila [150, 151]
PP2A	Phosphatase, Upregulation	Kc167 cells [152]
SCRIB	Upstream effector, Downregulation	Multiple [153, 154]
DLG1-4	Upstream effector, Downregulation	Drosophila [155]
LGL1-2	Upstream effector, Downregulation	Drosophila [155]
Ajuba	Scaffolding protein, Upregulation	Drosophila [156, 157]
ZYX (Zyxin)	Upstream effector, Upregulation	Drosophila [156, 158]
E-Cadherin	Upstream effector, Downregulation	Multiple [159, 160]
β-Catenin	Upstream effector, Downregulation	Skin [159, 161]
ZO1	Upstream effector, Upregulation	Mouse embryos [149]
ASPP2	Upstream effector, Upregulation	Multiple [162, 67]
PAR3	Upstream effector, Upregulation	Drosophila [163]
NF-2	Upstream effector, context dependent	Multiple [145, 164]
aPKC	Upstream effector, Upregulation	MDCK cells [165]
PAR6	Upstream effector, Upregulation	Mouse embryos [166, 149]
ACTIN	Upstream effector, Upregulation	Multiple [33, 167]
RHO Kinase	context dependent	NIH3T3 Cells [167]

- Reproducibility. Mouse development is highly conserved, even between different inbred wildtype strains. The small inter embryo variability makes it possible to look for even subtle changes and reliably compare with existing knowledge.

- Standardised culture. Compared to stem cell culture, pre-implantation embryo culture media is fully defined, which again means less experimental variability.

Mouse pre-implantation embryo model system however, has several disadvantage related to material quantity. Even though a pregnant mouse often contains around ten embryos this still only corresponds to a hundred cells. As a result, a lot of standard analytical techniques for protein quantification are highly impractical as they required tens of thousands of cells. Also, looking at later cell fate decisions is problematic due to experimental difficulties with culturing embryos after the implantation window.

Therefore, in order to avoid problems with material quantity and later differentiation events I have chosen to use stem cell based organoids.

1.7.1 Mouse pre-implantation development

The first cell fate decision during mouse development happens 3 days after fertilisation and creates two tissues: trophectoderm (TE) and the inner cell mass (ICM) [168, 169, 140, 170, 171] (Figure 1.7). Trophectoderm later develops into placental tissues [172] and the inner cell mass forms the rest of the embryonic body [173, 174]. From the perspective of geometrically driven cell fate decisions, this is one of the most notable examples, where tissues are consistently patterned into inside and outside cell populations. The outside can be identified as the trophectoderm and inside cell correspond to the inner cell mass. The early process by which cells are segregated into populations is not only interesting from the geometric sensing perspective, but also crucial for the stem cell technologies [175, 176], which rely on our understanding of transcriptional networks and signalling [177, 178, 179, 180, 181].

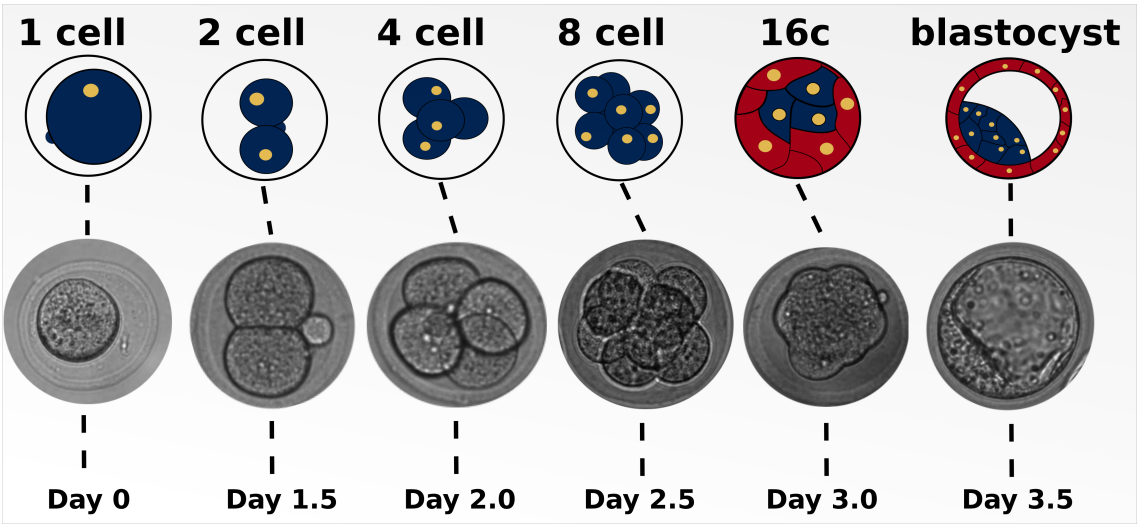


Figure 1.7: Summary of early mouse development, which begins with egg fertilisation and subsequent synchronised cell divisions, which divide the zygote (fertilised egg) into 2, 4, 8, 16 and 32 cell embryos. The first cell fate decision occurs approximately around the 16 cell stage. After the 32 cell stage embryos form a blastocyst, which escapes from its surrounding shell (Zona Pellucida) and implants into the uterus.

Despite recent progress, it is still not completely understood how cells make the decision to become TE or ICM cells at the time of differentiation. Several groups argue whether development is regulated at all or whether it is predetermined by asymmetric distribution of transcription factors, as is the case of invertebrates [182, 183]. Although existing evidence suggests, that the first cell fate decision is regulated [141, 184], it is unclear whether the cue is cell position [185], angle of cell division [186] or cell shape [135], as all of the theories have valid arguments. Also, due to reports of YAP/TAZ involvement in mechanotransduction, one of the theories considers mechanical forces and actin cytoskeleton, as a driver for cell differentiation [187].

If the first cell fate decision is considered to be regulated, there are several potential cues, to which it might be responding. Cell polarity is perhaps the most established signalling factor, as it has been shown that knockdown of cell polarity components results in failure to differentiate towards trophectoderm fate [149]. Since it has been shown that Hippo pathway controls cell fate specification at this stage [141], there have also been several other theories suggesting cell fate specification via sensing of mechanical tension and cell shape [167, 188].

Disentangling these potential cues is a difficult step without direct tissue manipulation, as cells on the outside invariably have flatter shape, fewer neighbours and are polarised. Genetic methods, such as gene knockouts or knockdowns can be used to test various hypotheses, however until now it has not been possible to test the role of geometry alone, without biochemical alterations. Looking at how Hippo pathway operates in the context of pre-implantation embryos and how it is affected by the overall tissue geometry is the focus of chapter 5.

1.8 Early stem cell organoid development

The discovery of transcriptional control networks operating in the inner cell mass during mammalian development led to creation of pluripotent stem cell technologies,

with a promise of personalised medicine. However, the lack of detailed mechanistic understanding has been one of the main obstacles during clinical translation relating to the lack of efficacy or even deaths due to teratoma formation [189]. In order to create more successful and sustainable tissue engineering technologies it is necessary to disentangle the differentiation mechanisms, which govern early tissue specification [178, 179, 181, 190, 191, 123].

After the first cell fate decision, which creates the pluripotent inner cell mass, it becomes increasingly difficult to study emergence of subsequent tissues. In part this is due to growing embryo complexity and in part it is due to less established tissue culture conditions. In order to look at later tissue development, stem cell culture is frequently used either in adhesion dishes [192], free floating spheroids [173] (also called organoids) or a combination of the two [193]. It is becoming increasingly recognised, that defined 3D culture environment is crucial for development of properly differentiated organoids.

While biochemical cues arguably dominate differentiation mechanisms, the role of tissue geometry is subtler and also more difficult to investigate. One of the examples is the second cell fate decision, which creates the primitive endoderm and epiblast lineages [194, 68, 180, 193, 195, 196, 197, 198, 199]. This is one of the most fundamental tissue differentiation events, on which many other organoid differentiation protocols rely [200, 201, 202, 107].

During early organoid development, the second cell fate decision (primitive endoderm and epiblast) takes place several days after withdrawal of conditions that maintain the pluripotent stem cell state (Figure 1.8). It resembles the first cell fate decision in pre-implantation embryos in a sense, that only the outermost cell layer of the organoid becomes differentiated. The outside layer appears distinct under the microscope [173] and expresses a variety of characteristic endoderm markers [198].

There are two dominant theories on the second cell fate decision, one stating, that

cells randomly express *nanog* and *gata6* transcription factors and then sort themselves into two tissues [203], while another implies an active fate regulation mechanism based on Fgf4 and Fgfr2 signalling [197, 198, 194]. With the methodology developed during this thesis it now becomes possible to directly look into the role of geometry during this tissue differentiation event defining the outer cell layer.

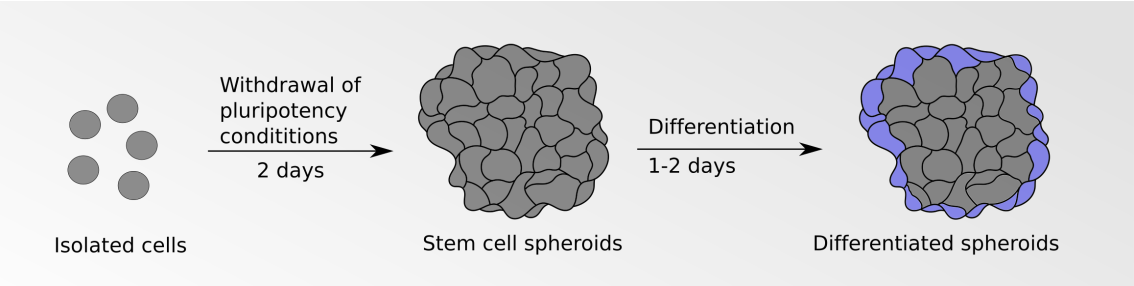


Figure 1.8: The second cell fate decision is similar to the first in that it creates a spherical tissue with inside/outside cell layers

1.9 Thesis aims

So far I have outlined the key challenges involved in investigating the means by which tissues can sense and regulate their shape. Previous experiments have largely focused on investigating mechanics at the microscopic and single cell level. Although this is useful from the perspective of fundamental biology, it also makes it difficult to integrate the information into a systematic understanding of tissue level mechanisms.

Micromanipulation methodology developed here makes it possible to test existing theories separately, as it becomes feasible to manipulate tissue shape and cell position, while investigating their mechanical responses. In addition to looking at pre-implantation biology, the embryos also present a consistent and well characterised system for testing the algorithms and methodology presented here. There is less known about the way cell fates are decided in stem cell organoids, and investigating these processes forms another important aspect of the thesis. Overall, the thesis is organised into the following aims:

- Develop methodology for controllably deforming tissues and measuring resulting mechanical changes (chapters 2 and 3).
- Adapt image analysis methodology to quantify geometric protein distribution within tissues (chapter 4).
- Test the role of tissue geometry during the earliest and most fundamental cell fate decisions in mouse embryos and embryoid bodies (chapters 5 and 6).

Chapter 2

Hydrogel tools for tissue micromanipulation

2.1 Introduction

Micromanipulation methodology is critical for investigating biochemical pathways responsible for sensing geometric tissue shape sensing. The means of translating information about cell's mechanical and topological environment into biochemical signals has been one of the most investigated areas in modern biology [5]. These signalling pathways are not only fundamentally interesting, but also important for a variety of developmental processes, tissue engineering and understanding cancer progression. After the rise of molecular biology tools for manipulating genetic cell information, the progress in the field of biomechanics has been largely limited by the lack of methods to mechanically deform and measure microscopic tissues.

Although there are multiple existing technologies, such as micropipette aspiration [204], atomic force microscopy [34], magnetic [42], optical [46] and microfluidic tweezers [51], there has been few ways to investigate whole tissue mechanics in a systematic manner. Furthermore, most of the existing methods have been limited to short timescale experiments, which are less relevant in the developmental biology context. Among the longer timescale techniques, one of the most successful tools was based on elastic hydrogel materials for controlling cell culture substrate stiffness.

While these techniques have worked particularly well for 2D culture, it has been more challenging to directly translate the knowledge into more relevant 3D contexts, although several examples suggested that it is feasible [52].

In order to create a 3D whole tissue micromanipulation platform, I extended the idea of using deformable elastic hydrogels. By creating defined 3D cavities, inside which developing tissues are grown, it is possible to establish an experimental platform, which can be used to define tissue shape and look at mechanotransduction pathways. Creating an experimental system for 3D tissue micromanipulation requires taking into account several requirements. Biocompatibility and mechanical reproducibility are paramount, but it should also be possible to pattern the hydrogels into defined microscopic shapes. Transparency is also desirable, as it allows microscopic examination during tissue development. Furthermore, several practical aspects are also important, such as material availability and mechanical stability.

Therefore, the first step in developing methodology is selecting an optimal hydrogel polymer and characterising it from mechanical, chemical and biological standpoints. Biological properties are mostly defined by the polymer backbone chemistry and mechanics result from the interplay of cross-linked polymer network and bound water molecules.

Methacrylated hydrogels are some of the most versatile and reliable biomaterials [205, 77, 206], which are rapidly gaining popularity in tissue engineering communities. These semi-synthetic materials can be patterned by light and made to mimic the stiffness and composition of natural tissues, which makes them suitable for both 2D and 3D cell culture [5, 52]. The most widely used materials include gelatin methacrylate (GelMA) [207, 96], hyaluronic acid methacrylate (HAMA) [208, 209] and polyethylene glycol diacrylates (PEGDA) [210, 211], which have been discovered over a decade ago. The former two biomaterials are usually used for mimicking the natural extracellular matrix, while PEGDA can make non-adhesive, inert hydrogels. Although

there are multiple cases where these materials were used for tissue engineering purposes, there is still a lack of systematic research, which would make them practical for unspecialised cell biology laboratories. Polyacrylamide gels belong to the same class of materials, however monomer toxicity makes it impossible to use for cell encapsulation, however being a micro-gel, polyacrylamide is otherwise superior in terms of mechanical reproducibility and robustness.

One of the less emphasised advantages of methacrylated polymers, is that this varied class of materials has a common cross-linking mechanism. This makes it possible to blend them together and create hydrogels with a wide variety of mechanical and biochemical properties. Three biopolymers were chosen due to their unique profiles: gelatin methacrylate, hyaluronic acid methacrylate and polyethylene glycol diacrylate. Gelatin methacrylate is the only polymer, which can without further modification directly support cell adhesion, through naturally occurring integrin binding domains [96]. Hyaluronic acid is unique in that it can increase hydrogel stiffness, without significantly altering overall hydrogel chemistry, as it can readily form hydrogels at concentrations lower than 0.1%. Finally PEGDA is biologically inert and can be used to reduce hydrogel degradation rates and cellular adhesion [212].

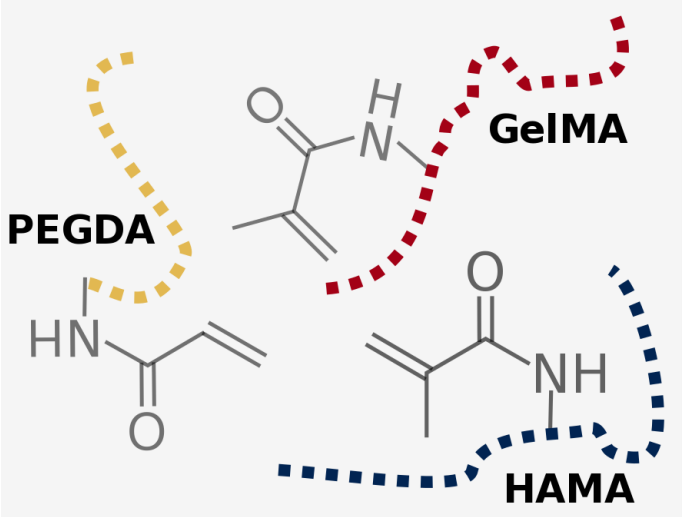


Figure 2.1: The common hydrogel cross-linking mechanisms allows to create blends combining different polymer backbones to achieve required bulk properties.

The main goal of this chapter is creating a well characterized and reproducible system for micro manipulating mammalian tissues. Hydrogel stiffness is central to the work, however difficult to relate to live tissues due to literature disagreements arising from different measurement techniques. One of the key aspects of this work is adapting a consistent measurement technique to create a link between tissue stiffness and hydrogel composition in order to create matching artificial culture environments. In order to choose an appropriate method for material characterisation, I considered a variety of approaches from AFM used for microscopic sub-cellular measurements to industrial material characterisation equipment.

For micro-gels, such as polyacrylamide, microscopic and macroscopic stiffness values usually agree [60, 213, 214], but for biomaterials such as collagen, microscopic and macroscopic measurements often do not match due to heterogeneity [215, 76, 34, 216, 217]. In order to avoid this issue and report stiffness values, which represent the mechanical environment perceived at a relevant developing tissue scale ($100\mu m$), I wanted to use a tool with an appropriate size indenter. Unfortunately, there were no available commercial devices working at such range, so I had to adapt a published method, based on microscopic indentation [213].

The next step was tuning hydrogel chemistry to specific cell types, which is necessary to ensure a biocompatible culture environment. Among the known factors, it mainly consists of ensuring cell adhesion via integrin binding molecules and natural matrix mimicking degradability. Since methacrylated materials share common cross-linking chemistry, they can be blended together to achieve required properties [212]. Therefore, three material components have been selected: gelatin for integrin adhesion, hyaluronic acid for tuning stiffness and polyethylene glycol for reducing gel degradability. Theoretically, blending these three materials should be sufficient to create a hydrogel variety that spans natural tissue stiffness and biocompatibility.

Finally, I also explored various hydrogel microfabrication techniques to create

shapes required for mechanotransduction experiments. These included a variety of published techniques based on sacrificial moulding [101] and photolithography. Photolithographic approaches could be accomplished with a variety of techniques using masks and collimated UV sources [91] or lasers [86], including confocal microscopy [218]. All of the three materials can be photo polymerised by using a variety of commercially available photo initiators, such as Irgacure 2959. This photo initiator is readily available, well characterised and biocompatible. As Irgacure 2959 operates at 365nm wavelength light, biocompatibility can be an issue, which can be solved by using longer wavelength photo initiators, such as Lithium acyl phosphinate [219].

2.2 Materials and methods

Polyethylene glycol diacrylate (PEGDA, MW 575), 2-Hydroxy-4'-(2-hydroxyethoxy)-2-methylpropiophenone (Irgacure 2959), Dimethyl sulfoxide (DMSO), 3-(Trimethoxy silyl) propyl methacrylate, Porcine type A gelatin, and hyaluronic acid (Streptococcus equi, unprocessed) were purchased from Sigma-Aldrich. An HCS DNA damage kit was purchased from Life Sciences. HEK293, LS180, CGR8 cell cultures were kindly provided by Christophe Royer, Shankar Srinivas lab. Methacrylated polymers were synthesised as previously reported [96, 212, 209], as well as LAP photoinitiator.

2.2.1 HEK293 and LS180 cell culture

Cells were cultured in T-25 flasks coated with 0.1% w/v. gelatin and used at passage nr. 50-60 (LS180) and 5-10 (HEK293). Cell culture media consisted of 90% DMEM medium (Gibco), 10% fetal calf serum (FCIII, Hyclone), 2mM L-glutamine, 100U/mL penicillin and 0.1mg/mL streptomycin. Cells were passaged every 3 days and seeded at 400,000 cells per T-25 flask.

2.2.2 CGR8 cell culture

Cells were cultured in T-25 flasks coated with 0.1% w/v. gelatin and used at passage nr. 50-60. Cell culture media consisted of 90% DMEM medium (Gibco), 10% fetal calf serum (FCIII, Hyclone), 1mM sodium pyruvate, 1mM non-essential amino acid mix, 0.1mM β-mercaptoethanol, 2mM L-glutamine, as well as 10^3U/mL leukaemia inducible factor (LIF). Cells were passaged every 2 days and seeded at 400,000 cells per T25 flask. For cell freezing and recovery, we used a medium containing 10% DMSO and 40% cell culture medium and 50% fetal calf serum.

2.2.3 Synthesis of gelatin methacrylate

Gelatin (1g) was dissolved at 40°C, while stirring in PBS (10mL, 10 mmol (hydrophosphate)). To this solution methacrylic anhydride (2mL, 13.4mmol) was added while stirring to yield an emulsion. The reaction was kept at 45°C for 50min and transferred into a dialysis tube (MWCO 12kDa). The mixture was dialysed against PBS for 2h, then against fresh PBS was replaced every 12h, until pH reached neutral. Then gelatin methacrylate was dialyzed against deionised water for 3d, replacing the water every 12h. Ultimately the solution was freeze-dried for 2d and the purity of GelMA was assessed by thermogravimetry. The yield was found to be 95% (950mg, white powder). The powder was dissolved in PBS buffer to make a 10% stock solution, which was autoclaved and stored at -20°C until further use.

2.2.4 Synthesis of hyaluronic acid methacrylate

The procedure was similar to Gelatin methacrylate synthesis, with a few changes to improve pH stability of the reaction. Hyaluronic acid (500mg) was dissolved in cold disodium phosphate solution (45mL, 100mM (Na_2HPO_4)). Methacrylic anhydride (1mL, 6.7mmol) was then added and the reaction was shaken to yield an emulsion. After 1h, Cresol red dye was added to monitor pH of the reaction and 10M NaOH (ap-

prox. 400μL, 4mmol) was added to neutralise the acid-producing reaction. The same was repeated after 5h. Then, additional methacrylic anhydride (0.6mL, 4.62mmol) was added and the reaction was left for 16h at 4°C. Then, more Cresol red was added and pH was balanced with 10M NaOH (approx. 400μL, 4mmol). The reaction was then transferred to a dialysis tube (MWCO 12kDa) and dialyzed against PBS, replacing the buffer after 2h and then every 12h, until pH became neutral. The hyaluronic acid methacrylate was then dialyzed against deionised water for 3d, replacing the water every 12h. The solution was then freeze-dried for 4d to yield a white powder (450mg, 90% yield), which was dissolved in PBS buffer, to make a 1% solution. After pH was balanced with 1M NaOH, the solution was autoclaved and stored at -20°C until further use.

2.2.5 Synthesis of Lithium acyl phosphinate photoinitiator (405nm)

Visible light photoinitiator was synthesised as described previously [219]. Briefly, Dimethyl phenylphosphonite (Acros Organics) was mixed with 2,4,6-trimethylbenzoyl chloride (Sigma-Aldrich). Under mixing, 3.2 g (0.018mol) of 2,4,6-trimethylbenzoyl chloride was added to an equal molar amount of dimethyl phenylphosphonite (3.0 g). The reaction mixture was stirred overnight, when a four-fold excess of lithium bromide (6.1 g) in 100 mL of 2-butanone was added and then heated to 50°C. After a solid precipitate formed the mixture was cooled to room temperature, allowed to rest for four hours and filtered. The filtrate was washed and filtered 3 times with 2-butanone and the solvent was removed by vacuum. The product, lithium phenyl-2,4,6-trimethylbenzoylphosphinate (LAP) was recovered as a white powder.

2.2.6 Hydrogel fabrication for cell culture

For 2D cell culture hydrogels were shaped into 150μm thick sheets by setting the gel between a coverslip of defined area and an inert surface. The glass coverslip

was pretreated with 3-(Trimethoxysilyl) propyl methacrylate by heating for 20min at 80°C and subsequently washing twice with absolute ethanol. Then, 15μL of a polymer mixture was placed on a Parafilm surface and a glass coverslip (11mm diameter) was placed on top. This layer of liquid was exposed to 400mJ/cm^2 of 365nm UV light (Stratalinker 2400, Stratagene. The glass coverslips with a hydrogel layer were then placed in 24-well plates and sterilized by a 5min 75% ethanol immersion. The gels were then equilibrated twice with at least 100-fold excess cell culture media for 15mins.

2.2.7 Mechanical hydrogel testing

Hydrogel stiffness was measured by a combination of a commercially available instrument Q800 DMA (TA instruments) and a custom built indentation device equipped with a 300μm diameter cylindrical stylus, as described previously [213]. DMA samples were prepared by setting gels (after 365nm photo polymerization) in a cylindrical mold (10mm diameter, 10mm height, 785μL). For all samples 400mJ/cm^2 UV exposure and 0.3% I2959 concentration were used to ensure complete cross-linking. Measurements from the DMA instrument were used to validate the measurements from indentation device, which was used to measure precious samples and mouse tissues, data of which are reported in the rest of the chapter.

Indentation samples were prepared by placing the polymer mixture (15μL) in a 2.1mm diameter plastic tube, exposing to UV light and then cutting the hydrogel to 2mm height cylinders. Stiffness (E) was calculated by averaging at least 5 readings and applying the equation 2.1 [213, 220], which requires known indentation depth (h, m), acting force (F, N), indenter radius (R, m) and Poisson's ratio (ν) assumed to be 0.5[213].

$$E = \frac{F}{2Rh}\left(1 - \nu^2\right) \tag{2.1}$$

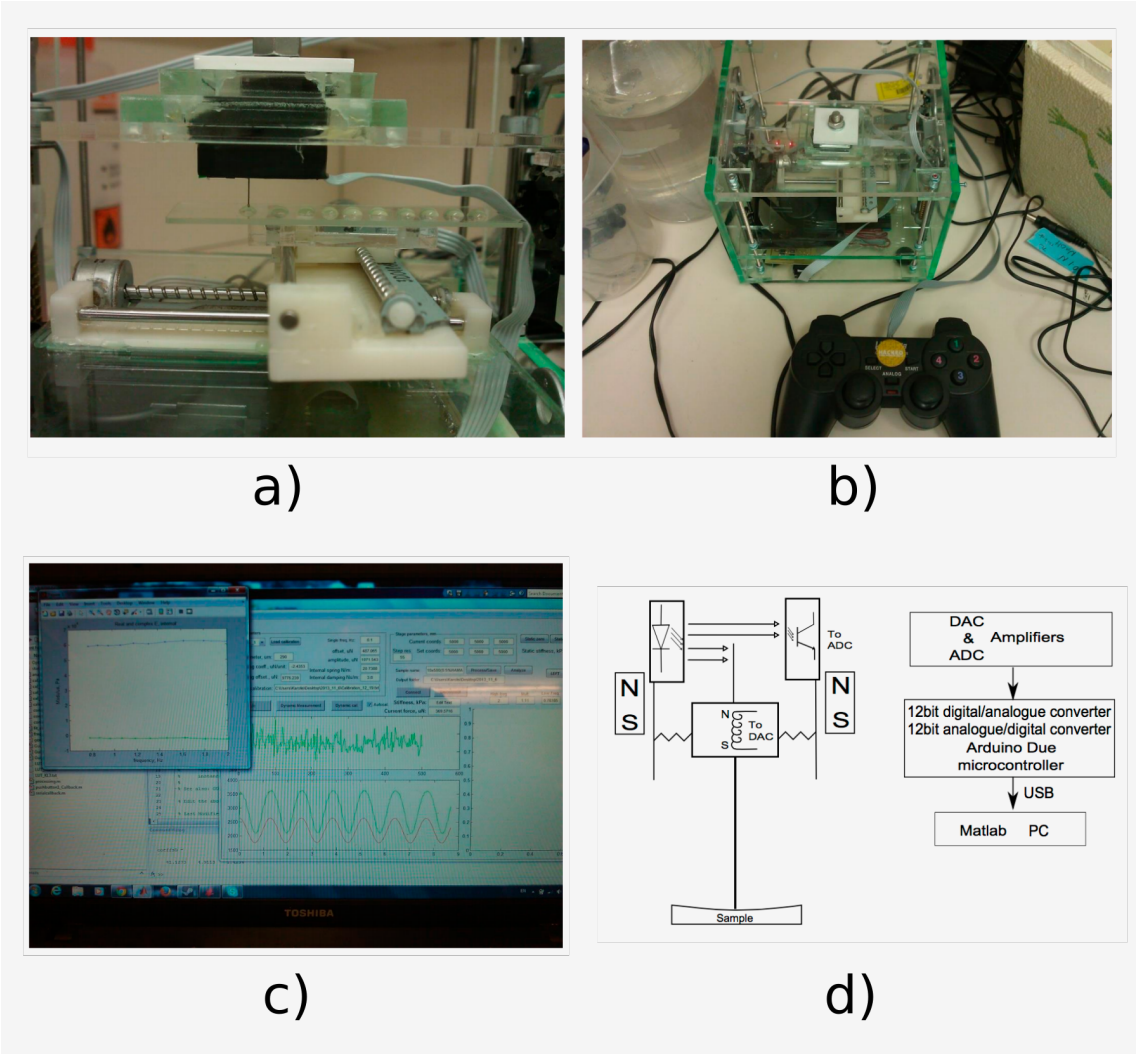


Figure 2.2: A device for measuring microscopic tissue stiffness: a), b) - Overall hardware setup, c) - Matlab based GUI, d) The principle schematic of a sensor consisting of a voice coil driven stylus and an optical window for position detection.

2.2.8 Biocompatibility testing

Mouse embryonic stem cells (CGR8) [221], colorectal cancer cells (LS180) [222] and human embryonic kidney cells (HEK293) [223] were cultured either on plastic or hydrogel covered surfaces. After 24h incubation the cells were washed from hydrogel surface with PBS solution and cellular area was measured with Fiji, while comparing the results to cell culture gelatin (0.1% w/v) coated glass coverslips.

2.2.9 Biodegradability measurements

Cylindrical hydrogels (15μL) were set in a 2.1mm diameter plastic tube by exposing to 365nm UV light. These hydrogels were then placed in a Collagenase I solution (1mg/mL, *Clostridium Histolyticum*) containing 150mM Tris and 10mM $CaCl_2$ buffer, at pH=7.7, 37^{o}C. Hydrogels were drained at selected time intervals, weight was recorded and samples were returned to collagenase solution [212]. Time points were recorded as triplicates and although stiffness was not recorded during degradation, the hydrogels could be seen becoming increasingly softer during the process.

2.2.10 Cell viability testing

HCS cell viability assay was used to simultaneously determine cell membrane permeability and DNA damage resulting from UV exposure. CGR8 embryonic stem cells were then encapsulated in 5% Gelatin methacrylate (100,000 cells/mL) in PBS using various concentrations of Irgacure and different degrees of UV exposure (Stratalinker 1800 UV cabinet, equipped with photodiode for exposure measurements). Cells were cultured for 16h and processed according to HCS kit protocol (Thermo Fischer) and imaged using a confocal microscope (LSM 710) and processed automatically using Imaris (Bitplane) software to measure levels of red and green fluorescence, which was partitioned into two populations (dead/alive) and relative cell counts measured.

2.2.11 Laser based direct-write hydrogel patterning

Gelatin methacrylate solution (5-10% in PBS, 15μL) containing 0.1% Lithium acyl phosphinate (LAP) was placed between a glass coverslip and a non-adhesive microscope slide (25x75mm). An unbranded 405nm laser pointer was focused to 10μm diameter dots and the gel was exposed to 0.5mW light for 45ms (Figure 2.3). Alternatively, 405nm laser from a confocal microscope (LSM 710) could be used to expose regions of the gel and created desired patterns.

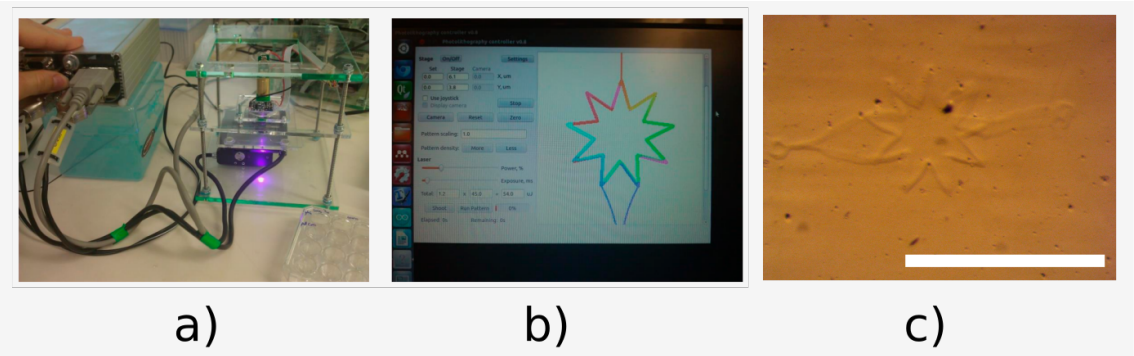


Figure 2.3: Laser based photolithography: a) Hardware setup for laser lithography, b) Graphical user interface (Qt based), c) A printed hydrogel pattern, scale bar - 1mm.

2.2.12 Using hydrogels to change tissue shape

Hydrogels with required thickness were created by photo-polymerising a selected volume of a hydrogel sandwiched between two inert glass surfaces. One option was embedding cells inside the hydrogels during polymerisation. Alternatively, two unpatterned hydrogel sheets were immersed under mineral oil and cells or tissues were placed between them. The surface tension forced the two hydrogel sheets together under oil compressing the tissues between them. Hydrogel stiffness (2.5-5kPa) could be used to control the level of compression. Finally, to avoid constant compression I developed a way to confine tissues in a closed space. This was done by creating one unpatterned hydrogel sheet (3x3mm) and one containing a pattern by photo-polymerising a hydrogel through a mask. Stacking these two sheets under oil created a cavity with a defined shape into which cells or tissues could be injected. This method was later simplified by moulding hydrogels over wires with a defined diameter to create cylindrical cavities, as these were sufficient for most experiments.

2.3 Results and discussion

2.3.1 Hydrogel stiffness

Surface stiffness has been recognised as one of the most important mechanical properties regarding tissue development [6, 25]. I found that the most reliable means of controlling stiffness is by varying polymer concentrations, which are summarised in Figure 2.4 along with stiffness values for the measured mouse tissues which are comparable to earlier reports [224, 225, 96]. As can be seen from Figure 2.4, hyaluronic acid methacrylate (HAMA) is particularly suitable for tuning stiffness, as it could form firm hydrogels even at low mass concentrations due to its high molecular weight and hydrophilic properties. PEGDA also increased hydrogel stiffness at a similar rate to gelatin methacrylate. In addition, the role of photo initiator concentration and UV exposure was also investigated for controlling blend stiffness (Figure 2.5) and it was found to have little effect beyond 0.1% for Irgacure 2959. This information can be used to create stiffness gradients, by using photomasks, as described previously [208, 226, 210].

2.3.2 Cell attachment

The ability to support cell adhesion is one of the most important biochemical properties, which determines cellular engagement with their surrounding matrix [52]. Three different cell lines HEK293 [223], LS180 [222] and CGR8 [227] were used to test hydrogels in their ability to support adhesion (Figure 2.6).

I found that cell attachment was not dependent on the total polymer concentration or stiffness of the blend. However, for HEK293 and CGR8 cells the fraction of gelatin methacrylate (GelMA) had to be greater than 30% (Figure 2.6b) for them to remain attached to the surface. This observation agrees with the current understanding of integrin based cell binding requiring substrates to contain RGD amino acid motifs, which in our case are naturally occurring in the gelatin component of the blend [228].

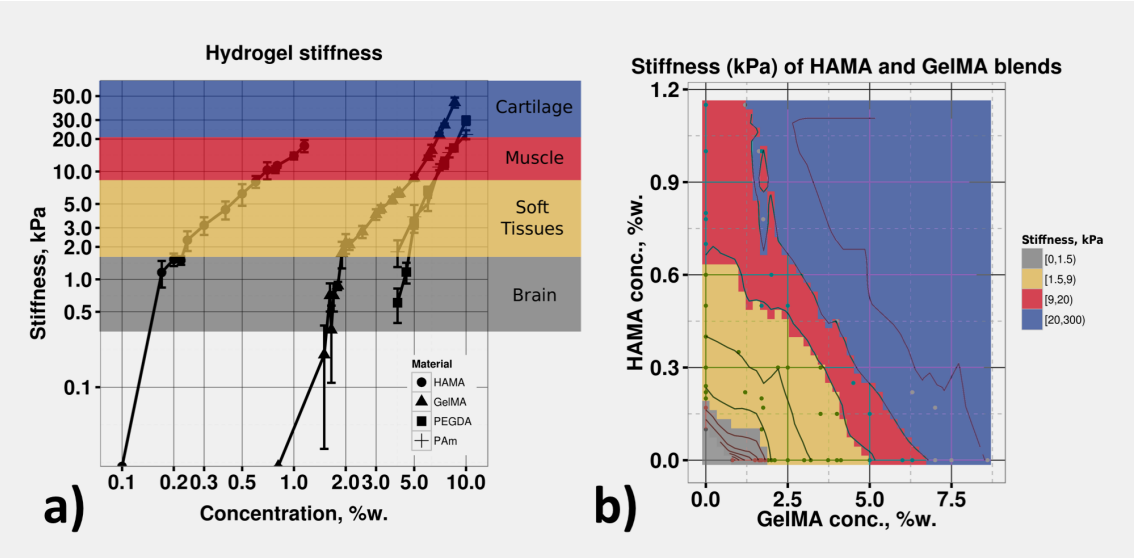


Figure 2.4: a) - Stiffness of pure methacrylated hydrogels, b) - Stiffness of HAMA and GelMA blends. Reported stiffness values are an average of at least 5 measurements, error bars correspond to standard error. Methacrylated hydrogel stiffness was measured by industrial DMA equipment, as well as the device described in Figure 2.2, for the different approaches the values agreed within 10%. Mouse tissues were measured only by the custom built device, due to their physical dimensions. Brain tissue is represented by the white matter, soft tissues are represented by an average measurement of uterine horns, liver, small intestine and skin. Muscle tissues are represented by myocardial tissue and calf muscle. The graph in panel b) was created by cubic interpolation of various measurements (dots). Colour scheme is harmonised between the panels and represents stiffness ranges.

Although substrate stiffness generally did not quantitatively alter cell attachment, I observed morphological differences among the cells growing on stiff and soft substrates (Figure 2.6a). The cells on stiff substrates appeared more spread out and elongated in contrast to equivalent cells on the soft surfaces. To quantify the shape and possible intra cellular tension I used circularity as a measure (Figure 2.6c), which is a ratio of an object's perimeter relative to a circle of the same area. While the cancer cell line LS180 did not display significant stiffness dependent shape changes, the embryonic stem cells and HEK293 line have exhibited statistically different shapes depending on surface stiffness. This is one of the indications that, material stiffness is important for mimicking the extracellular environment [6, 25, 3, 60].

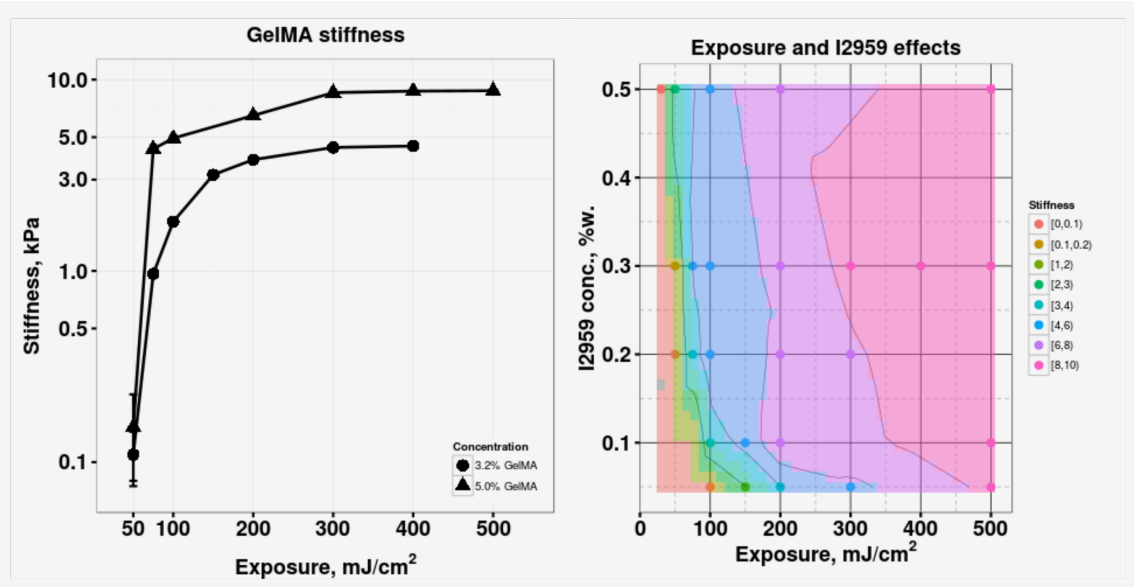


Figure 2.5: Stiffness dependence on light exposure and photo initiator concentration. The left panel shows the rise of stiffness with increasing light exposure for two different gelatin methacrylate compositions. Right panel also considers different photoinitiator concentrations, with colour legend on the right hand side. The values are averages of at least three measurements.

2.3.3 Biodegradability

During tissue development, natural extracellular matrices are often remodelled by embedded cells and a variety of matrix degrading enzymes, such as metallo-matrix proteases. This is one of potential geometric cues affecting tissue development [52]. Methacrylated gelatin makes it possible to create tuneable hydrogel systems, particularly when used in combination with inert gels, which can be used to tune hydrogel degradation rates. Collagenase cleaves a highly conserved region in collagen chain, which when mutated results in embryonic lethality [229]. Matrix remodelling is also important for processes such as vascularisation [97] and cancer metastasis [224].

To tune hydrogel degradability I used blends of gelatin methacrylate and PEGDA (Figure 2.7). Increasing PEGDA content resulted in increasingly inert hydrogels, while compositions exceeding 30% of PEGDA (in the PEGDA/GelMA mixture) did not disintegrate completely but swelled instead (Figure 2.7a). This was due to hydro-

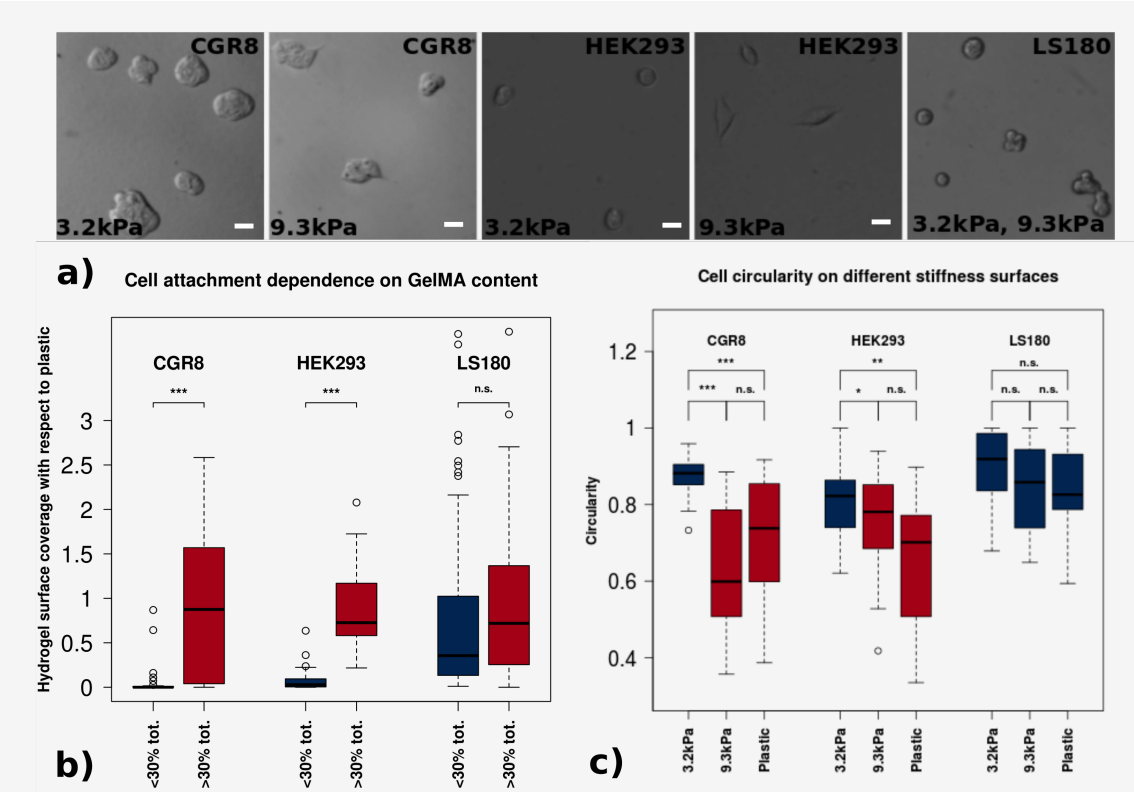


Figure 2.6: Cell attachment as a function of GelMA content. a) - Morphology of cells grown on different stiffness gels, scale bar: $10\mu m$. b) - Cell attachment to hydrogels containing more and less than 30% gelatin methacrylate in their composition. c) - Cell shape (measured by circularity) on various stiffness gels. P-values are represented by: n.s. - not significant, *** - < 0.005, ** - < 0.01, * - < 0.05

gels being partially degraded and relaxing their internal cross-linked networks, which allowed additional water uptake and increase in mass and volume. Lower PEGDA fractions than 30% resulted in degradable gels with varying half-lives (Figure 2.7b). In order to simultaneously tune stiffness and degradability, information in Figure 2.7 can be combined with Figure 2.4 to achieve a certain stiffness (total polymer concentration) and degradability (GelMA/PEGDA ratio). Considering cell adhesiveness, degradable GelMA and PEGDA compositions fall in the biocompatible region, where GelMA fraction is larger than 30% (Figure 2.6).

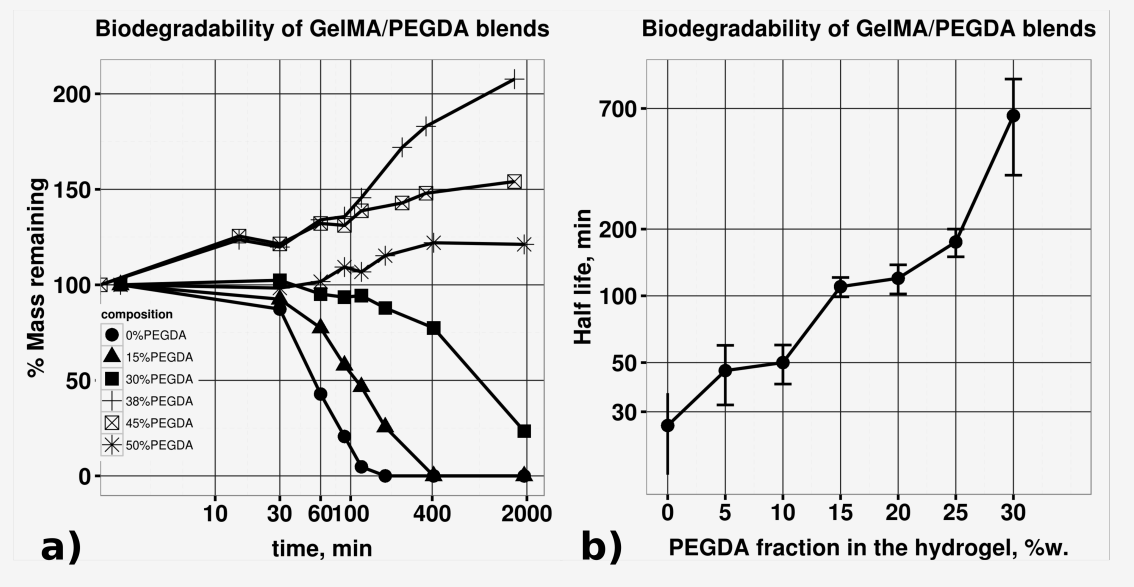


Figure 2.7: Tuning gel biodegradability by adding PEGDA: a) hydrogel mass change with time reflects two types of degradation (hydrogel dissolution and swelling), b) half-lives of different hydrogel blends show how adding inert polymers can be used to tune gel degradability. Measured values are averages of at least three measurements.

2.3.4 Hydrogel toxicity and micro patterning

One of the biggest advantages of this hydrogel system lies in its utility to not only work as 2D substrates, but also create 3D shapes with encapsulated cells [218, 86]. Since methacrylated hydrogels are photo polymerisable, it is possible to create patterned structures using photolithography, which are useful for defining developing tissue geometry.

The most commonly used photolithography system uses the widely available photo initiator Irgacure 2959 and 365nm UV light. I wanted to test the limits of UV exposure and Irgacure concentration, which would result in acceptable survival levels [230], while creating custom hydrogel shapes (Figure 2.8a). HCS DNA damage kit was used to simultaneously look at cytotoxicity (Figure 2.8b) and DNA damage (Figure 2.8c) of encapsulated CGR8 cells inside gelatin methacrylate hydrogels. Irgacure was found to be the major factor behind cytotoxicity, while DNA damage was predominantly caused by UV exposure. However, by limiting these factors to 0.1% Irgacure 2959

concentration and 200mJ/cm^2 UV exposure, cells can be encapsulated with survival rates exceeding 80%.

Similarly to Irgacure 2959, Lithium acyl phosphinate is another water soluble type I photo initiator, which is also biocompatible with live cell encapsulation. Since the material is an ionic lithium salt it has a much smaller cell permeability resulting in lower toxicity and because absorbs longer 405nm wavelength light, there is less damage to DNA. As the result, photo-damage induced cell death was not observed during encapsulation. Overall, either of the photo initiators could be used to create hydrogel shapes by using either ultraviolet lamp or laser based approaches (Figure 2.9). However, although photolithography could be used to create complex hydrogel shapes, in the remainder of the thesis tissue deformation methods used wire moulding and cylindrical cavities because of simplicity and reliability.

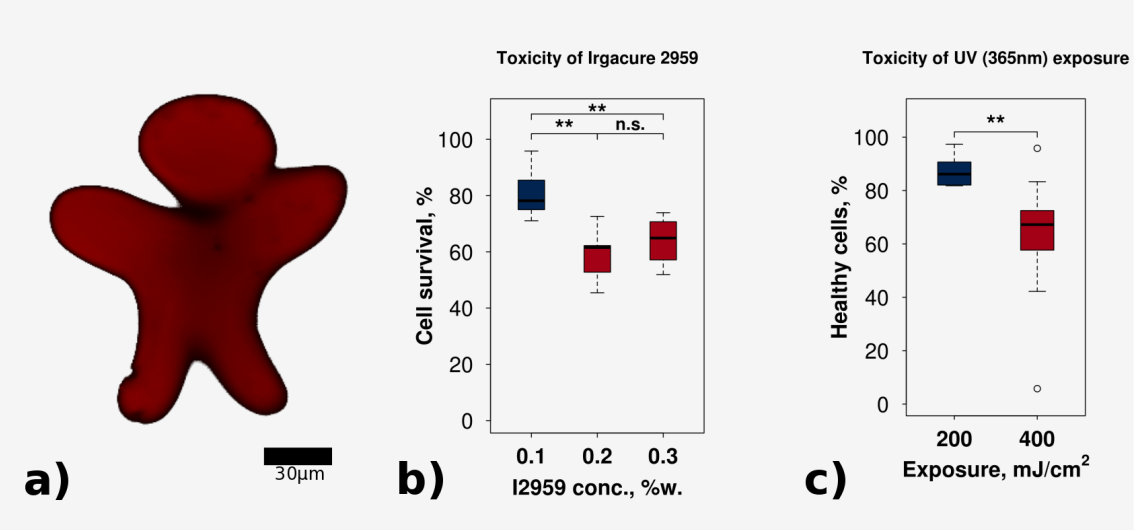


Figure 2.8: Summary of cell encapsulation. a) - An example custom hydrogel shape, which could be created by laser based photolithography. b) - Embedded cell viability as function of photoinitiator (Irgacure 2959) concentration. c) - Embedded cell viability as a function of UV (365nm) radiation exposure. P-values are represented by: n.s. - not significant, *** - < 0.005, ** - < 0.01, * - < 0.05

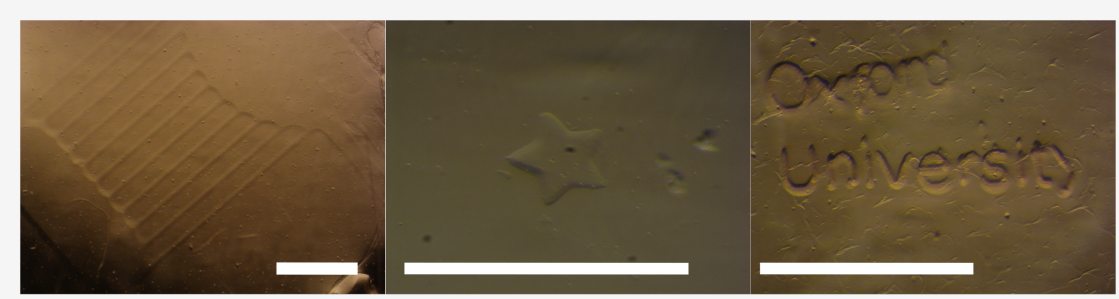


Figure 2.9: Comparison of different photolithography approaches. (a) - UV based photolithography using a mask, (b) - confocal microscope based photolithography, (c) - direct write photolithography using a focused 405nm pocket laser pointer. The figure shows representative pattern quality, scale bars - 300μm

2.3.5 3D tissue micromanipulation

I proceeded by using the micromanipulation system to change the shape of mouse embryos and embryoid bodies (EBs), which are clusters of embryonic stem cells (Figure 2.10). While biochemical characterisation is the subject of two final chapters, here I will be discussing the mechanical basis of basic tissue shape changes, which I will do by looking at transient tissue responses and investigate cell shape and position changes as a result of overall geometry change. For the remainder of the chapter I will focus on ES cell organoids using a GPI-GFP live reporter line [231], which made it possible to investigate these tissues by live imaging.

2.3.6 Defining embryoid body shape

In suspension, embryoid bodies are simple three dimensional structures which are also the foundation for most *in vitro* organoids [119, 200, 202, 232, 201, 115]. Geometric cues play essential roles during cell differentiation [25, 117, 233, 198, 234], however there are virtually no experimental systems, that allow one to consistently deform developing tissues over the relevant timescales of several days. I have used these tissues to both validate the tissue micromanipulation method and also investigate how mechanical properties of individual cells collectively define the mechanics of the

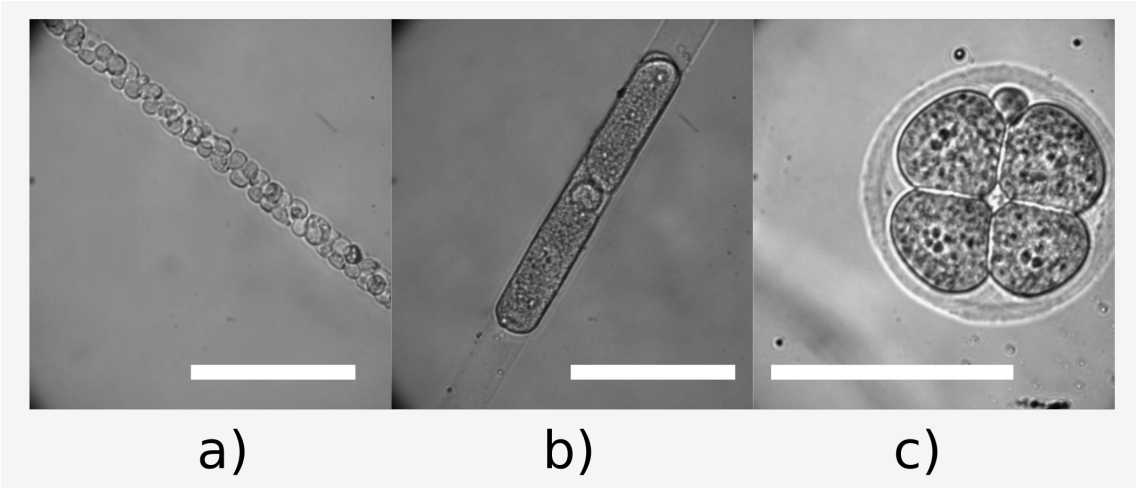


Figure 2.10: Examples of 3D tissue micromanipulation: a) CGR8 stem cells after cylindrical compression, b) 16 cell mouse embryo after cylindrical compression (uncompressed embryos are spherical), c) 4 cell mouse embryo after planar compression (uncompressed embryos are tetrahedral). Scale bars - 300μm

whole tissue. In suspension, cells invariably form spherical embryoid bodies (Figure 2.11, a), but the hydrogels allowed to define custom shapes. Cells constrained to form cylindrical structures showed intact nuclei and cytoskeleton and also continued to proliferate (for at least a week), demonstrating biocompatibility of this system (Figure 2.11, b, c).

When tissues were not grown in confinement, but transiently compressed from the spherical shape, their deformation was not instantaneous and initially exerted visible deformation onto the cylindrical channels (Figure 2.12, a). The progressive shape change made it possible to investigate the origins of intrinsic tissue stiffness, which is relevant not only for the embryo bodies, but also a variety of other developmental [235, 236] and disease contexts [122]. Confocal microscopy timelapse (Figure 2.12 a, b) was used to record the dynamics of cell shape changes.

Overall, tissue deformation from spherical to cylindrical shape was relatively fast and followed by the elongation of constituent cells, which eventually relaxed back to a more spherical shape, equivalent to cells seen in spherical embryoid bodies (Figure 2.12 b). The observation led to the hypothesis, that cells have an intrinsic tendency

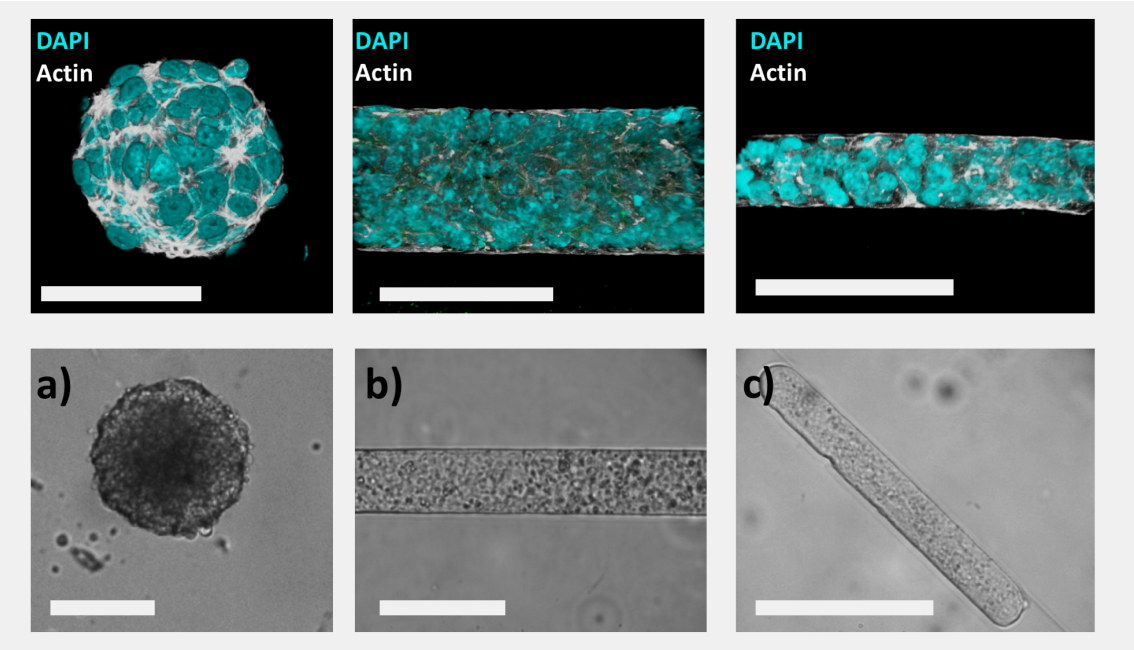


Figure 2.11: Defining 3D organoid shape with cylindrical 5% PEGDA hydrogels. Bottom: brightfield images of developing embryoid bodies. Top: maximum intensity projections of confocal microscopy images (cyan - nuclei, white - actin). a) 120μm embryoid body developing in suspension, b) embryoid body developing in a 80μm channel, c) embryoid body in a 30μm channel. Scale bars - 100μm.

to be spherical and this together with their interactions with the neighbours defines mechanical embryoid body properties.

2.3.7 Studying the origin of tissue stiffness

In order to study the molecular mechanism by which cells collectively respond to tissue shape changes I used chemical inhibitors to interfere with structural cytoskeletal and cell adhesion molecules. Cytochalasin D (CytoD) was used to inhibit actin polymerisation [237] and EDTA for binding calcium ions and preventing E-Cadherin mediated intercellular cohesion [238]. Incubation with Cytochalasin D prior to tissue compression resulted in greater cell elongation during compression and slower recovery (Figure 2.13), as compared to untreated tissues. The opposite effect was seen with EDTA, which reduced cell cohesion resulting in significantly rounder cells. Despite the opposite effects on cell shape, both inhibitors caused an observable tissue

softening. While untreated embryoid bodies 5 min. after compression caused 8.0 ± 2.1% indentation (r/(r + r)) of the hydrogel walls (Figure 2.12 a), CytoD treated embryoid bodies caused a 1.2 ± 2.2% deformation, and EDTA treatment resulted in 0.7 ± 2.0% indentation, indicating that tissues treated with these inhibitors were significantly softer.

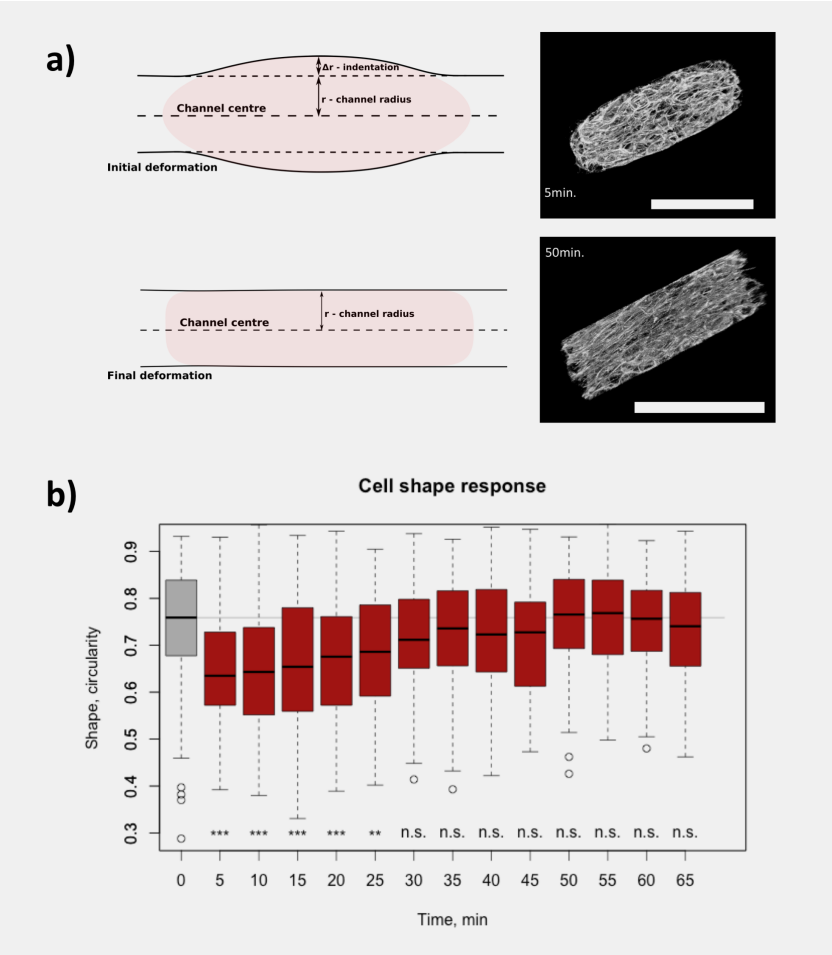


Figure 2.12: Studying mechanical embryoid body properties, by perturbing their shape via spherical tissue compression inside 60μm diameter cylindrical channels in 5% PEGDA hydrogels. a) - A comparison of initial (5 min. post compression) and equilibrium (50 min.) tissue shapes confined inside hydrogel channels. Images are maximum intensity projections of confocal microscopy images of GPI-GFP expressing embryonic stem cell embryoid bodies. b) Relaxation of constituent cell shape (red) after compression of spherical embryoid bodies. Statistical significance was tested for each time point with respect to the uncompressed tissue (grey). P-values are represented by: n.s. - not significant, *** - < 0.005, ** - < 0.01, * - < 0.05. All scale bars - 100μm.

Looking at how embryoid body cellular structure responded to deformation made it possible to formulate a hypothesis, that cell shape is defined by the interplay between the intercellular and extracellular forces (Figure 2.13). By using chemical inhibitors, it was possible to show, that both are required for the tissue to maintain stiffness, as during both EDTA and CytoD treatments, the tissues became softer. The change in cell shapes could also be explained by considering that cells tend towards rounded shapes, which is maintained by actin cytoskeleton, as shown by the CytoD treatment. This is further emphasised by the EDTA treatment, which reduces external forces acting on the cell, causing internal cytoskeletal tension to dominate.

2.4 Conclusions

Developing a robust and well characterized 3D tissue micromanipulation methodology involves considering a variety of material aspects. These can be best fulfilled by using methacrylated hydrogels due to their adaptable chemical properties. Blending three distinct methacrylated biomaterials GelMA, HAMA and PEGDA made it possible to create a tuneable hydrogel system, where several parameters could be simultaneously matched to mammalian soft tissues.

The shape of the gels could also be defined with a high degree of control using a number of available photo-patterning and moulding methods. To demonstrate the utility of this system, I used it to investigate how embryoid body mechanical properties are defined by the collective action of individual cells. By looking at the transient deformation of embryoid bodies and individual cells I formulated a hypothesis, that cells have a tendency to remain round inside the tissue, unless acted upon. This tendency originates from the cytoskeletal tension and the external forces are a result of tissue shape changes. The hypothesis was verified by using a pair of inhibitors to decrease cytoskeletal tension or inhibit intercellular interactions. In conclusion,

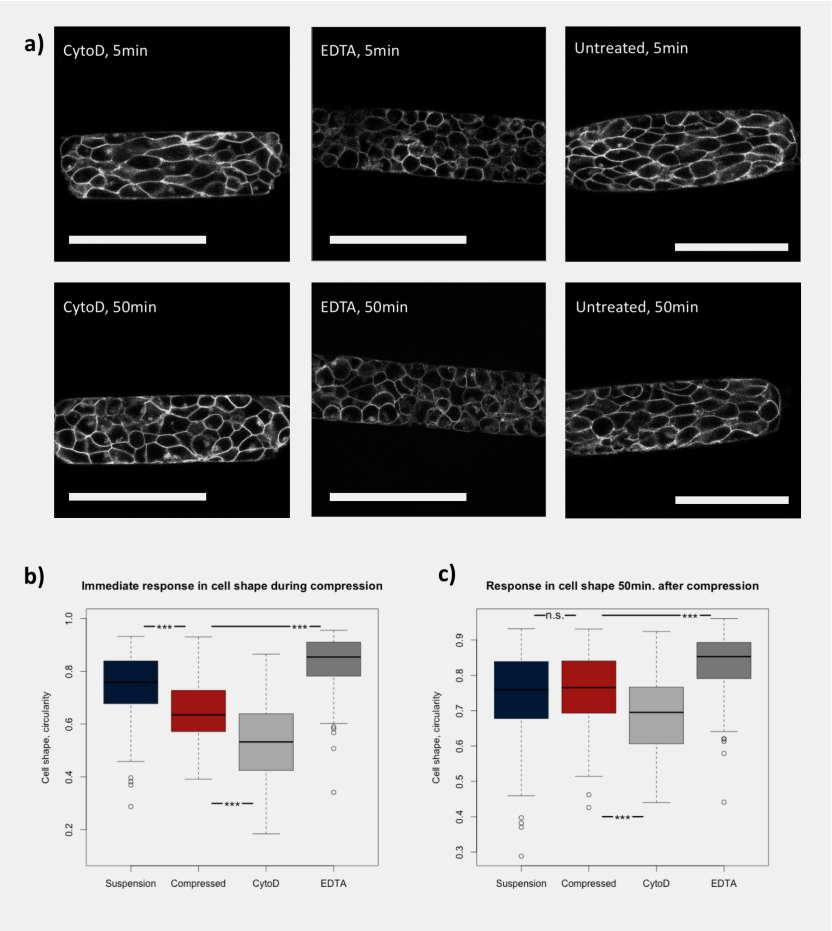


Figure 2.13: Using chemical inhibitors to probe the molecular mechanism responsible for maintaining tissue stiffness a) Images of inhibitor treated compressed GPI-GFP embryoid bodies, 5 and 50 minutes after compression. b) Quantification of cell shapes in treated and control embryoid bodies, 5 minutes after compression. c) Quantification of cell shapes in treated and control embryoid bodies, 50 minutes after compression. Each condition is represented by 5 embryoid bodies with at least 25 measured cells. P-values are represented by: n.s. - not significant, *** - < 0.005, ** - < 0.01, * - < 0.05. Scale bars - 100μm.

the chapter presents a characterized and validated (using embryoid bodies) tissue micromanipulation system.

Blending the three methacrylated polymers makes it possible to independently tune key hydrogel properties, however the rest of the thesis focuses on inert hydrogels mostly using polyacrylamide, which is the most mechanically robust material and can be used to create microscopic tissue deformations.

Chapter 3

Measuring tissue mechanics with deformable hydrogels

3.1 Introduction

The elastic properties of hydrogels are useful not only for deforming tissues, but also measuring mechanical forces from observed deformation using mathematical modelling [14, 108]. Compared to other characterization techniques, hydrogels have the advantages of tuneable chemistry and biocompatible conditions, which enable investigating tissues over longer time periods. Most of the progress in mechanical characterization has been made by using AFM [36] and micropipette techniques [204], which were optimised for high spatial and temporal resolution. Looking at single cells revealed a lot of information for fundamental mechanotransduction pathways, which define and react to cell stiffness and shape changes [239, 240, 241]. However, as tissues are defined by the collective behaviour of constituent cells, looking at the systematic consequences of tissue mechanics and geometry changes is more representative and informative of natural development. One major technical issue is the duration of the experiments, which may span days in order to capture developmentally relevant events. Traditional approaches like AFM, micropipette aspiration and bead micro rheology are generally not practical and suitable for such observations, which is the main motivation for developing a hydrogel based mechanical characterization

platform.

To address the mentioned issues, there already has been a shift towards less invasive and more biocompatible techniques to measure forces at a more systematic level. Forster resonance energy transfer tension sensors have been developed for studying intercellular tension *in vitro* [242] and possibly *in vivo* [55] and deformable oil droplets have been used to measure tissue level mechanical forces [110]. The disadvantage of using FRET sensors lies in the complex relationship between mechanical properties and the observed signal, which makes it difficult to interpret the results. Embedded oil droplets have the disadvantage of complex technical preparation, which is required to overcome the fundamental physical constraint of small objects becoming stiffer with decreasing size due to surface tensions. By contrast, hydrogels are another type of deformable objects, which due to their high water content do not posses a high surface tension making it possible to scale to smaller dimensions.

The previously described system for tissue micromanipulation can be extended with the aid of mathematical modelling, such that forces can be estimated from the deformation of the hydrogel cavities, where they are grown. Among the different possible cavity shapes, cylindrical channels offer the advantages of a relatively symmetric environment for simplified force calculation and being able to use this symmetry to estimate complete 3D shape, from 2D brightfield microscopy. This allows to avoid the use of confocal and light sheet microscopy, which are much more phototoxic and complex methods. In order to calculate the forces tissues experience during compression inside channels, it is necessary to develop a physical framework, which would allow to relate the observed deformations and involved forces. Simple elastic models have previously been used to lay the foundations of contact mechanics [111, 243, 244]. However, despite the existing 2D analogues of circular half-space indentation, full modelling of an object indenting a cylindrical channel is relatively complex. In order to simplify the problem and arrive at an analytical solution, it is possible to make

assumptions about the nature of the deformation and idealized material properties as long as the assumptions are validated by experimental evidence. For this reason, I chose oil droplets with known surface tension, which allows to estimate the deforming force. Furthermore, I chose to use mouse pre-implantation embryos, as they are one of the best characterized biological model systems, involving a profound mechanical development aspect.

There is already much known about the mechanics of pre-implantation embryos, because of their reproducible development and standardised culture conditions. Previous experiments have revealed the stiffness of individual blastomeres [11], nuclei, Zona Pellucida [56, 39, 245, 246], actin dynamics and contractile forces [187]. However, there is much less known about tissue scale internal pressures generated before and during embryo hatching. It is already known, that the pressure generated in the blastocysts arises as a result of water movement following an osmotic gradient [247, 248]. The gradient is generated by a pool of different redundant Na/K ATPase channels, which has been studied by genetic [249] and inhibitor experiments [248, 118]. Aquaporins are another important type of ion channels, which are responsible for facilitating water transport across otherwise impermeable epithelial cell layer [250]. Although there is already much known about the components playing a role in pressure generation and embryo hatching, we still do not know how they integrate into the overall system. For example, without measuring the pressure, we do not know what the osmolarity is inside the blastocyst cavity, how fast water diffuses across the epithelial cell layer or to what extent epithelial integrity is maintained during cell divisions.

Embryo hatching is an essential step in mammalian development preceeding implantation and also a major issue during *in vitro* fertilisation [251]. Therefore, it is important to understand the role of pressure generation during this process. It is presumed, that breakdown of the polysaccharide shell known as Zona Pellucida is

facilitated by several enzymes secreted by the embryo [252, 253, 254], however it is unclear how important it is to reach certain pressures during development. In order to answer these questions about the function of tissue pressure generation, I have adapted methodology presented in chapter 2.

3.2 Materials and methods

Acrylamide/Bis-Acrylamide (37.5:1) stock solution (40%), ammonium persulphate, TEMED, Gelatin (Porcine, Type A), Ouabain octahydrate, sucrose and collagenase I from *Clostridium Histolyticum* were purchased from Sigma-Aldrich. KSOM evolve media was purchased from Millipore.

3.2.1 Animal experiments

All animal experiments were carried out according to UK Home Office project license PPL 30/2887 compliant with the UK animals (Scientific Procedures) Act 1986 and approved by the local Biological Services Ethical Review Process. To obtain wild-type embryos C57BL/6 males were crossed with CD1 females (Charles River). All mice were maintained in a 12-hour light-dark cycle. Noon of the day finding a vaginal plug was designated 0.5dpc (days post coitum). In order to dissect the embryos, the pregnant females were culled by cervical dislocation and death was confirmed by exsanguination in accordance with the schedule one of the Animal Scientific Procedures Act. Embryos of the appropriate stage were dissected in M2 medium (Sigma-Aldrich) at room temperature. Pre-implantation embryos were collected by oviduct and uterus flushing and then cultured in KSOM Evolve media.

3.2.2 Preparing cylindrical hydrogels

Hydrogels with cylindrical cavities were prepared by casting polyacrylamide gels around a small diameter wire (40μm). Acrylamide/bisacrylamide (37.5:1) mixture

was used to prepare gels (5% by mass), which corresponded 4.2kPa stiffness. Ammonium persulphate (0.1%) and TEMED (1%) were added to polymerise polyacrylamide. After the wire was removed forming cylindrical cavities, the hydrogels were equilibrated in embryo culture medium by changing the solution three times in one hour. The embryos were then inserted into the channels by a glass capillary having a diameter slightly larger than the embryo itself. It was used to stretch the hydrogel channel before injecting the embryos and letting the channels relax and deform the embryos.

3.2.3 Inhibitor experiments

After mouse dissection, collected embryos were placed either in KSOM evolve media or the same media containing compounds for interfering with pressure development: sucrose (50mM - 1M), Ouabain (0.1 - 0.2mM) and Collagenase (0.1 - 0.5mg/mL).

3.2.4 Imaging setup and Image analysis

Imaging was performed on a modified Zeiss Axiovert Spinning disc confocal microscope equipped with a Hamamatsu emCCD camera and a 37°C and 5% CO2 incubator. Images were recorded every 6 minutes and mouse embryos were cultured for 8h intervals between the 3.0 and 4.0dpc developmental stage. The images were then analysed by ImageJ software with a custom algorithm to automatically detect embryo outlines. The outlines were exported as a list of coordinates and then analysed by a MATLAB script to determine channel width, the extent of hydrogel deformation, embryo curvature at the ends of the channel as well as the contacting region, as well as embryo volume and surface area. The geometric parameters were then used to calculate tissue pressure, which was then obtained by a combination of a mathematical model and experimental measurements using FC-77 oil droplets with measured surface tension (35mN/m). Zona Pellucida thickness was measured manually by using ImageJ.

3.2.5 Calibrating the pressure exerted by cylindrical cavities

FC-77 oil droplets were used because of their inertness towards different types of media and invariant surface tension of 35mN/m, which was determined by the critical droplet radius method and previous reports. Different size droplets were inserted into three different stiffness channels with three different diameters. Deformed droplet profiles were captured by ImageJ, measuring channel diameter, the extent of indentation and curvature at the ends of the droplets as well as contacting regions. Curvature measurements allowed to determine the pressure difference between the ends and the sides of the droplet, which is offset by hydrogel compression. The force was then calculated by multiplying the surface area, which is in contact between the droplet and the hydrogel channel. By using Laplace equation, the pressure exerted by the hydrogels can be found from the differences in surface tension (Equation 3.1, Figure 3.1, a). The equation balances the external pressure of the hydrogel and the internal pressure due surface curvature differences at points P_{P1} and P_{P2}. R_a is radius of curvature at point P_{P1} and R'_a, R'_b are radii of curvature at point P_{P2}.

$$P_{external} = P_{P1} - P_{P2} = \sigma\left(\frac{1}{R_a} + \frac{1}{R_a}\right) - \sigma\left(\frac{1}{R'_a} + \frac{1}{R'_b}\right) = 2\sigma\left(\frac{2}{R_a} - \frac{1}{R'_a} - \frac{1}{R'_b}\right) \tag{3.1}$$

3.2.6 Mathematical model derivation

The following model has been derived with assistance from Dr. John Biggins (Cavendish Laboratory, University of Cambridge). The contact profiles formed after a sphere is compressed inside a cylindrical environment closely resemble an ideal arc, which indicates, that pressure distribution along the contact is relatively homogeneous. This makes it possible to use a model for an evenly pressurized cylindrical cavity. The system can be mathematically described by considering the longitudinal cross-section of the cylinder as in (Figure 3.1, b).

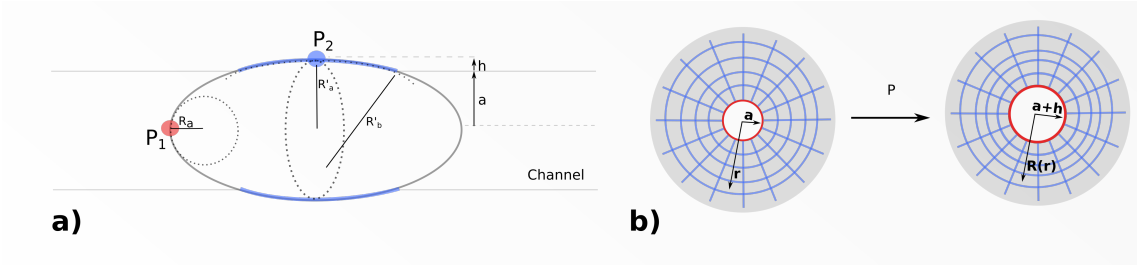


Figure 3.1: A) Modelling spherical droplet deformation. B) Cylindrical cavity expansion under pressure.

When pressure P is applied to a cylindrical cavity, it expands to a larger radius a + h. The deformation gradient of the material can be described in a cylindrical coordinate system (r, ϕ , z) by Equation 3.2, the system is invariant to pressure change in the z direction. Equation describes deformation of the channel, which is achieved by hydrogel material displacement, which keeps the overall volume constant and imposes a constraint in Equation 3.3, which can be used to solve for R(r) in Equation 3.4. With the post deformation condition, knowing that R(a)=a + h, it allows to find the constant 'c' in Equation 3.5.

$$F = \begin{pmatrix} R'(r) & 0 & 0 \\ 0 & R(r)/r & 0 \\ 0 & 0 & 1 \end{pmatrix} \tag{3.2}$$

$$Det(F) = \frac{R'(r)R(r)}{r} = 1 \tag{3.3}$$

$$R(r) = \sqrt{r^2 + c^2} \tag{3.4}$$

$$Given,\ R(a) = a + h \rightarrow c^2 = h(2a + h) \tag{3.5}$$

The energy associated with the elastic shape change of the hydrogel per unit volume can then be expressed by Equation 3.6. If cavity is pressurized by pressure P, the equilibrium will be achieved by minimising the effective energy expressed in

Equation 3.8 and Equation 3.9. The latter can be solved for P to give the final expression in Equation 3.11, where 'a' is channel diameter without applied pressure, 'h' is indentation into the channel with pressure and μ is shear modulus, $\mu = E/(2(1+\nu)) = E/3$ for an ideal non-compressible material, with E as Young's modulus.

$$E = \frac{1}{2}\mu\left(Tr(F \cdot F^T) - 3\right) = \frac{1}{2}\mu\left(R'(r)^2 + \frac{R(r)^2}{r^2} - 2\right) \tag{3.6}$$

$$E_{unitz} = \int E2\pi r dr = \left[\frac{1}{2}\mu\pi c^2 ln\left(\frac{r^2}{c^2 + r^2}\right)\right]_a^\infty = \frac{1}{2}\mu\pi c^2 ln\left(1 + \frac{c^2}{a^2}\right) \tag{3.7}$$

$$E_{ef} = E_{elastic} - PV = E_{elastic} - P\pi R(a)^2 = \frac{1}{2}\mu\pi c^2 ln\left(1 + \frac{c^2}{a^2}\right) - \pi\left(a^2 + c^2\right) \tag{3.8}$$

$$\frac{dE_{ef}}{dc} = \pi c\left(\frac{\mu c^2}{a^2 + c^2} + \mu ln\left(\frac{c^2}{a^2} + 1\right) - 2P\right) = 0 \tag{3.9}$$

$$P = \mu\left(\frac{h(2a+h)}{2(a+h)^2} + ln\left(1 + \frac{h}{a}\right)\right) \tag{3.10}$$

$$P = \frac{1}{6}E\left(1 + 2ln\left(j\right) - j^{-2}\right), j = \frac{a+h}{a} \tag{3.11}$$

The derived expression allows to calculate the pressure, which is causing elastic channel deformation solely on the indentation into the channel. The expression is derived for an ideal scenario of the whole channel deformation, however can also be applied to spherical objects with diameter larger than the channel, which is true for all of the tissues experiencing deformation. Overall the agreement between the model and experimental evidence is shown in Figure 3.2.

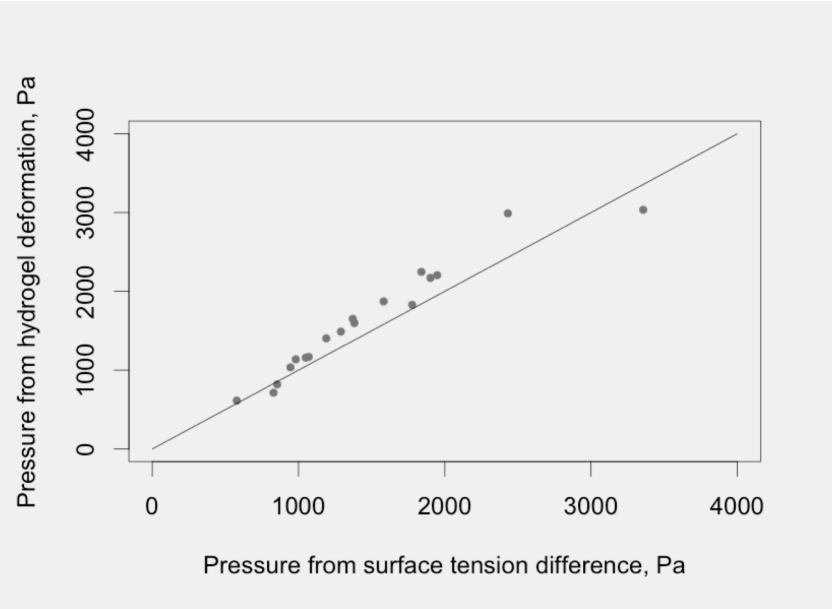


Figure 3.2: Agreement between the mathematical model using hydrogel deformation and pressure data calculated from droplet surface tension. Line fit is 1:1 agreement with $R^2 = 0.9225$

.

3.3 Results and Discussion

3.3.1 Pressure evolution during blastocyst development

Looking at individual blastocysts revealed a steady and often linear pressure increase during the early stages. The pressure is generated because of water movement, across a semi-permeable epithelial cell layer, which causes an increase in volume. However, Zona Pellucida restricts volumetric expansion, which then results in a pressure increase (Figure 3.3). One of the pre-requisites for cavity formation is the tight seal between epithelial cells, which makes it possible to maintain the internal pressure [255]. Despite the growth and cell divisions in the epithelial layer, the embryo is able to maintain the internal pressure, except for minor drops seen during the relatively synchronised sixth round of cell divisions (Figure 3.4, a).

Pressure and volume measurements also made it possible to derive other important physiological parameters such as internal osmolarity (Equation 3.12, Figure 3.4, b),

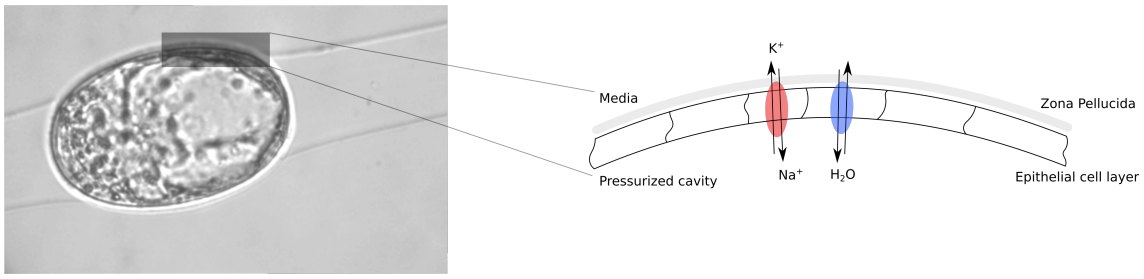


Figure 3.3: Key components responsible for blastocyst pressure development. Internal blastocyst pressure is generated by ion movement across a semi-permeable epithelial cell layer and following water flux. Ion transport is mediated by NA/K ATPase ion channels, which use ATP to move three sodium ions out of the cell for two potassium ions transported inwards. Water transport is mediated by aquaporin channels and largely follows the osmotic gradient. Overall, mechanical pressure is maintained by a semi-rigid shell Zona Pellucida.

as well as the rate of ion (Equation 3.13) and water transport (Figure 3.5). In the equations, P is the internal pressure, V - volume, N - number of ions, Δc - ion concentration difference between media and blastocoel cavity, R - ideal gas constant, k_B - Boltzmann constant, T - temperature, t - time.

Before the round of cell divisions there seemed to be a steady ion and water flux into the embryo, which suggests a relatively constant number of ion channels per cell (Figure 3.5). Furthermore, the rate of water transport is independent on the pressure of the blastocyst cavity, which suggests, that pressure dynamics are limited by the rate of ion, but not water transport (Figure 3.5, c). Pressure measurements made it possible to estimate, that on average pressurized cavities contained 0.53mOsm of additional electrolytes. However, looking at the relationship between water and osmolarity changes in Figure 3.5 d, it could be seen that on average every transported ion produced a $2.02 \times 10^{-6} \mu m^3$ volume increase and there were 10 million of ions transported every second. This would correspond to transport of a solution containing 0.82mOsm of additional electrolytes, or 0.41mM if the solution was NaCl.

$$P = \Delta c \times RT = \frac{N}{V} \times k_B T \tag{3.12}$$

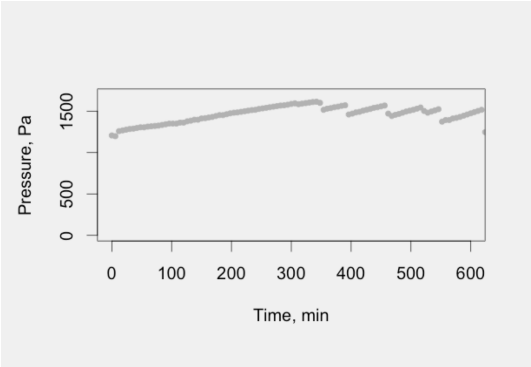


Figure 3.4: A representative internal pressure seen during blastocyst development. An embryo at 3.5 dpc was compressed in a $40\mu m$ 5% polyacrylamide channel and the internal pressure was measured from channel deformation.

$$\frac{dN_{ions}}{dt} = \left(\frac{dP}{dt} \times V(t) + \frac{dV}{dt} \times P(t)\right) / k_B T \tag{3.13}$$

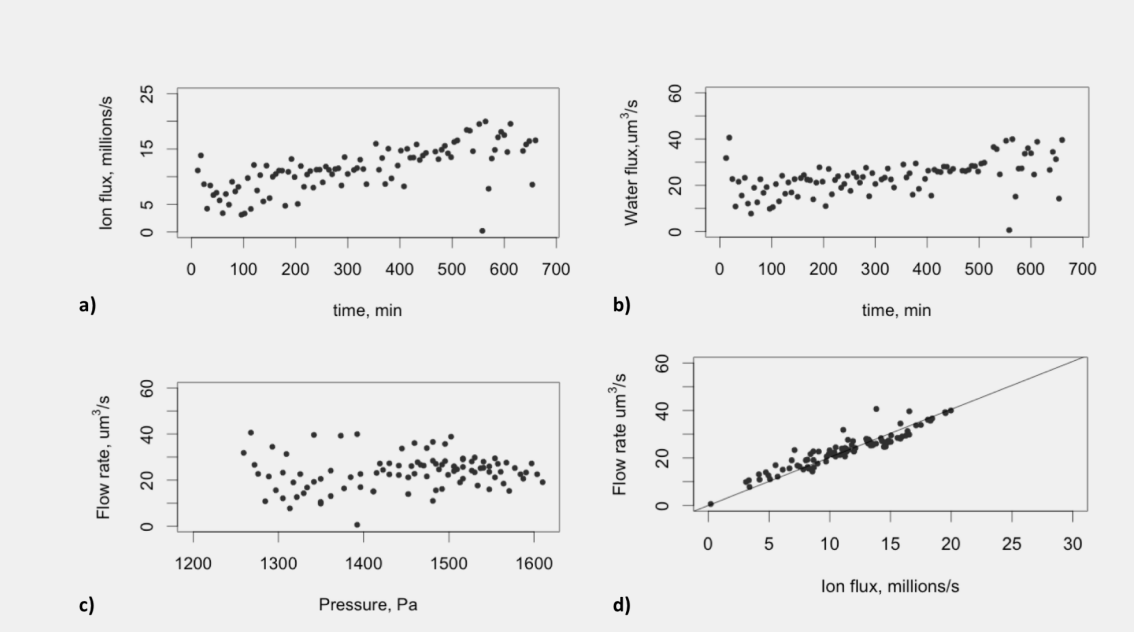


Figure 3.5: The rates of ion and water transport into the blastocyst cavity. a) - A representative rate of ion transport across the epithelial layer. b) - A representative water flow across the epithelial layer. c) Water transport as a function of internal blastocyst pressure. d) - Water transport as a function of ion transport, $R^2 = 0.98$.

In addition to measuring pressure and water transport, brightfield images can also be used to measure the starting thickness of Zona Pellucida (in equations t_0) and

starting embryo radius (in equations R_0). This makes it possible to model the embryo as a thin shell pressure vessel and estimate Young's modulus of Zona Pellucida [256]. In order to do this, an embryo has to be modelled as a spherical balloon, where plane stress dominates material behaviour [257], which is assumed to be linear, elastic and incompressible (Poisson ratio 0.5). As pressure increases and the balloon expands, the effective circumferential strain at a given time (ϵ) can be expressed as a relative increase in sphere radius in Equation 3.14:

$$\epsilon = \frac{(\Delta R + R) - R}{R_0} = \frac{\Delta R}{R_0} \tag{3.14}$$

Assuming, that in-plane stress (σ) is the same in all directions, because of spherical symmetry, and that shear stress vanishes in all dimensions because of the radial symmetry of expansion, the resulting in-plane stress can be expressed as in Equation 3.15:

$$\sigma = \sigma_0 + \frac{E}{1-\nu^2}(\epsilon + \nu\epsilon) = \sigma_0 + \frac{E}{1-\nu}\frac{\Delta R}{R_0} \tag{3.15}$$

Stress in a thin wall spherical vessel can be calculated given the final and starting thicknesses (t_0 and t_f) of the shell, the internal pressure and the radius of the vessel:

$$\sigma_0 = \frac{P_0 R_0}{2t_0}, \sigma = \frac{(P_0 + \Delta P)(R_0 + \Delta R)}{2t_f} \tag{3.16}$$

The final thickness of the shell can also be calculated by making an assumption, that it is incompressible ($\nu = 0.5$) and the shell maintains the same volume (V_z) throughout embryo expansion (Equation 3.17):

$$V_z = 4\pi R_0^2 t_0 = 4\pi(R_0 + \Delta R)^2 t_f \rightarrow t_f = t_0 \left(\frac{R_0}{R_0 + \Delta R}\right)^2 \tag{3.17}$$

In order to arrive at an expression relating pressure and radius change Equation 3.17 can be substituted into Equation 3.16 and Equation 3.15, which makes it possible

to calculate shell stiffness by measuring blastocyst pressure (P), its radius (R) and starting shell thickness (t_0) (Equation 3.18). The same equation can be used to derive an expression for the pressure inside the cavity, if shell stiffness is known (Equation 3.19).

$$\frac{(P_0+\Delta P)(R_0+\Delta R)^3}{2t_0R_0^2} = \frac{P_0R_0}{2t_0} + 2E\frac{\Delta R}{R_0} = \frac{P_0R_0^3 + 4Et_0\Delta RR_0}{2t_0R_0^2} \tag{3.18}$$

$$E = \frac{(P_0+\Delta P)(R_0+\Delta R)^3 - P_0R_0^3}{4t_0R_0\Delta R} \tag{3.19}$$

$$(P_0+\Delta P) = \frac{4Et_0R_0\Delta R + P_0R_0^3}{(R_0+\Delta R)^3},\ if\ P_0 = 0,\ \Delta P = \frac{4Et_0R_0\Delta R}{(R_0+\Delta R)^3} = \frac{4Et_0\epsilon}{R_0(1+\epsilon)^3} \tag{3.20}$$

The model leads to an interesting conclusion, that there exists a critical pressure, which an expanding elastic vessel can sustain. After this pressure is reached, it becomes easier to increase the size and the volume of the vessel until wall thickness decreases to a bursting point (Figure 3.6). This can also be seen in real pressure vessels, while inflating balloons, as after a certain point during initial inflation, it becomes easier to inflate it further. In this context the expression is particularly useful for determining shell stiffness from pressure and embryo radius estimates (Figure 3.7, a). The critical expansion point of around 50% is independent from any of the parameters, while the critical pressure depends linearly on Zona Pellucida stiffness and the ratio between the shell thickness and embryo radius.

3.3.2 Descriptive statistics

After creating the theoretical framework described in the previous section I wanted to look at embryo micro-physiology at the population level. By looking at larger sample sizes, it becomes possible to form and strengthen the hypotheses, before making the

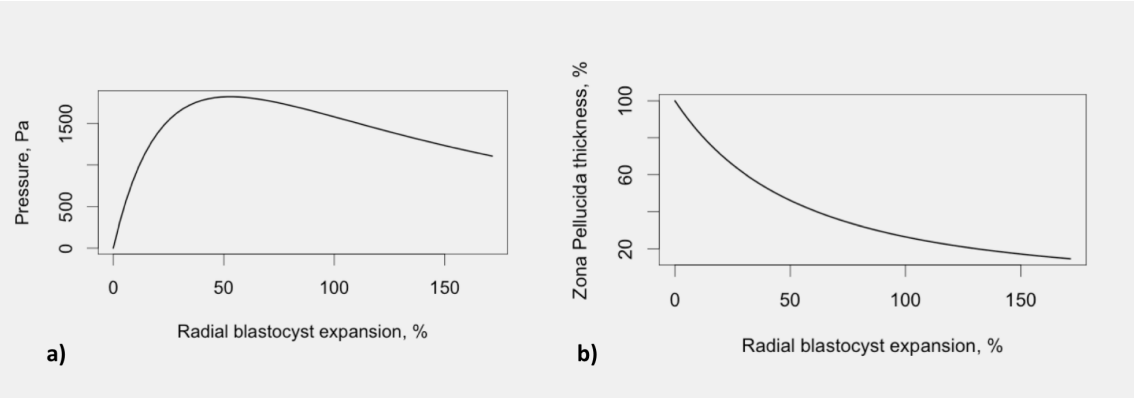


Figure 3.6: A mathematical model for blastocyst expansion, based on E=32.5kPa, $t_0 = 3.5\mu$m, $R_0 = 37\mu$m. The model demonstrates, that initial volume increase results in a fast pressure rise, however the pressure goes through a maximum with further cavity expansion.

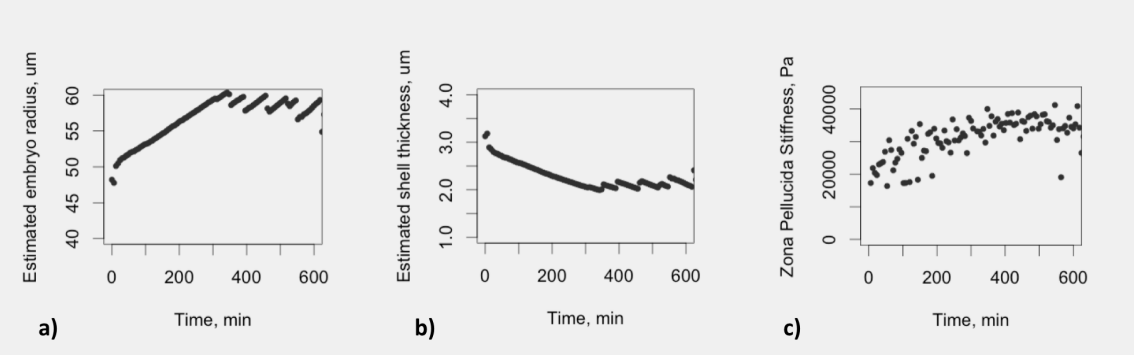


Figure 3.7: Changes in a) embryo radius, b) shell thickness, c) and Zona Pellucida stiffness, during blastocyst expansion

next step of using perturbation experiments to infer causation. In general, there are two basic measured properties: cavity pressure and embryo volume, from which embryo osmolarity and water flow rates can be derived. Although they are measured independently, volume and pressure are interconnected by the mechanical properties of Zona Pellucida, which can also be calculated by measuring embryo radius and shell thickness and using the mentioned mechanical model.

The embryos developed relatively similar average and maximum pressures (Figure 3.8 a), which demonstrates that the average pressure developed in a blastocyst is close to the maximum pressure, which agrees with the elastic balloon model (Figure 3.6 a),

implying, that the embryo is usually in the 30-70% radial expansion region, where the pressure is relatively constant. Pressure measurements made it possible to estimate, that on average pressurized cavities contained 0.53mOsm of additional electrolytes.

Overall, the measured pressures were comparable to other published cases involving epithelial ion transport. For example, kidney glomeruli develop 15mmHg (2kPa) [258]. However the internal osmolarity of 0.29Osm was much lower than that of urine (0.8Osm [259, 260]). Measuring the rates of ion transport responsible for osmolality and volume increase revealed, that every second embryos pump around $22\mu m^3$ of a solution with 10 million ions (Figure 3.9), which would be analogous to 0.41mM NaCl.

Since it is known, that ionic transport is mediated by well characterized Na/K ATPases, it is possible to estimate the number of involved ion channels per cell. I used Ouabain to verify, that ion transport was mediated by these channels (Figure 3.10). The drug is a small molecule inhibitor, which works by blocking Na/K ATPAse channels resulting in reduced fluid flow into the blastocyst cavity.

The rates of pump turnover have previously been calculated from radioactivity measurements and reported to be around 3600(Na^+)/min [261], 3000(K^+, Rb^+)/min [262] and 2000(ATP)/min [263]. Since for every ATP molecule pump transfers 2 K^+ ions into the cells and 3 Na^+ outside, the average rate for Na^+ transport can be estimated to be 4700/min. Since the dominant counter ion in the media is Cl^-, sodium efflux can be estimated to be responsible for half of the seen osmotic flux 3.3×10^8/min. Since an average 32 cell embryo contains 20 trophectoderm cells [185], ion flux per cell is 1.7×10^7/min, which would involve 3.5×10^3 active ion transporters per cell.

Zona Pellucida stiffness measurements relied on the thin-shell pressure vessel mechanical model, which estimated a 23kPa Young's modulus for the shell material of $4.3\mu m$ average thickness (Figure 3.11). The thickness was measured at the start of the experiments, at 3.25dpc, during the early stages of of blastocoel cavity formation.

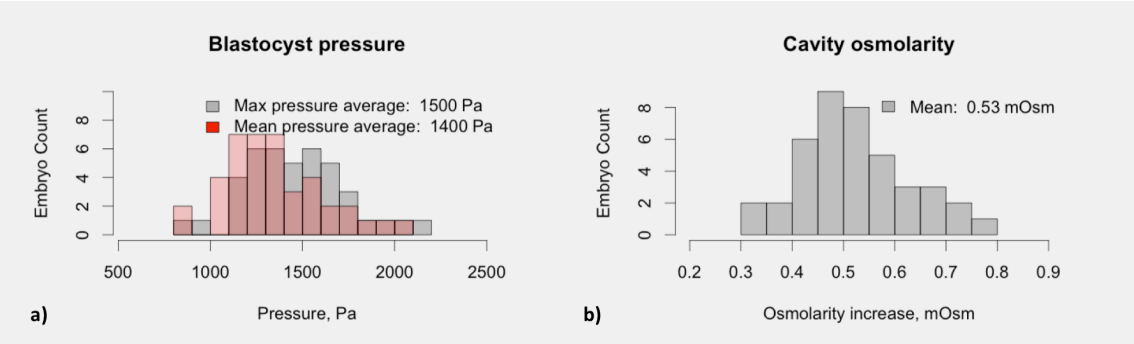


Figure 3.8: Embryo pressure and cavity osmolarity measured in 41 blastocysts. The small difference between maximum and mean pressures demonstrates, that embryo spends most of the time near maximal pressure, which agrees with the thin-shell pressure vessel model.

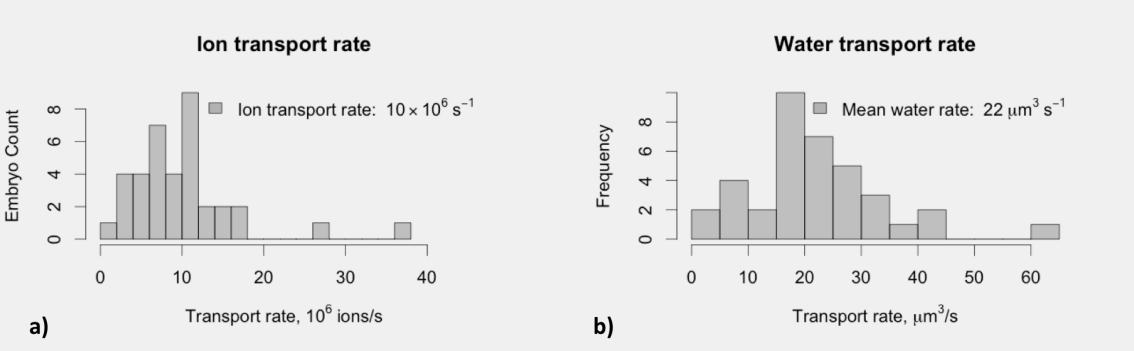


Figure 3.9: The flux of water and ions across the trophectoderm layer in 41 blastocysts. The embryos showed a large variability in rates of water and ion transport.

Zona Pellucida stiffness was evaluated during the course of cavity expansion from the rates of embryo radius and pressure increase. Even though the elastic model relies on major assumptions about the idealised material properties of Zona Pellucida, the average value of 23kPa agrees relatively well with previously published reports using localised stiffness measurements by micropipette aspiration - 37kPa, [39], micro-tactile sensor - 22.3kPa [265] and injection needles - 42.2kPa [245].

Having measured key micro-physiological embryo parameters, I wanted to look for possible unexplained relationships between them. Figure 3.12 considers all of the mentioned parameters in a single correlation matrix. As expected, the strongest relationship was between the maximum pressure and average cavity osmolarity, which is

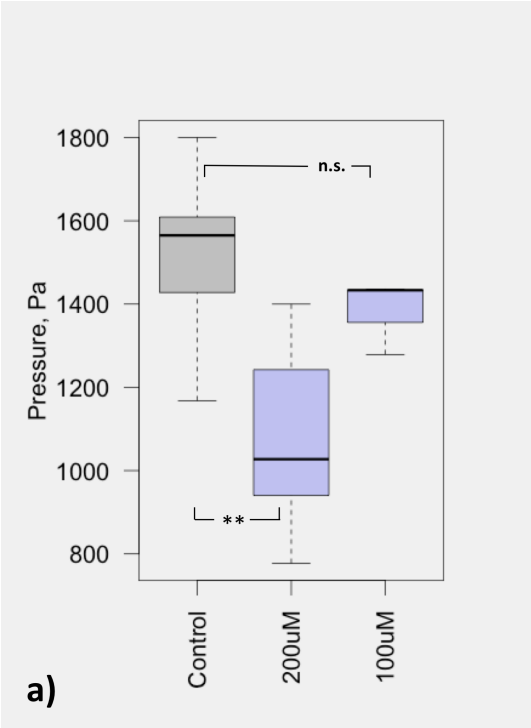


Figure 3.10: Ion transport inhibition by Ouabain. a) decrease in maximum embryo pressure. 100 and 200 μM inhibitor concentrations were used and embryos treated by 200 μM were affected to a statistically significant level. At least 7 embryos in each condition, P-values are represented by: n.s. - not significant, *** - < 0.005, ** - < 0.01, * - < 0.05.

derived from mean pressure. Next, the link between water and ion flux was already discussed and the correlation between total volume and these two was also unsurprising to find. None of the parameters could explain variations in Zona Pellucida stiffness, however, there was a slight anti-correlation with thickness, measured at the start of the experiments.

3.3.3 Perturbing media osmolarity

Measuring pressure and volume during development made it possible to characterize the embryos but to test the hypotheses about the origin of osmotic pressure and the relative rates of water transport, the system had to be perturbed to diverge from the physiological conditions. Solution osmolarity is one of the most important parameters that defines embryo development, hence it was the first to be used for

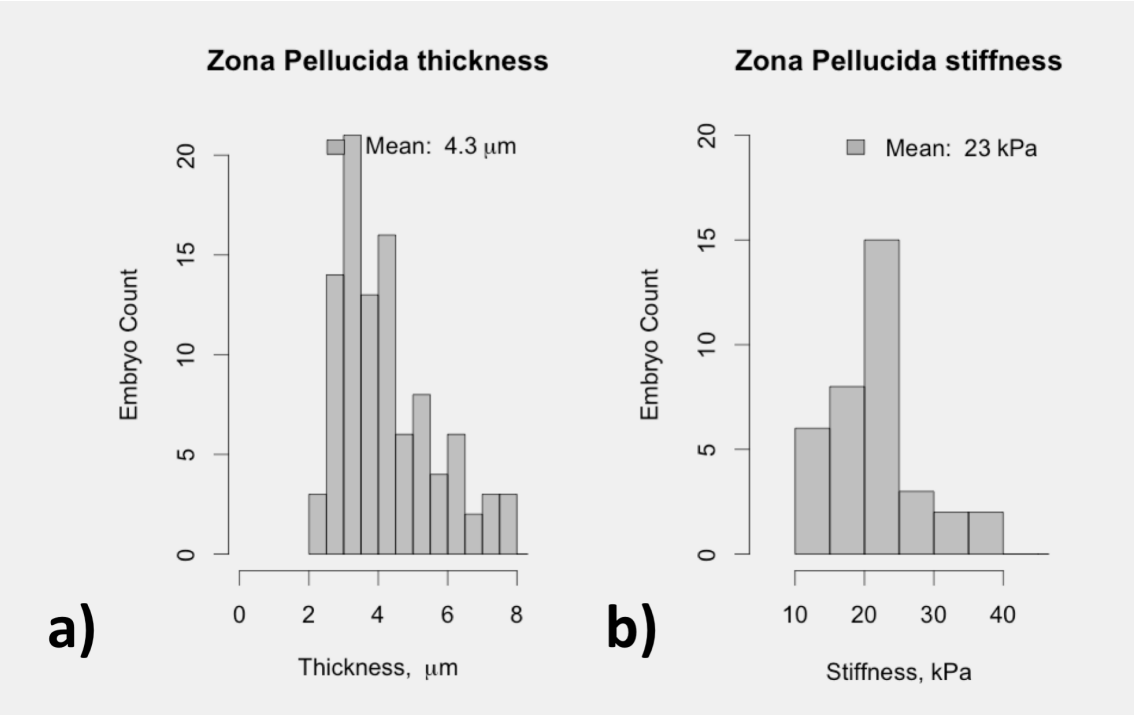


Figure 3.11: Zona Pellucida mechanical properties measured in 39 blastocysts. Zona thickness was measured in 3.25dpc embryos by optical microscopy. Zona stiffness was calculated by using the thin-shell pressure vessel model and the measured thickness and embryo radius.

perturbation. Changing solution osmolarity made it possible to gain insight into the active regulation by the embryo and active responses to this environment variable. Transient changes in solution osmolarity also made it possible to look at the rates of water transfer across the epithelial layer, which is otherwise hidden behind the limiting kinetics of ion transport. At the moment of osmolarity increase in embryo culture media there is an imbalance between the internal and external osmotic pressures (Figure 3.13, a), which causes water movement proportional to the pressure difference (Figure 3.13, b). This movement is mediated by the aquaporin membrane channels, responsible for water transport. By plotting the rate of volume change against the pressure difference it becomes possible to calculate the rate of water movement for every pascal pressure difference, which in this case is $1.50 \mu m^3 Pa^{-1} s^{-1}$. During the acute osmolarity change, embryos were capable of moving over $500 \mu m^3$/s, which

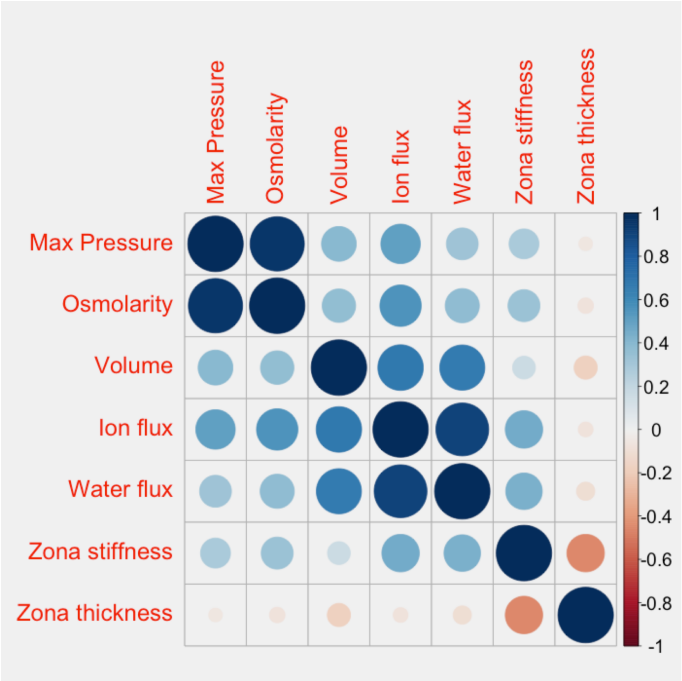


Figure 3.12: Corellogram exploring relationships between embryo micro physiology variables. Different variables are named on the sides of the diagram, with the circles at their intersection representing the correlation between them. The colour codes the slope of the correlation and the size of the circle represents correlation coefficient.

would correspond to 1.7×10^{13} water molecules per second, which is several orders of magnitude faster than the ion transport rate seen during development. This further supports the hypothesis, that ion transport is the rate limiting step for blastocyst expansion.

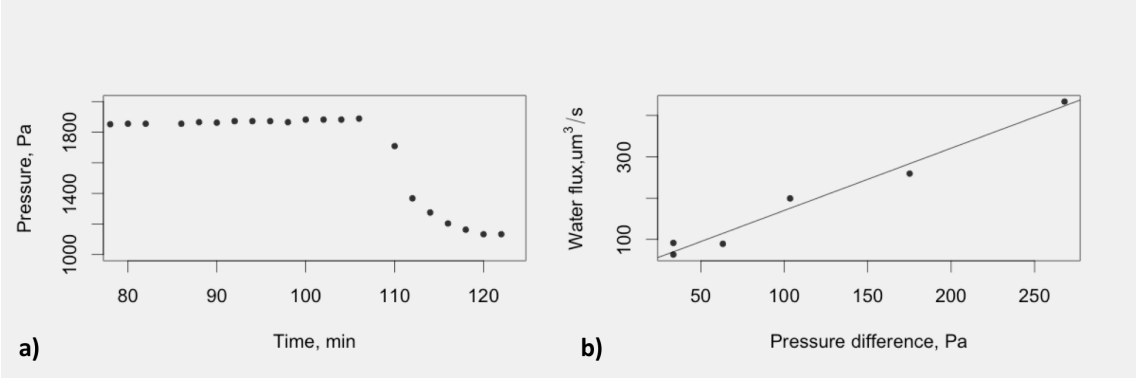


Figure 3.13: A transient pressure and volume response to changing media osmolarity. a) - Pressure decrease after addition of sucrose at timepoint 107. b) - Correlation between water flow and pressure difference across the epithelial layer, $R^2 = 0.98$.

3.3.4 Epithelial integrity during cell divisions

Monitoring pressure and volume changes at high temporal resolution revealed occasional pressure drops Figures 3.4 and 3.14. Upon closer examination, that these pressure and volume decreases coincided with the division of epithelial cells making up the trophectoderm tissue. Epithelial integrity is one of the requirements for developing a pressurized cavity and cell divisions on average caused a 30pL±11pL volume decrease, which comprised 5% of the total volume. The pressure drops were most likely caused by the failure to maintain the sealing binding of intercellular junction proteins, such as Occludins, during cytokinesis events (membrane divisions).

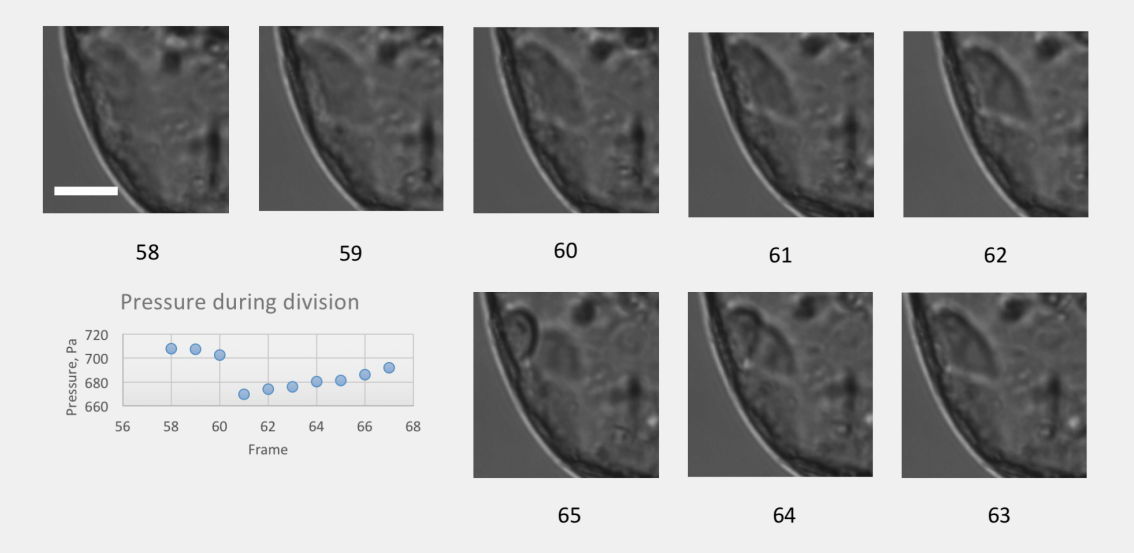


Figure 3.14: The pressure drop during cell divisions, frame numbers mark 6min. time points. Scale bar - 10μm

3.3.5 Blastocyst hatching

The ultimate result of blastocyst pressure development is hatching. This is required for embryo implantation into the uterus and timing has to be carefully tuned. When hatched too early, there is a risk for ectopic pregnancy [266] and late hatching risks missing the window of receptivity [84]. There were two distinctive modes of embryo hatching, one involving a small hole in the shell, which I termed 'pinhole' and the

other - complete breaking of the shell, to which I referred to as 'rupture'. Both of the hatching events took place at similar pressures, however embryos with pinhole type hatching usually had a thicker Zona Pellucida (Figure 3.15). Overall, hatching probability can be summarised in Figure 3.16, which takes into account the average pressure generated during development and Zona Pellucida thickness. Shell thickness was a better predictor for hatching probability, which approached certainty, as thickness decreased beyond 2μm.

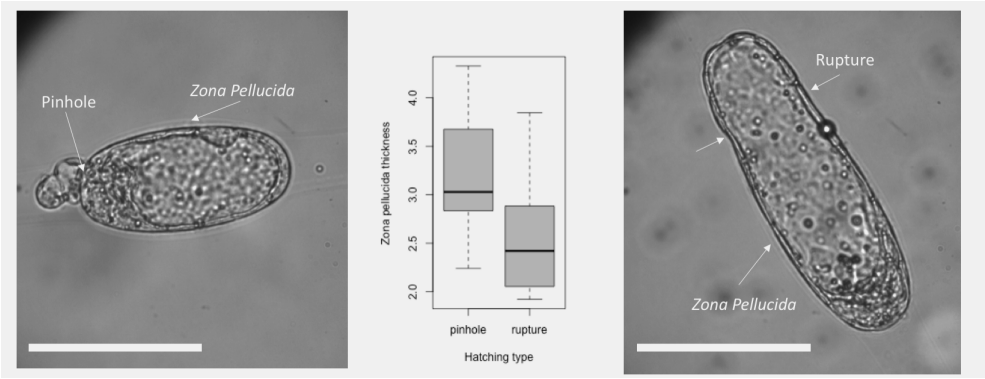


Figure 3.15: Hatching types and the difference in Zona Pellucida thickness. Left panel illustrates 'pinhole' type hatching and right panel demonstrates Zona Pellucida rupture. Middle panel compares Zona Pellucida thickness at which these hatching processes occur. N(pinhole)=12, N(rupture)=22, p=0.016 (t.test). Scale bar - 100μm

3.3.6 Investigating the mechanism of embryo hatching

Looking at hatching rates revealed, that Zona Pellucida thickness was a powerful predictor for embryo hatching probability. However, it is still unclear, what mechanism drives this thickness decrease. According to the balloon model, a perfectly elastic shell would become thinner as the embryo expands, but in order to reach less than 2μm, which is 20% of the starting thickness, an embryo would need to expand to more than twice the original diameter. Experimental data indicates, that embryos do not expand more than 60% of the starting size, which suggests, that either Zona

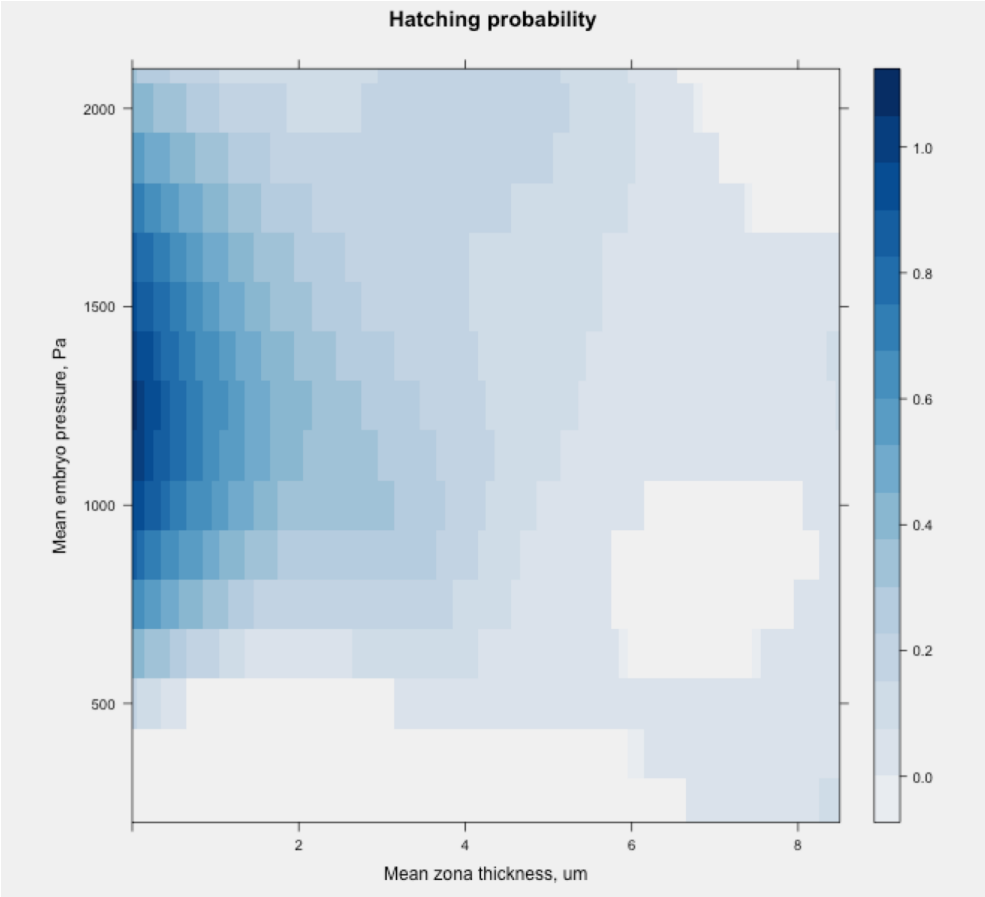


Figure 3.16: Summary of hatching probability with varying embryo pressure and Zona Pellucida thickness. After shell thickness decreases beyond 2μm embryo hatching approaches certainty.

Pellucida does not act as an idealized material and becomes softer with stretching, or becomes thinner due to the action of embryo secreted enzymes.

In order to study how hatching is affected by embryo generated pressure and by the presence of digestive enzymes, which can decrease the thickness of Zona Pellucida [267, 268], I used the hatching data from osmolarity experiments in combination with data obtained during embryo culture in media containing 0.5mg/mL Collagenase I. I statistically modelled the experiment as a survival study, which could be described by the Cox model regularly used in clinical studies Figure 3.17. Kaplan-Meier statistic was then used to estimate the significance between treatment and control groups.

Between the control group and sucrose treated embryos the likelihood coefficient

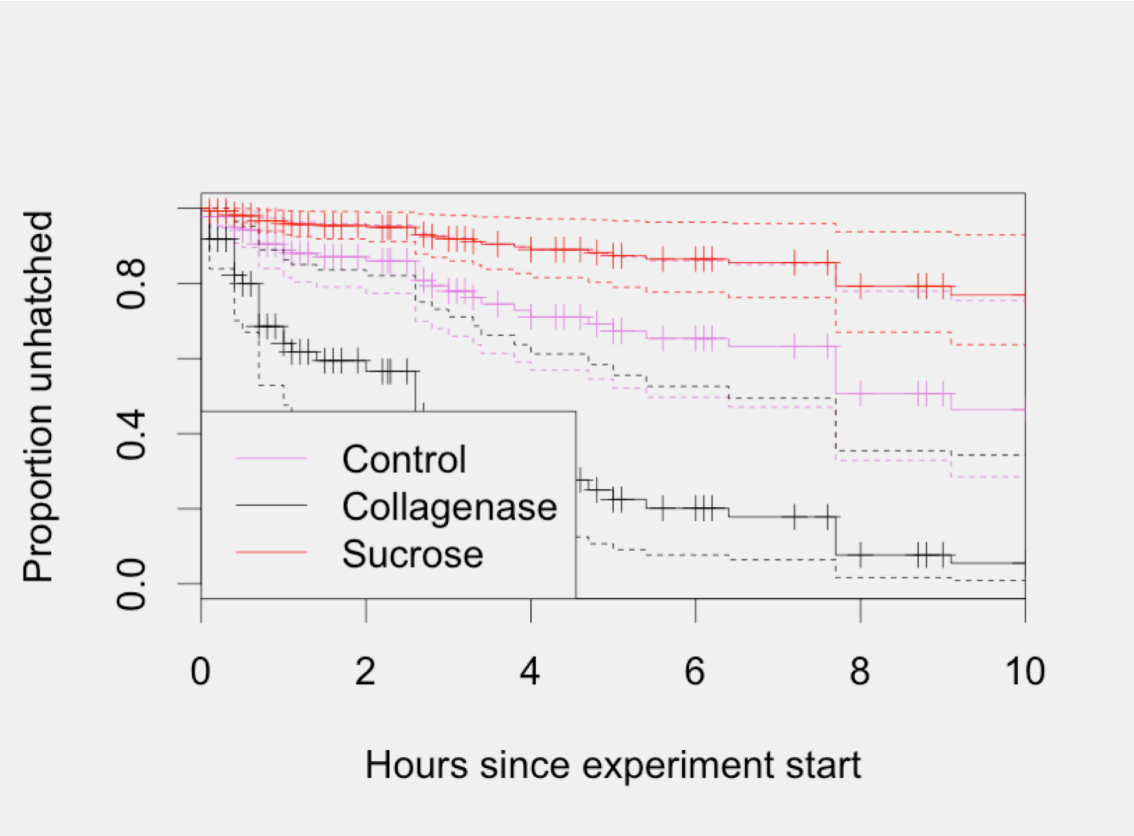


Figure 3.17: Embryo hatching modelled as a survival study. Crosses represent points fitted to a Cox statistical model and dotted lines represent the confidence intervals.

was -1.075, which means, that a given point in time sucrose treated embryos were nearly 3 times less likely to hatch than the controls (P-value of 0.021). Similarly, for Collagenase treated embryos, they were 3.8 times more likely to hatch than the controls (P-value was 0.016).

3.4 Conclusions

In the context of the thesis, this chapter establishes a biocompatible technique for measuring tissue-level pressures. To validate the mathematical model behind the framework, the method has been verified in several ways, including oil droplets, based on known surface tension, and pre-implantation embryos, based on existing body of known information about the action of ion channels and development of a pressurized

hyper-osmotic cavity.

From the context of embryology, a quantitative study of the events leading to the event of embryo hatching made it possible to create a detailed model describing the process. Breaking the gel-like shell (Zona Pellucida) surrounding the embryo involves a combination of embryo pressurization, as well as breakdown of the chemical structure by secreted enzymes. This is the first case to report how progressive embryo pressurization and Zona Pellucida thinning leads to a well-timed breakdown of this shell. Mechanical characterization also revealed molecular details of blastocyst cavity pressurization, which is driven by the balance between rising osmolarity, volume and containment inside the shell, which leads to pressure increase. The overall mechanical and molecular understanding of the process of embryo hatching can not only be applied for IVF technologies, but to also model systems in different contexts, including development of cysts and luminal tissues.

Chapter 4

Microscopy based biochemical tissue characterisation

4.1 Introduction

Mammalian development is a wide field that investigates how tissue complexity is generated and how diverse cell types are consistently organised into a complete organism. A common challenge in the field is the three-dimensional spatial analysis of protein distribution within tissues [269, 132]. Cutting edge optical microscopy and image analysis tools are routinely used for spatial analysis of plant, fruit fly, nematode and zebrafish development [270, 271, 272, 273, 130, 129]. However, historically there has been little success with mammalian tissue segmentation and particularly, sub-cellular level fluorescence measurements. Given the variability of different tissues, existing software is usually optimised to work with specific cases. For example, full cell segmentation tools like MorphographX (Figure 4.1) work well with plant cells, where high quality fluorescence signals make it possible to capture complete cell shapes.

As animal and mammalian samples usually contain more noise, it becomes more difficult to accurately segment and analyse individual cells. One of the most reliable solutions is offered by Imaris software, which makes it possible to manually outline the cells (Figure 4.2), because humans are adept at image analysis. However, manual outlining is time consuming, which is particularly a problem for time lapse imaging,

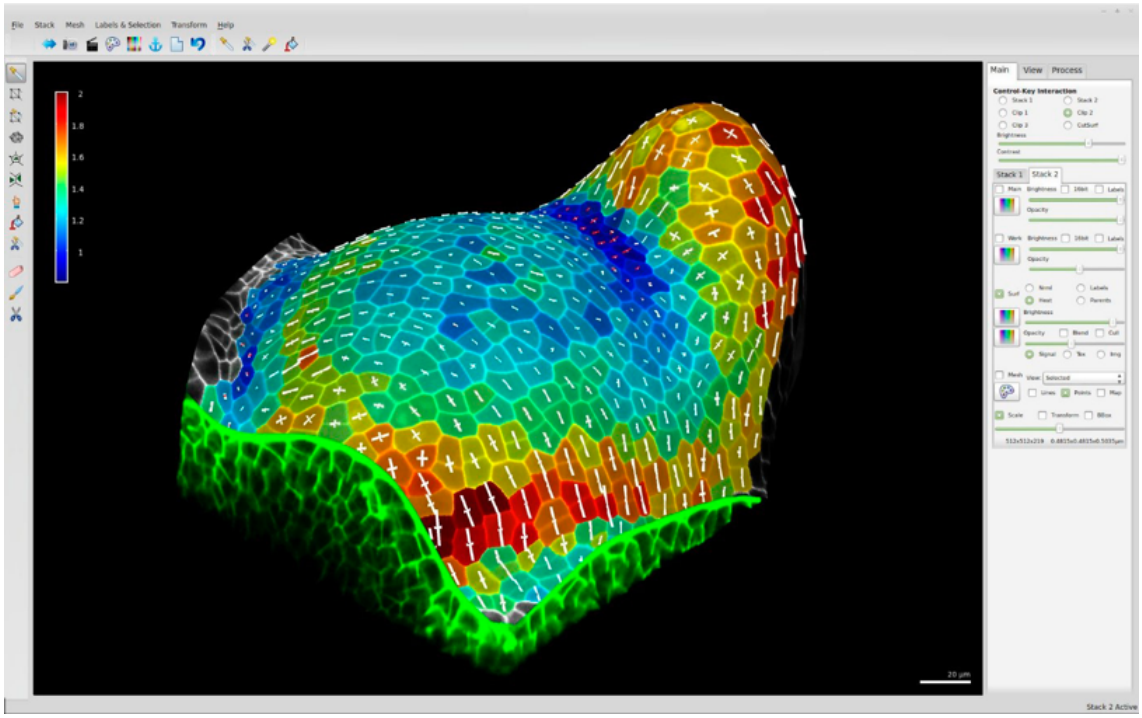


Figure 4.1: MorphographX, developed by the Max Planck institute. The image represents segmentation into single cells of a plant root tissue image.

where data quantity multiplies with every time point and manual outlining becomes impossible. In order to automate image segmentation, there has been a shift towards machine learning segmentation approaches. A notable example including such strategy is the tool RACE [129], which uses neural networks for tissue segmentation into individual cells (Figure 4.3). Arguably, this is one of the most successful approaches for automated segmentation of mammalian tissues, especially from membrane signals. However, unless a generalised artificial intelligence is developed, even for well-trained eyes it is still often impossible to fully segment the cells based on their outlines alone, because of limiting image quality. In cases, where the issues with image quality prevent complete tissue segmentation, the images often still contain a lot of useful information. In this chapter I describe how much of such information can be extracted without completely segmenting the cells.

In order to avoid the problems with image quality and full cell segmentation, I

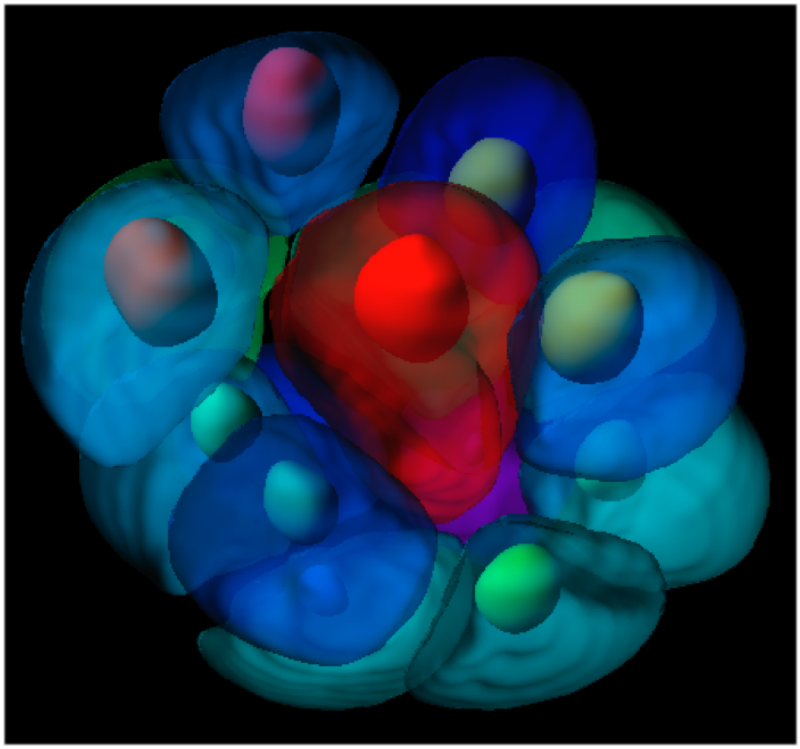


Figure 4.2: 16 cell embryo single cell segmentation by manual outlining on Imaris (Bitplane) software

have explored an approach that uses well defined cell features, such as nuclei, to perform partial, but robust segmentation using well established techniques [273, 131]. After identifying the most likely nuclear positions, samples of other sub-cellular regions (cytoplasm and membrane) are taken, based on their distance form the closest nuclei. The overall process resembles the steps unconsciously taken when looking at immunofluorescence images. First, the most obvious features, the nuclei are identified, then the cytoplasm is identified by what is not captured by the nuclear stain and membranes are expected to be found somewhere between neighbouring cells (Figure 4.4). Although such assumptions are not perfect, their probabilistic nature makes it possible to achieve high accuracy when making a large number of measurements [127]. The major limitation of this sampling based approach is that it does not provide information on cell shape or the total sum of fluorescence or cell tracking. However, the unique aspect is that it allows to process routine lower quality images, investi-

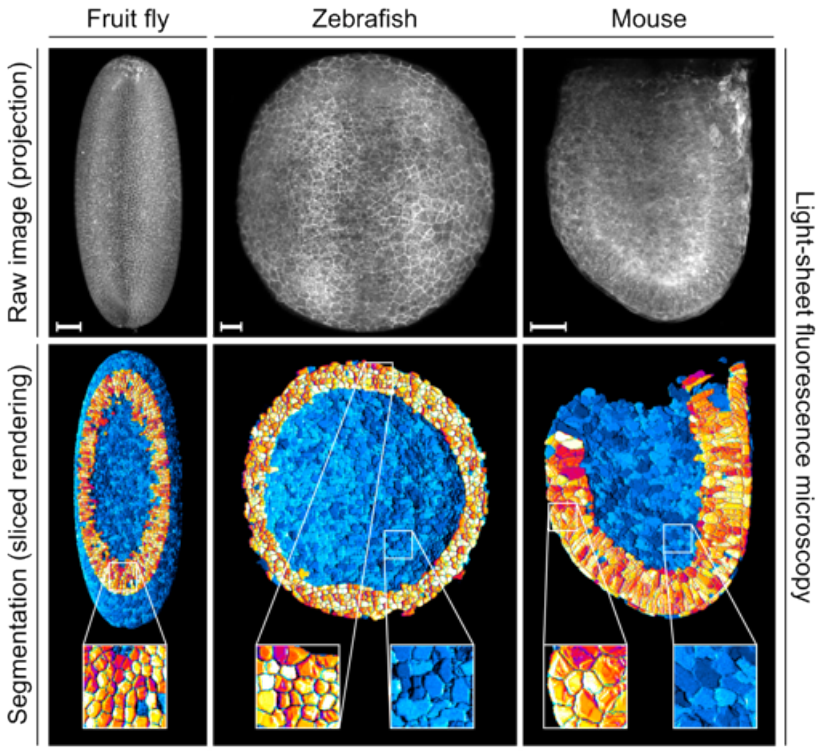


Figure 4.3: Automated tissue segmentation by the RACE machine learning tool [129]. The figure demonstrates software performance, as it is used to automatically segment lower optical quality images obtained by confocal and Light-sheet microscopy.

gate multiple cell compartments and quantify spatial protein fluorescence distribution within a tissue.

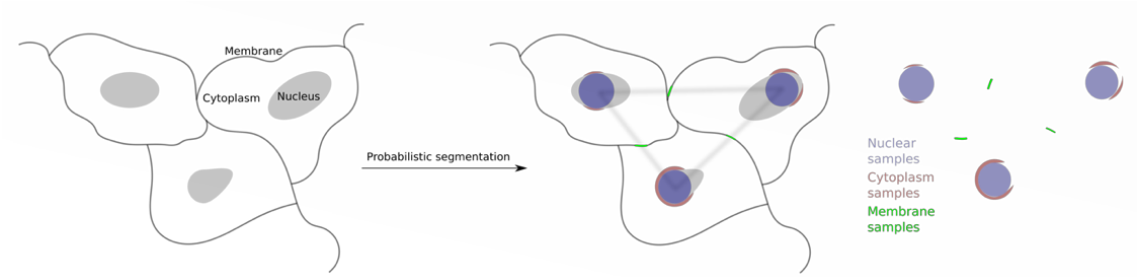


Figure 4.4: Probabilistic image segmentation, based on spherical nuclei detection followed by segmentation into nuclear and cytoplasmic regions and membrane detection on the basis of membrane distance to the closest nuclei.

Dealing with multiple spatial and fluorescence variables raises additional challenges in terms of signal normalisation, data analysis and visualisation. Normalising signals is crucial, because it allows to avoid variations due to image acquisition and

optical variations within tissues, which affect fluorescence intensity. A commonly used approach involves taking ratios of nearby cellular compartments, such as nuclei and cytoplasm. This has been previously used for investigating the Hippo pathway, where YAP localisation could be quantified by taking the ratio of nuclear and cytoplasmic fluorescence at the same time normalising the raw signals [274].

In order to analyse cell populations using fluorescence based protein estimates, the first step is performing dimensionality reduction followed by a variety clustering approaches [275, 276]. Such steps allow to identify cell populations, statistically test the difference between then and analyse how their location within the tissue correlates with biochemistry. Together with manipulation and force measurement approaches mentioned previously it becomes possible to test a large range of hypotheses on geometric cues for mammalian tissue development.

4.2 Materials and Methods

Vectashield (w. DAPI, H-1200) was purchased from Vector laboratories, Phalloidin atto 647 was purchased from Sigma (65906-10MMOL). Mouse anti-YAP monoclonal (sc-101199) and goat anti-Nkx2.5 (N-19) (sc-8697) polyclonal antibodies were purchased from Santa Cruz biotech. Rabbit anti-CDX2 (#3977S) monoclonal and rabbit anti-pERM (T567) (#3149P) monoclonal antibodies were purchased from Cell Signalling. Rat anti-Uvomorulin/E-cadherin (U3254-100UL) monoclonal antibody was purchased from Sigma. Rabbit anti-SRF (PA5-27307) polyclonal antibody was purchased from Thermo Fischer. We used the following secondary antibodies from Life Technologies: goat anti-rabbit AlexaFluor 488 (A11008), donkey anti-goat AlexaFluor 488 (A11055), donkey anti-mouse AlexaFluor 555 (A31570), donkey anti-rabbit AlexaFluor 647 (A31573). All animal experiments were performed according to procedures outlined in Chapter 3.

4.2.1 Stem cell culture

CGR8 cells were cultured in T-25 flasks coated with 0.1% w/v. gelatin and used at passage nr. 50-60. Cell culture media consisted of 90% DMEM medium (Gibco), 10% fetal calf serum (FCIII, Hyclone), 1mM sodium pyruvate, 1mM non-essential amino acid mix, 0.1mM beta-mercaptoethanol, 2mM L-glutamine, as well as 10^3U/mL leukemia inducible factor (LIF). Cells were passaged every 2 days and seeded at 400,000 cells per T25 flask. For cell freezing and recovery, we used a medium containing 10% DMSO and 40% cell culture medium and 50% fetal calf serum. Embryoid bodies were formed by aggregating cells in hanging drops and growing for 2 days before fixation.

4.2.2 Immunohistochemistry

To perform immunofluorescence on pre-implantation embryos and embryoid bodies, tissues were fixed for 20 min. at room temperature in 4% PFA. The embryos were then washed 3 X in PBT - 0.1% for 10 min, permeabilised in PBT - 0.25% for 40 min and washed again in PBT - 0.1%. The tissues were transferred to a blocking solution for 1h at 4^oC. Primary antibodies were then added to the solution and incubated overnight (o/n) at 4^oC. The embryos were washed in PBT - 0.1% and incubated for 1h at 4^oC in PBT - 0.1% with the secondary antibodies, then subsequently washed 2X PBT - 0.1% for 15 min and mounted in Vectashield with DAPI for at least 6 hours.

4.2.3 Post-implantation embryos

To perform immunofluorescence dissected embryos were fixed for 1 hour at room temperature in 4% PFA. The embryos were then washed 3X in PBT - 0.1% for 15 min, permeabilised in PBT - 0.25% for 40 min and washed again 3X in PBT - 0.1%. The embryos were transferred to blocking solution overnight (o/n) at 4^oC.

Primary antibodies were then added to the solution and incubated o/n at 4^oC. The embryos were washed 3x in PBT - 0.1% and incubated o/n 4^oC in PBT - 0.1% with the secondary antibodies, then subsequently washed 3x PBT - 0.1% for 15 min and mounted in Vectashield with DAPI for at least 24 hours at 4^oC.

4.2.4 Software and statistics

The software and graphical user interface were written in MATLAB (v. 2015b, Mathworks) and compiled using the in-built compiler for Mac OSX and Windows operating systems. 3D image visualisation has been done using Volocity software (Perkin Elmer) and Imaris software (v 6.1) has been used for manual cell outlining and analysis. R statistics package alongside 'cluster' library was used for automatic normalised cluster detection (PAM algorithm) and cell population analysis.

4.3 Results and discussion

The overall strategy relies on detecting well resolved tissue elements, such as nuclei or membranes and then analysing their closest environment to take samples of subcellular region fluorescence. Depending on which cell marker is available, the first step is to detect well resolved objects, such as nuclei or membranes, after which their closest environment is analysed. This creates the probabilistic aspect of the analysis, as it relies on making assumptions, based on probabilities, that a certain cell element is at a specific location within the cell. For example, cytoplasm closest to a nucleus is most likely to belong to the same cell.

4.3.1 Nuclei detection

Available nuclear detection techniques differ in their accuracy, throughput and noise tolerance. One of the fastest and robust methods for spherical object detection is based on Hough transform, which is a tensor voting technique for the most probable

circle positions within an image. The original algorithm is developed for 2D image analysis, however it can be extended for 3D measurements, by slicing the image into sections, analysing them as separate images and then deconvolving into 3D objects, as done previously [129]. In this case confocal image stack were analysed as separate images to detect circular nuclear cross-sections, the coordinates of which were then merged a 3D point cloud (Figure 4.5). The latter would be used as starting points in the subsequent analysis of individual cells.

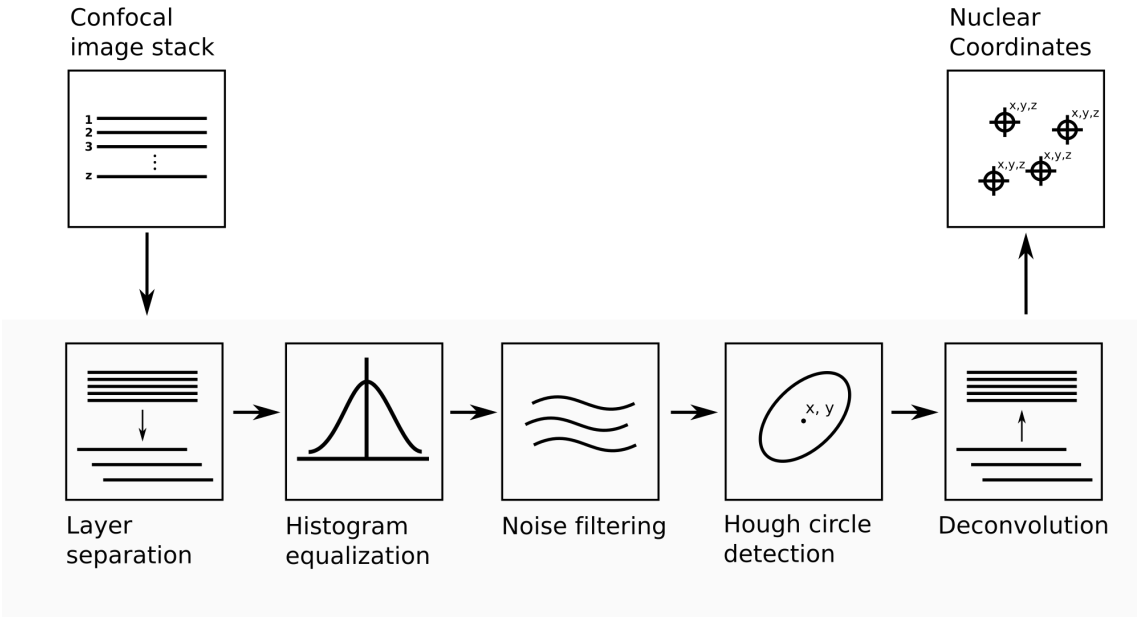


Figure 4.5: Image analysis strategy for detecting nuclear positions

4.3.2 Cell fluorescence sampling from detected nuclei

When nuclei are used as reference points, then a region from the confocal image is cropped around each detected point and classified according to the intensity of the nuclear stain into cytoplasmic and nuclear regions. The fluorescence from both regions was then averaged with cytoplasm pixels being weighed according to their distance to the detection point. This was done to represent the probability, that pixels closer to the nucleus are more likely to belong to the same cell as the nucleus. The fluorescence

levels along with the nuclear coordinates were recorded and this formed the basis of segmentation and quantification (Figure 4.6).

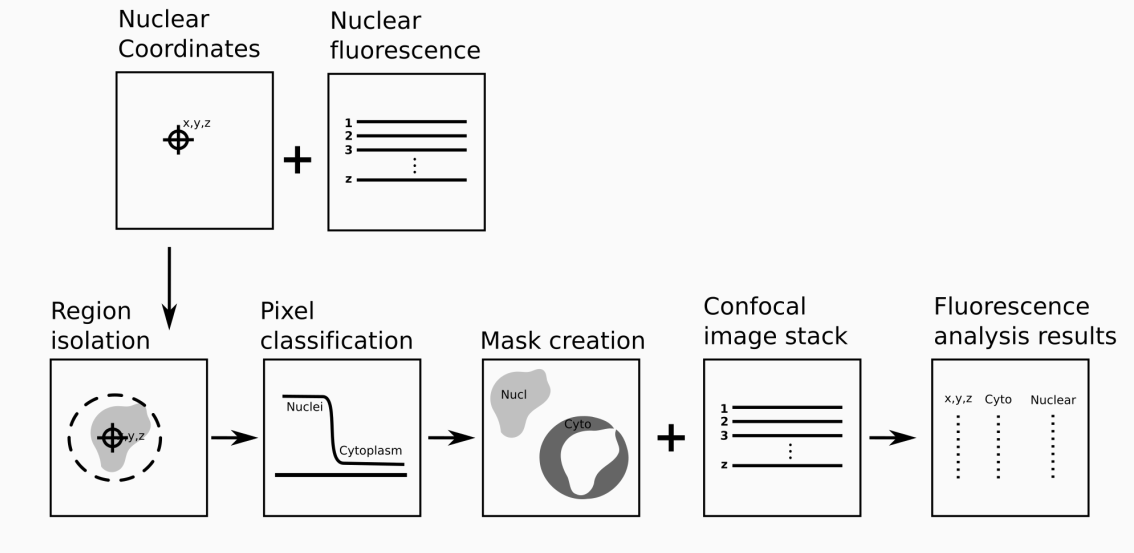


Figure 4.6: The algorithm for extracting cell nuclear and cytoplasmic fluorescence based on nuclear coordinates

If in addition to the nuclear stain, a membrane stain was available, it was possible to add another fluorescence reading for exposed and contacting membranes regions, which is particularly useful for looking at membrane localised proteins. In order to detect outside surface, the membrane fluorescence marker was thresholded and the outer pixels were assigned to the closest nucleus as an exposed membrane sample. To detect the contacting membrane samples, a line was drawn between two neighbouring nuclei and the highest intensity region for membrane fluorescence along the line was designated as a contacting membrane sample and was assigned to both nuclei (Figure 4.7).

4.3.3 Membrane element detection

In cases where nuclear markers are not available as a reference, membrane fluorescence could be used to create the points of reference for subsequent analysis. To detect membrane regions in space, a 3D stack was processed to normalise contrast and

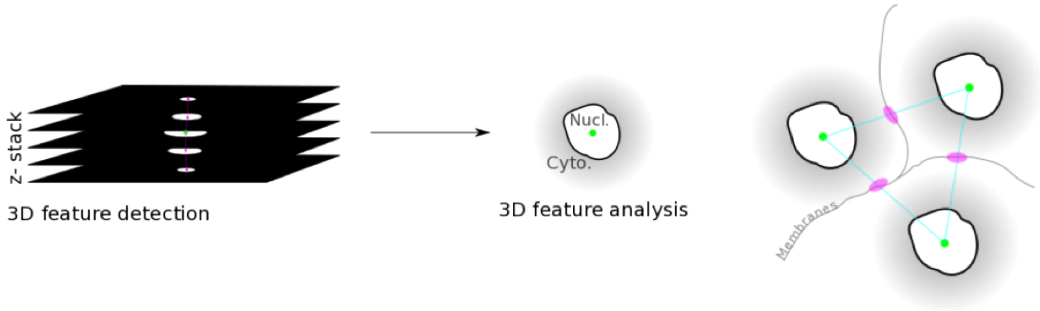


Figure 4.7: A combined algorithm to sample nuclear, cytoplasmic and membrane regions

filter noise. Then a 3D Canny Edge detector [277] was applied to find membrane edges, to which spheres were fitted using an outlier tolerant RANSAC algorithm. The detected membranes were represented by a location of the fitted sphere and a vector representing membrane curvature and direction (Figure 4.8). This information would then be the starting point for sampling membrane and cytoplasmic fluorescence intensities. The advantage of this method is that it looks for fragments of membranes, which is more tolerant to noise, than other approaches dealing with total membrane segmentation.

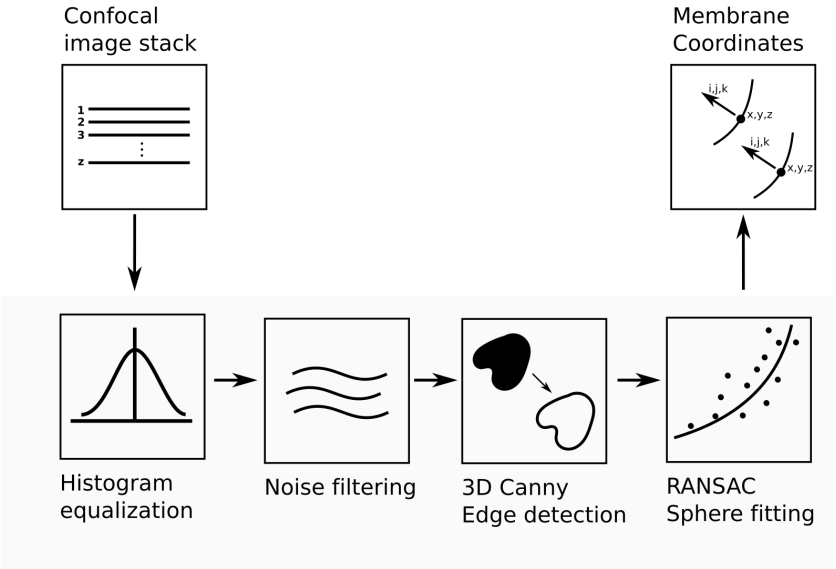


Figure 4.8: Membrane fragment detection algorithm

4.3.4 Cell fluorescence sampling from detected membranes

When only membrane stains are available, the membrane fragment detection algorithm (Figure 4.8) can be used to extract membrane locations, from which sampling masks for membrane and cytoplasm fluorescence can be created. The mask considers a narrow region in space around the detected point to sample membrane fluorescence and draws a normal to membrane surface to sample cytoplasm on the either side. These masks are used on 3D image stacks to analyse membrane and cytoplasmic fluorescence distribution in space (Figure 4.9).

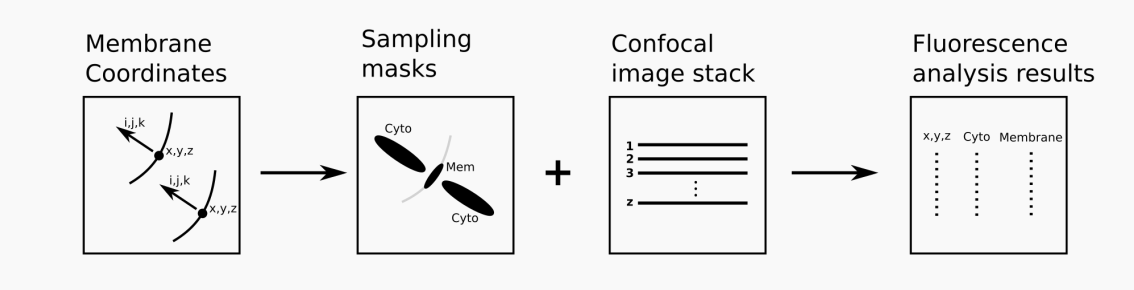
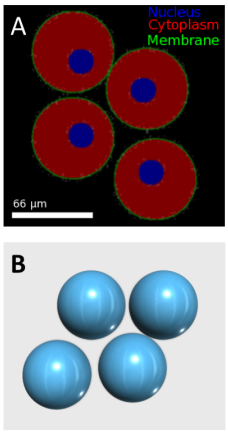


Figure 4.9: Analysis of membrane and cytoplasmic fluorescence based on membrane fragment detection

4.3.5 Method validation with CAD images

To validate this probabilistic analysis approach, I have used computer generated 3D images to compare the accuracy of standard manual outlining (using Imaris, Bitplane) and sampling based automated approaches (Figure 4.10). Mock-up tissues composed of several spherical objects were created on Google SketchUp and converted to a stack of images, which were then filled with known brightness fluorescence. Manual outlining was the most accurate method of image segmentation and in addition to quantifying protein fluorescence, it could also be used to estimate the proportion of exposed cell surface, which is useful for cell polarity studies. In general, fluorescence measurement errors fell below 10%, except for feature detection relying on membrane fragments. The most likely source of error for membrane based feature detection came

from the detection algorithm while fitting spheres, which is responsible for identifying both membrane segment position and orientation.



Algorithm		Use scenario	Exposed surface error	Nuclear stain error	Cytoplasmic stain error	Membrane stain error
Manual	Cell outlines	Need high accuracy or exposed surface	3.2%	- 6.6%	0.7%	6.4%
Automatic	Membrane fluorescence	Only a membrane stain is available	NA	NA	-28%	-15.7%
	Nuclear fluorescence	Only nuclear stain is available	NA	-7.8%	-8.6%	NA
	Membrane and nuclear fluorescence combination	Nuclear and membrane stains are available	NA	-7.8%	-8.6%	-4.2%

Figure 4.10: Accuracy of sampling based image segmentation. A) - A section of a computer generated image for testing image analysis methods. B) - A 3D rendering of computer generated objects for testing image analysis methods. Method accuracy was assessed by comparing measured fluorescence levels to known intensity values in computer generated images.

4.3.6 Method validation with pre-implantation embryos

The mouse pre-implantation embryo is a model system where cell fate is strongly influenced by tissue geometry [278]. The genetic basis of pluripotent Inner Cell Mass (ICM) specification has been studied in great depth [140] and this large amount of existing information about pre-implantation embryo development makes it possible to validate the analytical approach.

During the process of the first cell fate decision, Hippo pathway becomes differentially activated in different cells [186]. The transcription factor Cdx2 promotes TE fate and represses ICM fate [181]. Cdx2 expression is driven by the transcription factor Tead4 working together with the transcriptional co-activator Yap [140]. Yap shuttles between the cytoplasm (where it is inactive) and the nucleus (active), in a

tightly regulated manner [186]. The differential localisation of Yap protein is the basis of Hippo signalling and ultimately controls tissue patterning.

To estimate the errors resulting from the automated image analysis approach I used manual cell outlining to create a ground-truth dataset, to which automated analysis results could be compared. The graph represents fluorescence measurements for nuclear and cytoplasmic partitions of Hippo pathway component Yap (Figure 4.11). Figure 4.12 shows the masks used for fluorescence sampling. Most of the measurements focused on the activity of Hippo pathway and further discussion can be found in chapter 5.

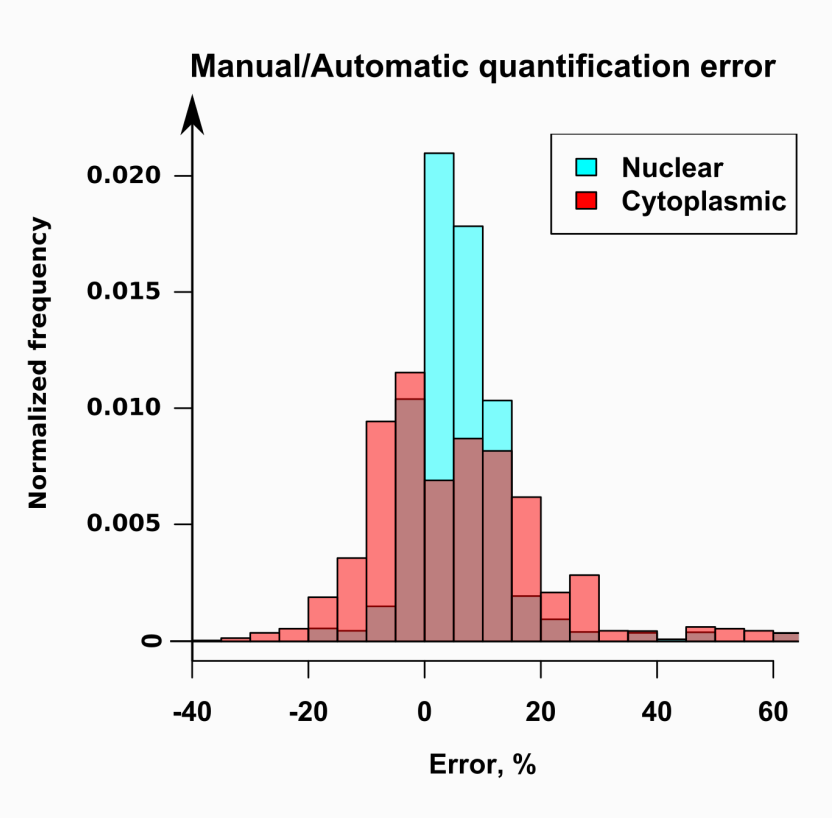


Figure 4.11: Agreement between manual and automatic analysis approaches. The ground-truth dataset was created by manually outlining embryo cells to segment cell nuclei and cytoplasm. The same embryos were then processed automatically and the differences in fluorescence measurements are represented as histograms here.

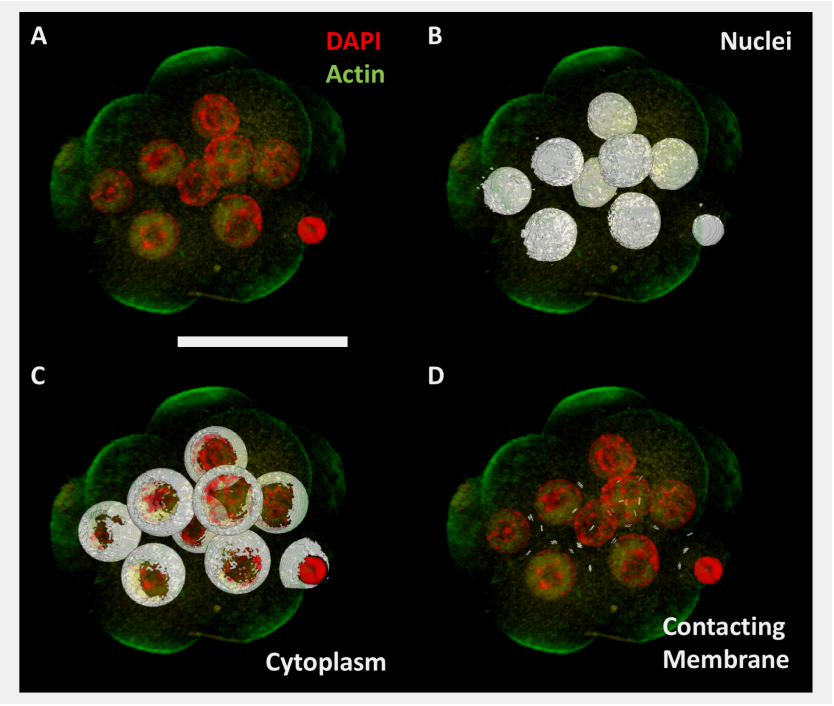


Figure 4.12: Fluorescence sampling masks for mouse pre-implantation embryos. A) - A maximum intensity projection of a confocal image. B) - Masks for sampling nuclear fluorescence. C) - Masks for sampling cytoplasmic fluorescence. D) - Masks for sampling contacting cell regions for membrane fluorescence. Scale bar - 50μm.

4.3.7 Method validation with embryonic hearts

While mouse pre-implantation embryos present an ideal case for testing automatic image segmentation, because it is possible to also manually outline the cells for comparison, they do not necessarily represent a typical mammalian tissue. A more representative mammalian tissue is the embryonic heart (Figure 4.13) with a larger number of cells and closely spaced nuclei.

To test the ability of the image analysis approach for this problem, I examined the localisation of Nkx2.5 and Srf - two transcription factors important for cardiomyocyte formation [279]. In order to represent protein concentrations of these two transcription factors I used a ratio of nuclear to cytoplasmic fluorescence, as the latter is expected to represent background signal for internal normalisation. To reduce the dynamic range of the measurements and normalise the distribution of the values, I used a natural

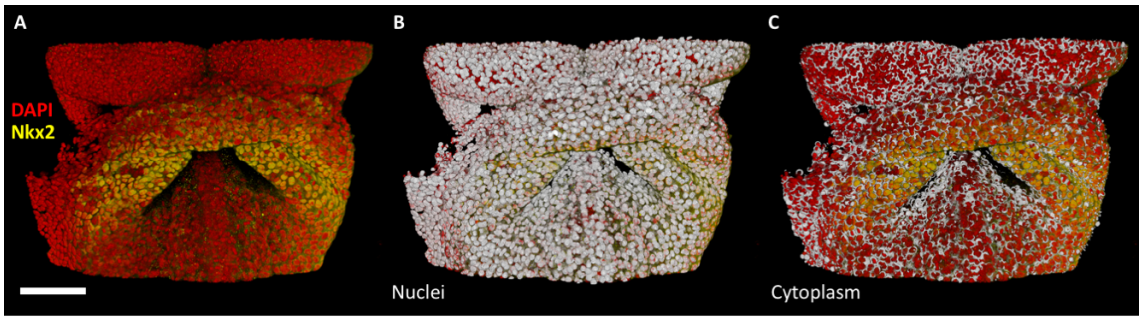


Figure 4.13: Segmentation masks for embryonic heart tissue. The tissue was dissected, stained and imaged by Dr. Richard Tyser (Srinivas lab). A) - Maximum intensity projection of a confocal microscopy image. B) - Masks for sampling cell nuclei. C) - Masks for sampling cell cytoplasm. Scale bar - 50μm

logarithm of the ratio. In addition to these normalised fluorescence measurements, I also measured cell distance to the two manually designated regions - head folds and heart tube.

The four variables formed a dataset, which was clustered using partitioning around mediods (PAM, R 'Clara' package) [280]. The method was chosen over other clustering approaches [275] due to computational efficiency in dealing with large datasets. The analysis indicated, that both proteins were preferentially expressed in the heart region and there was a region specific correlation between nuclear levels of Nkx2.5 and Srf (Figure 4.14).

4.3.8 Development of 'SilentMark'

As to my knowledge, there are no existing software tools with the ability to analyse spatial protein expression patterns, the above mentioned algorithms were developed into a software package designed for general use (Figure 4.15). The package is a standalone application, based on a GUI designed on Matlab. It accepts 3D images as stacks of files, or the most commonly used confocal microscopy '.lsm' format. User is required to enter two intuitive and robust parameters - an estimate of the diameter of the nuclei and an estimate of nuclear channel brightness for thresholding. These two parameters were chosen, because they allow to work with different types of tissues and

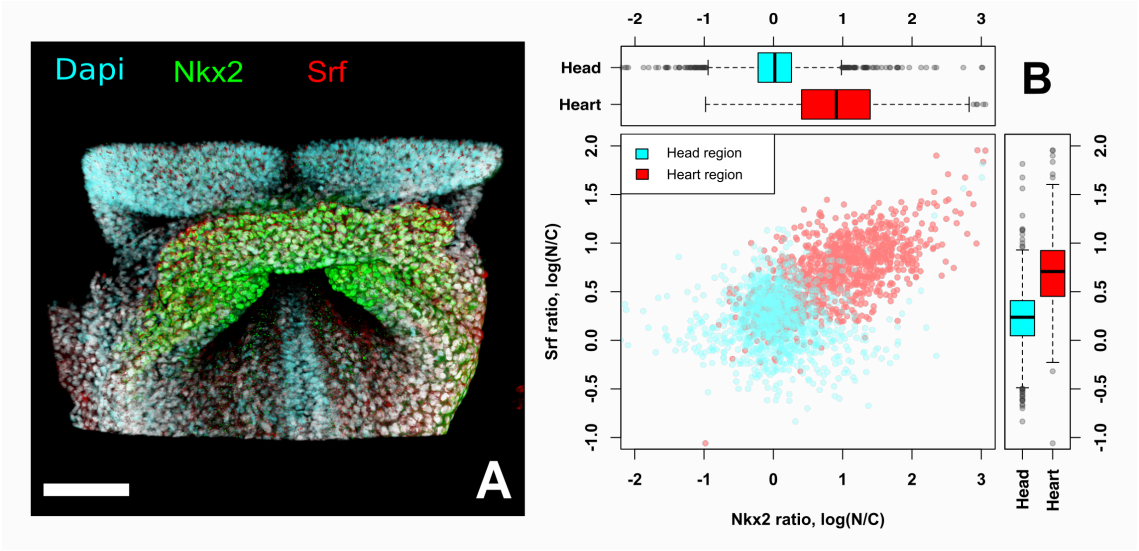


Figure 4.14: Image analysis of Srf and Nkx2 localisation in the embryonic heart. A) - Maximum intensity projection of a confocal image. Heart region is roughly identified by the Nkx2 stain and head folds are two semi-circular structures top of the image. B) - Corellation between Nkx2 and Srf proteins in selected head and heart regions. Bar plots represent average protein levels in the two regions. Inter-region P-values $<$ 0.001, cell measurements are from a single heart tissue. Scale bar - 50μm

image qualities and analysis is least sensitive to mistakes made, while specifying them. All of the remaining parameters needed for the analysis are derived and optimised by the software.

The software will output a list (csv format) of detected objects (nuclei or membrane fragments), each of which will have a measure of nuclear and cytoplasmic fluorescence as well as membrane, if there is a fluorescent marker. The data will also contain object coordinates to describe spatial protein distribution, automatically calculated distance to exposed surface and distance to regions of interest, if they are designated manually in 3D. This information is then used by statistical software tools for further analysis.

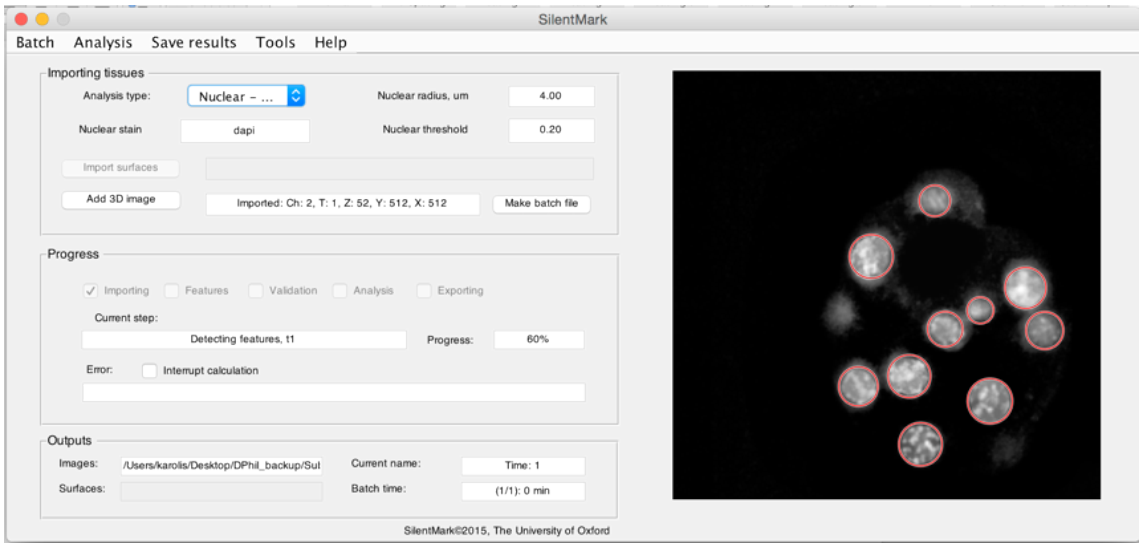


Figure 4.15: SilentMark graphical user interface

4.3.9 Using scRNA-seq data to extend spatial protein quantification

The main fundamental limitation of this type of protein analysis (and confocal microscopy in general) is low throughput. Usually only two proteins are imaged at once, because of antibody availability and spectral crowding during the imaging setup. Generally, this limitation is solved by another analytic approach - single-cell RNA-seq (scRNA-seq), which allows to look at thousands of genes at the same time. However, RNA sequencing requires sample destruction and cannot directly provide information on spatial protein distribution. Given the two fundamentally complementary strengths of these two approaches I explored a probabilistic strategy to combine the two different types of information provided by these strategies based on the common protein signal levels (Figure 4.16).

The two methods provide a fundamentally different type of information (levels of protein and transcripts used for making the proteins). They are not always correlated, because in addition to mRNA levels, protein levels also depend on their stability, translational regulation and post-translational modifications. As a result, only half of the proteins are correlated to RNA levels in mammalian cell lines[281]. If it is

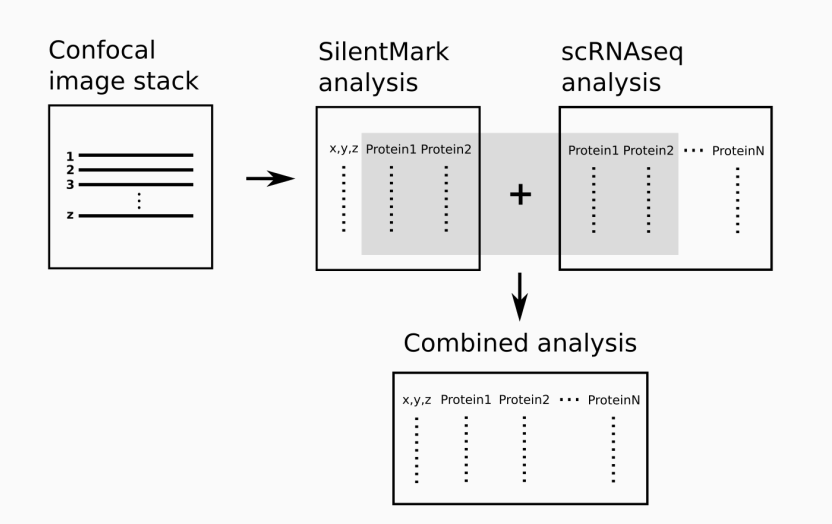


Figure 4.16: The strategy of combining geometric protein distribution analysis with scRNA-seq data

possible to identify proteins, which are transcriptionally regulated it also becomes possible to use geometric protein distribution to predict geometric distribution of their mRNA within tissue cells and use it to correlate the remaining mRNA from scRNA-seq. In this case I will focus on Cdx2 transcription factor, which has both protein and RNA levels highly correlated with trophectoderm fate [282].

In order to convert protein and mRNA levels into a dimensionless scale, which could be used for comparing different types of data, it is necessary to create a standardized scale. One way to create such normalised scale (standard score) is to subtract the population mean and divide it by the standard deviation $\sigma(X)$ (Equation 4.1), (Figure 4.17). This strategy works best for normally distributed variables and normality can be first checked by performing a quantile-quantile plot or a similar test. This scale can then be used to create a predictive model for estimating either the geometric parameters from SilentMark data, or modelling unknown protein expression from the scRNA-seq data.

$$score = \frac{X - \bar{X}}{\sigma(X)} \tag{4.1}$$

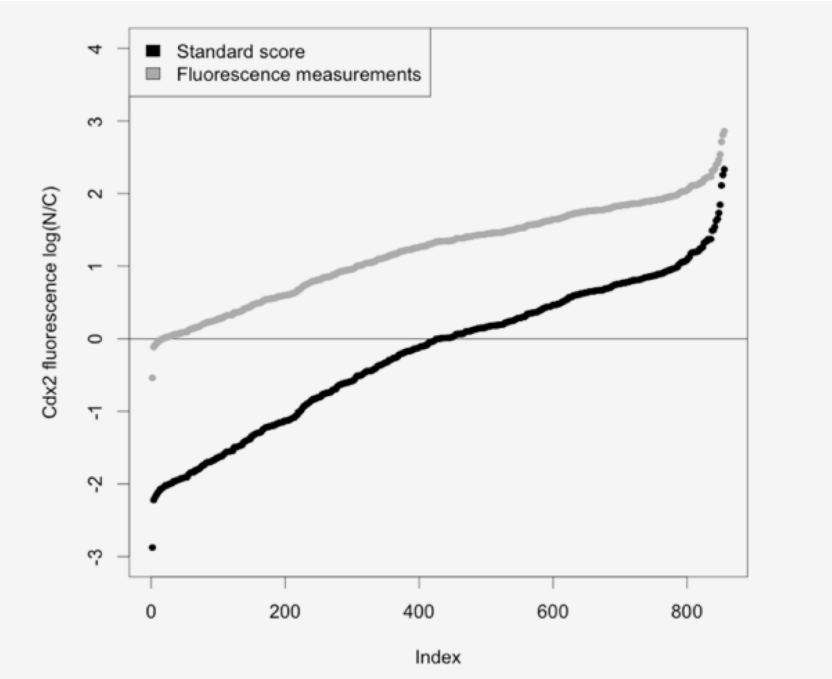


Figure 4.17: Creating a standard score from Cdx2 fluorescence measurements. The figure presents Cdx2 fluorescences levels before and after normalisation, which creates a standard score centred at 0 and with measurements within a standard deviation falling between -1 and +1.

Cdx2 is differentially expressed in the outside cells (Figure 4.18) it has a good quality antibody available and is localised in the nucleus, which helps with measuring normalized fluorescence levels. Creating the statistical link between values is best achieved when enough measurements are available (>50) and they are normally distributed. I have created standardized scores for Cdx2 fluorescence, as well as transcript levels from single cell RNA sequencing data, which are represented as RPKM [283]. Using RPKM is a way to normalise sequencing reads to the length of the transcript and the total number of sequencing reads, such that the value represents mRNA quantity.

To statistically define the relationship between Cdx2 levels and cell distance from embryo surface (Figure 4.18) I used decision tree modelling rather than linear regressions, which allows to model highly non-linear data. To avoid overfitting highly noisy

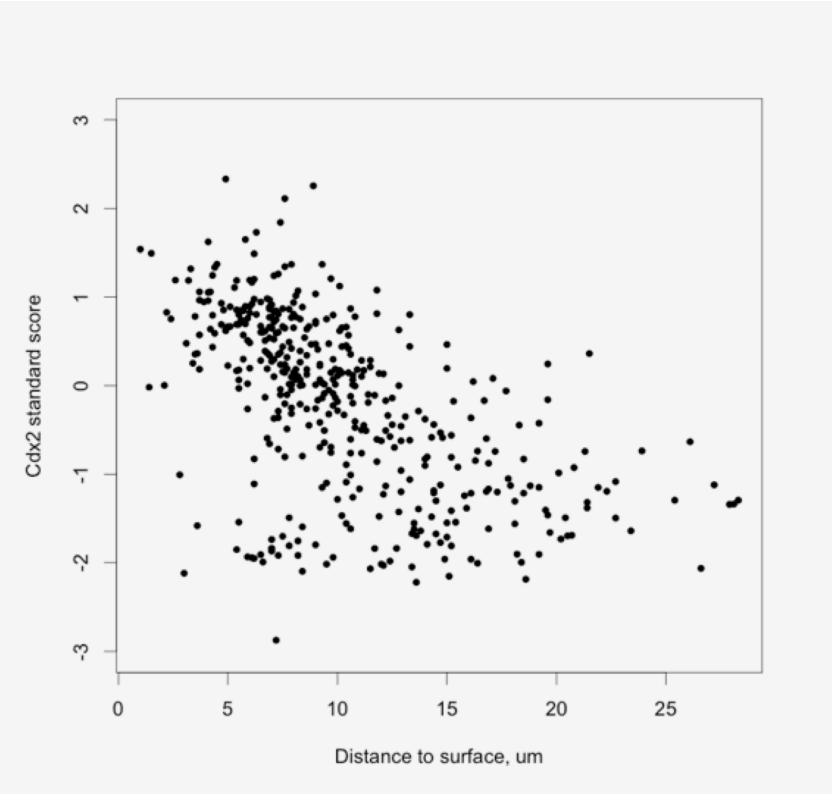


Figure 4.18: Cdx2 expression variation with distance from embryo surface. Cdx2 fluorescence level variation with cell distance from embryo surface in 4 late 32 cell stage embryos, as measured by SilentMark.

data I used Random Forest methodology [284]. Once the distance to surface could be modelled by standardized Cdx2 levels, I could then add the distance geometric descriptor to scRNA-seq gene expression data, based on the internally standardised Cdx2 levels in that dataset (Figure 4.19). The graph represents correlations between different genes expressed in various cells and the newly added geometry descriptor. There was an expected positive correlation between Cdx2 and Eomes transcription factors, which were expressed at higher levels in cells closer to the outside. There was a slightly positive correlation between Pou5f1 (Oct4) and Nanog transcription factors defining the inner cell mass, which is further from the outside surface. There was also a negative correlation between the proteins expressed in the inside outside cells, as well as actin and E-cadherin. Using this technique, the surface distance variable could now be used to investigate correlations with the different transcript levels.

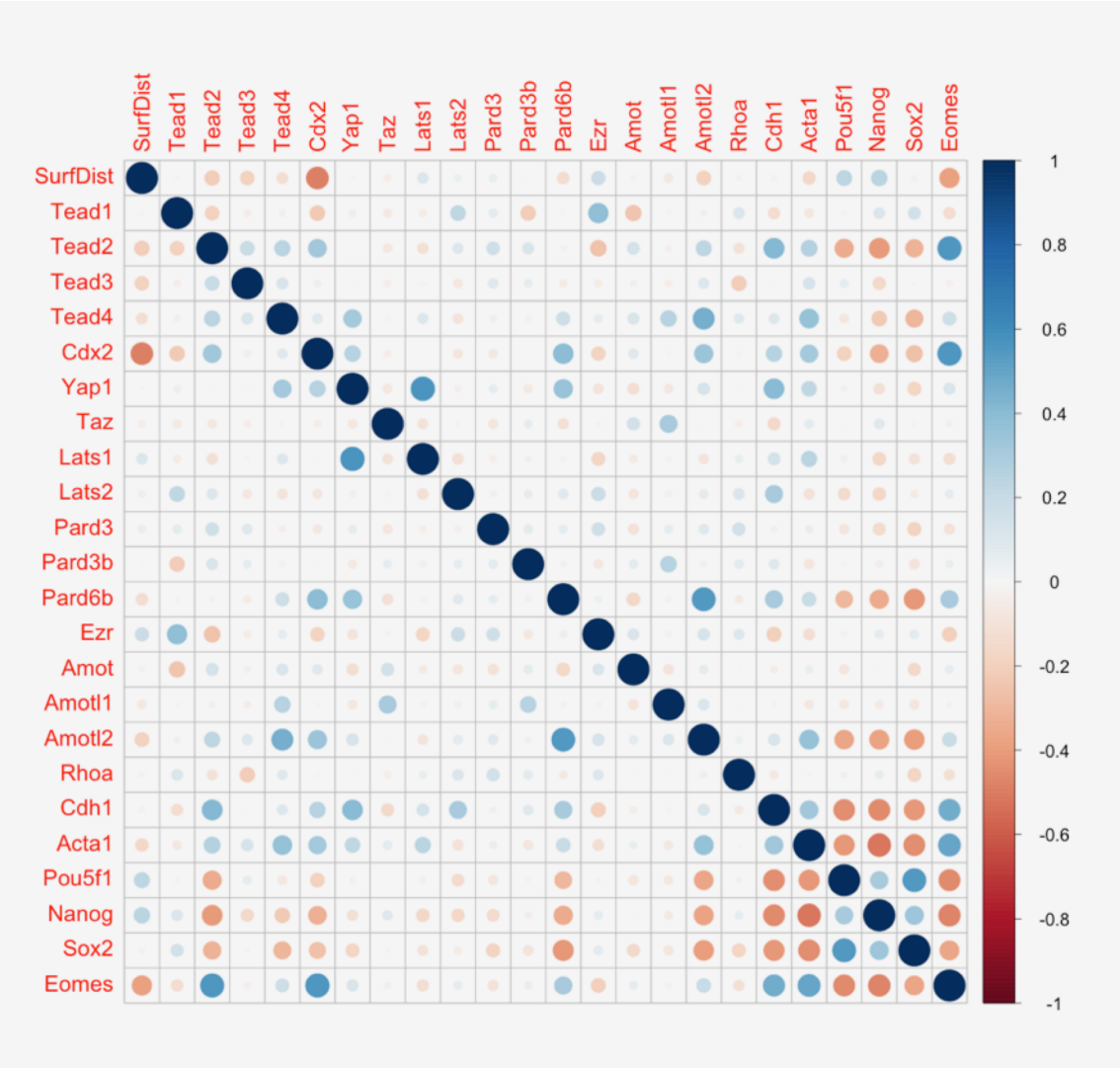


Figure 4.19: Integrating distance measurements into single cell RNAseq data (40 cell embryos). A geometric descriptor (cell distance to surface) has been added to the dataset by using information available on geometric protein distribution from Silent Mark analysis. Circle size indicates the correlation coefficient between variable pairs and colour represents the slope with blue being positively correlated and red - negatively.

Even through using Cdx2 as a single protein to create the link between the two different types of data is not the perfect example, it still proves the general utility of the method. From a statistical perspective, the overall performance can be improved by adding an additional fluorescent protein into the model and using proteins, whose expression levels are limited by their transcription and generally have a normally

distributed expression levels (rather than on/off).

4.4 Conclusions

In summary, I have created an image analysis tool, which processes 3D immunofluorescence images in a sampling based manner in order to avoid the common difficulties with segmenting whole cells. Although not without its own disadvantages, the method has a relatively small bias, can be used with lower quality images and simultaneously provides information about nuclear, cytoplasmic and membrane fluorescence, as well as distance based descriptors of tissue geometry.

Analysis automation also enables high-throughput quantification and statistical analysis of spatial protein organisation, often involving subtle differences in protein levels, which are undetectable by visual analysis. Furthermore, having a numerical representation of protein levels makes it possible to discover statistical relationships between proteins and geometry. This makes it possible to statistically test hypotheses and also use modelling to create quantitative relationships, which can be used to add geometric descriptors to other high-throughput datasets, such as scRNA-seq.

Chapter 5

The role of tissue geometry during the first mammalian cell fate decision

5.1 Introduction

The course of mammalian development is abundant with complexity, which is tightly controlled by regulatory mechanisms. Most of the development is defined by interlinked combinations of chemical, genetic and mechanical cues coming from multiple sources. In such context the first cell fate decision may appear simplistic, as it happens in a self-contained 16 cell cluster [168, 285, 286, 170]. However, the timing of the event coincides with major metabolic changes [287], a shift from maternal to embryonic gene expression [179] and emergence of cell polarity [288]. Therefore, despite the apparent lack of complexity, it is difficult to disentangle factors, which are responsible for cell fate emergence. As a result, despite the published information, the first cell fate decision event remains one of the most studied and enigmatic events during mammalian development [187].

The first time cells choose their fate, there are two distinct geometric environments, or niches - the outside and the inside of the spherical tissues. One of the earliest observations was that the emergence of two tissues (trophectoderm and the inner cell mass) corresponds to their positions within the embryo with a high degree

of regulation [171]. This has been seen during disaggregation and re-aggregation experiments, which produced a single outside layer of trophectoderm cells regardless of original blastomere source and stage.

One view suggests, that the embryo is organised on the basis of pre-programmed patterning events and cells occupy their positions based on their fates. This theory is supported by the evidence of differential mRNA localisation by FISH experiments [183] and single cell RNA sequencing [182]. Also much of invertebrate development is regulated by pre-determined factor localisation in early cells [289]. However, in contrast to invertebrate development, early cells appear to be identical before the first cell fate decision, and also capable of switching fates [290]. This led to an alternative view, arguing that cell fates are actively decided and regulated by their relative location within the embryo (Figure 5.1).

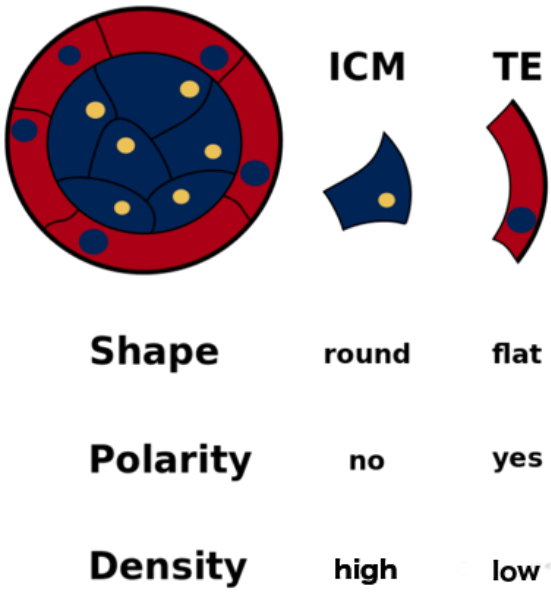


Figure 5.1: The two geometric niches in the pre-implantation embryos. Cells occupying the niches are not only different biochemically, but also exhibit morphological differences. Compared to inner cells, the outer cells are flatter, they have an outer surface, which makes them polarised and have fewer neighbours as they are exposed to the outside.

The theory based on active cell fate regulation has received a lot of support af-

ter the recent discovery of Hippo pathway role during pre-implantation development [141]. It was found, that the fate decision was driven by an asymmetric distribution of Yap and Taz Hippo pathway components, but not their target transcription factor Tead4, which was uniformly distributed. This view has been contested by other reports suggesting, that Tead4 is in fact asymmetrically distributed, but this view did not receive widespread support [142]. Further evidence came from genetically disrupting polarity and Hippo pathway components [149, 144], which led to cell differentiation failure. Although the discovery revealed a fundamental molecular process, it also raised further questions about the role of cell geometry and the timing of differentiation.

Since Yap and Taz proteins are at the center of the Hippo pathway, the discovery of their involvement led to implication of various other upstream factors found in different contexts. The first potential targets were cell adhesion molecules Cadherins [291, 292, 160, 293], which were found during the original discovery of the Hippo pathway in drosophila [133]. As Yap and Taz were also involved in mechano-sensing, this also added the possible cell shape and tension mechanical cues [294, 25]. Finally, cell polarity was also found to play a major role in cell fate decision through Angiomotin scaffolding proteins [144, 149, 147]. All of these possible upstream signalling factors led to a complex molecular pathway (Figure 5.2), but little information about the direct role of geometry itself, assumed to be the most upstream regulator of cell fates.

Without a way to directly change embryo shape and cell location it was previously impossible to isolate the involvement of mechanical cues [295]. Therefore, I adapted the methods developed here in order to perturb cell mechanical and geometric environment and isolate upstream development cues.

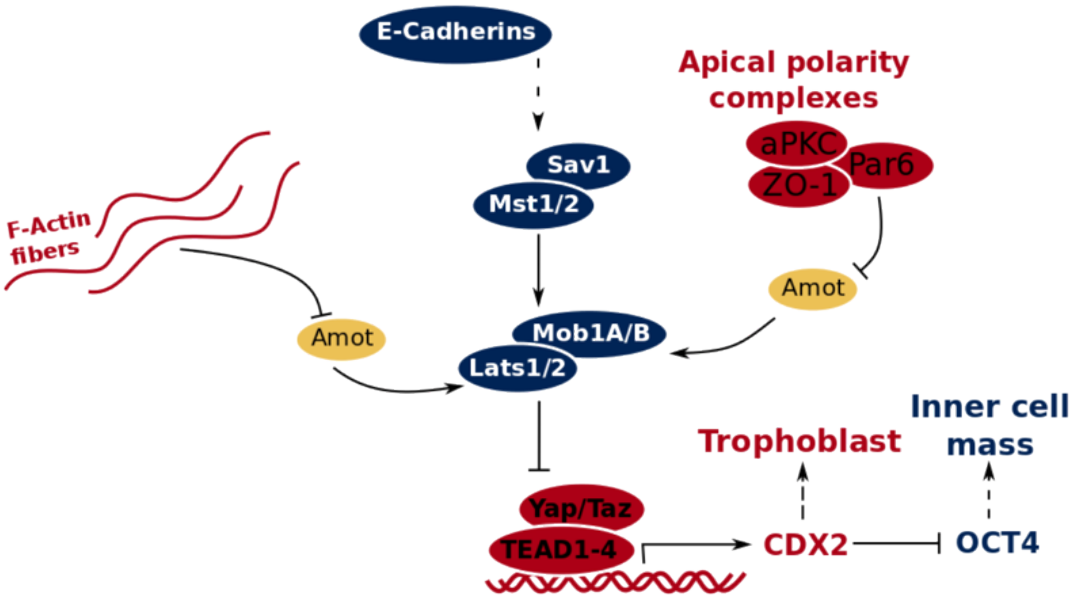


Figure 5.2: The Hippo pathway specific to pre-implantation development.

5.2 Materials and Methods

Phalloidin Atto 647 was purchased from Sigma (65906-10MMOL). Mouse anti-Yap monoclonal (sc-101199) antibody was purchased from Santa Cruz biotech. Rabbit anti-Cdx2 (#3977S) and rabbit anti-pERM (T567) (#3149P) monoclonal antibodies were purchased from Cell Signalling. Rat anti-Uvomorulin/E-cadherin (U3254-100UL) monoclonal antibody was purchased from Sigma. I used the following secondary antibodies from Life Technologies: goat anti-rabbit AlexaFluor 488 (A11008), donkey anti-mouse AlexaFluor 555 (A31570), donkey anti-rat AlexaFluor 647 (A21247). Vectashield (w. DAPI, H-1200) was purchased from Vector laboratories.

5.2.1 Mouse strains, husbandry and embryo collection

All animal experiments were carried out according to UK Home Office project license PPL 30/3155 and 30/2887 compliant with the UK animals (Scientific Procedures) Act 1986 and approved by the local Biological Services Ethical Review Process. To obtain wild-type embryos C57BL/6 males were crossed with CD1 females (Charles

River) and to obtain LifeAct-EGFP embryos [296] LifeAct-EGFP males were also crossed with CD1 females. All mice were maintained in a 12-hour light-dark cycle. Noon of the day finding a vaginal plug was designated 0.5dpc (days post coitum). In order to dissect the embryos, the pregnant females were culled by cervical dislocation and death was confirmed by exsanguination in accordance to the schedule one of the Animal Scientific Procedures Act. Embryos of the appropriate stage were dissected in M2 medium (Sigma-Aldrich) at room temperature. Pre-implantation embryos were collected by oviduct and uterus flushing.

5.2.2 Hydrogel compression experiments

Planar polyacrylamide hydrogels (4-5%) for studying geometric cues were synthesised as described previously. To compress the embryos between two hydrogel sheets, they were cut to 2 x 2mm square pieces, equilibrated with embryo culture media and placed under mineral oil, which caused the hydrogel sheets to adhere to each other due to surface tension. The embryos were then carefully inserted between the sheets (250μm thickness) and the water was carefully removed from gap between the sheets to compress the embryos.

Hydrogels with cylindrical cavities were prepared by casting acrylamide solution around a small diameter wire (25μm). Acrylamide/bisacrylamide (37.5:1) mixture was used to prepare gels (5% by mass), which corresponded to approximately 4.2kPa stiffness. Ammonium persulphate (0.1%) and TEMED (1%) were added to polymerize polyacrylamide. After the wire was removed forming cylindrical cavities, the hydrogels were equilibrated in embryo culture medium KSOM, by changing the solution three times in one hour. The embryos were then inserted into the channels by a glass capillary having a diameter slightly larger than the embryo itself. It was used to stretch the hydrogel channel before injecting the embryos and letting the channels relax and deform the embryos.

At the end of the experiments, embryos inside the hydrogels were fixed with 4% formaldehyde for 30 minutes at 4^oC and the embryos were removed from the polyacrylamide channels. The embryos were then immunostained for various proteins involved in geometry sensing during the first cell fate decision event.

5.2.3 Embryo immunostaining

Formaldehyde fixed embryos were incubated in 0.15% Triton PBS solution for 5 minutes twice before being transferred to 0.25% Triton in PBS solution for 25 minutes at room temperature. The embryos were then washed 0.15% Triton PBS solution for 5 minutes twice before being transferred to a blocking solution containing 1% BSA and 5% goat serum in PBS for 50 minutes at 4^oC. The blocking solution was used to prepare primary antibody solution with antibodies diluted 1/100 from starting stocks. Embryos were placed in this solution overnight with a minimum of 8 hours. Embryos were then placed in 0.15% Triton PBS solution for 15 minutes, before transferring to a solution (0.15% Triton PBS) containing secondary antibodies (at 1/100 dilution) and Phalloidin (1/50 dilution) for 50 minutes. After this step, the embryos were incubated in 0.15% Triton PBS for 25 minutes before being transferred to a drop (10μL) of Vectashield containing DAPI. Embryos were then imaged with Zeiss LSM 710 after at least a 4h incubation period.

5.2.4 Live imaging of LifeAct embryos

Mice were dissected as described previously and embryos were collected in M2 medium. Embryos were then injected into 25μm hydrogel channels, which were equilibrated in KSOM media prior to the experiments. The gels were then placed into 8 well chambers containing enough media to partially submerge the gels, which were covered with mineral oil to prevent evaporation and gels from physically moving during the experiments. Embryos were imaged on Zeiss LSM 710 microscope every 12 minutes, using

2% of the available 488nm laser power. Experiments were done at 3.0dpc, which corresponds to 11pm-7am the third day after mouse mating. Microscope settings were as follows: 40X water immersion objective at 256X1024 resolution, which results in 0.277μm pixel size and 2.5μm intervals between slices. Pixels were averaged 4 times, with line step of 2 resulting in 2.55μs pixel dwell time. 5.2AU Pinhole was used with detector gain of 600 (digital gain of 1.0) and offset of -2. A single 3D stack took 34s to scan.

5.3 Results and discussion

I took several approaches to look at the first cell fate decision. To begin with, I looked at published single cell RNA-seq data to investigate transcription profiles of genes known to be involved in the first cell fate decision. Afterwards, I performed immunostaining of Hippo pathway components at various development stages to look at protein-level changes. This allowed to form hypotheses about the timing and nature of the first cell fate decision, which I tested by using hydrogels to alter embryo shape and eventually look at the cellular rearrangements by live-imaging of Life Act embryos.

5.3.1 Analysis of transcriptional basis of the first cell fate decision

To look at transcriptional changes during early development, I used previously published single cell RNA sequencing data [283]. It included sequencing of zygote, 2 cell embryos (early, mid and late, which I designated 2, 2.5 and 3), 4 cell, 8 cell, 16 cell, 32 cell (early, mid and late, which I designated 32, 40 and 48). The original publication looked at mono and bi-allelic gene expression in closely related embryonic cells. I wanted to look at how various components involved in cell differentiation are expressed during development. To begin with, I investigated mRNA of known

downstream transcription factors corresponding to trophectoderm [181, 297, 141, 278] (*cdx2* and *eomes* in Figure 5.3) and inner cell mass (*oct4 (pou5f1)*, *klf4*, *Nanog*, *sox2* in Figure 5.4). *Cdx2* was stably transcribed from the 16 cell stage with low levels appearing at the 8 cell stage. *Eomes* took longer to appear and became transcribed from the 32 cell stage onwards. Similarly, *oct4* was transcribed from the 8 cell stage, while *nanog* and *sox2* appeared slightly later. *Klf4* was expressed earliest, with the transcription peak appearing at the late 2 cell stage. This indicates, that before differentiation cells are more similar to the inner cell mass and fate segregation is defined by the appearance of trophectoderm markers. However, despite the early appearance of these transcripts, cell populations are not fully defined until the 32 cell stage [298], where trophectoderm and inner cell mass signals mutually repress each other resulting in stable cell fates (Figure 5.5).

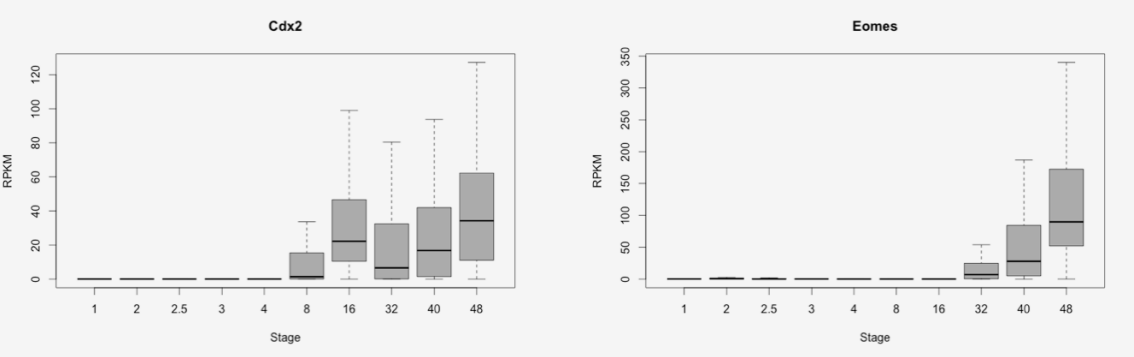


Figure 5.3: Transcription of known trophectoderm factors. The boxplots are representative of individual cells within embryos at each particular stage. scRNAseq data from [283]

Looking at the upstream signalling elements (Figure 5.6), RNA of core Hippo pathway homologues *yap* and *taz* appeared much earlier, most likely due to maternal transcription [177]. In contrast, *tead4* factor, which is responsible for driving *cdx2* transcription appears later, but still before the fate decision itself occurring at the 8-32 cell stage.

Signalling upstream of the core Hippo pathway becomes less certain, however is

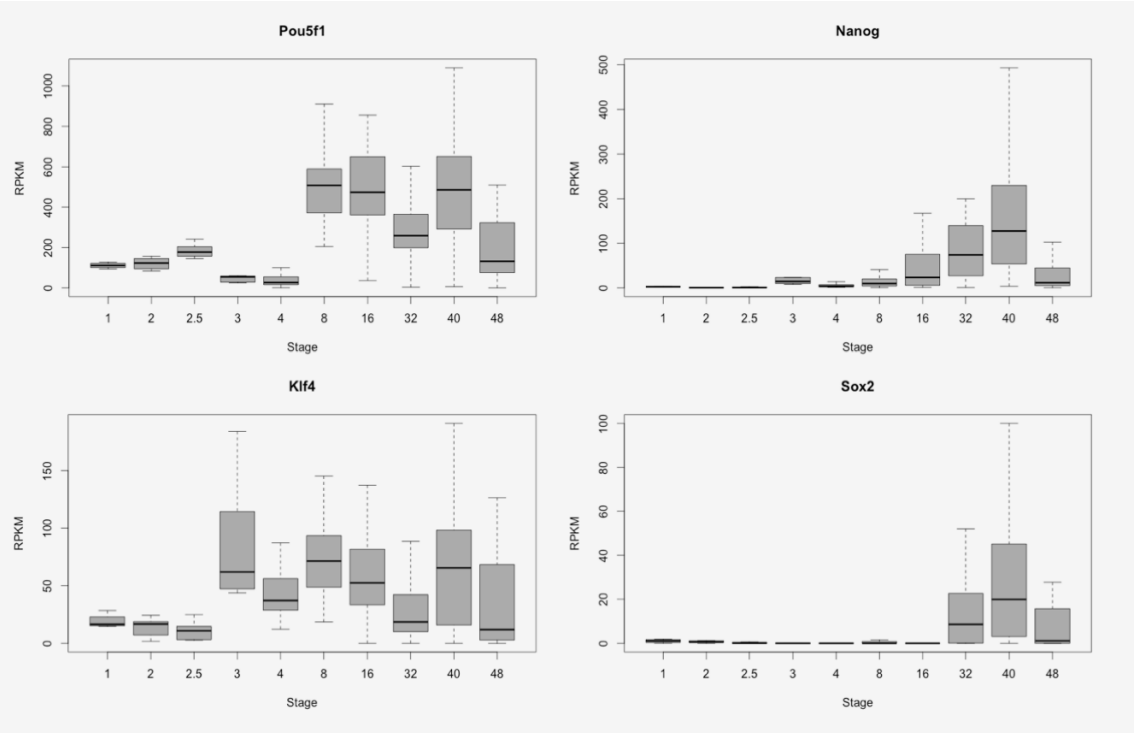


Figure 5.4: Transcription of known inner cell mass factors. The boxplots are representative of individual cells within embryos at each particular stage. scRNAseq data from [283]

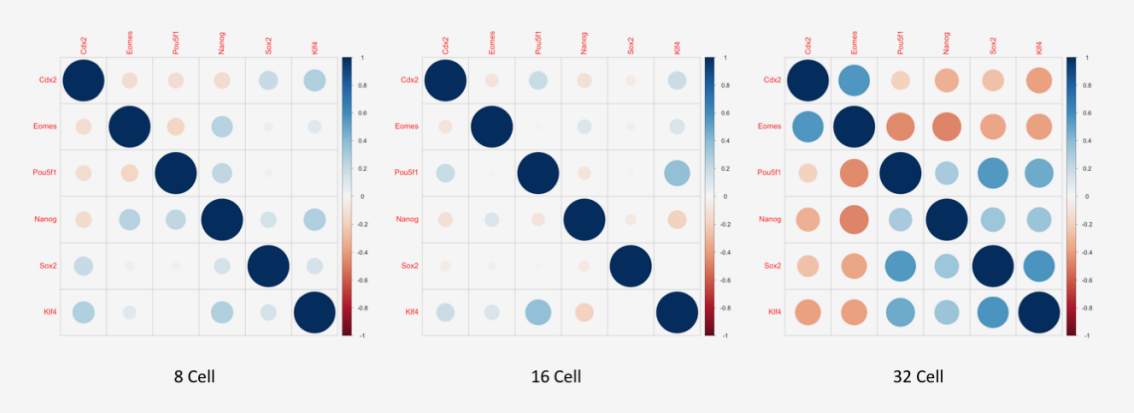


Figure 5.5: Correlations between selected transcription factors demonstrating the emergence of two cell populations at the 32 cell stage. scRNAseq data from [283]

suspected to involve cell polarity components or actin cytoskeleton [167]. Therefore, I also wanted to look at how transcript levels change throughout the course of development (Figure 5.7). Three apical polarity components *par6*, *par3* and *radixin* (*Rdx*) had a high level of maternal transcription, which decreased and stabilised around the

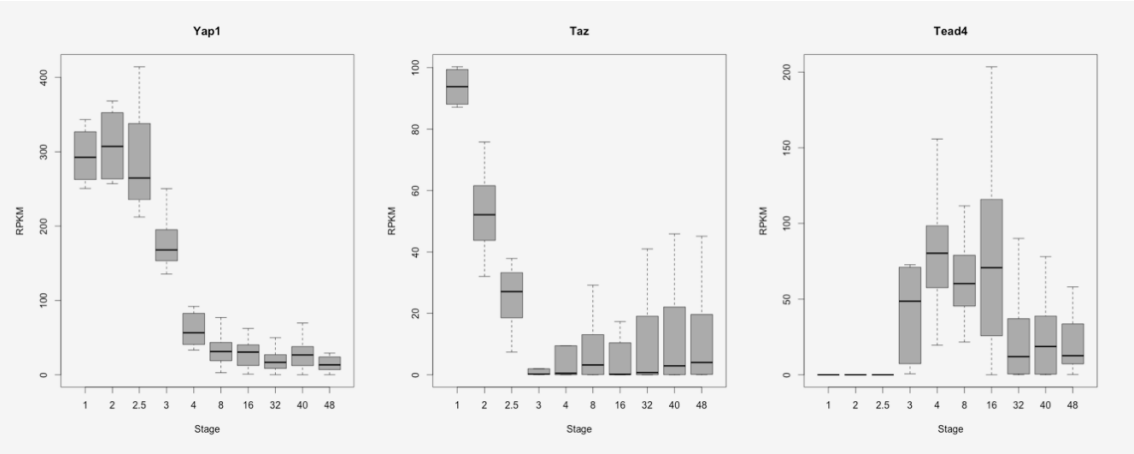


Figure 5.6: Transcription of core Hippo pathway components. The boxplots are representative of individual cells within embryos at each particular stage. scRNAseq data from [283]

time of cell fate decision. *e-cadherin*, a basal polarity protein responsible for intercellular adhesion had an opposite trend, increasing transcript levels during the course. Similarly, Actin (*acta1*) and the suspected sensing molecule Angiomotin (*amot*, *amot like-2*) showed a rapid increase in transcript levels.

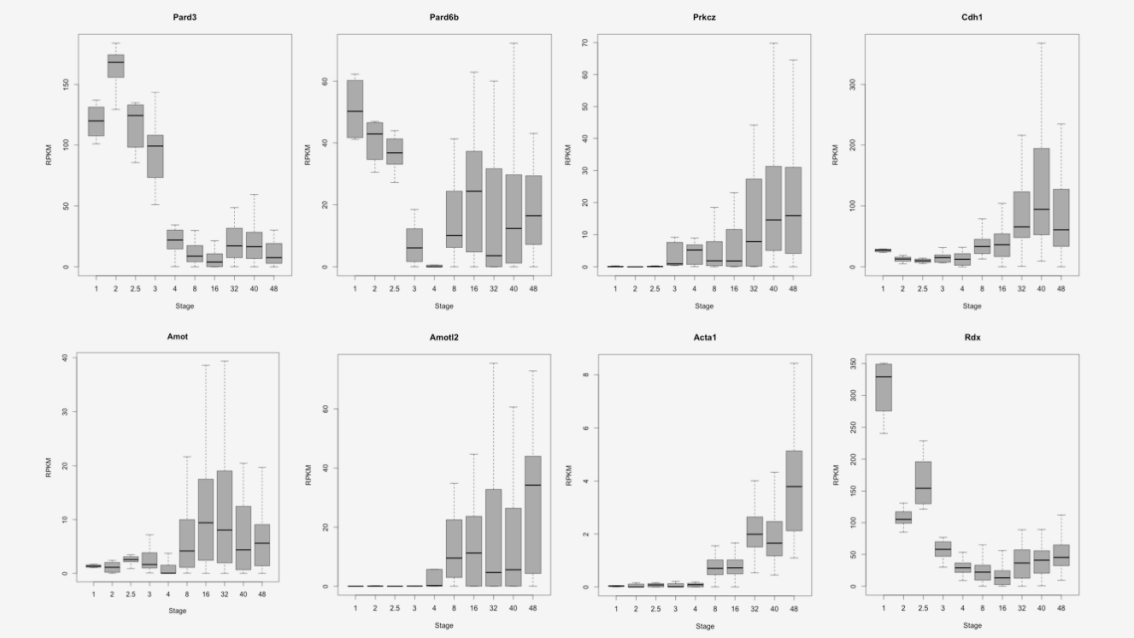


Figure 5.7: Transcription of various cell polarity components. The boxplots are representative of individual cells within embryos at each particular stage. scRNAseq data from [283]

Overall, looking at RNA of proteins suspected to be involved in the first cell fate decision revealed a general increase in most components. The data was complicated by the switch between maternal and embryonic gene transcription and generally provided little evidence for distinct cell populations before the mid-32 cell stage, even when looking at established embryonic transcription factors (Figure 5.5). Early transcription of *tead4* factor (Figure 5.6) is suspected to create the conditions for embryo patterning, which is expected to be controlled by *yap* and *taz* homologous Hippo pathway proteins. Their transcription profile revealed little insight, except for large maternal RNA presence and that Yap levels are generally larger and more uniform among the individual cells. Looking at polarity proteins (*par6*, *par3*, *apkc-z* (*prkcz*), *radixin* (*Rdx*) and *e-cadherin*), there was a marked transcriptional increase (removing the maternal bias) around the time of cell fate decision. Actin and Angiomotin levels also increased around the time, so it is unclear from the transcriptional picture, which of the mechanisms may be driving the cell fate decision.

5.3.2 Protein level embryo patterning during the first cell fate decision

While RNA sequencing has the advantage of being able to simultaneously look at a large number of different targets, transcription does not necessarily represent protein levels and also protein-level signal transduction is not visible to transcriptomic analysis. To address these issues I used immunostaining combined with image analysis to look at protein level changes.

This approach provided a more reliable information on protein levels, but the drawback was that at one time I could only look at a pair of proteins (in addition to nuclei and actin) and only those with available primary antibodies. I started with Cdx2, which is the downstream effector of Hippo pathway and marks cell differentiation into the trophectoderm lineage [181, 297, 278], which then sets up embryo patterning. Judging by the immunostaining (Figure 5.8), weak Cdx2 expression started

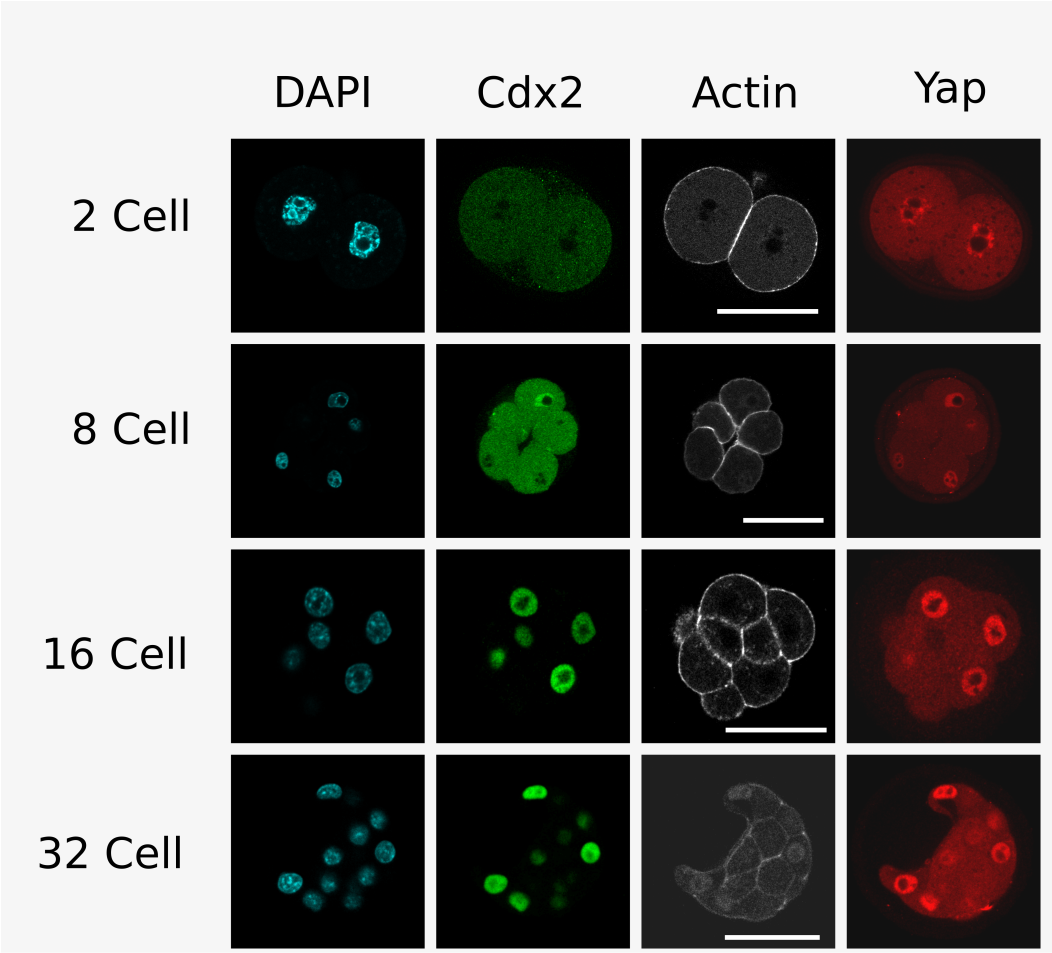


Figure 5.8: Cdx2 and Yap patterning during pre-implantation development, looking at downstream Hippo signalling. The embryos were immunostained for DAPI, Cdx2, Actin and Yap at various stages immediately after collection. The figure shows optical sections through spherical embryos. Images are representative of 5 x 2 cell, 4 x 8 cell, 6 x 16 cell and 4 x 32 cell embryos. Scale bars - 50μm

at the 8 cell stage, although it was fully expressed from the 16 cell stage onwards, which is in agreement with transcript levels in single cell RNA sequencing data. Unlike for Cdx2, Yap protein levels did not seem to correspond to transcript levels, as there was no large presence of the maternal Yap protein during the early stages. With emergence of the two tissues Yap localisation changed, as it was excluded from the inner cells and localised more strongly in the nuclei of Trophectoderm cells.

Upstream of Yap signalling, I looked at the emergence of apical-basal cell polarity by looking at phospho-ERM (Ezrin/Radixin/Moesin), which are the proteins respon-

sible for linking actin cytoskeleton to apical plasma membrane [299, 247, 300, 301, 302] (Figure 5.9). The first signs of pERM membrane localisation were visible at the 8 cell stage; however, it was initially distributed in a uniform fashion. The apical-basal polarity emerged, as cells compacted (8c stage) and a clearer basal membrane aspect was defined by tight cell adhesion to neighbours. pERM was then localised to the apical surface, however, it was not until the 16 cell stage, when apical surface was completely covered with the protein and tight junction complexes became visible.

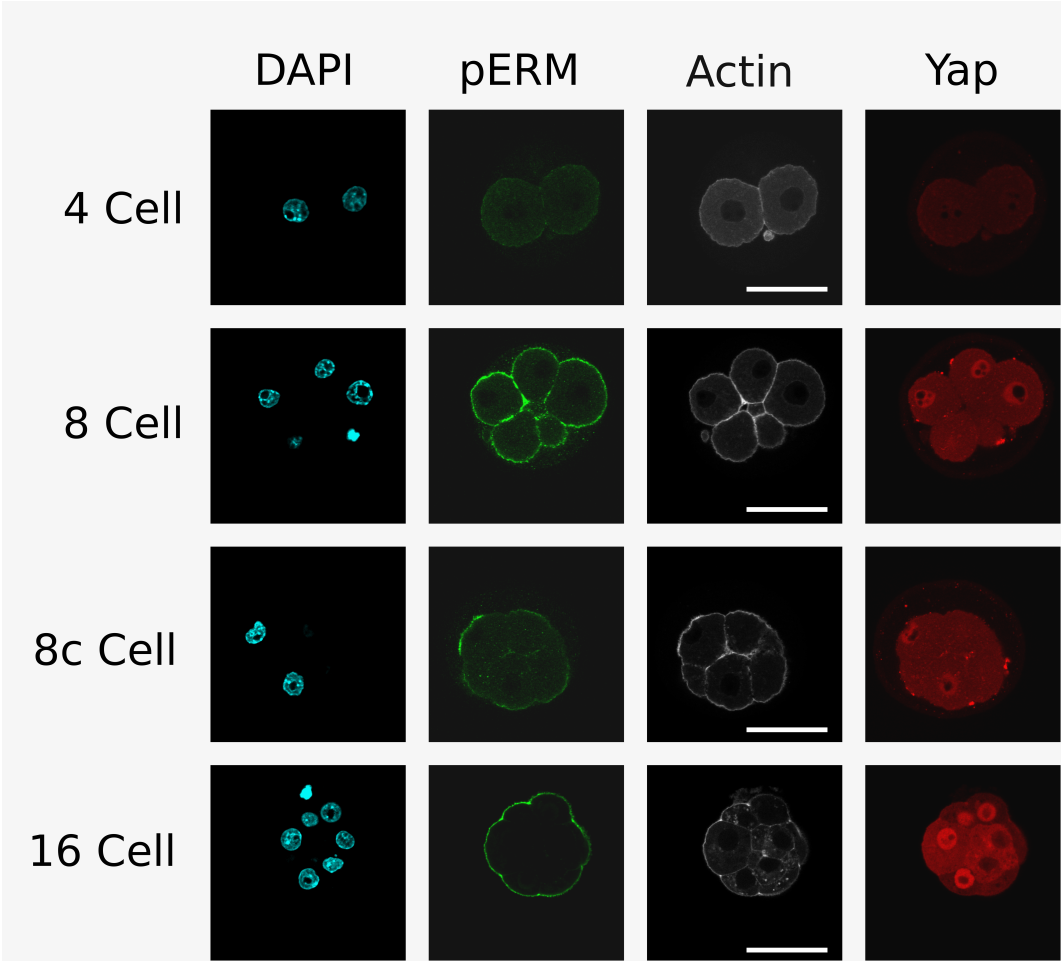


Figure 5.9: Phosphorylated ERM and Yap patterning during pre-implantation development, looking at upstream Hippo signalling. The embryos were immunostained for DAPI, pERM, Actin and Yap at various stages immediately after collection. The figure shows optical sections through spherical embryos. Images are representative of 2 x 4 cell, 3 x 8 cell, 3 x 8 cell (compacted) and 6 x 16 cell embryos. Scale bars - 50μm

5.3.3 Analysis of protein level patterning

To quantify and better understand the protein changes occurring in single cells during the cell fate decision I used the image analysis platform to extract geometric protein distribution information and explore potential relationships between the different proteins as well as their localisation. To begin with, I looked at the relationship between Yap and its downstream target Cdx2. The relationship at the 8 cell stage was not present (Cdx2/Yap correlation $R^2 = 0.12$) and developed with time (Figure 5.10, A). Interestingly, the correlation at the 16 cell stage was weaker (Cdx2/Yap correlation $R^2 = 0.24$) than the 32 cell stage (Cdx2/Yap correlation $R^2 = 0.76$), which indicates, that the cell fates are not fully established before the 32 cell stage. Figure 5.10, B reveals Yap localisation pattern, that emerges as embryos develop from the 2 cell to 64 cell stages. Since cells vary in size during the course of development, I normalised surface distance by cell radius, which also makes it more intuitive to identify the outer and inner cell populations. Cells with their centers closer to the outside than their radius are most likely to belong to the outer cell population of the tissue, while cells further than two radii are most likely to be in the inside of the embryo. The pattern of nuclear localised Yap emerged with the 16 cell stage, which was also the first time, when there was enough space in the embryo to allow the inner cell population to appear.

To analyse how embryo geometry dictates the emergence of two cell populations, I used a combination of automatically analysed tissues and manually outlined samples. The cells were outlined by two visiting project students Annemarie Kip and Deborah Fortin. In order to automatically detect two cell populations, I used clustering methods (partitioning around mediods) from the 'Clara' package on R. After the fate decision, clusters roughly represented the trophectoderm and the inner cell mass populations, while before the decision they were arbitrary. For every embryo, constituent cells were clustered and then cluster averages for every embryo were used to create

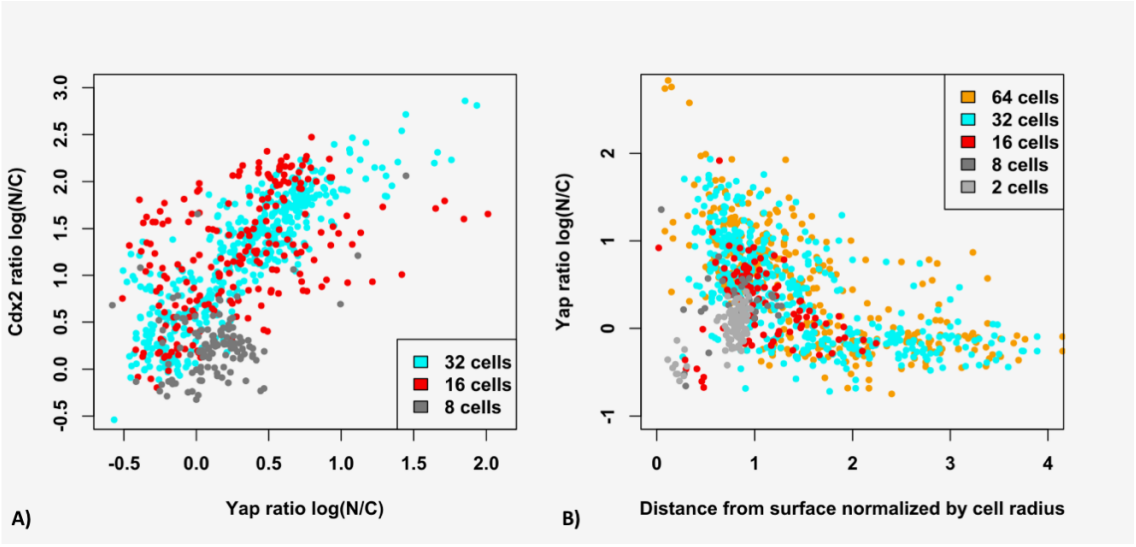


Figure 5.10: Cdx2 and Yap protein distribution analysis during the first cell fate decision event. A) - correlation between Cdx2 and Yap proteins at various embryonic stages ($R^2(8\,\text{cell}) = 0.12$, $R^2(16\,\text{cell}) = 0.24$, $R^2(32\,\text{cell}) = 0.76$). Cells are taken from 12 different embryos. B) - Differential Yap localisation during various developmental stages. Cells were manually outlined from: 10 x 2-cell embryos, 4 x 8 cell embryos, 5 x 16 cell embryos, 4 x 32 cell embryos, 3 x 64 cell embryos.

plots seen in Figure 5.11. Figure 5.11, A shows data from manual cell outlining, which made it possible to measure exposed cell surface. This is a more precise representation of cell geometry than surface distance (Figure 5.11, B), however manual cell outlining requires a considerable time investment of around 300 hours for 1000 cells. The graph in Figure 5.11, A shows, that even at the 8 cell stage, two populations start emerging based on the amount of exposed cell surface and nuclear Yap localisation (which is not seen by measuring surface distance). By the 16 cell stage embryo is already organised into two cell populations, one with half of the surface exposed and one with less than 20% exposed. Due to manual outlining imperfections, exposed surface fraction was over-estimated for inner cells, as cells with around 10% exposed surface were usually fully inside the embryo.

The same technique of clustering cells into two populations based on protein levels and their geometric parameters (amount of exposed surface or surface distance) can be used to classify measurements of membrane proteins, such as actin (Figure

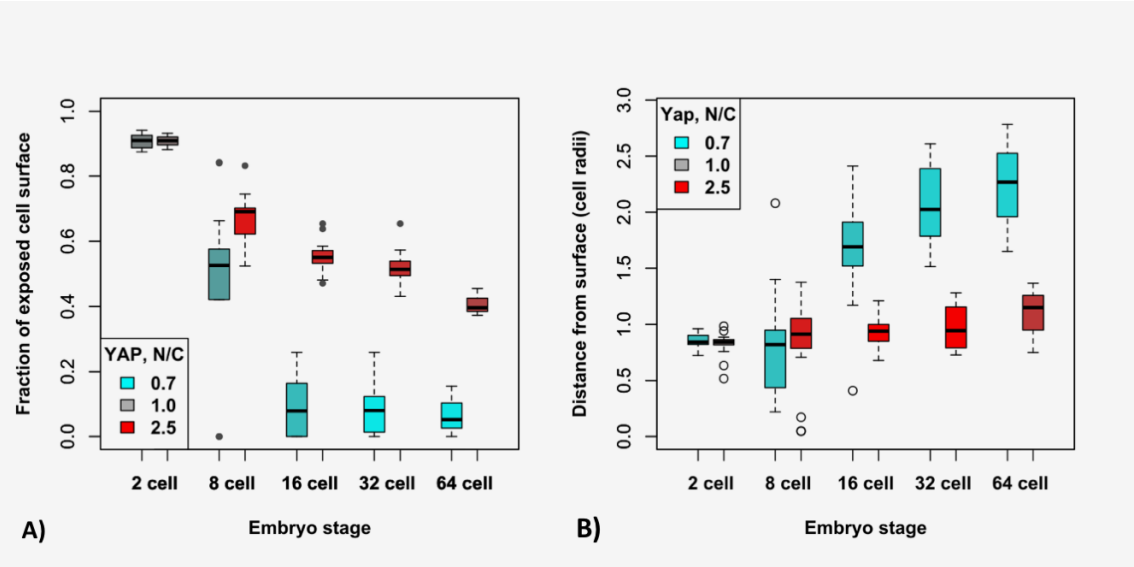


Figure 5.11: Emergence of two geometrically distinct cell populations during pre-implantation development after automatic (unbiased) embryo cell clustering. For every embryo cells were clustered into two populations based on Yap localisation and either A) - exposed surface fraction or B) - distance from surface. The boxplots represent clustered population measurements and after the 16 cell stage can be identified with TE and ICM populations. Cells were taken from a pool of: 10 x 2-cell embryos, 4 x 8 cell embryos, 5 x 16 cell embryos, 4 x 32 cell embryos, 3 x 64 cell embryos.

5.12). Based on fluorescence of actin bound to the basal membrane aspects, the cells were also partitioned into two populations. This revealed that outer cells generally contained higher actin levels than the inner ones, which is often associated with higher cytoskeletal tension and higher Hippo pathway activity leading to nuclear Yap localisation.

To sum up, looking at transcriptomic and protein level information it was possible to reinforce the current understanding, that earliest cell population differences begin to arise during the 8 cell stage, however only at the 16 cell distinct cell populations emerge in terms of their distinct geometric location and Yap localisation. It also appears that the relationship between Yap and Cdx2 proteins in not fully established before the 32 cell stage. Although the data is useful for characterising early development, it provides little insight into the mechanism responsible for the emergence of trophectoderm and inner cell mass populations, or whether development is geomet-

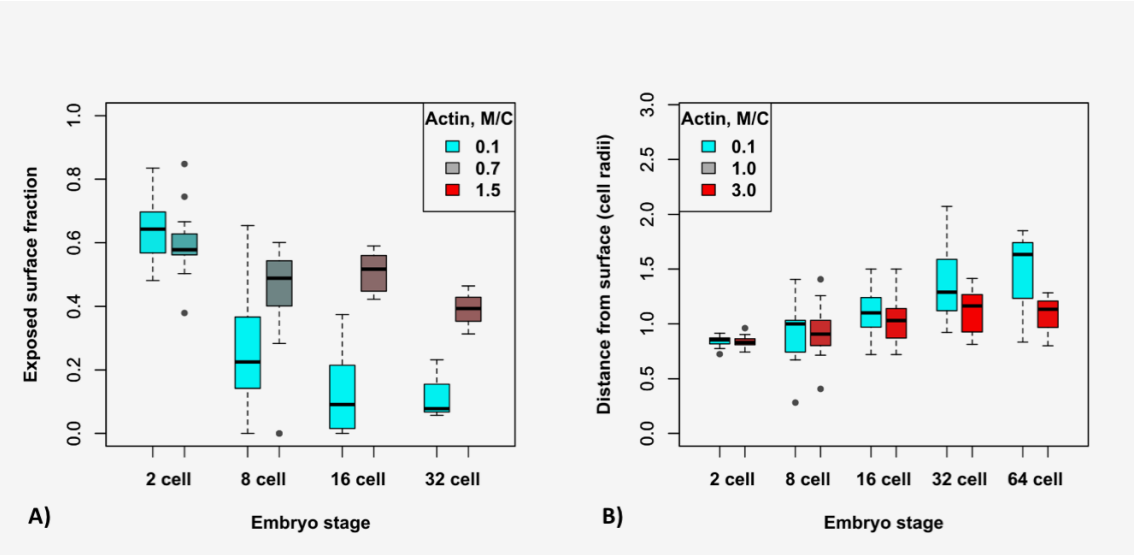


Figure 5.12: Population emergence based on actin levels and cell geometry (amount of exposed surface or distance to surface). For every embryo cells were clustered into two populations based on actin levels (logarithm of membrane to cytoplasmic ratio) and either A) - exposed surface fraction or B) - distance from surface. The boxplots represent clustered population measurements and after the 16 cell stage can be identified with TE and ICM populations. Cells were taken from a pool of: 10 x 2-cell embryos, 4 x 8 cell embryos, 5 x 16 cell embryos, 4 x 32 cell embryos, 3 x 64 cell embryos.

rically regulated at all. In order to answer this question, I used the hydrogel based manipulation system to alter tissue shape and cell position.

5.3.4 The first cell fate decision is actively regulated by tissue geometry

In order to test the hypothesis, that cell fate is actively regulated by tissue geometry I used tissue deformation methodology to change embryo shape and analyse resulting cell differentiation. To deform the embryos, they could either be inserted into various diameter channels, which resulted in a cylindrical shape change without sustained compression or alternatively, embryos could be sandwiched between two hydrogel sheets, which caused a sustained compression and resulted in a planar configuration. My hypothesis was that mechanically forcing cells to occupy outer positions would cause them to differentiate to trophectoderm tissue.

During compression culture, spherical embryos (Figure 5.13, A) would successfully adopt alternative shapes including cylinders with various diameters (Figure 5.13, B) and flattened oblate morphology (Figure 5.13, C). The level of compression was controlled by either choosing different channel diameters or tuning gel stiffness, which determined the compressive force. Embryo cells responded by adjusting cell fates to form a single outside cell layer positive for trophectoderm marker Cdx2.

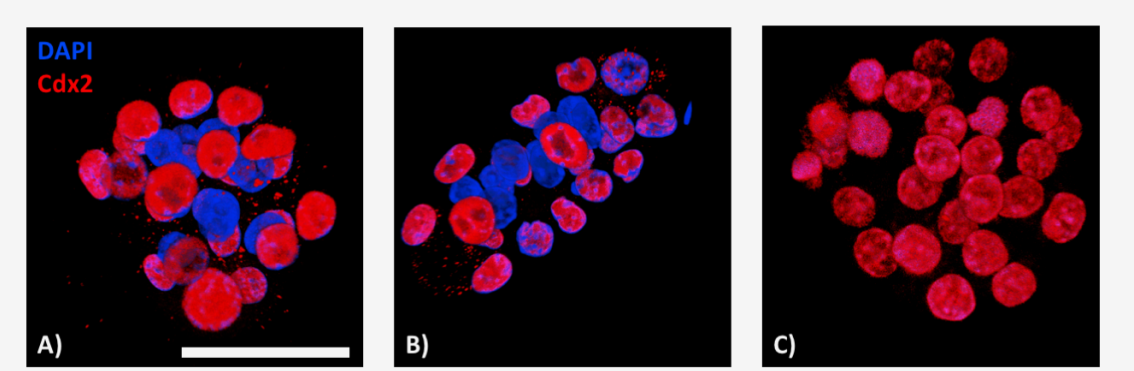


Figure 5.13: Changing embryo shape with hydrogels. A) - Uncompressed spherical embryo stained for DAPI (nuclei) and Cdx2 (TE marker), B) - Cylindrical embryos grown in hydrogel cavities, C) - Planar embryos after hydrogel sheet compression. Scale bar - 50μm. Changes in cell fates are analysed in higher detail in Figure 5.14

In cases of extreme deformation (for 2 experiments out of 10 compressing to 25μm embryo diameter), where all cells would be forced to occupy outer tissue surface, it was possible to create embryos consisting solely of Cdx2 positive cells (Figure 5.14, A). In milder compression experiments, a number of cells remained inside and their number decreased with increasing tissue deformation (Figure 5.14, B). The deforming force was estimated from hydrogel indentation, as described previously.

Furthermore, compressing embryos at the 16 cell stage did not change cell relative position despite changing overall tissue shape. This was similar to the case in chapter 2, where tissue shape change was achieved by individual cell shape changes rather than their rearrangement. As a result the embryos did not display the increase in Yap levels, which was observed in embryos compressed at the 8 cell stage (Figure 5.14,

C). This is an important observation, because it implies, that the cell fate decision mechanism operates before the 16 cell stage [187]. In order to further explore the role of cell geometry during the fate decision I used manually outlined embryos to quantify individual cell geometry.

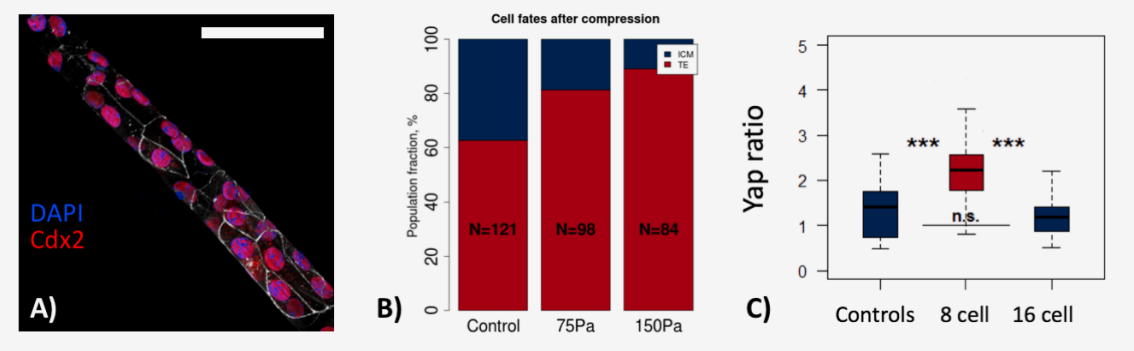


Figure 5.14: A summary of changes in embryo patterning. A) - An extreme case of embryo being composed solely of trophectoderm tissue identified by Cdx2. B) - Quantification of cell fates (estimated by Cdx2 levels) in 16 cell embryos following two different levels of compression at the 8 cell stage. C) - A comparison of average nuclear/cytoplasmic Yap ratios in 32 cell embryos compressed at the 8 cell and 16 cell stages. There are 9 control embryos (121 cells), 6 embryos compressed at the 8 cell stage (98 cells) and 6 embryos at the 16 cell stage (84 cells). P-values are represented by: n.s. - not significant, *** - < 0.005, ** - < 0.01, * - < 0.05.

5.3.5 The role of individual cell geometry

Looking for potential geometric cues, it is important to consider the upstream Hippo pathway elements. One of the major recent discoveries of Hippo pathway involvement in geometry sensing looked at how shapes and size of individual cells influence Yap transduction into the nucleus and its subsequent activity. As an extension of the *in vitro* experiments, it has also been proposed, that cell shape can be controlling Yap transduction into the nucleus in pre-implantation embryos, thereby driving the first cell fate decision [1]. However, without a way to controllably deform the tissues and cells there has been no way test such hypothesis.

I used manually outlined 2 to 64 cell stage embryos to investigate possible relationships between cell shapes and their fate commitments. At 32 and 64 cell stages,

cells with higher nuclear Yap levels (Trophectoderm tissue) appeared flatter than cell with lower nuclear Yap cells, as measured by sphericity (Figure 5.15, A). This is a geometric descriptor, that quantifies an object's similarity to a sphere (score of 1 for perfect sphere). As can be seen in the plot, as embryos progressed from the 2 cell stage towards the 64 cell stage, cell sphericity decreased. The significant differences between cell sphericity appeared at the 32 cell stage, which is after the window of cell fate decision. My hypothesis is that the decrease in cell sphericity is caused by the pressurization of the blastocoel cavity and resulting tension of outer trophoblast layer cells. Despite the apparent differences between cell shapes in two different populations at the 32 cell stage, during the time of the first cell fate decision at the 8 and 16 cell stages, there was no significant correlation between cell shape and Yap localisation.

Since cell sphericity did not significantly affect Yap localisation during cell fate decision, I manually analysed the same set of embryos to investigate another geometric factor - exposed cell surface (Figure 5.15, B). The fraction of cell's exposed surface is also more indicative of cell polarity, which is among known upstream molecular Hippo pathway affecters [166]. From the plot (Figure 5.15, B) looking at the relationship between exposed cell surface and nuclear Yap localisation it could be seen that the first time cell populations become different is at the 16 cell stage, which coincides with the window of cell fate determination.

Although cell polarity is the likely mechanism by which cells sense their position within the tissue, it is still not clear why only some of the cells polarise within the 16 cell embryo, whereas all the cells can be considered equivalent in the 8 cell embryos [186]. Previous observation, that embryos responded to changes in geometry only when compressed before the 16 cell stage suggests that cell fates are decided during the synchronised round of cell divisions.

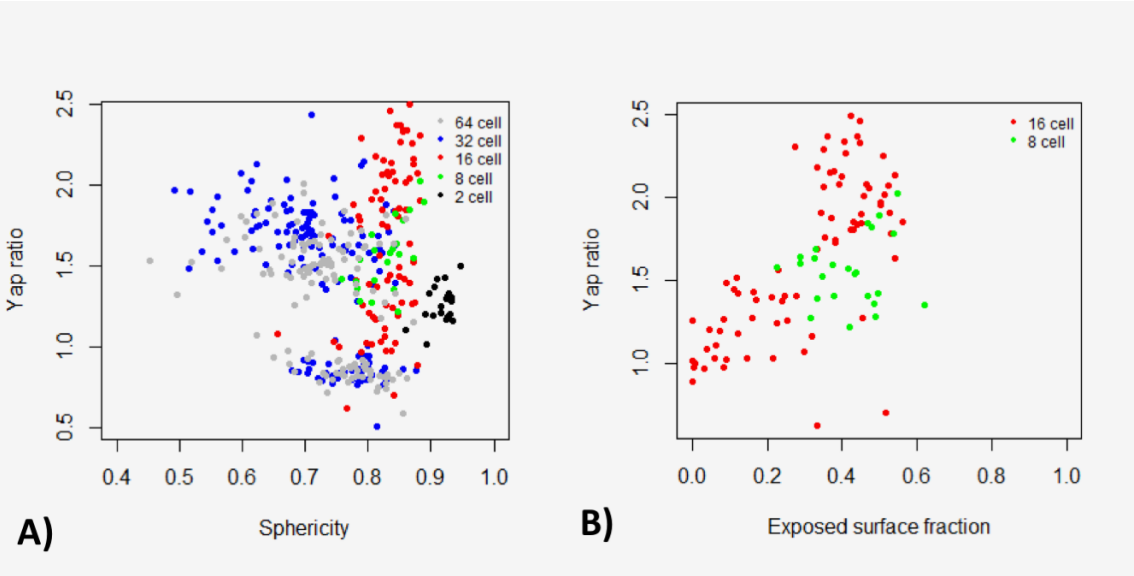


Figure 5.15: Emergence of geometric cell differences during the first cell fate decision. A) - Cell populations at various embryo stages based on levels of nuclear Yap and cell sphericity, as measured by manual outlining. B) - Cell populations at 8-cell and 16-cell stages based on levels of nuclear Yap and exposed cell surface, as measured by manual outlining on Imaris software following surface quantification by Silent Mark. Cells were taken from a pool of: 10 x 2-cell embryos, 4 x 8 cell embryos, 5 x 16 cell embryos, 4 x 32 cell embryos, 3 x 64 cell embryos.

5.3.6 The process of outer cell polarisation

In order to look at the events that create two distinct cell populations during the fate decision I looked at cell polarity by immunostaining for phospho-ERM proteins, which mark apical cell membranes (Figure 5.9, 5.16, 5.17, A, B). I compressed embryos at different stages and cultured for 12h to see whether the additional cells on the outer surface would become spontaneously polarised. If this was the case, it would imply, that cell position is actively sensed by the exposed surface.

For embryos compressed at the 16 cell stage (6 embryos), only less than 10% of the cells moved to the outside, as judged by the ratios of outer/inner cells. Also, if they did, they remained unpolarised even after 12h of compressed embryo culture, as judged by outer surface patches not covered by polarity proteins (Figure 5.17, C). In contrast, embryos compressed at the 8 cell stage, close to the round of cell division

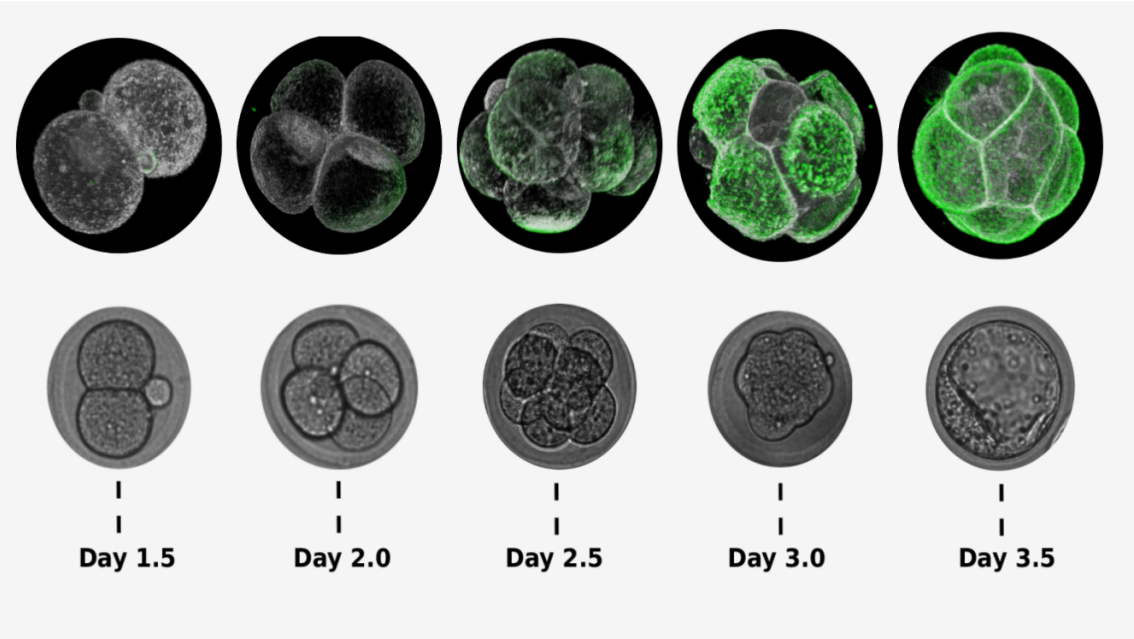


Figure 5.16: Summary of apico-basal cell polarity development. The first polarised cells appear at the 8 cell stage (Day 2.5) and first differences in cell polarity between the inner and outer cell emerge at the onset of the 16 cell stage (Day 3.0). During the blastocyst stage (Day 3.5), outer cells are fully polarised. Green - pERM, gray - actin

(Figure 5.17, B) would become fully polarised by the 16 cell stage (Figure 5.17, D). This suggests, that cell polarity seen at the 16 cell stage is set during the cell division event [186], rather than acquired on the basis of exposed surface alone. However, based on the previous observation of cell fate bias during compression experiments inheritance of cell polarity is likely to be affected by geometric cell properties, such as the shape and amount of exposed surface. And although immunostaining combined with different compression timings was sufficient to look at cell polarity regulation, it was not possible to track the process of cell division itself.

5.3.7 The role of polarised cell divisions

In order to take a more detailed look at cell division events in constrained environments, I performed live imaging of membrane fluorescent Life Act embryos [296, 303]. The LifeAct embryos express a small, actin binding oligopeptide fused to EGFP,

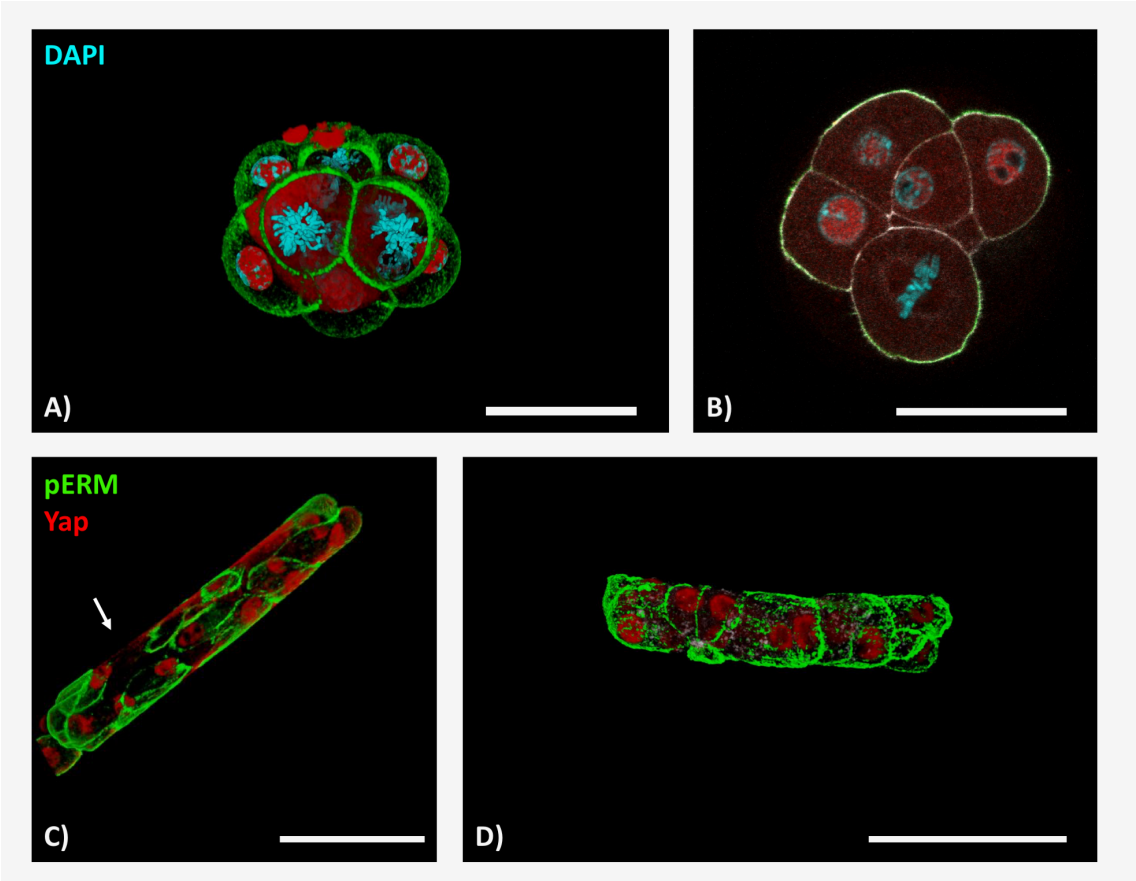


Figure 5.17: Cell polarity development during the first cell fate decision. A) - An uncompressed 16 cell embryo with outer cell polarity marked by pERM (phospho-Ezrin/Radixin/Moesin). B) - An optical section of an uncompressed 16 cell embryo with outer cell polarity marked by pERM. C) Failure of 16 cell embryo cells to polarise (marked by an arrow). D) Uniform polarisation of outer cells in embryos compressed at the 8 cell stage (5/5 embryos). Scale bars represent 50μm

which allows to visualise actin cytoskeleton. This is advantageous over other membrane markers, because actin distribution is also functionally relevant and can be used to estimate cytoskeletal tension and cell polarisation.

Since the embryos are no longer spherical, classifying cell divisions based on division angle becomes subjective, because the frame of reference in a cylinder is different from spherical coordinates. Therefore, classified cell division based on the resulting positions of daughter cells. A division, which produced two outside cells was defined as symmetric and a division, which produced one inside and one outside cell was

defined as asymmetric. Out of 17 imaged embryos and 41 cell division events, no divisions produced two inside cells.

After 8 cell embryo (Figure 5.18 A, B) division, resulting blastomeres rearranged to occupy inner and outer cell positions regardless of the immediate location after the division event (Figure 5.18, C). In order to compare the effect of embryo compression with uncompressed controls I calculated inside and outside cell population estimates 13(inside) / 68(outside) based on their final cell position. Uncompressed and published [185] embryos produced 25(inside) / 57(outside) cells, which is significantly different (p-value = 0.045, by chisq test). This demonstrates, that cell populations are affected by tissue compression.

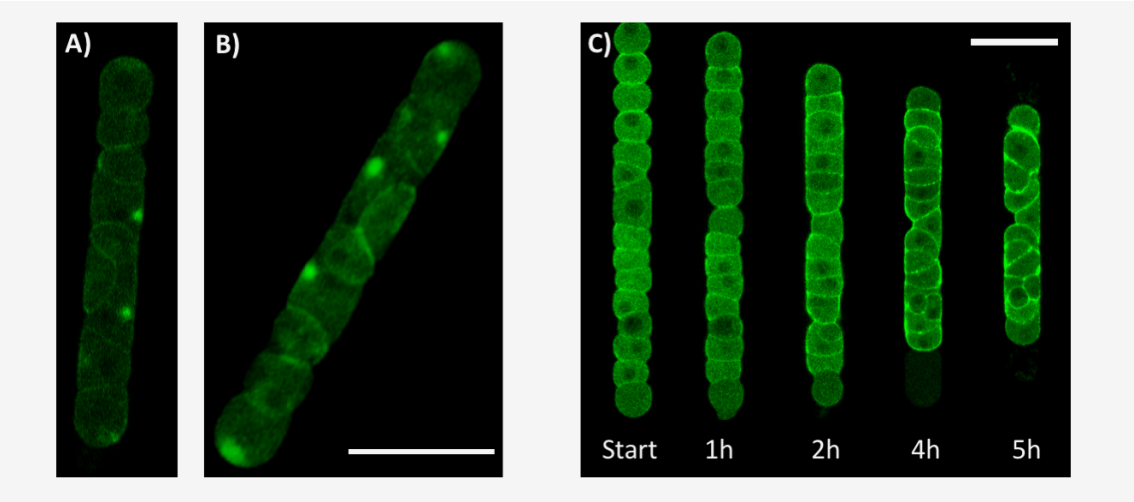


Figure 5.18: Live imaging of dividing LifeAct blastomeres. A) - 8 cell embryo section, B) 8 cell embryo maximum intensity projection before the round of cell division. The bright spots are transient concentrations of actin and polarity components, which disperse 2h before cell division. C) 16 cell embryo formed immediately after cell division under confinement and resulting embryo compaction and cell rearrangement. Deforming channel size - 40μm. Scale bars - 75μm

Finally, to assess embryo morphology and Hippo pathway activity I also analysed imaged embryos by immunostaining for Yap localisation (Figure 5.19). The pattern was analogous to previous compression experiments without live imaging with 90% of cells being outside and having nuclear Yap localisation.

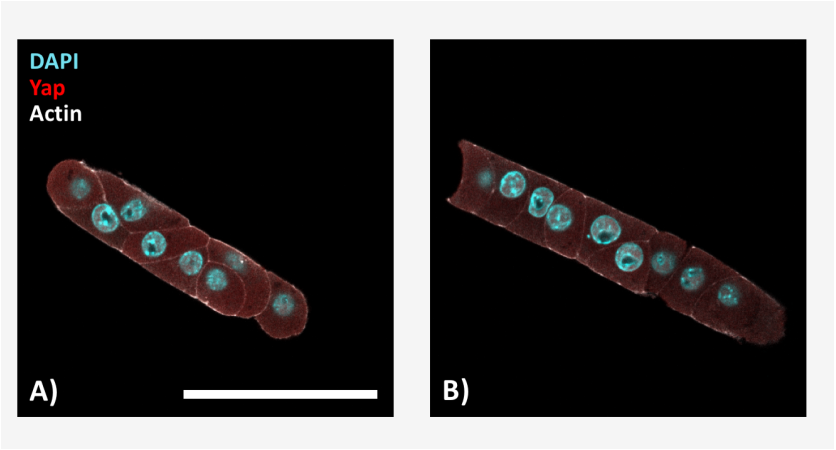


Figure 5.19: A), B) - Two representative (5 embryos) immunostainings of Hippo pathway component Yap in 16 cell embryos following live imaging. LifeAct signal degraded during tissue fixation and staining and was not visible. Scale bars - 75μm

5.4 Conclusions

Overall, the chapter takes an in-depth look into the tissue patterning event, that occurs after the first cell fate decision during mammalian development. The event has been investigated for nearly a century, which revealed a lot of molecular details, however the observation, that tissue formation is apparently regulated by geometry remained a mystery due to the inability to mechanically change tissue shape.

Published single cell RNA sequencing data [177] made it possible to look at the transcript levels of upstream and downstream Hippo pathway elements possibly involved in geometry sensing via the Hippo pathway. However, the data was complicated by remaining maternal transcripts and the fact, that a lot of upstream signalling happens at the protein level. I then proceeded to look at protein distribution by immunostaining for several proteins involved in Hippo pathway. *Cdx2* showed a similar distribution seed in the transcriptomic data, but this was not the case for *yap*, activity of which was defined by nuclear/cytoplasmic localisation rather than total levels.

I used the image analysis platform to look at the process of the first cell fate decision from the perspective of Yap correlation with cell's distance from the exposed

surface, its shape and the amount of exposed surface. The observations indicated, that the first cell fate decision occurs before or during the 16 cell stage and that cell shape is not likely to play a role in the differentiation event. I then used tissue micromanipulation techniques to demonstrate that cell fates are dependent on tissue geometry (Figure 5.14) and I looked at how exposed cell surface and polarity may be responsible for geometry sensing.

I found, that cell polarity develops gradually as cells progress from the 2 cell stage and that 8 cell blastomeres are the first to be fully polarised, after the compaction event, which engages E-Cadherins between neighbouring cells (Figure 5.16). 16-cell embryo cells resulting after the division event rearrange to occupy either the inside or outside positions within the embryo and the numbers of cells resulting inside or outside is dependent on overall tissue shape. This observation was confirmed by live imaging of Life-act embryos and cell tracking after their divisions.

Much of the discrepancy in the literature about the first cell fate decision can be justified by considering the complexity of the events involved in geometry sensing. It may appear, that flat cells are inclined to become trophectoderm [135, 25], but the shape is not correlated with Hippo signalling before forming the blastocoel cavity. Although it may seem like cell fate is regulated by exposed surface, cells can actually rearrange into pre-defined positions depending on whether their surface contains apical polarity components [186]. However, cell fates are not fully pre-determined either, as the symmetry of cell divisions and polarity inheritance at the 8 to 16 cell transition is affected by systematic tissue geometry, as shown here. Figure 5.20 summarises the suggested mechanism. The remaining question is how the symmetry of cell divisions (polarity inheritance) is influenced by their geometric environment [304, 305] and how this affects apical polarity protein distribution among the daughter cells.

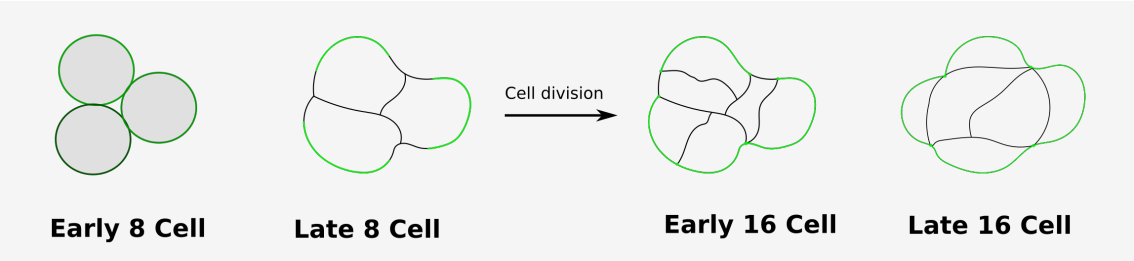


Figure 5.20: The proposed mechanism of the first cell fate decision. Cells first become polarised during early 8 cell embryo compaction which establishes the apicobasal polarity. Then during cell division daughter cells inherit apical polarity components in a geometrically regulated fashion, which determines eventual cell location in the late 16 cell embryos [186].

Chapter 6

The role of tissue geometry during the second mammalian cell fate decision

6.1 Introduction

Revealing regulatory mechanisms responsible for the first cell fate decision made it possible to reprogram cells into induced pluripotent cells [175]. This principal discovery enabled a whole discipline of regenerative medicine and tissue engineering based on reprogrammed cells. However, growing tissues *in vitro* has proven to be challenging due to remaining unknown signalling cues for later fate decisions required for recreating reproducible development. Mechanical cues in particular, have proven to be difficult to uncover, due to the lack of micromanipulation strategies [196, 193, 107], which would allow to test hypotheses based on tissue shape.

Hippo pathway is one of the most accepted signalling cascades capable of translating external cues about tissue geometry and mechanical properties [25, 2, 135, 306, 148]. The previous chapter focused on embryo specific Hippo pathway and how changes in tissue geometry indirectly result in differential activation of molecular signalling and eventual cell differentiation. Similarly to the embryos, mouse embryonic stem cell aggregates also display inside - outside patterning during embryoid body formation *in vitro* [195], however the mechanism is even less certain.

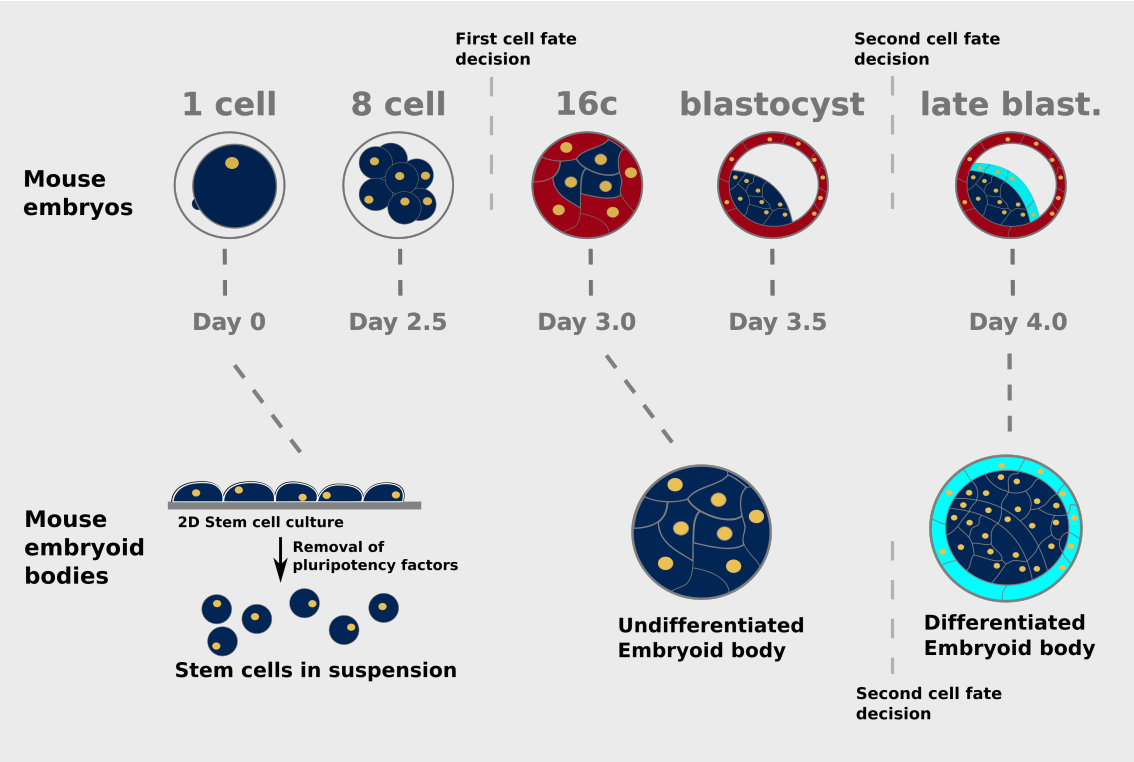


Figure 6.1: The second cell fate decision operating in early mouse embryos and embryonic stem cell based embryoid bodies. The second cell fate decision creates a layer of primitive endoderm cells (cyan), which surround a pluripotent epiblast mass (dark blue). During embryoid body culture, the fate decision happens 4 days after removing stem cells from pluripotent conditions and aggregating cells in suspension or hanging drops.

Formation of the primitive endoderm cell layer corresponds to the second cell fate decision during normal embryonic development (Figure 6.1). The mechanism by which this happens in the embryo is intensely studied, but is still not widely agreed upon. One view suggests, that cell fates arise stochastically [198, 194, 307] and their eventual positions result from cell differentiation. An alternative view argues that cell fates are actively regulated by signalling [68, 308, 309]. Regardless of the different theories about molecular development mechanisms [310], the consistent inside-outside cell pattern resulting from the second cell fate decision suggests, that the event is also geometrically regulated.

Given the diverse interactome of the Hippo pathway [136], it is likely that YAP

and TAZ proteins are involved during the second cell fate decision event, therefore I wanted to investigate the pathway's potential for geometric sensing, which results in two cell populations. Epiblast cells are the inner population of the spherical structure and are characterised by high Nanog [311], Oct4 [312] and Sox2 [313] expression. At the same time, the endoderm cell layer is defined by Sox17 [314], Gata6 [198] and Gata4 [315] transcription factors. Despite the well established transcriptional networks, there is a lack of mechanistic understanding of the signalling, that would link the downstream transcriptional targets and upstream elements, such as polarity [316, 317, 68]. Hippo pathway is one of the potential mechanisms for linking the two signalling modes and the micromanipulation tools developed in the first two chapters make it possible to test hypotheses on how information about tissue geometry may be transduced.

6.2 Materials and Methods

Phalloidin Atto 647 was purchased from Sigma (65906-10MMOL). Mouse anti-YAP monoclonal (sc-101199) antibody was purchased from Santa Cruz biotech. Rat anti-Uvomorulin/E-cadherin (U3254-100UL) monoclonal antibody was purchased from Sigma. I used the following secondary antibodies from Life Technologies: goat anti-rabbit AlexaFluor 488 (A11008), donkey anti-mouse AlexaFluor 555 (A31570), donkey anti-rat AlexaFluor 647 (A21247). Vectashield (w. DAPI, H-1200) was purchased from Vector laboratories.

DMEM (11960-085), Penicillin/Streptomycin (15140-163) and Glutamine (25030-13) were purchased from Invitrogen. 2-mercaptoethanol (M-7522) and Sodium Pyruvate (S8636) were purchased from Sigma. MEM Non-essential amino acids (11140) bovine serum and fetal calf serum (26140-079) were purchased from Gibco.

6.2.1 CGR8 cell culture

CGR8 cells [221] were used for experiments not involving cell differentiation. Cells were maintained in T-25 flasks coated with 0.1% w/v. gelatin and used at passage numbers 40-60. Cell culture media consisted of 90% DMEM medium (Gibco), 10% fetal calf serum (FCIII, Hyclone), 1mM sodium pyruvate, 1mM non-essential amino acid mix, 0.1mM beta-mercaptoethanol, 2mM L-glutamine, as well as 10^3U/mL leukaemia inducible factor (LIF). Cells were passaged every 2 days and seeded at 400,000 cells per T25 flask. For cell freezing and recovery, we used a medium containing 10% DMSO and 40% cell culture medium and 50% fetal calf serum.

Embryoid bodies were formed by either dispersing 5mL of culture media with 10,000 cells/mL into a non adhesive polystyrene petri dish or forming hanging 10L droplets containing around 100 cells on the top of a petri dish lid. Culture media was changed every 2 days and embryoid bodies were collected and manipulated using glass capillaries.

6.2.2 CCE cell culture and differentiation

CCE cells [318] were used for differentiation experiments looking at how the second cell fate is related to tissue geometry. The cell line was maintained by Dr. Christophe Royer. CCE cells prior to differentiation were grown on an inactivated layer of STO feeder cells, which were maintained in DMEM containing 10% bovine serum, 2mM glutamine and 100 units/mL of Pennicilin/Streptomycin. STO cells were mitotically inactivated by treatment with Mitomycin. CCE cells were then seeded on a confluent inactivated STO cell layer and cultured in DMEM containing 15% fetal calf serum, 100 units/mL of Pennicilin/Streptomycin, 2mM glutamine and 0.1mM beta-mercapto ethanol. Cells media was changed daily and cells were passaged at half confluency.

Cell differentiation was induced by first collecting the cells by incubation with 0.25% trypsin for 5 min at 37°C and then reseeding in hanging drops of 10μL with

1×10^4 cells/ml for 48 hours. Formed embryoid bodies were then collected and polled into a petri dish containing DMEM with 15% fetal calf serum, 100units/mL Penicillin/Streptomycin, 0.1mM beta-mercapto ethanol, 2mM Glutamine, MEM essential amino acids and 1mM sodium pyruvate.

6.2.3 Hydrogel compression experiments

Hydrogels with cylindrical cavities were prepared by casting acrylamide solution around various diameter wires (12-60μm). Acrylamide/bisacrylamide (37.5:1) mixture was used to prepare gels (5% by mass), which corresponded to approximately 4.2kPa stiffness. Ammonium persulphate (0.1%) and TEMED (1%) were added to polymerize polyacrylamide. After the wire was removed forming cylindrical cavities, the hydrogels were equilibrated in cell culture media, by changing the solution three times in one hour. Embryoid bodies of around 100μm were then inserted into the channels by a glass capillary having a slightly larger diameter. They were then allowed to grow for up to 10 days, while changing the media surrounding the 3x3x0.5mm gels pieces every two days.

At the end of the experiments, cylindrical embryoid bodies inside the hydrogels were fixed with 4% formaldehyde for 30 minutes at 4^oC and removed by mechanically tearing up polyacrylamide channels with tungsten needles. The tissues were then immunostained for various proteins involved in geometry sensing during the first cell fate decision event.

6.2.4 Tissue immunostaining

Formaldehyde fixed embryos were incubated in 0.15% Triton PBS solution for 5 minutes twice before being transferred to 0.25% Triton in PBS solution for 25 minutes at room temperature. The embryos were then washed 0.15% Triton PBS solution for 5 minutes twice before being transferred to a blocking solution containing 1% BSA and 5% goat serum in PBS for 50 minutes at 4°C. The blocking solution was used

to prepare primary antibody solution with antibodies diluted 1/100 from starting stocks. Embryos were placed in this solution overnight with a minimum of 8 hours. Embryos were then placed in 0.15% Triton PBS solution for 15 minutes, before transferring to a solution (0.15% Triton PBS) containing secondary antibodies (at 1/100 dilution) and Phalloidin (1/50 dilution) for 50 minutes After this step, the embryos were incubated in 0.15% Triton PBS for 25 minutes before being transferred to a drop (10μL) of Vectashield containing DAPI. Embryos were then imaged with Zeiss LSM 710 after at least a 4h incubation period.

6.2.5 FRAP experiments with YAP-GFP fusion protein

CGR8 cells expressing a YAP-GFP fusion protein were cultured as described previously and used to form embryoid bodies, which were injected into 25μm-60μm hydrogel cavities, pre-equilibrated in culture media prior to the experiments. The gels were then placed into 8 well chambers containing enough media to partially submerge the gels, which were covered with mineral oil to prevent evaporation.

2x2μm Nuclear regions in the cells expressing YAP-GFP fusion proteins were bleached by scanning 100 times with full power of the 488nm laser on Zeiss LSM 710 confocal microscope. The tissues were then scanned every 3 seconds with the following settings: 12% of the available 488nm laser power, 40X water immersion objective at 512X1024 resolution, which corresponded to 0.2595x0.2595μm pixel size, which were averaged 2 times. Fluorescence recovery after photo bleaching (FRAP) data was analysed offline in R Studio.

6.3 Results and discussion

In order to form hypotheses about Hippo pathway involvement in the second cell fate decision, I took a similar approach to the previous chapter looking at pre-implantation embryo development. The first step was to revisit published reports using RNA se-

quencing data to look at transcriptional changes related to Hippo pathway activity. Besides the work on pre-implantation embryos [283, 282], I could not find published single cell transcriptomics data on cell based differentiation *in vitro*. However, there were reports looking at stem cell conversion into the two lineages by total RNA sequencing. One was using Sox17 over expression, which is one of the known drivers for the primitive endoderm fate (GSE61102) and the other report used soluble Fgf4 factors to stimulate primitive endoderm differentiation [319]. I then followed up transcriptional profiling by looking at protein level effects by immunostaining experiments. Gata6 [198] was used as the key marker of endoderm formation, as well as Oct4 [312] and Nanog for the epiblast. Immunostainings have been quantified with the image analysis software package developed earlier and allowed to look at protein level relationships and sub-cellular protein localisation leading to signalling mechanisms. Having looked at the relationships between different level signalling components I then investigated the effects of changing tissue geometry and looked at several hypotheses about molecular signalling by using chemical inhibitors. I have also used live imaging of a reporter line YAP-GFP to reveal the rates of YAP nuclear transport to put it in the perspective of other signalling elements.

6.3.1 Transcriptional control of the second cell fate decision

Previous work on endoderm formation mechanisms [314, 319] makes it possible to look at several components involved in signal transduction at the RNA level. One of the Publicly available datasets (GSE61102) looks at cell differentiation, as one of the transcription factors Sox17 is induced by doxycycline. This makes it possible to estimate changing RNA levels of signalling components in time (Figure 6.2) and their changing concentrations make it possible to look for relationships at the transcriptional level (Figure 6.3). As can be seen in Figure 6.2, YAP transcript levels followed those of Gata6, as well as Angiomotin, which has been implicated as an upstream

Hippo pathway signalling component.

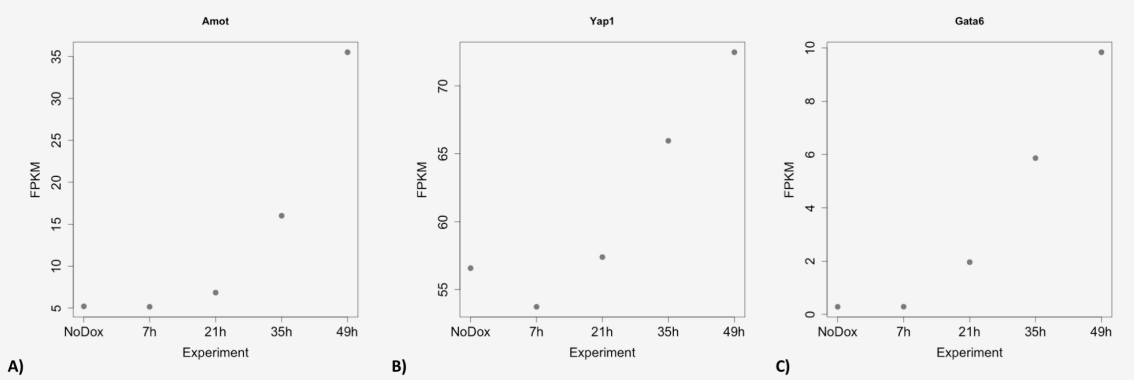


Figure 6.2: Transcriptional profiles Hippo pathway components Yap and Angiomotin, as well as endoderm marker Gata6. X axis marks time after Sox17 induction.

Figure 6.3 takes a broader look at several signalling factors potentially involved in geometry sensing and cell fate determination. The data can be generalised in two oppositely correlated groups, the first one containing pluripotency markers, such as *nanog*, *oct4 (pou5f1)*, *sox2* and *myc*. The second one can be subdivided into possible Hippo pathway targets *tead4*, *eomes* and *cdx2* which were active during pre-implantation development, also core Hippo proteins *yap*, *taz*, *lats1* and *lats2*, as well as polarity components *aspp2 (trp53bp2)*, *par3*, *par6*, *ezrin*, *radixin*, *protein kinase C (Zeta)*,*angiomotin*, *rho GTPase*, and finally characteristic endoderm transcription factors *gata6*, *gata4* and *sox2*. I omitted *sox17*, because it was being actively changed exogenously.

The two broad transcription factor families in Figure 6.3 cluster together, which suggests their involvement in the transition from the pluripotent state to the endoderm fate. Considering the Hippo pathway, there was a promising link between several endoderm markers and core kinases Lats1/2. Furthermore, there was also a strong correlative link to apical polarity proteins Par3/Par6d and their downstream signalling component Angiomotin-like1/2. The link to core homologues Yap/Taz was not particularly strong, however as their activity is regulated by phosphorylation and

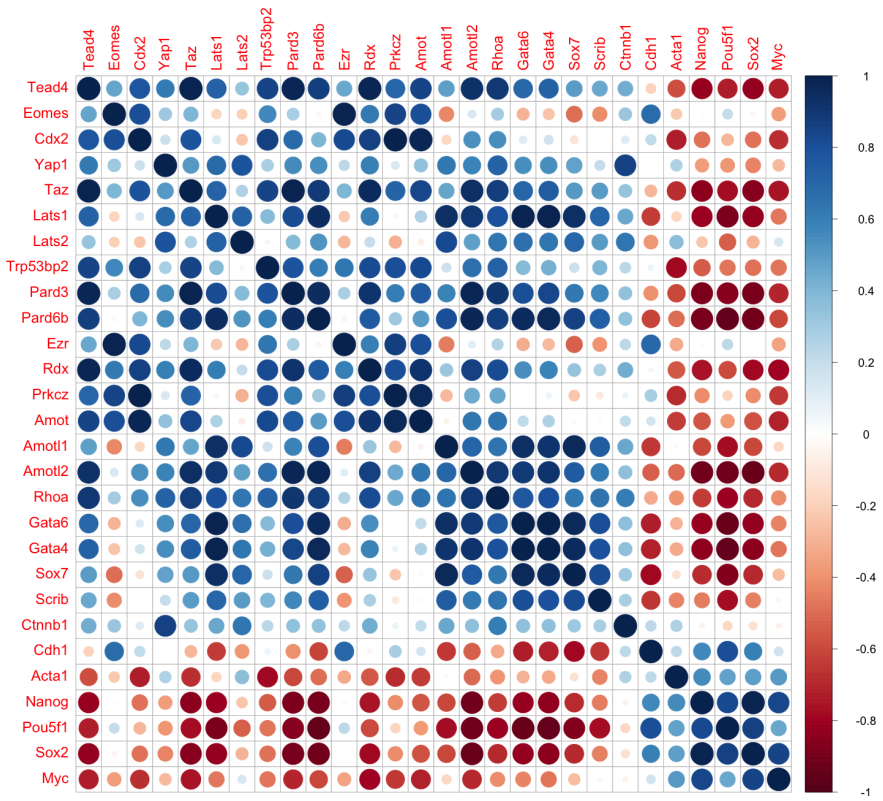


Figure 6.3: Correlation of transcriptional profiles of different signalling components. The graph represents correlations between RNA levels of various genes during the course of Sox17 transcription factor over expression, which drives the cell fate decision. Colour represents the slope of the correlation and circle size represents correlation coefficient between the different pairs of correlation coefficients.

nuclear shuttling, RNA levels are not particularly informative. The next step was to investigate several selected protein components by immunostaining.

6.3.2 Inside/outside protein patterning during the second cell fate decision

While transcriptomics allowed to simultaneously look at a large number of candidate species, immunostaining depends on available antibodies and the number of fluorescence channels. I have chosen to look at Gata 6 transcription factor by immunostaining embryoid bodies, as this transcription factor reliably marks differentiation towards endoderm lineage (Figure 6.4 C). Similarly, Nanog and Oct 4 were chosen to mark the cells belonging to the epiblast lineage (Figure 6.4 B, C). Par 6 was selected

to mark apical cell polarity, which appears after the second cell fate decision (Figure 6.4 A, B). Finally, Yap was chosen as the key Hippo signalling component to assess pathway activity in response to differences in tissue geometry (Figure 6.4 A).

Looking at Yap localisation prior to cell differentiation (Figure 6.4, A), there was slight bias towards nuclear localisation in the outer cells (Figure 6.5, B). Before cell differentiation, the cells were not polarised as can be seen by Par 6 polarity marker expression (Figure 6.4, A). I have also used this marker as a negative control for radial protein distribution analysis, which showed, that there was no significant bias resulting from the analysis technique itself, apart from a few outliers (Figure 6.5, A). Although nuclear Yap localisation before cell differentiation was subtle, it was consistent among all samples in both CGR8 and CCE embryonic stem cell lines. While in this population nuclear/cytoplasmic Yap ratio sometimes approached 1 (log(N/C) approached 0), Yap in the inner tissue cells (distance from surface of more than 3 cell radii) was consistently excluded from the nucleus into the cytoplasm, which indicates an active Hippo pathway resulting in Yap phosphorylation.

After the differentiation event, outer cell layer had a more profound nuclear Yap localisation (Figure 6.7, B), which was also correlated with a large increase in Gata 6 marking formation of the endoderm cell population (Figure 6.7, D). Inner tissue cells expressed Oct 4 and Nanog transcription factors, which indicate the epiblast lineage. Oct 4 expression was uniformly nuclear among the cells, which were either inside the tissue or were outside, but not polarised (Figure 6.4, B), as judged by the Par 6 stain. Immunofluorescence analysis indicated that cells in the outer layers expressed lower levels of Oct 4. This population of low Oct 4 cells (Figure 6.5, D) extended further into the tissue, than cells marked with other endoderm markers, like Gata6 (Figure 6.5, C). This could be an artefact of tissue analysis, as the outside surface is detected automatically, which creates a bias in the case of touching tissues. Similarly, another epiblast marker Nanog also showed localisation in the inner cells, however, it

was not expressed uniformly among all the cells and sometimes inconsistently among the tissues, as can be seen in (Figure 6.4, C). Generally, Gata 6 and Nanog showed a negative correlation (Figure 6.6, A), but they were not mutually exclusive, which mirrors the situation seen in pre-implantation embryos at the early stages of the cell fate decision [198]. Based on a batch of 6 embryoid bodies simultaneously stained for Oct4 and Par6, correlating expression of these factors by SilentMark analysis was not successful (Figure 6.6, B). This was due to the curved shape of the outer cells, which made it difficult to automatically detect exposed cell surface. Even though, it is visually evident that cells with high levels of Par 6 in their outer membranes do not contain nuclear Oct 4 (Figure 6.4, B).

Looking at the immunostainings of key protein components present in embryoid bodies made it possible to formulate further hypotheses, that Yap is regulated even before the event of differentiation, afterwards becoming localised in the nucleus and strongly associated with expression of Gata 6. The inside/outside pattern is similar to the first cell fate decision in pre-implantation embryos, which also develops a single layer of polarised cells with Yap localised in the nucleus, leaving an internal core of pluripotent cells. However, the geometry sensing mechanism has to be different from the embryos, because outer cells prior to the fate decision event are not polarised, so the polarity has to be acquired de novo, rather than inherited via cell division geometry. While the links between cell polarity and Yap localisation can be implied from the mechanism driving the first cell fate decision, the causative link between Gata6 and Yap is also less clear despite the strong relationship seen during immunostaining analysis (Figure 6.7, D). Previous reports show conflicting observations that Yap target Tead4 is either not required for embryoid body differentiation during complete gene knockout [320] or that Tead4 knockdown embryos show reduced populations of endoderm and increased numbers of epiblast cells [321]. Therefore it is unclear, whether Hippo pathway operates analogously to embryos and I wanted to investigate

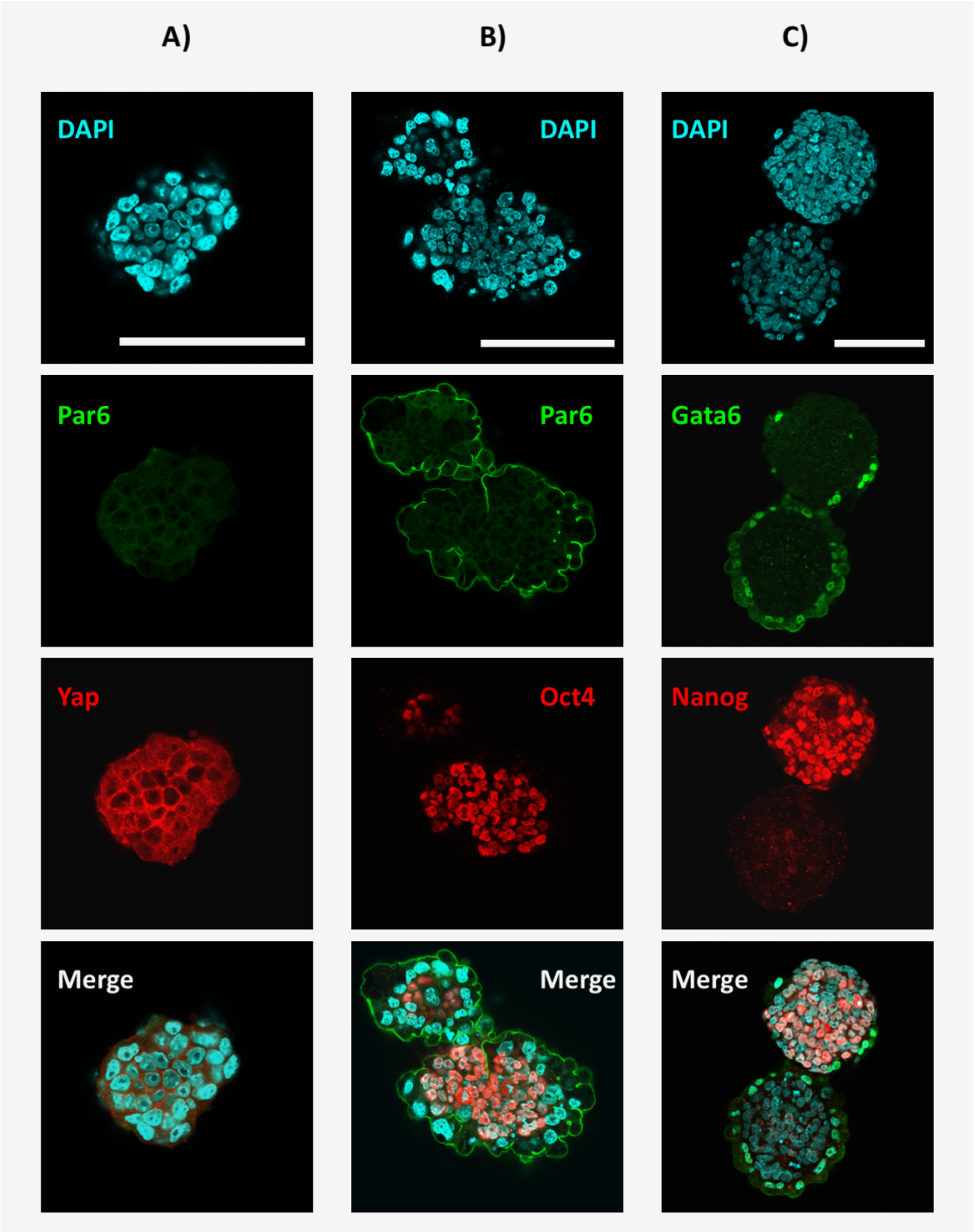


Figure 6.4: Immunostaining of key signalling components. A) CGR8 cell embryoid bodies before differentiation (images representative of 15 embryoid bodies), B) and C) CCE embryoid bodies after outer cell layer differentiation (images representative of 6 and 7 embryoid bodies). Scale bars represent 50μm

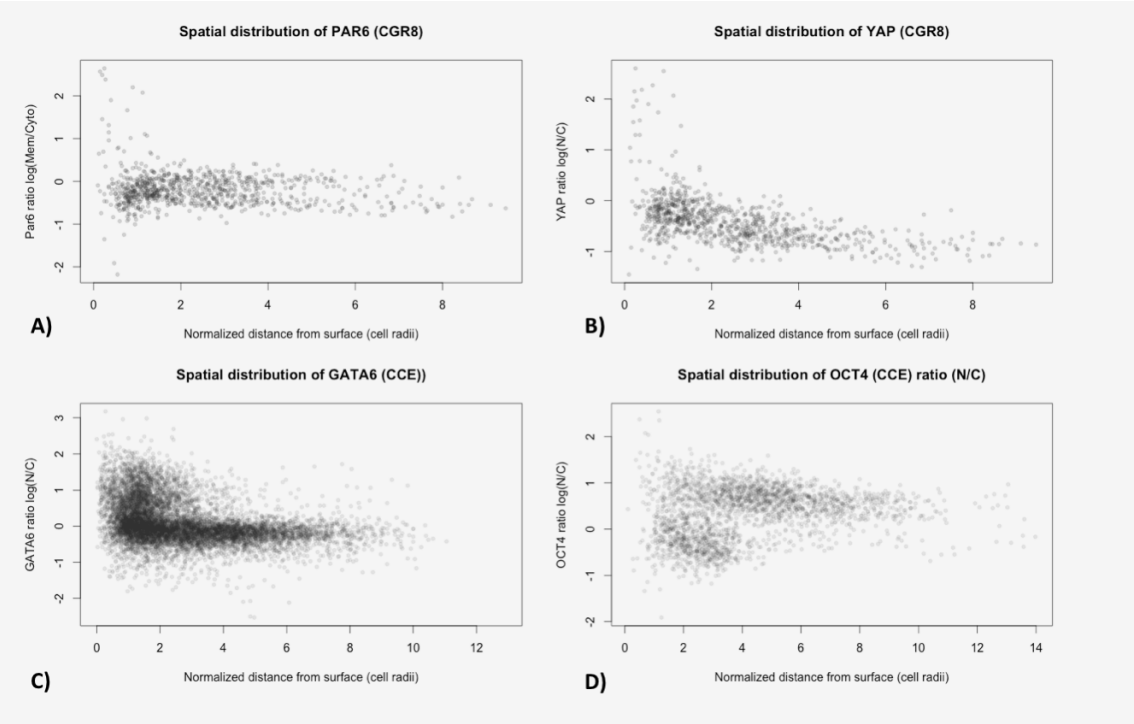


Figure 6.5: Differential localisation of various proteins potentially involved in sensing tissue geometry. A) - Spatial distribution of membrane Par6 fluorescence (ratio of membrane/cytoplasmic fluorescence) within embryoid body cells in 4 embryoid bodies. B) - Spatial distribution of membrane nuclear Yap localisation (ratio of nuclear/cytoplasmic fluorescence) within embryoid body cells in 3 embryoid bodies. C) - Spatial distribution of GATA6 expression in cells of 5 embryoid bodies. D) - Spatial distribution of OCT4 expression in cells of 3 embryoid bodies. All analyses done by SilentMark after tissue immunostaining.

further.

6.3.3 Hippo pathway activity during tissue deformation

Using hydrogel channels it was possible to change the shape of developing tissues in order to reveal the responses in Yap protein localisation and cell differentiation to endoderm lineage marked by Gata 6. CGR8 cells were used to grow embryoid bodies in the presence of LIF in order to assess protein expression patterns before cell differentiation. CCE cell based organoids were differentiated inside hydrogel channels after removing them from STO cell feeder layer and growing for 3 days. Generally, both the CGR and differentiated CCE cell organoids displayed the pattern, that was

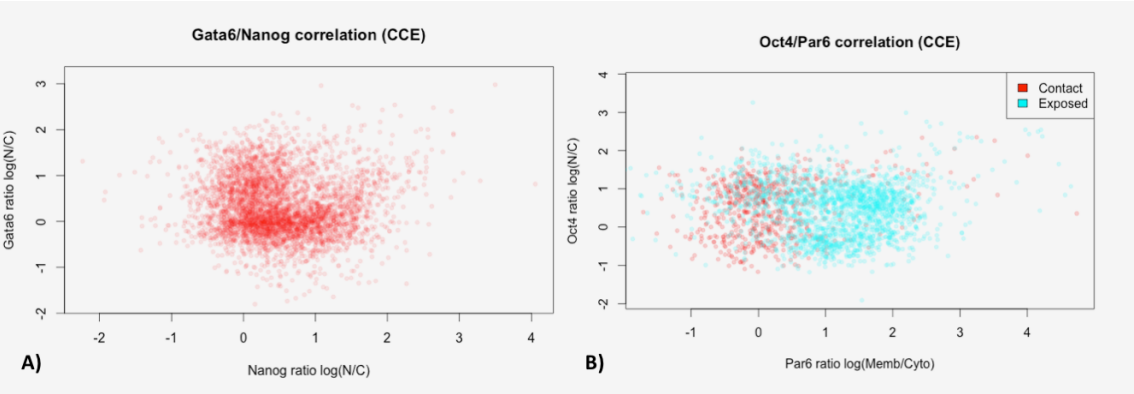


Figure 6.6: Correlations of several signalling components after the second cell fate decision event. A) - Relationship between primitive endoderm marker Gata6 and pluripotent epiblast marker Nanog (4 embryoid bodies in correspondingFigure 6.4, C). B) - A relationship between cell polarity marker Par6 and pluripotency marker Oct4 (3 embryoid bodies in correspondingFigure 6.4, B)

seen in spherical embryoid bodies (Figure 6.8). One outer cell layer differentiated to become endoderm and furthermore, differentiation was not dependent on whether the cells were on the sides or the ends of the cylindrical tissues. To further assess the extent of differentiation I performed statistical analysis of the stained tissues (Figure 6.9). Yap levels agreed reasonably among the two different cell types before and after differentiation, with undifferentiated cells having a larger population of cytoplasmic yap cells (Figure 6.9, A). There was a shift in both Yap and Gata6 localisation in response to geometry change. After surface area increase, there was a larger number of cells having nuclear Yap ($\log(N/C)>0$) (Figure 6.9 B, C), in addition to larger numbers of Gata6 positive cells (Figure 6.9, D), consistent with the observations from the immunostainings (Figure 6.8).

Since both Gata 6 and Yap responded to changes in tissue geometry, this suggests, that the cell differentiation event is regulated by geometry to some extent and seeing that Yap responds to geometric changes even prior to cell differentiation suggests that Hippo pathway may respond by a similar mechanism to pre-implantation embryos. In order to look into the upstream signalling elements resulting in Yap localisation difference, I have used inhibitors affecting actin cytoskeleton. Small molecule in-

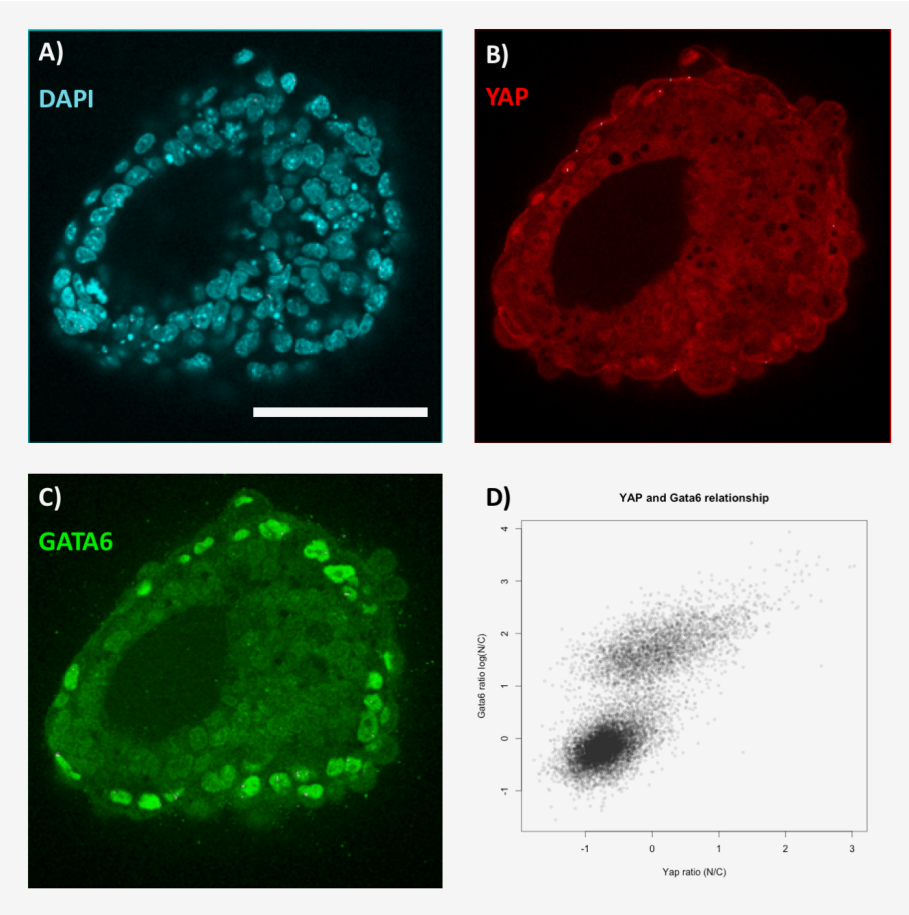


Figure 6.7: Hippo pathway involvement after the second cell fate decision. A) - nuclear staining of an embryoid body containing a cavity. B) - Yap localisation in differentiate embryoid bodies. C) - Gata6 localisation in differentiated embryoid bodies. D) Correlation between Yap and Gata6 localisation. Images representative of 5 embryoid bodies. Scale bars represent 50μm

hibitors are reliable and well characterised [322] and include those interfering with actin-myosin contractility, e.g. blebbistatin [323, 52, 187, 11] or actin polymerization, e.g. cytochalasin D [237, 64, 324]. However, before continuing to explore the link between actin and Yap localization, I wanted to determine the rate of nuclear Yap transport, as I could not find any prior experimental measurements. Since Yap acts as a signalling molecule via transcriptional co-activation, it has to be transported into the nucleus and if the transport is particularly slow, this could potentially be the rate limiting step in the whole regulatory signalling pathway.

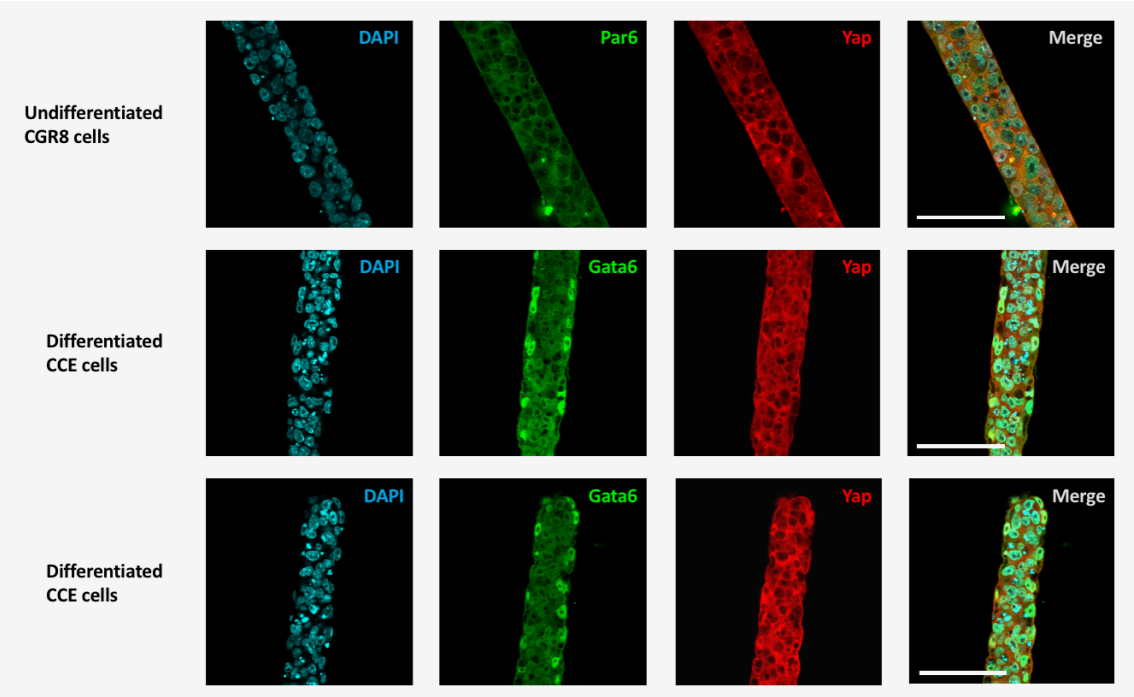


Figure 6.8: Hippo pathway activity in confined (40μm channels) embryoid bodies during the second cell fate decision event. The top row shows undifferentiated cells with partial nuclear Yap localisation in the outer cells. The two lower panels show embryoid bodies after differentiation (sections through the middle and the end of the cylindrical tissue). Images representative of 6 and 7 embryoid bodies. Scale bars represent 50μm

6.3.4 Investigating nuclear Yap transport rates

In order to look at the kinetics of intercellular protein shuttling I employed the technique of fluorescence recovery after photobleaching (FRAP) [325, 326]. The technique involves bleaching a fluorescent region of a cell with a laser and then looking at fluorescence recovery kinetics, which represents mobility of the fluorescent species. In this case I have used a fusion protein between Yap and GFP [327] in order to track movement of Yap across the nuclei and cytoplasm. The plasmid containing Yap GFP construct was created by Dr. Christophe Royer and transfected to CCE cells using a commercially available Lipofectamine kit.

Undifferentiated cells transiently expressing Yap GFP generally exhibited a nuclear localization pattern that was analogous to *in vitro* cultured organoids (Figure

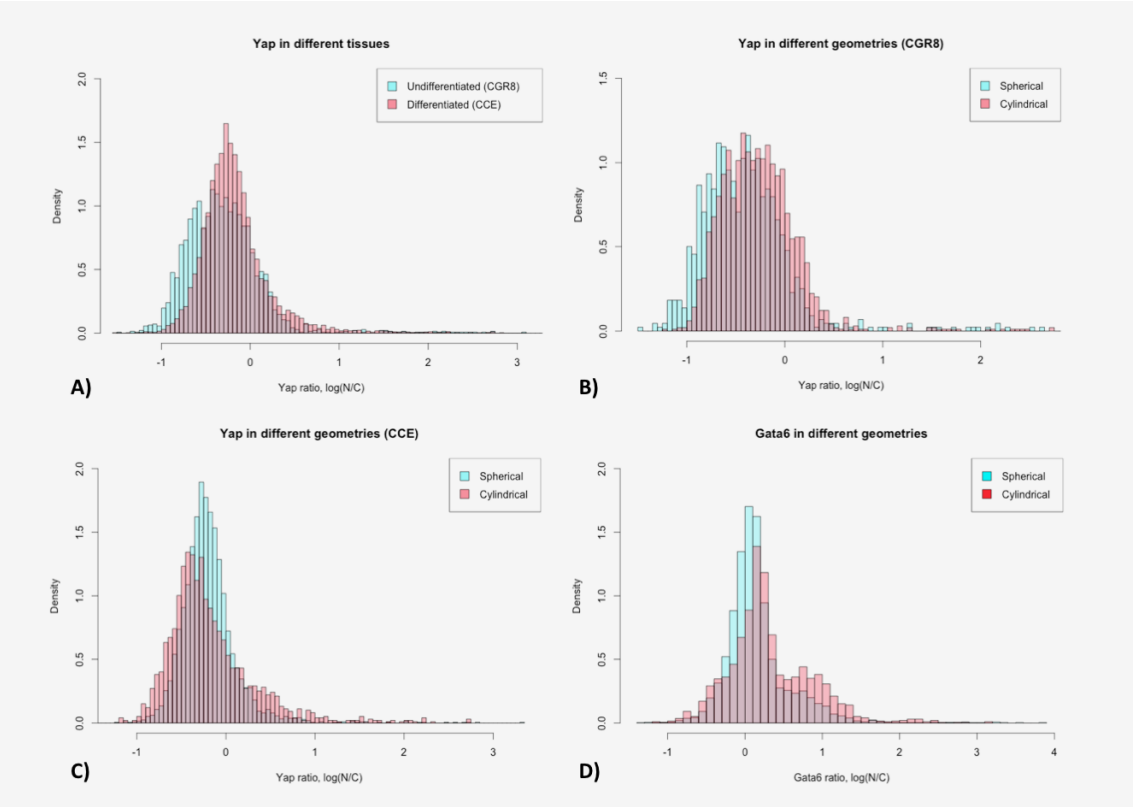


Figure 6.9: Analysis of Yap and Gata6 localisation during tissue shape change. A) - Nuclear Yap localisation before and after tissue differentiation (4 embryoid bodies). B) - Nuclear Yap localisation following compression of undifferentiated EBs (4 embryoid bodies). C) - Nuclear Yap localisation following compression of differentiated EBs (4 embryoid bodies). C) - Gata6 levels in embryoid bodies grown in spherical and cylindrical environments (4 embryoid bodies).

6.10, A). Contrasting Yap levels in the nuclei and the cytoplasm made it possible to identify, target and exclusively photo-bleach the nuclear region of the cells. Fluorescent protein diffusion within the nuclear compartment was faster than the temporal resolution of the acquisition and generally occurred within a second to equalise fluorescence within the nuclear region. A slower fluorescence increase then followed within the timescale of a minute, which could be attributed to Yap GFP moving from the cytoplasm into the nucleus (Figure 6.10, B).

Overall the half-lives of nuclear Yap diffusion were relatively varied among the samples, most likely due to sensitivity of the FRAP method and relatively low flu-

orescence levels. Measurements of 77 samples showed a relatively wide distribution with a median half life of 15.6s (Figure 6.10, B). The value is several times smaller than for EGFP nuclear diffusion alone [328], which suggests, that YapGFP construct is actively transported into the nucleus. However, given the lack of the nuclear localization signal on the protein [329], the exact mechanism of how and why Yap localises into the nucleus remains unknown. To look at potential changes in Yap transport rates, I have measured the nuclear half-lives of the YapGFP construct, in addition to measuring nuclear/cytoplasmic rates and distances of the cells to the surface of the tissue (Figure 6.11). Since the experiments were done at different times after transfection, I have also assessed potential changes in Yap transport rates as a function of time, when separate cells compact to form an embryoid body.

Since Yap ratio was relatively conserved before and after cell bleaching (Figure 6.11, A, B), this indicates, that Yap transduction process, regulating the ratio of nuclear and cytoplasmic levels is relatively dynamic and able to respond to rapid changes. There was little dependence of nuclear Yap half-life and cell distance from the surface (Figure 6.11, B), although the correlation may be beneath the high levels of noise, coming from the technique itself. The same was true for looking at how the rates of nuclear transport depended on time after cells started to aggregate into the tissues. Although it seems like the initial half-lives are larger, than 10h after the start of the experiments (Figure 6.11, C), the difference was in fact statistically insignificant due to the large variance in the measurements.

Overall, FRAP measurements of GFP labelled Yap protein revealed, that the timescale of nuclear to cytoplasmic protein transport was on the order of 10s of seconds, faster than rates of transcription and is unlikely to be the limiting step in signal transduction. In order to look at potential upstream signals, I wanted to explore two potential signalling elements - GPCR surface receptors and actin/myosin cytoskeleton. GPCRs have been shown previously to be involved in Hippo signalling [148, 306]

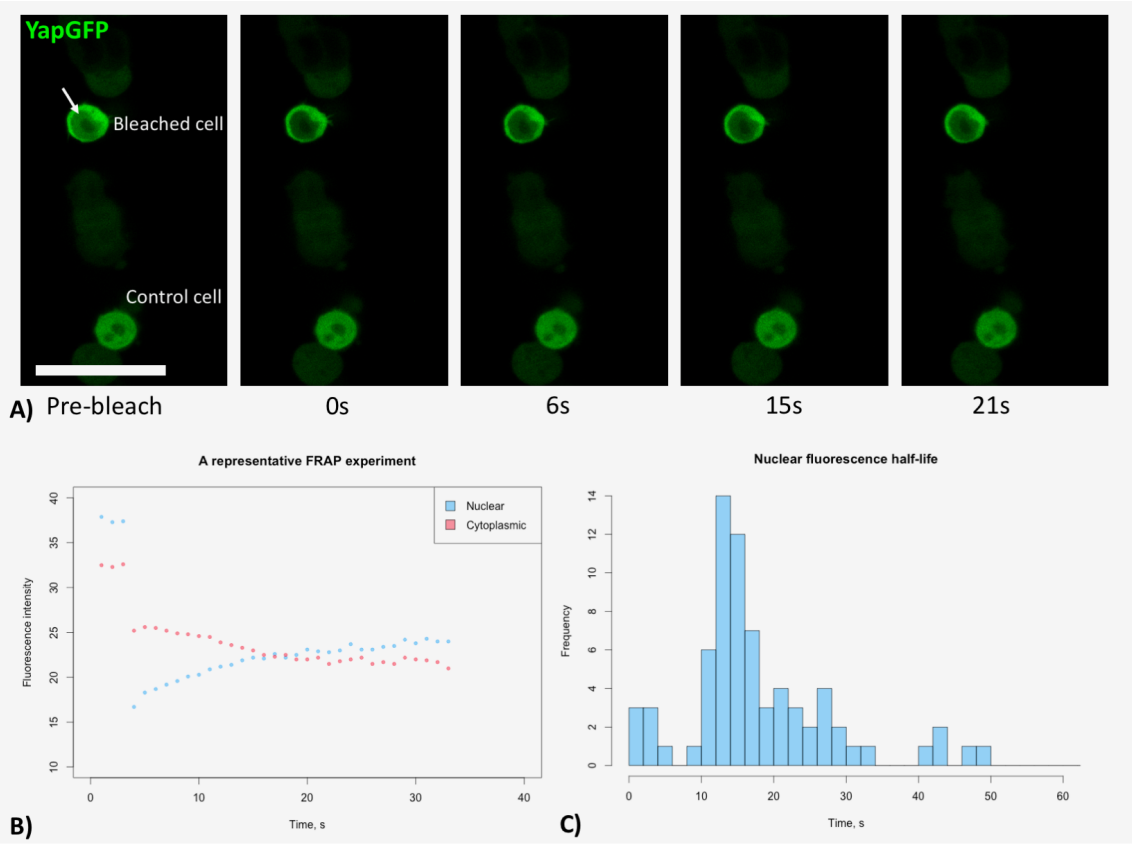


Figure 6.10: FRAP experiments to determine the rate of nuclear Yap transport. A) - Representative timelapse of nuclear fluorescence recovery after bleaching (arrow marks the bleached nucleus). B) - An example graph showing time dependence of fluorescence recovery. C) - Summary of fluorescence recovery half-lives showing the statistical measurement distribution. Scale bar represents 25μm

and Dobutamine has been used to inhibit the pathway by targeting adrenergic receptors [327]. In addition to dobutamine experiments, I also wanted to explore the role of actomyosin cytoskeleton, which is involved not only in tension sensing [33, 65, 302], but also polarity maintenance [330, 331, 332].

6.3.5 Hippo pathway link to G-protein coupled receptors

Dobutamine is one of the recognised small molecule inhibitors [143], that has previously been used to study the Hippo pathway. It acts through blocking adrenergic receptors, which are involved in MSTII kinase phosphorylation, which in turn phosphorylates Lats kinases and eventually Yap, leading to its exclusion from the nucleus,

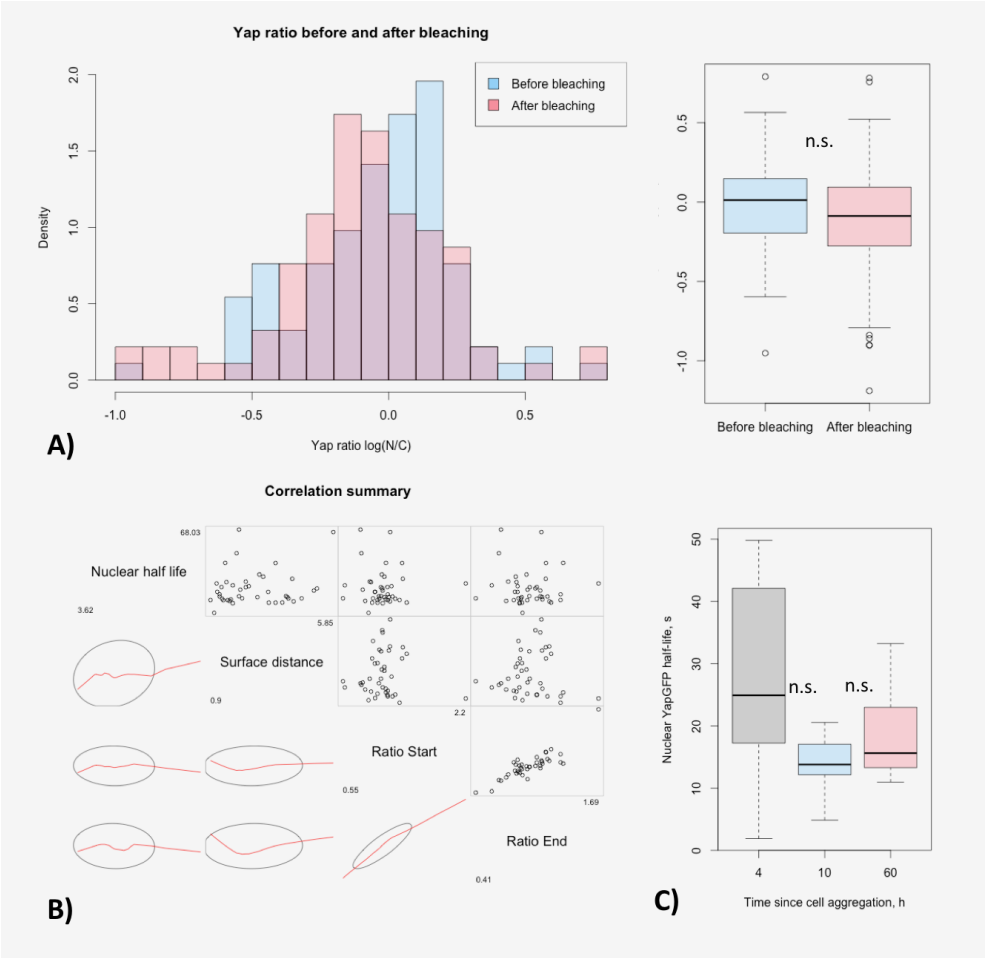


Figure 6.11: Summary of FRAP experiments looking at Yap transport rates. A) - Nuclear/Cytoplasmic Yap ratio in the cells before the bleaching experiment and after fluorescence recovery. B) Correlations of fluorescence recovery half-life with various factors. C) - The role of cell cohesion in nuclear Yap transport. Statistical significance was tested via t-tests.

where it otherwise acts as a transcriptional coactivator of Tead4 transcription factor.

To perform the experiments, I have used 30μM dobutamine to treat differentiating CCE embryoid bodies at day 2, after withdrawing them from the pluripotency conditions. Dobutamine was applied for 9 hours before the embryoid bodies were fixed and stained for Yap indicating the Hippo pathway activity and Gata6, which is a marker of endoderm differentiation (Figure 6.12, A). Due to the variability in protein levels, it was difficult to assess the effects of the inhibitor prior to statistical analysis, which showed overlapping distributions for both nuclear level of Yap (Figure

6.12, B) and Gata 6 (Figure 6.12, C). I also analysed separately the two cell populations characterized by high and low Yap levels. There was a slight decrease in Gata 6 levels in the high nuclear Yap cell population after dobutamine treatment (Figure 6.12, D), however it was not statistically significant (p-value of 0.055 after a t-test). The difference between Gata6 levels in low nuclear Yap cells was even smaller and also not statistically significant.

6.3.6 Actin/myosin inhibitor effects on Yap localisation

In order to investigate the role of actin cytoskeleton as a potential upstream Hippo pathway signal I have used a pair of small molecule inhibitors. Cytochalasin D is a fungal compound, that is able to bind actin monomers effectively stalling polymerization of actin filaments and creation of a functional actin cytoskeleton. Growing undifferentiated CGR8 cell based embryoid bodies inside cylindrical channels made it possible to simultaneously assess the changes in Yap localisation as well as changes in tissue shape, which can be used to estimate mechanical forces generated internally.

Immunostaining images revealed that Cytochalasin D treatment caused a marked decrease in actin levels (Figure 6.13) as well as a more subtle change in Yap localisation. Quantifying the images confirmed these observations on a broader population level (Figure 6.14, A), which makes it possible to create the association between actin cytoskeleton and Hippo signalling. Treating embryoid bodies with Cytochalasin D also resulted in a slight reduction of cell distance to exposed surface (Figure 6.14, B), however the difference was too small to be statistically significant.

To further investigate the link between the cytoskeleton and Hippo signalling I have used another small molecule inhibitor. In contrast to Cytochalasin D, Blebbistatin affects Myosin ATPase ability [333, 332], which results in the loss of intracellular tension. To study the effects of this inhibitor I used a GPI-GFP expressing embryonic stem cell line [231] marking cell membranes, which were indicative of the inhibitor's

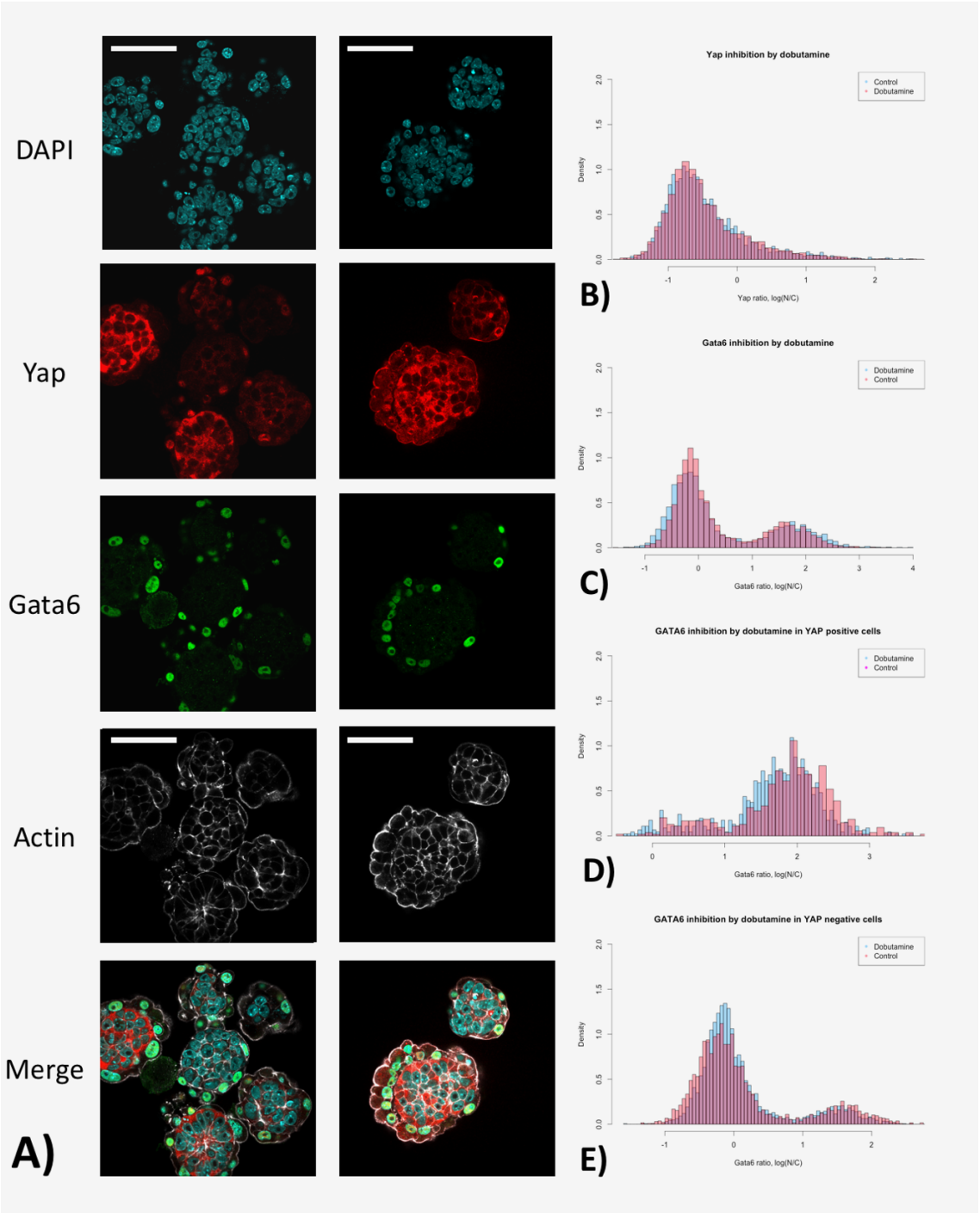


Figure 6.12: Dobutamine effects on Hippo signalling. A) - Immunofluorescence images of control embryoid bodies (left column) and treated embryoid bodies (right column). B) - Analysis of the role of dobutamine in Yap localisation. C) - Analysis of the role of dobutamine in Gata6 localisation. C) and D) analogous analysis in isolated cell populations. Analyses are representative of 12 (control) and 12 (treatment) embryoid bodies.

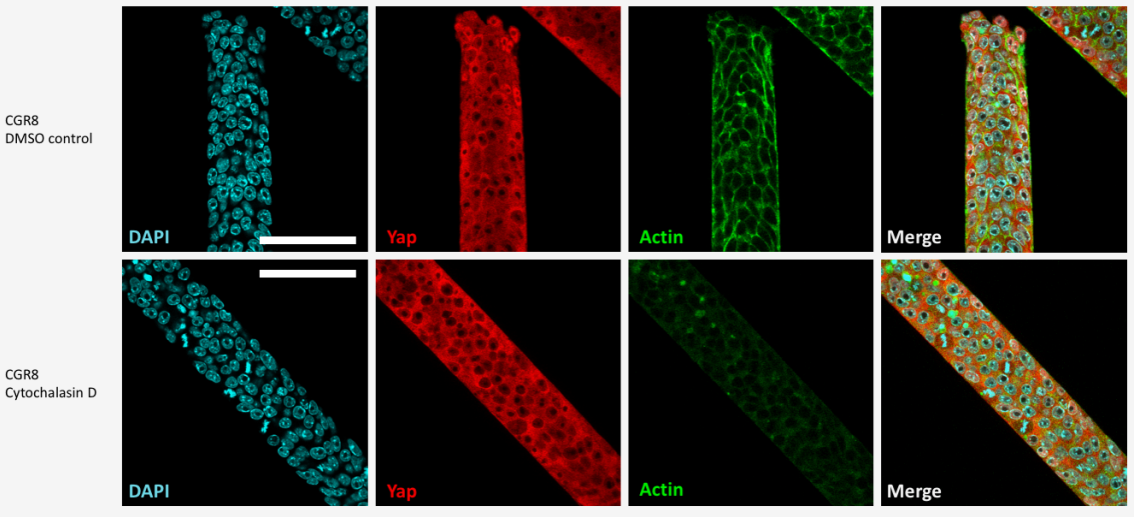


Figure 6.13: Immunostaining of Cytochalasin D treated embryoid bodies compressed in 40μm channels. Images are representative of 7 control compressed embryoid bodies and 6 treated embryoid bodies. Scale bars - 50μm

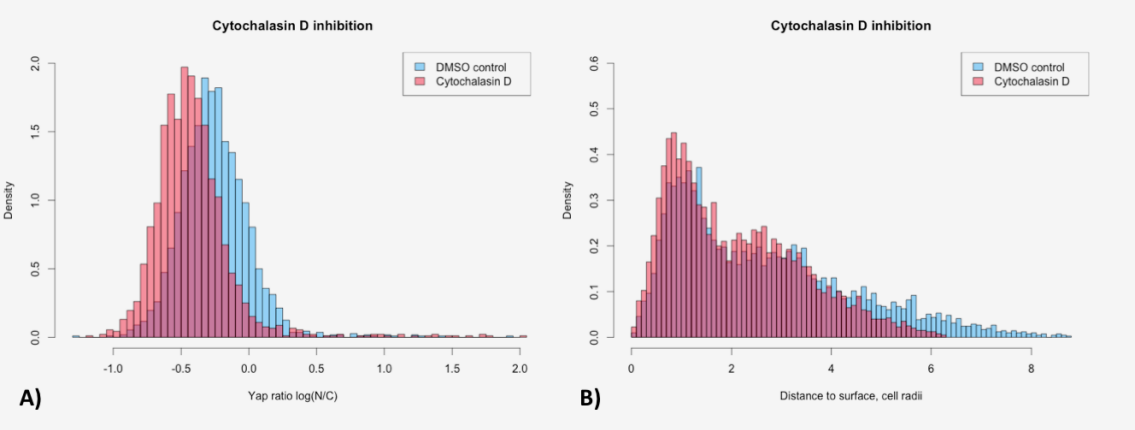


Figure 6.14: Analysis of Cytochalasin D treated embryoid bodies. Population level changes in A) Yap ratio, B) Cell position. Analysis is representative of 6 (control) and 6 (treatment) embryoid bodies.

effects on cytoskeleton. Overall, the effects were similar, in that nuclear Yap localisation was reduced and also tissues were thinner inside channels (Figure 6.15).

I then continued to quantify the changes in Yap localisation and cell position within the tissues, exploring the combined effects of the inhibitor, tissue compression itself and compression timing (either at the single cell stage or one day after embryoid body formation). I began by looking for Yap localisation and tissue differentiation

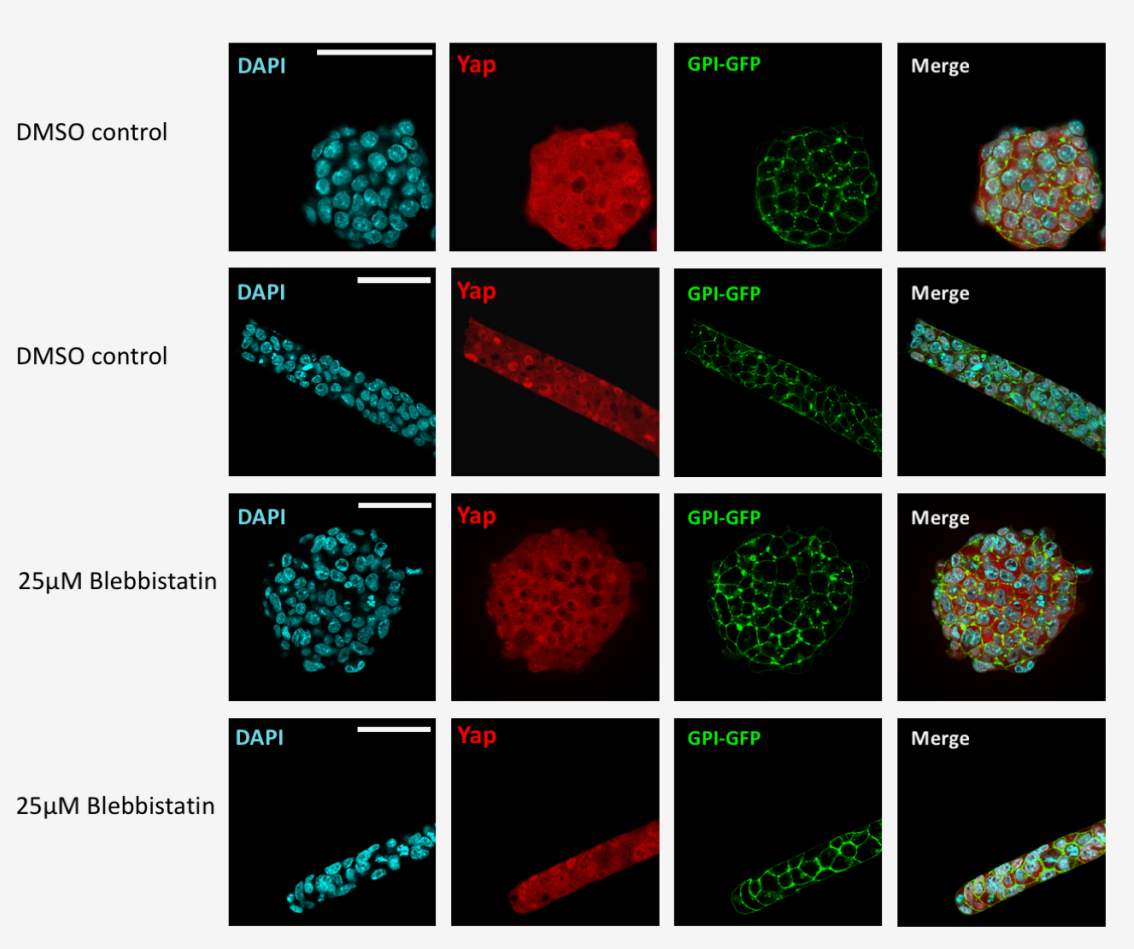


Figure 6.15: Effects of blebbistatin on Hippo pathway activity. Images are representative of 6 embryoid bodies in each condition. Scale bars - 50μm

differences in embryoid bodies compressed before cell aggregation and 1 day after cell aggregation, when they have already formed cohesive spheres. Compression timing had no effect on either Yap localisation or cell position within the tissue (Figure 6.16). This further strengthens the hypothesis, that Yap localisation actively responds to changing tissue geometry.

Looking at the effects of tissue compression, cylindrical tissues had increased nuclear Yap localisation and expectedly cells were closer to the outside surface comparing to their spherical controls (Figure 6.17). This also added to the argument, that nuclear Yap localisation is driven by exposed cell surface. Blebbistatin treatment had an opposite effect to tissue compression as embryoid bodies significantly

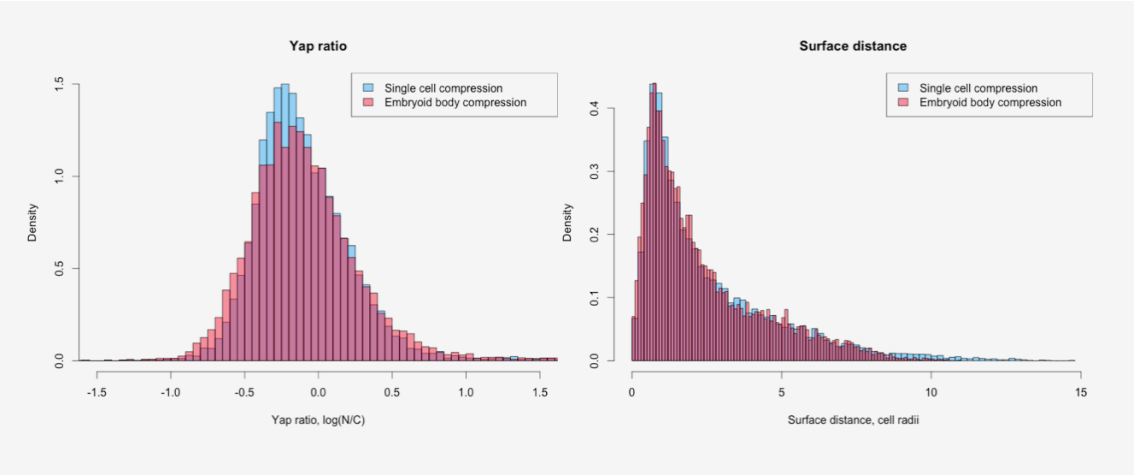


Figure 6.16: The role of embryoid body compression timing. A) - Changes in Yap localisation, B) - Changes in cell distance from outer tissue surface. Compression timing did not have an effect on either of the biological outcomes. Analysis is representative of 12 (early compression) and 12 (later compression) embryoid bodies.

reduced nuclear Yap localisation (Figure 6.18). Also, looking at compressed tissues alone, blebbistatin inhibitor caused a reduction in cell distance to the outside surface (Figure 6.18), which was due to overall reduction of tissue diameter, caused by the loss of cytoskeletal tension and the ability to deform hydrogel channels. These findings indicated, that even before the cell fate decision, Yap localisation was affected by tissue geometry and actin cytoskeleton. In order to look for the effects on tissue differentiation, I performed experiments with differentiating embryoid bodies grown from the CCE stem cell line.

There were two different experiments regarding blebbistatin during CCE cell differentiation. One condition looked at the effects of a transient 2-hour exposure during the differentiation window, 2 days after removal from the STO cells maintaining pluripotency and another condition used sustained blebbistatin treatment from the start of the 2-day window until the end of the experiment 3 days later, when embryoid bodies have differentiated. Figure 6.19 looks at the morphological differences in differentiated embryoid bodies, including average embryoid body cross sectional area and shape, numerically described by circularity measure.

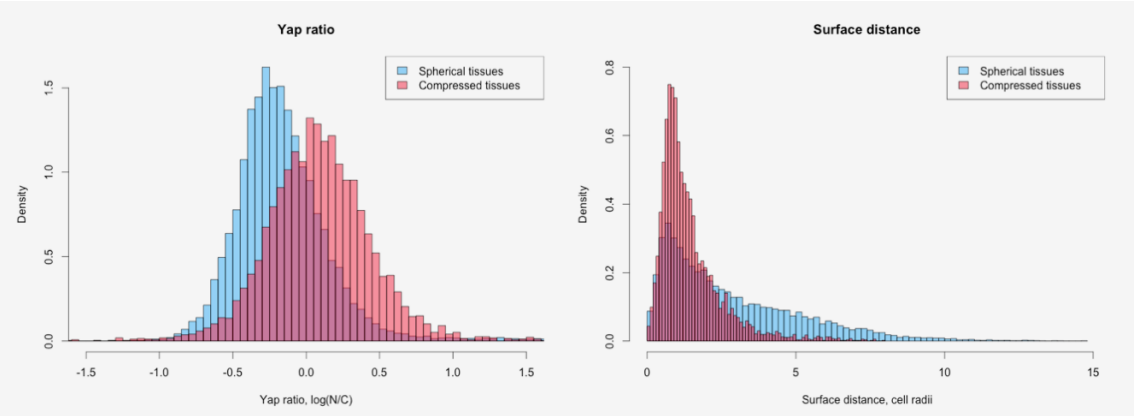


Figure 6.17: The effects of tissue compression. A) - Changes in Yap localisation, B) - Changes in cell distance from outer tissue surface. Tissue compression caused both an increase in nuclear Yap localisation and decrease of cell distance from outer tissue surface. Analysis is representative of 12 (spherical) and 12 (cylindrical) embryoid bodies.

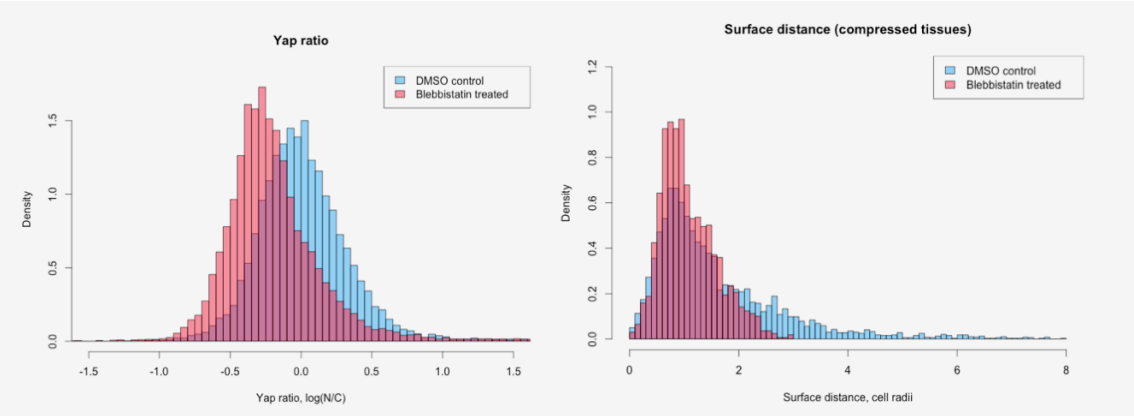


Figure 6.18: The effects of blebbistatin treatment. A) - Changes in Yap localisation, B) - Changes in cell distance from outer tissue surface. Analysis is representative of 12 (control) and 12 (treatment) embryoid bodies.

Overall, the embryoid bodies appeared normal and did not show extensive apoptosis even after sustained treatment with 25μM blebbistatin. Sustained and pulsed exposures caused seemingly opposing effects. Sustained treatment yielded visibly smaller (Figure 6.19, B) and more circular (Figure 6.19, C) embryoid bodies, whereas pulsed treatment resulted in larger tissues, presumably because of increased aggregation, which was also seen during immunostaining images (Figure 6.20), which were used to characterize the differentiation event. Overall, immunostainings showed a

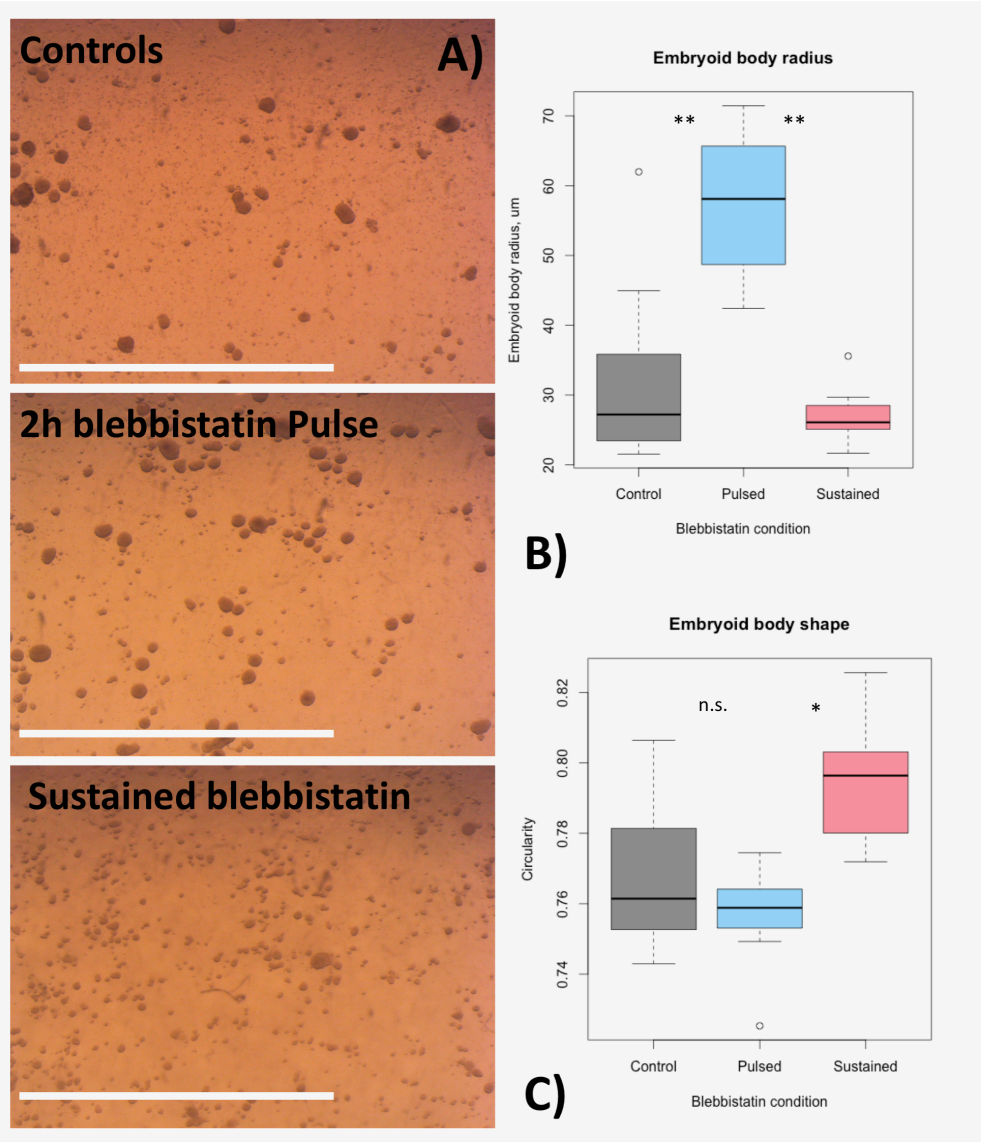


Figure 6.19: Blebbistatin effects on differentiated CCE cells. A) - Morphological changes in embryoid body size and shape seen in brightfield images. B) - Quantification of EB size changes. C) - Quantification of EB shape changes. Scale bars - 5mm, N = 10 for each of the conditions. P-values are represented by: n.s. - not significant, *** - < 0.005, ** - < 0.01, * - < 0.05.

normal nuclear morphology and actin cytoskeleton was relatively intact. However, the higher apical actin signal seen in the outer cell layer of the control tissues was no longer present in blebbistatin treated samples. This suggests that the inhibitor has potentially interfered with cell polarity.

In addition to changes in actin patterns in treated embryoid bodies, blebbistatin

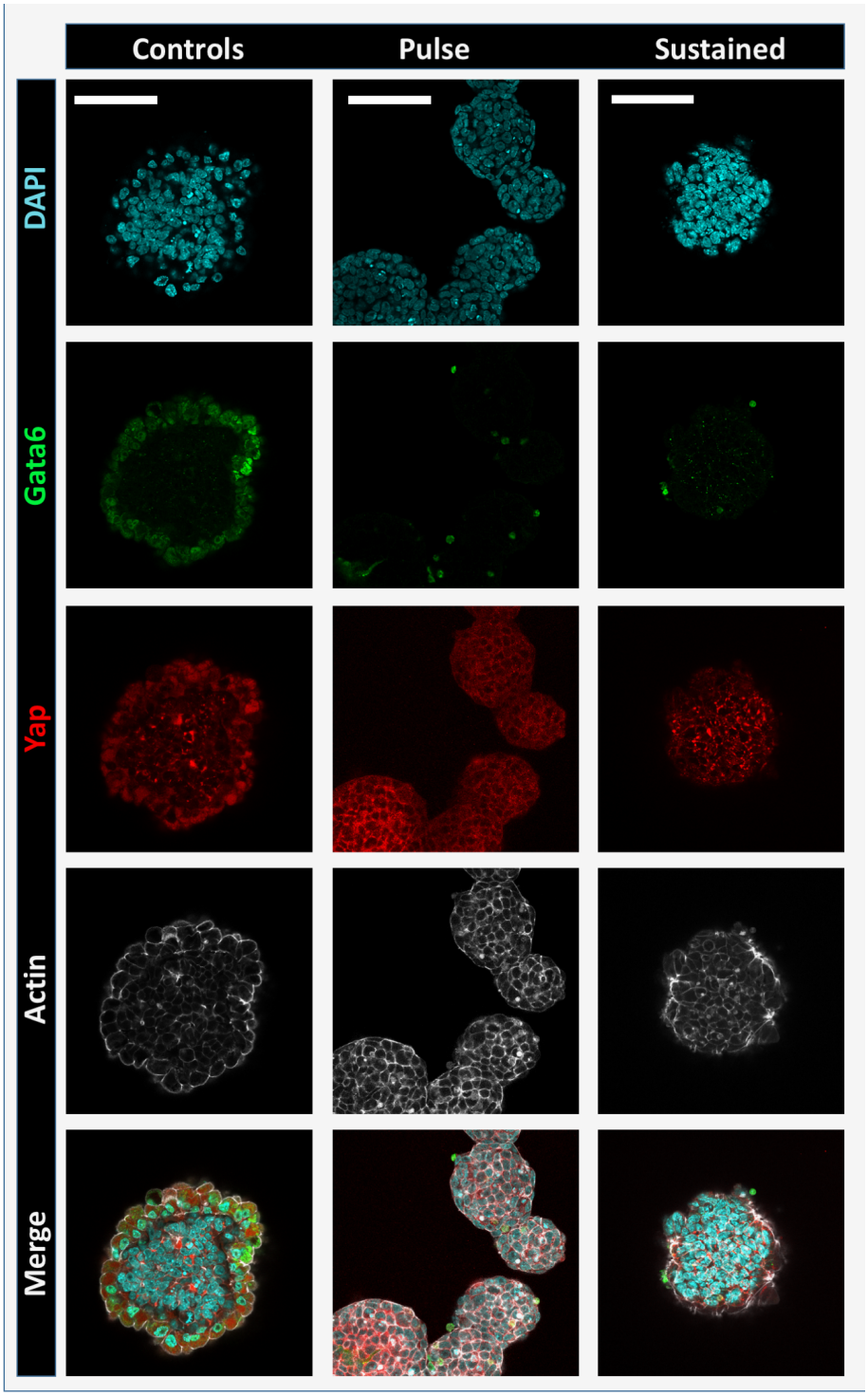


Figure 6.20: Immunostaining of blebbistatin effects on differentiating CCE cells. The columns represent control, 2h treatment and sustained treatment. Blebbistatin caused a decrease in Gata6 levels, as well as nuclear Yap localisation and disruption of actin fibers. There are 5 embryoid bodies per each condition. Scale bars - 50μm

exposure has also affected the levels of Gata6, as well as Yap localisation on a subtler level. In order to quantify the changes seen during inhibitor experiments, I have analysed the images of immunostained embryoid bodies (N>5 for each condition). In order to simultaneously statistically test multivariate conditions I have used the anova test. The change in Yap levels was relatively minor (Figure 6.21, A), but statistically significant by the Anova test (P-value $<2e^{-16}$). The differences in Yap levels appeared even during the Pulsed treatment experiment (Figure 6.21, B), however the largest change in Gata 6 levels occurred during the sustained treatment, although even the transient exposure caused a statistically significant shift in Gata 6 (Figure 6.21 B, D) (P-value $<2e^{-16}$, by Anova test). The changes seen in these individual proteins were also reflected in their relationship (Figure 6.21, E).

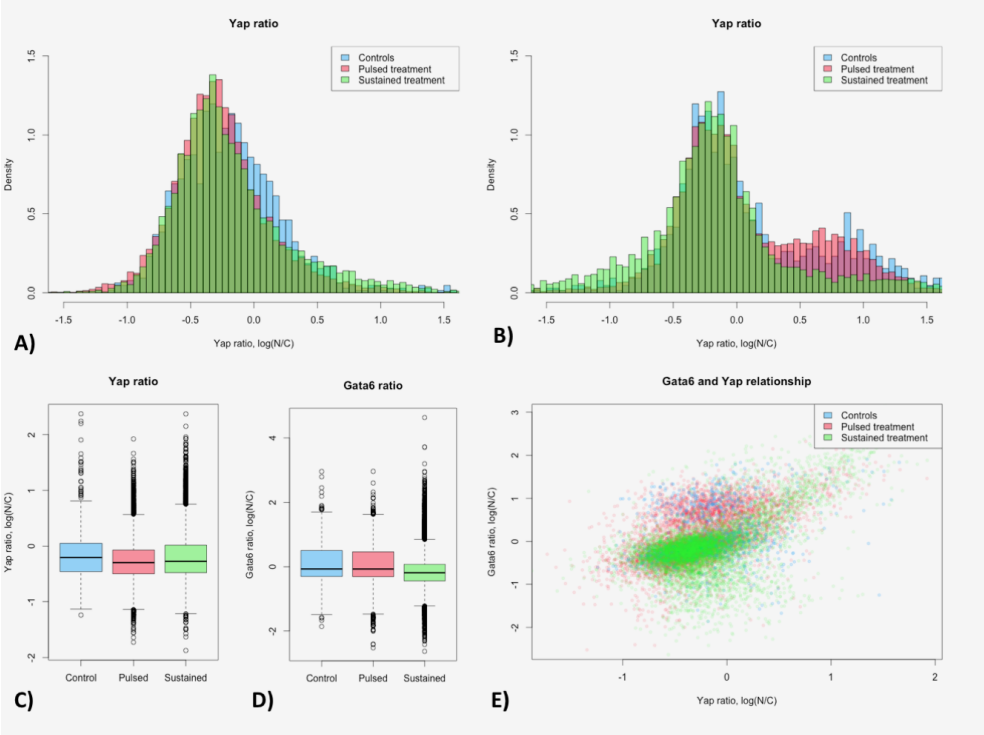


Figure 6.21: Quantification of blebbistatin effects on CCE cell differentiation. A) - Changes in Yap ratio during blebbistatin treatment, B) - Changes in Gata6 levels after blebbistatin treatment. C), D) - Changes in Yap and Gata6 averages due to blebbistatin treatment. E) Changes in correlation between Yap and Gata6 after Blebbistatin treatment. Blebbistatin treatment caused a decrease in Gata 6 levels. There are 5 embryoid bodies per each condition.

To sum up, the changes seen during inhibitor experiments suggest, that actin cytoskeleton is likely to be involved in the second cell fate decision. Both cytochalasin D affecting actin polymerization and Blebbistatin affecting Myosin activity, caused a decrease in nuclear Yap localisation, even before the formation of the endoderm layer, as judged by Gata 6 expression. Blebbistatin also caused a decrease in differentiation towards endoderm layers, but only when the inhibitor was constantly applied after the differentiation window.

6.4 Conclusions

The second cell fate decision is typically regarded, as controlled by stochastic gene expression, followed by cell sorting and fgf based signalling. However, as this tissue patterning event results in a single layer of polarised differentiated cells, it conceptually shares a lot in common with the first cell fate decision, which happens a day earlier during embryo development. Transcriptional analysis of the core Hippo pathway components using published RNAseq data revealed not only the presence, but also a general increase of the main proteins involved in Hippo signalling cascade, including Tead4, Yap, Lats and Angiomotin (Figure 6.3). Upstream effectors of the Hippo pathway are generally not agreed upon, however they most likely involve signals from apical cell polarity complexes, actin cytoskeleton, G-protein coupled receptors or cell adhesion molecules, such as E-Cadherins. To look at which of the mentioned molecules could act as upstream Hippo pathway components and whether the cell fate decision is regulated at all, I used the tissue micromanipulation strategies in addition to several chemical inhibitors.

The studies suggested, that tissues respond to geometry changes and that additional surface creates more cells with increased nuclear Yap. This regulatory capacity was replicated in various scenarios using several embryonic stem cell lines (CGR8, GPI-GFP and CCE), before and after cell differentiation. After cell differentiation,

the changes in nuclear Yap levels were partially mirrored by changes in Gata 6 expression, however the correlation was not absolute, such that all strongly nuclear positive cells contained higher levels of Gata 6, but not all Gata 6 positive cells contained strongly nuclear Yap (Figure 6.7, D). This is in contrast to Hippo signalling in pre-implantation embryos, where Cdx2 expression and Yap localisation are more exclusively related. This makes the link between Yap and Gata 6 questionable, however the discrepancies may be caused by temporal dynamics of Yap localisation, which occurs at the minute timescale and over time may integrate to drive slower changes in transcriptional activities.

Looking at the potential upstream signalling targets, I have tested adrenergic receptors by dobutamine inhibition and the role of cytoskeleton by two inhibitors. Dobutamine inhibition did not show any effect on cell differentiation or Yap localisation, however both Cytochalasin D and Blebbistatin caused a decrease in nuclear Yap localisation and the latter caused the eventual lack of differentiation towards the endoderm (Figure 6.21, E). It remains to be seen, whether the link between actin cytoskeleton and Yap phosphorylation is achieved by cell polarity formation or other specialised molecules, such as actin capping proteins [33]. Given that tissues treated with blebbistatin aggregated easily or failed to form visible apical actin structures seen in the controls, it is likely that actin cytoskeleton is one of the pre-requisites to maintain cell polarity.

To sum up, the chapter reveals a strong link between tissue geometry, Hippo signalling and differentiation of the outer cell layer. Using mechanical tissue deformation, it was possible to establish a causative link to tissue geometry and then actin cytoskeleton via small molecule inhibitors. To complete the study it is still necessary to find the link between Hippo pathway and endoderm transcription factors, such as Gata 6, as despite the correlation between these components (Figure 6.7, D, Figure 6.21, E), the causative link remains unclear. Although there is more evidence

about the upstream effectors, it is also unclear how different actin localisation results in activated Hippo signalling. Revealing these links would mean Hippo pathway a common geometry regulating mechanism between the first two cell fate decisions.

Chapter 7

Conclusions

The thesis started with the goal of revealing molecular mechanisms by which tissues can sense and control their shape during mammalian development. Despite the apparent complexity, mammalian development is highly consistent, which suggests existing regulatory mechanisms ensuring reproducible tissue shape and size formation. In addition to controlling development, the same feedback mechanisms also form the foundation of three dimensional *in vitro* cell culture, where geometric tissue organisation becomes important for their appropriate function. This is particularly relevant for the modern fields of drug screening, personalised medicine and tissue engineering, relying on cultured three dimensional tissues.

To look at the effects of mechanical cell environment, previous decade saw a shift of focus towards mechanotransduction and translating geometric cues to changes in gene expression. The field generally became dominated by single cell approaches and methods with high temporal and spatial resolution, which allowed to look for fast events acting on a short scales. This led to the characterization of intercellular mechanisms, like those involving cilia for sensing fluid fluid flow [334, 335], Rho kinases for cytoskeletal tension [336, 337], and focal adhesion complexes for sensing extracellular stiffness [338].

Despite the development of high resolution tools, there has been a lack of methodology, which would allow to look at changes in tissue geometry and mechanical prop-

erties at a more system level. Since most mammalian development happens in tissues with considerable three dimensional complexity, my goal of investigating geometry regulation led to the need of developing more relevant techniques for manipulating tissue shape, measuring forces, as well as biological outcomes. These techniques were covered in the first several chapters and generally relied on using hydrogels to change tissue shape and measure mechanics. Analysing biological outcomes for developmental biology purposes is usually done via immunostaining, because it is one of the few techniques, which can provide information on the relative cell location within tissues. However, I also had to develop analytical methodology to quantify cell fluorescence levels, as otherwise it is difficult to numerically test hypotheses or objectively compare larger numbers of samples.

In the final chapters I took a detailed look at the first cell fate decision in mouse embryos, which despite a large amount of prior research, still contains a lot of unknowns, particularly the regulatory aspects involving geometry. By deforming the embryos and altering cell localisation, it was possible to confirm the hypothesis that tissue differentiation is driven by differences in cell geometric environment. Uncovering the molecular factors responsible for this transition has proven challenging, because neither cell shape, polarity nor distance to surface could alone explain tissue patterning. Cell shape, sometimes regarded as a mechanotransduction cue [25] was insufficient to cause differential Yap localisation during the window of cell fate decision. Differences in Yap localisation were strongly correlated by cell polarity, however, since all 8-cell embryo blastomeres become polarised, cell polarity alone was not sufficient to explain the origin of geometric and molecular asymmetry. After performing timelapse experiments it became evident that cells can localise differently within the tissue regardless of their initial position after the 8-cell blastomere division. This could be attributed to differential inheritance of cell polarity components [186], which then set up the the differences in cell fate. It is still unclear what is the underlying

mechanism driving polarised cell division, however, cell divisions are not random and are affected by geometry, which could be seen during timelapse imaging of cylindrical embryos. This leads to new hypotheses for further work on how geometric cell environment controls the details of spindle formation and cytokinesis during cell divisions under spatial constraints.

After investigating the role of geometry during the first cell fate decision in preimplantation embryos I wanted to look at the subsequent differentiation event, which patterns the inner cell mass to also create an inside-outside pattern of primitive endoderm and the epiblast tissues. I used embryonic stem cell organoids to study this process *in vitro*, as working with cells made it more directly relevant to translational applications requiring well defined three dimensional tissue culture. To study the involvement of Hippo pathway, I began by investigating existing RNA sequencing data to look for the presence of transcripts from the Hippo pathway component proteins. I then used immunostaining to look at geometric localisation of key proteins involved in Hippo pathway, as well as Gata 6, a marker of endoderm lineage. Since there was a correlation between cell distance to exposed surface and Yap localisation, as well as endoderm markers, I continued to investigate differentiation process by deforming the tissues to assess the role of geometry. Both Yap localisation and Gata 6 levels responded to increasing exposed tissue surface, which raised further hypotheses about the upstream signalling components. I have tested the involvement of G-protein coupled receptors by using Dobutamine small molecule inhibitor, however there was no change in biological outcomes. I then proceeded to investigate the role of cytoskeleton, by using an actin polymerization inhibitor cytochalasin D and Myosin inhibitor blebbistatin, both of which interfered with normal actin distribution in the outer cells and caused Yap localisation to the cytoplasm. Blebbistatin treatment also resulted lower levels or endoderm differentiation and a significant loss of intra-tissue tension. This creates a strong argument, that the second cell fate decision is also

mechanically regulated, most likely involving actin cytoskeleton. However, the link between nuclear Yap localisation and Gata6 is still unclear, as even though the two components are strongly correlated, the relationship is not absolute.

Overall, the thesis looked at cell fate decisions, which involve a fundamental aspect of geometric regulation. Developing methodology, which allows to change tissue shape without chemical or genetic interference, made it possible to investigate cues, which can potentially sense tissue and cell shape during embryonic embryonic development. Most of the studies focused on the Hippo pathway, which not only defined the first cell fate decision, but also was involved during the subsequent cell differentiation event in geometrically dependent manner. Given the pre-existing information on Hippo pathway involvement in cancer and adult tissue development [135], the cascade is likely to be among the most universal tissue shape sensors.

The future work will involve making the software package available online in a form of a web application and also building a theoretical framework for calculating mechanical forces in more complex deformed tissues. Also, it will include looking at unanswered biological questions, such as the role of cell geometry in determining cell division angles and continue looking at biological mechanisms, which are responsible for sensing tissue geometry in mouse stem cell organoids.

References

[1] Tadanori Mammoto, Akiko Mammoto, and Donald E Ingber. Mechanobiology and developmental control. *Annual review of cell and developmental biology*, 29:27–61, oct 2013.

[2] Stefano Piccolo, Sirio Dupont, and Michelangelo Cordenonsi. The biology of YAP/TAZ: hippo signaling and beyond. *Physiological reviews*, 94(4), 2014.

[3] Tadanori Mammoto and Donald E Ingber. Mechanical control of tissue and organ development. *Development (Cambridge, England)*, 137(9):1407–20, may 2010.

[4] C S Chen, M Mrksich, S Huang, G M Whitesides, and D E Ingber. Geometric control of cell life and death. *Science*, 276(May), 1997.

[5] Brendon M Baker and Christopher S Chen. Deconstructing the third dimension: how 3D culture microenvironments alter cellular cues. *Journal of cell science*, 125(Pt 13):3015–24, jul 2012.

[6] Adam J Engler, Shamik Sen, H Lee Sweeney, and Dennis E Discher. Matrix elasticity directs stem cell lineage specification. *Cell*, 126(4):677–89, aug 2006.

[7] Jean-Léon Maître, Hélène Berthoumieux, Simon Frederik Gabriel Krens, Guillaume Salbreux, Frank Jülicher, Ewa Paluch, and Carl-Philipp Heisenberg. Adhesion functions in cell sorting by mechanically coupling the cortices of adhering cells. *Science (New York, N.Y.)*, 338(6104):253–6, oct 2012.

[8] Ramsey A. Foty and Malcolm S. Steinberg. The differential adhesion hypothesis: A direct evaluation. *Developmental Biology*, 278(1):255–263, 2005.

[9] Nicolas Desprat, Willy Supatto, Philippe-Alexandre Pouille, Emmanuel Beaurepaire, and Emmanuel Farge. Tissue deformation modulates twist expression to determine anterior midgut differentiation in Drosophila embryos. *Developmental cell*, 15(3):470–7, sep 2008.

[10] MaximE. Dokukin, NataliiaV. Guz, and Igor Sokolov. Quantitative Study of the Elastic Modulus of Loosely Attached Cells in AFM Indentation Experiments. *Biophysical Journal*, 104(10):2123–2131, may 2013.

[11] Zhan Li, Yuanwei Gong, Shujin Sun, Yu Du, Dongyuan Lü, Xiaofeng Liu, and Mian Long. Biomaterials Differential regulation of stiffness , topography , and dimension of substrates in rat mesenchymal stem cells. *Biomaterials*, 34, 2013.

[12] Ryuji Hiramatsu, Toshiki Matsuoka, Chiharu Kimura-Yoshida, Sung-Woong Han, Kyoko Mochida, Taiji Adachi, Shuichi Takayama, and Isao Matsuo. External mechanical cues trigger the establishment of the anterior-posterior axis in early mouse embryos. *Developmental cell*, 27(2):131–44, oct 2013.

[13] Benedikt Sabass, Margaret L M.L. Gardel, C.M. Clare M Waterman, and U.S. Ulrich S Schwarz. High resolution traction force microscopy based on experimental and computational advances. *Biophysical journal*, 94(1):207–220, 2008.

[14] Valentina Peschetola, Valérie M Laurent, Alain Duperray, Richard Michel, Davide Ambrosi, Luigi Preziosi, and Claude Verdier. Time-dependent traction force microscopy for cancer cells as a measure of invasiveness. *Cytoskeleton (Hoboken, N.J.)*, 214(April):201–214, feb 2013.

[15] Benoit Ladoux and Alice Nicolas. Physically based principles of cell adhesion mechanosensitivity in tissues. *Reports on progress in physics. Physical Society (Great Britain)*, 75(11):116601, nov 2012.

[16] Carlos Borau, Taeyoon Kim, Tamara Bidone, José Manuel García-Aznar, and Roger D. Kamm. Dynamic Mechanisms of Cell Rigidity Sensing: Insights from a Computational Model of Actomyosin Networks. *PLoS ONE*, 7(11), 2012.

[17] Sari Tojkander, Gergana Gateva, and Pekka Lappalainen. Actin stress fibers–assembly, dynamics and biological roles. *Journal of cell science*, 125(Pt 8):1855–64, apr 2012.

[18] Ulrich S Schwarz and Margaret L Gardel. United we stand: integrating the actin cytoskeleton and cell-matrix adhesions in cellular mechanotransduction. *Journal of cell science*, 125(Pt 13):3051–60, jul 2012.

[19] Ronen Zaidel-Bar. Job-splitting among integrins. *Nature cell biology*, 15(6):575–577, jun 2013.

[20] David W Dumbauld, Ted T Lee, Ankur Singh, Jan Scrimgeour, Charles A Gersbach, Evan A Zamir, Jianping Fu, Christopher S Chen, Jennifer E Curtis, and Susan W Craig. How vinculin regulates force transmission. *Proceedings of the National Academy of Sciences*, 110(24):9788–9793, 2013.

[21] Benoit Ladoux, Ester Anon, Mireille Lambert, Aleksandr Rabodzey, Pascal Hersen, Axel Buguin, Pascal Silberzan, and René-Marc Mège. Strength dependence of cadherin-mediated adhesions. *Biophysical journal*, 98(4):534–42, feb 2010.

[22] Boris Martinac. Mechanosensitive ion channels: molecules of mechanotransduction. *Journal of cell science*, 117(Pt 12):2449–2460, 2004.

[23] Soon-Mi Lim, Jerome P Trzeciakowski, Harini Sreenivasappa, Lawrence J Dangott, and Andreea Trache. RhoA-induced cytoskeletal tension controls adaptive cellular remodeling to mechanical signaling. *Integrative biology : quantitative biosciences from nano to macro*, 4(6):615–27, jun 2012.

[24] Nikhil Jain, K Venkatesan Iyer, Abhishek Kumar, and G V Shivashankar. Cell geometric constraints induce modular gene-expression patterns via redistribution of HDAC3 regulated by actomyosin contractility. *Proceedings of the National Academy of Sciences*, 110(28):3–8, 2013.

[25] Sirio Dupont, Leonardo Morsut, Mariaceleste Aragona, Elena Enzo, Stefano Giulitti, Michelangelo Cordenonsi, Francesca Zanconato, Jimmy Le Digabel, Mattia Forcato, Silvio Bicciato, Nicola Elvassore, and Stefano Piccolo. Role of YAP/TAZ in mechanotransduction. *Nature*, 474(7350):179–83, jun 2011.

[26] Paul a Janmey, Rebecca G Wells, Richard K Assoian, and Christopher a McCulloch. From tissue mechanics to transcription factors. *Differentiation; research in biological diversity*, pages 1–9, aug 2013.

[27] Hongwei Lv, Lisha Li, Meiyu Sun, Yin Zhang, Li Chen, Yue Rong, and Yulin Li. Mechanism of regulation of stem cell differentiation by matrix stiffness. *Stem cell research & therapy*, 6(1):103, 2015.

[28] Justin D Mih, Aleksandar Marinkovic, Fei Liu, Asma S Sharif, and Daniel J Tschumperlin. Matrix stiffness reverses the effect of actomyosin tension on cell proliferation. *Journal of cell science*, 125(Pt 24):5974–83, 2012.

[29] Sergey V. Plotnikov and Clare M. Waterman. Guiding cell migration by tugging. *Current Opinion in Cell Biology*, 25(5):619–626, 2013.

[30] Benjamin L. Bangasser and David J. Odde. Master equation-based analysis of a motor-clutch model for cell traction force. *Cellular and Molecular Bioengineering*, 6(4):449–459, 2013.

[31] Clarence E Chan and David J Odde. Traction dynamics of filopodia on compliant substrates. *Science (New York, N.Y.)*, 322(5908):1687–91, 2008.

[32] Seiichiro Ishihara, Motoaki Yasuda, Ichiro Harada, Takeomi Mizutani, Kazushige Kawabata, and Hisashi Haga. Substrate stiffness regulates temporary NF-κB activation via actomyosin contractions. *Experimental cell research*, pages 1–12, oct 2013.

[33] Mariaceleste Aragona, Tito Panciera, Andrea Manfrin, Stefano Giulitti, Federica Michielin, and Nicola Elvassore. A Mechanical Checkpoint Controls Multicellular Growth through YAP / TAZ Regulation by Actin-Processing Factors Mechanical Regulation of Cell Proliferation through. *Cell*, pages 1–13, 2013.

[34] Yu-Wei Chiou, Hsiu-Kuan Lin, Ming-Jer Tang, Hsi-Hui Lin, and Ming-Long Yeh. The influence of physical and physiological cues on atomic force microscopy-based cell stiffness assessment. *PloS one*, 8(10):e77384, jan 2013.

[35] Shirish Vichare, Mandar M. Inamdar, and Shamik Sen. Influence of cell spreading and contractility on stiffness measurements using AFM. *Soft Matter*, 8(40):10464, 2012.

[36] Anand Pillarisetti, Jaydev P Desai, Hamid Ladjal, Andrew Schiffmacher, Antoine Ferreira, and Carol L Keefer. Mechanical phenotyping of mouse embryonic stem cells: increase in stiffness with differentiation. *Cellular reprogramming*, 13(4):371–380, 2011.

[37] Adam Engler, Lucie Bacakova, Cynthia Newman, Alina Hategan, Maureen Griffin, and Dennis Discher. Substrate compliance versus ligand density in cell on gel responses. *Biophysical journal*, 86(1 Pt 1):617–28, jan 2004.

[38] Guillaume T Charras and Mike a Horton. Single cell mechanotransduction and its modulation analyzed by atomic force microscope indentation. *Biophysical journal*, 82(6):2970–81, jun 2002.

[39] Morteza Khalilian, Mahdi Navidbakhsh, Mojtaba Rezazadeh Valojerdi, Mahmoud Chizari, and Eftekhari Yazdi. Estimating Young ' s modulus of zona pellucida by micropipette aspiration in combination with theoretical models of ovum Estimating Young ' s modulus of zona pellucida by micropipette aspiration in combination with theoretical models of ovum. *J. R. Soc. Interface*, 7:687–694, 2010.

[40] Emad Moeendarbary, Léo Valon, Marco Fritzsche, Andrew R Harris, Dale a Moulding, Adrian J Thrasher, Eleanor Stride, L Mahadevan, and Guillaume T Charras. The cytoplasm of living cells behaves as a poroelastic material. *Nature materials*, 12(3):253–61, mar 2013.

[41] F Ziemann, J Rädler, and E Sackmann. Local measurements of viscoelastic moduli of entangled actin networks using an oscillating magnetic bead microrheometer. *Biophysical journal*, 66(6):2210–6, jun 1994.

[42] a R Bausch, W Möller, and E Sackmann. Measurement of local viscoelasticity and forces in living cells by magnetic tweezers. *Biophysical journal*, 76(1 Pt 1):573–9, jan 1999.

[43] Philip Kollmannsberger, Claudia Tanja Mierke, and Ben Fabry. Nonlinear viscoelasticity of adherent cells is controlled by cytoskeletal tension. *Soft Matter*, 7(7):3127, 2011.

[44] Hu Zhang and Kuo-Kang Liu. Optical tweezers for single cells. *Journal of The Royal Society Interface*, 5(24):671–690, 2008.

[45] Peyman Honarmandi, Hyungsuk Lee, Matthew J Lang, and Roger D Kamm. A microfluidic system with optical laser tweezers to study mechanotransduction and focal adhesion recruitment. *Lab on a chip*, 11(4):684–94, feb 2011.

[46] Kevin B Roth, Charles D Eggleton, Keith B Neeves, and David W M Marr. Measuring cell mechanics by optical alignment compression cytometry. *Lab on a chip*, 13(8):1571–7, apr 2013.

[47] Utkur Mirsaidov, Jan Scrimgeour, Winston Timp, Kaethe Beck, Mustafa Mir, Paul Matsudaira, and Gregory Timp. Live cell lithography: using optical tweezers to create synthetic tissue. *Lab on a chip*, 8(12):2174–81, dec 2008.

[48] Anna Linnenberger, Martha I Bodine, Callie Fiedler, Justine J Roberts, Stacey C Skaalure, Joseph P Quinn, Stephanie J Bryant, Michael Cole, Robert R McLeod, C D James, R Davis, M Meyer, A Turner, S Turner, G Withers, L Kam, G Banker, H Craighead, M Isaacson, J Turner, W Shain, D W Branch, B C Wheeler, G J Brewer, and D E Leckband. Three dimensional live cell lithography. *Biomed. Eng. J. Neurosci. Methods*, 47(1602):17–21, 2013.

[49] Justin K Valley, Paul Swinton, W John Boscardin, Tom F Lue, Paolo F Rinaudo, Ming C Wu, and Maurice M Garcia. Preimplantation mouse embryo selection guided by light-induced dielectrophoresis. *PloS one*, 5(4):e10160, jan 2010.

[50] Benjamin Landenberger, Henning Hofemann, Simon Wadle, and Alexander Rohrbach. Microfluidic sorting of arbitrary cells with dynamic optical tweezers. *Lab on a Chip*, 12(17):3177–3183, 2012.

[51] William J. Polacheck, Ran Li, Sebastien G. M. Uzel, and Roger D. Kamm. Microfluidic platforms for mechanobiology. *Lab on a Chip*, 13(12):2252, 2013.

[52] Sudhir Khetan, Murat Guvendiren, Wesley R Legant, Daniel M Cohen, Christopher S Chen, and Jason a Burdick. Degradation-mediated cellular traction directs stem cell fate in covalently crosslinked three-dimensional hydrogels. *Nature materials*, 12(5):1–8, mar 2013.

[53] N Q Balaban, U S Schwarz, D Riveline, P Goichberg, G Tzur, I Sabanay, D Mahalu, S Safran, a Bershadsky, L Addadi, and B Geiger. Force and focal adhesion assembly: a close relationship studied using elastic micropatterned substrates. *Nature cell biology*, 3(5):466–72, may 2001.

[54] Charlène Gayrard and Nicolas Borghi. FRET-based Molecular Tension Microscopy. *Methods*, 2015.

[55] Fanjie Meng and Frederick Sachs. Visualizing dynamic cytoplasmic forces with a compliance-matched FRET sensor. *Journal of Cell Science*, 124(Pt 2):261–269, 2011.

[56] Massimiliano Papi, Roberto Brunelli, Lakamy Sylla, Tiziana Parasassi, Maurizio Monaci, Giuseppe Maulucci, Mauro Missori, Giuseppe Arcovito, Fulvio Ursini, and Marco De Spirito. Mechanical properties of zona pellucida hardening. *European Biophysics Journal*, 39(6):987–992, 2010.

[57] Schanila Nawaz, Paula Sánchez, Kai Bodensiek, Sai Li, Mikael Simons, and Iwan A T Schaap. Cell Visco-Elasticity Measured with AFM and Optical Trapping at Sub-Micrometer Deformations. *PLoS ONE*, 7(9), 2012.

[58] R. D. Gonzalez-Cruz, V. C. Fonseca, and E. M. Darling. PNAS Plus: Cellular mechanical properties reflect the differentiation potential of adipose-derived

mesenchymal stem cells. *Proceedings of the National Academy of Sciences*, 109(24):E1523–E1529, 2012.

[59] Nikolay I. Nikolaev, Torsten M??ller, David J. Williams, and Yang Liu. Changes in the stiffness of human mesenchymal stem cells with the progress of cell death as measured by atomic force microscopy. *Journal of Biomechanics*, 47(3):625–630, 2014.

[60] Justin R Tse and Adam J Engler. Preparation of hydrogel substrates with tunable mechanical properties. *Current Protocols in Cell Biology*, Chapter 10(June):10.16, jun 2010.

[61] S. R. K. Vedula, M. C. Leong, T. L. Lai, P. Hersen, A. J. Kabla, C. T. Lim, and B. Ladoux. Emerging modes of collective cell migration induced by geometrical constraints. *Proceedings of the National Academy of Sciences*, 109(32):12974–12979, 2012.

[62] Stefano Piccolo, Michelangelo Cordenonsi, and Sirio Dupont. Molecular Pathways: YAP and TAZ Take the Centerstage in Organ Growth and Tumorigenesis. *Clinical cancer research : an official journal of the American Association for Cancer Research*, jul 2013.

[63] Eric N Olson and Alfred Nordheim. Linking actin dynamics and gene transcription to drive cellular motile functions. *Nature reviews. Molecular cell biology*, 11(5):353–65, may 2010.

[64] Francesc Miralles, Guido Posern, Alexia-ileana Zaromytidou, and Richard Treisman. Actin Dynamics Control SRF Activity by Regulation of Its Coactivator MAL. *Cell*, 113:329–342, 2003.

[65] Chih-Chao Yang, Hillary K. Graves, Ivan M. Moya, Chunyao Tao, Fisun Hamaratoglu, Andrew B. Gladden, and Georg Halder. Differential regulation of the

Hippo pathway by adherens junctions and apical-basal cell polarity modules. *Proceedings of the National Academy of Sciences*, 112(6):201420850, jan 2015.

[66] Chiao-lin Chen. Cell Polarity Regulates Organ Growth Through the Hippo Pathway. *Scanning Electron Microscopy*, 2011.

[67] Christophe Royer, Sofia Koch, Xiao Qin, Jaroslav Zak, Ludovico Buti, Ewa Dudziec, Shan Zhong, Indrika Ratnayaka, Shankar Srinivas, and Xin Lu. ASPP2 links the apical lateral polarity complex to the regulation of YAP activity in epithelial cells. *PLoS ONE*, 9(10):14–17, 2014.

[68] Gail Doughton, Jun Wei, Nicolas Tapon, Melanie J. Welham, and Andrew D. Chalmers. Formation of a polarised primitive endoderm layer in embryoid bodies requires Fgfr/Erk signalling. *PLoS ONE*, 9(4), 2014.

[69] Hynda K. Kleinman and George R. Martin. Matrigel: Basement membrane matrix with biological activity. *Seminars in Cancer Biology*, 15(5 SPEC. ISS.):378–386, 2005.

[70] Gabriel Benton, Hynda K. Kleinman, Jay George, and Irina Arnaoutova. Multiple uses of basement membrane-like matrix (BME/Matrigel) in vitro and in vivo with cancer cells. *International Journal of Cancer*, 128(8):1751–1757, 2011.

[71] Yoshiki Sasai. Cytosystems dynamics in self-organization of tissue architecture. *Nature*, 493(7432):318–26, jan 2013.

[72] Sabrina Schlie-Wolter, Anaclet Ngezahayo, and Boris N Chichkov. The selective role of ECM components on cell adhesion, morphology, proliferation and communication in vitro. *Experimental cell research*, pages 1–9, apr 2013.

[73] M Deforet, V Hakim, H G Yevick, G Duclos, and P Silberzan. Emergence of collective modes and tri-dimensional structures from epithelial confinement. *Nature communications*, 5(May):3747, jan 2014.

[74] Sebastian J Streichan, Christian R Hoerner, Tatjana Schneidt, Daniela Holzer, and Lars Hufnagel. Spatial constraints control cell proliferation in tissues. *Proceedings of the National Academy of Sciences of the United States of America*, 111(15):5586–91, may 2014.

[75] Monica A. Serban, Yanchun Liu, and Glenn D. Prestwich. Effects of extracellular matrix analogues on primary human fibroblast behavior. *Acta Biomaterialia*, 4(1):67–75, 2008.

[76] Chad D Markert, Xinyi Guo, Aleksander Skardal, Zhan Wang, Shantaram Bharadwaj, Yuanyuan Zhang, Keith Bonin, and Martin Guthold. Characterizing the micro-scale elastic modulus of hydrogels for use in regenerative medicine. *Journal of the Mechanical Behavior of Biomedical Materials*, pages 1–13, 2013.

[77] Prathamesh M Kharkar, Kristi L Kiick, and April M Kloxin. Designing degradable hydrogels for orthogonal control of cell microenvironments. *Chemical Society reviews*, 42(17):7335–72, sep 2013.

[78] Alireza Rezania, Jennifer E Bruin, Payal Arora, Allison Rubin, Irina Batushansky, Ali Asadi, Shannon O'Dwyer, Nina Quiskamp, Majid Mojibian, Tobias Albrecht, Yu Hsuan Carol Yang, James D Johnson, and Timothy J Kieffer. Reversal of diabetes with insulin-producing cells derived in vitro from human pluripotent stem cells. *Nature Biotechnology*, 32(11):1121–1134, sep 2014.

[79] W E Hennink and C F van Nostrum. Novel crosslinking methods to design hydrogels. *Advanced drug delivery reviews*, 54(1):13–36, jan 2002.

[80] Carole E. Schanté, Guy Zuber, Corinne Herlin, and Thierry F. Vandamme. Chemical modifications of hyaluronic acid for the synthesis of derivatives for a broad range of biomedical applications. *Carbohydrate Polymers*, 85(3):469–489, jun 2011.

[81] Shawn C Owen, Stephanie A Fisher, Roger Y Tam, Chelsea M Nimmo, and Molly S Shoichet. Hyaluronic Acid Click Hydrogels Emulate the Extracellular Matrix. *Langmuir*, 29:7393?7400, 2013.

[82] Huaxing Zhou, Jiyeon Woo, Alexandra M Cok, Muzhou Wang, Bradley D Olsen, and Jeremiah a Johnson. Counting primary loops in polymer gels. *Proceedings of the National Academy of Sciences of the United States of America*, 109(47):19119–24, nov 2012.

[83] William M Gramlich, Iris L Kim, and Jason a Burdick. Synthesis and orthogonal photopatterning of hyaluronic acid hydrogels with thiol-norbornene chemistry. *Biomaterials*, 34(38):9803–11, dec 2013.

[84] Cong Zhang, Michael J Large, Raj Duggavathi, Francesco J Demayo, John P Lydon, Kristina Schoonjans, Ertug Kovanci, and Bruce D Murphy. Liver receptor homolog-1 is essential for pregnancy. *Nature medicine*, 19(8):1061–6, aug 2013.

[85] Max C Darnell, Jeong-Yun Sun, Manav Mehta, Christopher Johnson, Praveen R Arany, Zhigang Suo, and David J Mooney. Performance and biocompatibility of extremely tough alginate/polyacrylamide hydrogels. *Biomaterials*, 34(33):8042–8, nov 2013.

[86] Aleksandr Ovsianikov, Severin Mühleder, Jan Torgersen, Zhiquan Li, Xiao-Hua Qin, Sandra Van Vlierberghe, Peter Dubruel, Wolfgang Holnthoner, Heinz Redl, Robert Liska, and Jürgen Stampfl. Laser photofabrication of cell-containing

hydrogel constructs. *Langmuir : the ACS journal of surfaces and colloids*, 30(13):3787–94, apr 2014.

[87] Pranav Soman, Peter H Chung, a Ping Zhang, and Shaochen Chen. Digital microfabrication of user-defined 3D microstructures in cell-laden hydrogels. *Biotechnology and bioengineering*, 110(11):3038–47, nov 2013.

[88] David B Kolesky, Ryan L Truby, a Sydney Gladman, Travis a Busbee, Kimberly a Homan, and Jennifer a Lewis. 3D bioprinting of vascularized, heterogeneous cell-laden tissue constructs. *Advanced materials (Deerfield Beach, Fla.)*, 26(19):3124–30, may 2014.

[89] Thomas Billiet, Elien Gevaert, Thomas De Schryver, Maria Cornelissen, and Peter Dubruel. The 3D printing of gelatin methacrylamide cell-laden tissue-engineered constructs with high cell viability. *Biomaterials*, 35(1):49–62, jan 2014.

[90] Kan Yue, Grissel Trujillo-De Santiago, Mario Mois Es Alvarez, Ali Tamayol, Nasim Annabi, and Ali Khademhosseini. Synthesis, properties, and biomedical applications of gelatin methacryloyl (GelMA) hydrogels. *Biomaterials*, 73:254–271, 2015.

[91] Catherine a Goubko, Ajoy Basak, Swapan Majumdar, and Xudong Cao. Dynamic cell patterning of photoresponsive hyaluronic acid hydrogels. *Journal of biomedical materials research. Part A*, pages 1–11, mar 2013.

[92] Marina Diolos, Ivan Donati, Gianluca Turco, Milena Cadenaro, Roberto Di Lenarda, Lorenzo Breschi, and Sergio Paoletti. Use of methacrylate-modified chitosan to increase the durability of dentine bonding systems. *Biomacromolecules*, 15(12):4606–4613, 2014.

[93] Ilse De Paepe, Heidi Declercq, Maria Cornelissen, and Etienne Schacht. Novel hydrogels based on methacrylate-modified agarose. *Polymer International*, 51(10):867–870, 2002.

[94] Oju Jeon and Eben Alsberg. Regulation of Stem Cell Fate in a Three-Dimensional Micropatterned Dual-Crosslinked Hydrogel System. *Advanced Functional Materials*, page 4765?4775, apr 2013.

[95] Narendra Reddy, Qiuran Jiang, Enqi Jin, Zhen Shi, Xiuliang Hou, and Yiqi Yang. Bio-thermoplastics from grafted chicken feathers for potential biomedical applications. *Colloids and surfaces. B, Biointerfaces*, 110C:51–58, apr 2013.

[96] Jason W Nichol, Sandeep T Koshy, Hojae Bae, Chang M Hwang, Seda Yamanlar, and Ali Khademhosseini. Cell-laden microengineered gelatin methacrylate hydrogels. *Biomaterials*, 31(21):5536–44, jul 2010.

[97] Ruei-Zeng Lin, Ying-Chieh Chen, Rafael Moreno-Luna, Ali Khademhosseini, and Juan M Melero-Martin. Transdermal regulation of vascular network bioengineering using aphotopolymerizable methacrylated gelatin hydrogel. *Biomaterials*, 34(28):6785–6796, jun 2013.

[98] Jason a Burdick, Cindy Chung, Xinqiao Jia, Mark a Randolph, and Robert Langer. Controlled degradation and mechanical behavior of photopolymerized hyaluronic acid networks. *Biomacromolecules*, 6(1):386–91, 2005.

[99] Guoyou Huang, Lin Wang, Shuqi Wang, Yulong Han, Jinhui Wu, Qiancheng Zhang, Feng Xu, and Tian Jian Lu. Engineering three-dimensional cell mechanical microenvironment with hydrogels. *Biofabrication*, 4, 2012.

[100] Melissa A. Kinney, Tracy A. Hookway, Yun Wang, and Todd C. McDevitt. Engineering three-dimensional stem cell morphogenesis for the development of

tissue models and scalable regenerative therapeutics. *Annals of Biomedical Engineering*, 42(2):352–367, 2014.

[101] Jordan S Miller, Kelly R Stevens, Michael T Yang, Brendon M Baker, Duc-Huy T Nguyen, Daniel M Cohen, Esteban Toro, Alice a Chen, Peter a Galie, Xiang Yu, Ritika Chaturvedi, Sangeeta N Bhatia, and Christopher S Chen. Rapid casting of patterned vascular networks for perfusable engineered three-dimensional tissues. *Nature materials*, 11(9):768–74, sep 2012.

[102] Xingnan Li, Lincoln Nadauld, Akifumi Ootani, David C Corney, Reetesh K Pai, Olivier Gevaert, Michael a Cantrell, Paul G Rack, James T Neal, Carol W-M Chan, Trevor Yeung, Xue Gong, Jenny Yuan, Julie Wilhelmy, Sylvie Robine, Laura D Attardi, Sylvia K Plevritis, Kenneth E Hung, Chang-Zheng Chen, Hanlee P Ji, and Calvin J Kuo. Oncogenic transformation of diverse gastrointestinal tissues in primary organoid culture. *Nature medicine*, 20(7):769–77, jul 2014.

[103] Pranav Soman, Peter H Chung, a Ping Zhang, and Shaochen Chen. Digital microfabrication of user-defined 3D microstructures in cell-laden hydrogels. *Biotechnology and bioengineering*, 110(11):3038–47, nov 2013.

[104] Julia Dahlmann, George Kensah, Henning Kempf, David Skvorc, Anke Gawol, David a. Elliott, Gerald Dräger, Robert Zweigerdt, Ulrich Martin, and Ina Gruh. The use of agarose microwells for scalable embryoid body formation and cardiac differentiation of human and murine pluripotent stem cells. *Biomaterials*, 34(10):2463–2471, 2013.

[105] Marissa T Cooke and Todd C Mcdevitt. Magnetic manipulation and spatial patterning of multi-cellular stem cell aggregates. *Integrative Biology*, pages 1224–1232, 2011.

[106] K R Stevens, M D Ungrin, R E Schwartz, S Ng, B Carvalho, K S Christine, R R Chaturvedi, C Y Li, P W Zandstra, C S Chen, and S N Bhatia. InVERT molding for scalable control of tissue microarchitecture. *Nature communications*, 4(May):1847, jan 2013.

[107] Zhen Ma, Jason Wang, Peter Loskill, Nathaniel Huebsch, Sangmo Koo, Felicia L. Svedlund, Natalie C. Marks, Ethan W. Hua, Costas P. Grigoropoulos, Bruce R. Conklin, and Kevin E. Healy. Self-organizing human cardiac microchambers mediated by geometric confinement. *Nature Communications*, 6(May):7413, 2015.

[108] Christian Franck, Stacey a Maskarinec, David a Tirrell, and Guruswami Ravichandran. Three-dimensional traction force microscopy: a new tool for quantifying cell-matrix interactions. *PloS one*, 6(3):e17833, jan 2011.

[109] Olivia du Roure, Alexandre Saez, Axel Buguin, Robert H Austin, Philippe Chavrier, Pascal Silberzan, Pascal Siberzan, and Benoit Ladoux. Force mapping in epithelial cell migration. *Proceedings of the National Academy of Sciences of the United States of America*, 102(7):2390–5, feb 2005.

[110] Otger Campàs, Tadanori Mammoto, Sean Hasso, Ralph a Sperling, Daniel O'Connell, Ashley G Bischof, Richard Maas, David a Weitz, L Mahadevan, and Donald E Ingber. Quantifying cell-generated mechanical forces within living embryonic tissues. *Nature methods*, 11(2):183–9, feb 2014.

[111] J a Williams and R S Dwyer-Joyce. Contact Between Solid Surfaces. *Modern Tribology Handbook*, 1:121–162, 2001.

[112] Rong Long, Matthew S. Hall, Mingming Wu, and Chung Yuen Hui. Effects of gel thickness on microscopic indentation measurements of gel modulus. *Biophysical Journal*, 101(3):643–650, 2011.

[113] Jiaping Zhang, Xuanhe Zhao, Zhigang Suo, and Hanqing Jiang. A finite element method for transient analysis of concurrent large deformation and mass transport in gels. *Journal of Applied Physics*, 105(9), 2009.

[114] Takanori Takebe, Masahiro Enomura, Emi Yoshizawa, Masaki Kimura, Hiroyuki Koike, Yasuharu Ueno, Takahisa Matsuzaki, Takashi Yamazaki, Takafumi Toyohara, Kenji Osafune, Hiromitsu Nakauchi, Hiroshi Y. Yoshikawa, and Hideki Taniguchi. Vascularized and complex organ buds from diverse tissues via mesenchymal cell-driven condensation. *Cell Stem Cell*, 16(5):556–565, 2015.

[115] Tokushige Nakano, Satoshi Ando, Nozomu Takata, Masako Kawada, Keiko Muguruma, Kiyotoshi Sekiguchi, Koichi Saito, Shigenobu Yonemura, Mototsugu Eiraku, and Yoshiki Sasai. Self-formation of optic cups and storable stratified neural retina from human ESCs. *Cell Stem Cell*, 10(6):771–785, 2012.

[116] Sanjay Kumar and Valerie M. Weaver. Mechanics, malignancy, and metastasis: The force journey of a tumor cell. *Cancer and Metastasis Reviews*, 28(1-2):113–127, 2009.

[117] Paul J. Wrighton and Laura L. Kiessling. Forces of change: Mechanics underlying formation of functional 3D organ buds. *Cell Stem Cell*, 16(5):453–454, 2015.

[118] F M Manejwala, E J Cragoe, and R M Schultz. Blastocoel expansion in the preimplantation mouse embryo: role of extracellular sodium and chloride and possible apical routes of their entry. *Developmental biology*, 133(1):210–20, 1989.

[119] Francesco Antonica, Dominika Figini Kasprzyk, Robert Opitz, Michelina Iacovino, Xiao-Hui Liao, Alexandra Mihaela Dumitrescu, Samuel Refetoff, Kathelijne Peremans, Mario Manto, Michael Kyba, and Sabine Costagliola. Genera-

tion of functional thyroid from embryonic stem cells. *Nature*, 490(7422):66–71, 2012.

[120] Shankar Srinivas, Tristan Rodriguez, Melanie Clements, James C Smith, and Rosa S P Beddington. Active cell migration drives the unilateral movements of the anterior visceral endoderm. *Development (Cambridge, England)*, 131:1157–1164, 2004.

[121] Shiro Yui, Tetsuya Nakamura, Toshiro Sato, Yasuhiro Nemoto, Tomohiro Mizutani, Xiu Zheng, Shizuko Ichinose, Takashi Nagaishi, Ryuichi Okamoto, Kiichiro Tsuchiya, Hans Clevers, and Mamoru Watanabe. Functional engraftment of colon epithelium expanded in vitro from a single adult Lgr5 stem cell. *Nature medicine*, 18(4):618–23, 2012.

[122] Hongmei Yu, Janna Kay Mouw, and Valerie M Weaver. Forcing form and function: biomechanical regulation of tumor evolution. *Trends in cell biology*, 21(1):47–56, jan 2011.

[123] Liying Yan, Mingyu Yang, Hongshan Guo, Lu Yang, Jun Wu, Rong Li, Ping Liu, Ying Lian, Xiaoying Zheng, Jie Yan, Jin Huang, Ming Li, Xinglong Wu, Lu Wen, Kaiqin Lao, Ruiqiang Li, Jie Qiao, and Fuchou Tang. Single-cell RNA-Seq profiling of human preimplantation embryos and embryonic stem cells. *Nature structural & molecular biology*, 20(9):1131–9, sep 2013.

[124] J N Wilcox. Fundamental principles of in situ hybridization. *The journal of histochemistry and cytochemistry*, 41(12):1725–1733, 1993.

[125] A E Smits-van Prooije, R E Poelmann, A F Gesink, M J Van Groeningen, and Chr Vermeij-keers. The cell surface coat in neurulating mouse and rat embryos , studied with lectins. *Anatomy and Embryology*, 175:111–117, 1986.

[126] Periklis Pantazis and Willy Supatto. Advances in whole-embryo imaging: a quantitative transition is underway. *Nature reviews. Molecular cell biology*, 15(5):327–39, 2014.

[127] Kishore R. Mosaliganti, Ramil R. Noche, Fengzhu Xiong, Ian A. Swinburne, and Sean G. Megason. ACME: Automated Cell Morphology Extractor for Comprehensive Reconstruction of Cell Membranes. *PLoS Computational Biology*, 8(12), 2012.

[128] Fraunhofer Itwm. Survey of 3d image segmentation methods. *Keywords image processing 3d image segmentation binarization*, 123(123):Kaiserslautern, Germany, 2007.

[129] Johannes Stegmaier, Fernando Amat, William C Lemon, George Teodoro, Ralf Mikut, Philipp J Keller, Johannes Stegmaier, Fernando Amat, William C Lemon, Katie Mcdole, Yinan Wan, George Teodoro, and Ralf Mikut. Real-Time Three-Dimensional Cell Segmentation in Large-Scale Microscopy Data of Developing Technology Real-Time Three-Dimensional Cell Segmentation in Large-Scale Microscopy Data of Developing Embryos. *Developmental Cell*, 36(2):225–240, 2016.

[130] Xinghua Lou, Minjung Kang, Panagiotis Xenopoulos, Silvia Muñoz-Descalzo, and Anna Katerina Hadjantonakis. A rapid and efficient 2D/3D nuclear segmentation method for analysis of early mouse embryo and stem cell image data. *Stem Cell Reports*, 2(3):382–397, 2014.

[131] J Illingworth and J Kittler. The adaptive hough transform. *IEEE transactions on pattern analysis and machine intelligence*, 9(5):690–698, 1987.

[132] Johannes Schindelin, Ignacio Arganda-Carreras, Erwin Frise, Kaynig Verena, Mark Longair, Tobias Pietzsch, Preibisch Stephan, Kevin Eliceiri, Pavel Toman-

cak, and Albert Cardona. Fiji: an open-source platform for biological-image analysis. *Nature methods*, 9(7):676, 2012.

[133] Yan Huang, Stella Onyeri, Mbonda Siewe, Aliakbar Moshfeghian, and Sundararajan V Madihally. In vitro characterization of chitosan-gelatin scaffolds for tissue engineering. *Biomaterials*, 26(36):7616–27, dec 2005.

[134] Duojia Pan. Hippo signaling in organ size control. *Genes & development*, 21:886–897, 2007.

[135] Fa-xing Yu and Kun-liang Guan. The Hippo pathway : regulators and regulations. *Genes & development*, 27:355–371, 2013.

[136] Young Kwon, Arunachalam Vinayagam, Xiaoyun Sun, Noah Dephoure, Steven P Gygi, Pengyu Hong, and Norbert Perrimon. The Hippo Signaling Pathway Interactome. *Science (New York, N.Y.)*, 737, oct 2013.

[137] a. L. Couzens, J. D. R. Knight, M. J. Kean, G. Teo, a. Weiss, W. H. Dunham, Z.-Y. Lin, R. D. Bagshaw, F. Sicheri, T. Pawson, J. L. Wrana, H. Choi, and a. C. Gingras. Protein Interaction Network of the Mammalian Hippo Pathway Reveals Mechanisms of Kinase-Phosphatase Interactions. *Science Signaling*, 6(302):rs15–rs15, nov 2013.

[138] Ilenia Bernascone and Fernando Martin-Belmonte. Crossroads of Wnt and Hippo in epithelial tissues. *Trends in cell biology*, 23(8):380–9, aug 2013.

[139] Jing Cai, Nailing Zhang, Yonggang Zheng, Roeland F. De Wilde, Anirban Maitra, and Duojia Pan. The Hippo signaling pathway restricts the oncogenic potential of an intestinal regeneration program. *Genes and Development*, 24(21):2383–2388, 2010.

[140] Noriyuki Nishioka, Shinji Yamamoto, Hiroshi Kiyonari, Hiroko Sato, Atsushi Sawada, Mitsunori Ota, Kazuki Nakao, and Hiroshi Sasaki. Tead4 is required for specification of trophectoderm in pre-implantation mouse embryos. *Mechanisms of development*, 125(3-4):270–83, 2007.

[141] Noriyuki Nishioka, Ken-ichi Inoue, Kenjiro Adachi, Hiroshi Kiyonari, Mitsunori Ota, Amy Ralston, Norikazu Yabuta, Shino Hirahara, Robert O Stephenson, Narumi Ogonuki, Ryosuke Makita, Hiroki Kurihara, Elizabeth M Morin-Kensicki, Hiroshi Nojima, Janet Rossant, Kazuki Nakao, Hitoshi Niwa, and Hiroshi Sasaki. The Hippo signaling pathway components Lats and Yap pattern Tead4 activity to distinguish mouse trophectoderm from inner cell mass. *Developmental cell*, 16(3):398–410, mar 2009.

[142] B. Saha, P. Home, and S. Paul. Reply to Sasaki et al.: TEAD4 is predominantly cytoplasmic in the inner cell mass of mouse blastocysts. *Proceedings of the National Academy of Sciences*, 109(50):E3391–E3392, nov 2012.

[143] Randy Johnson and Georg Halder. The two faces of Hippo: targeting the Hippo pathway for regenerative medicine and cancer treatment. *Nature reviews. Drug discovery*, 13(1):63–79, jan 2014.

[144] Chuen Yan Leung and Magdalena Zernicka-Goetz. Angiomotin prevents pluripotent lineage differentiation in mouse embryos via Hippo pathway-dependent and -independent mechanisms. *Nature communications*, 4:2251, jan 2013.

[145] Hideki Murakami, Tetsuya Mizuno, Tetsuo Taniguchi, Makiko Fujii, Futoshi Ishiguro, Takayuki Fukui, Shinya Akatsuka, Yoshitsugu Horio, Toyoaki Hida, Yutaka Kondo, Shinya Toyokuni, Hirotaka Osada, and Yoshitaka Sekido.

LATS2 is a tumor suppressor gene of malignant mesothelioma. *Cancer Research*, 71(3):873–883, 2011.

[146] Ling Xiao, Yuanhong Chen, Ming Ji, and Jixin Dong. KIBRA regulates hippo signaling activity via interactions with large tumor suppressor kinases. *Journal of Biological Chemistry*, 286(10):7788–7796, 2011.

[147] Bin Zhao, Li Li, Qing Lu, Lloyd H Wang, Chen-Ying Liu, Qunying Lei, and Kun-Liang Guan. Angiomotin is a novel Hippo pathway component that inhibits YAP oncoprotein. *Genes & development*, 25(1):51–63, jan 2011.

[148] Xiaoming Dai, Peilu She, Fangtao Chi, Huan Liu, Daqing Jin, Yiqiang Zhao, Xiaocan Guo, Dandan Jiang, Tao P Zhong, Bin Zhao, Ying Feng, Huan Liu, Daqing Jin, Yiqiang Zhao, Xiaocan Guo, Dandan Jiang, Kun-Liang Guan, Tao P Zhong, and Bin Zhao. Phosphorylation of Angiomotin by Lats1/2 Kinases Inhibits F-actin Binding, Cell Migration, and Angiogenesis. *The Journal of biological chemistry*, 288(47):34041–51, nov 2013.

[149] Yoshikazu Hirate, Shino Hirahara, Ken-ichi Inoue, Atsushi Suzuki, Vernadeth B Alarcon, Kazunori Akimoto, Takaaki Hirai, Takeshi Hara, Makoto Adachi, Kazuhiro Chida, Shigeo Ohno, Yusuke Marikawa, Kazuki Nakao, and Akihiko Shimono. Polarity-Dependent Distribution of Angiomotin Localizes Hippo Signaling in Preimplantation Embryos. *Current Biology*, 23(13):1181–1194, 2013.

[150] Julian C. Boggiano, Pamela J. Vanderzalm, and Richard G. Fehon. Tao-1 phosphorylates Hippo/MST kinases to regulate the Hippo-Salvador-Warts tumor suppressor pathway. *Developmental Cell*, 21(5):888–895, 2011.

[151] Carole L C Poon, Jane I. Lin, Xiaomeng Zhang, and Kieran F. Harvey. The sterile 20-like kinase Tao-1 controls tissue growth by regulating the Salvador-Warts-Hippo pathway. *Developmental Cell*, 21(5):896–906, 2011.

[152] Paulo S. Ribeiro, Filipe Josu, Alexander Wepf, Michael C. Wehr, Oliver Rinner, Gavin Kelly, Nicolas Tapon, and Matthias Gstaiger. Combined Functional Genomic and Proteomic Approaches Identify a PP2A Complex as a Negative Regulator of Hippo Signaling. *Molecular Cell*, 39(4):521–534, 2010.

[153] Morvarid Mohseni, Jianlong Sun, Allison Lau, Stephen Curtis, Jeffrey Goldsmith, Victor L Fox, Chongjuan Wei, Marsha Frazier, Owen Samson, Kwok-Kin Wong, Kwok-Kim Wong, Carla Kim, and Fernando D Camargo. A genetic screen identifies an LKB1-MARK signalling axis controlling the Hippo-YAP pathway. *Nature cell biology*, 16(1):108–17, jan 2014.

[154] C.-L. Chen, M. C. Schroeder, M. Kango-Singh, C. Tao, and G. Halder. Tumor suppression by cell competition through regulation of the Hippo pathway. *Proceedings of the National Academy of Sciences*, 109(2):484–489, 2012.

[155] Min Zhao, Przemyslaw Szafranski, Chad Albert Hall, and Scott Goode. Basolateral junctions utilize warts signaling to control epithelial-mesenchymal transition and proliferation crucial for migration and invasion of drosophila ovarian epithelial cells. *Genetics*, 178(4):1947–1971, 2008.

[156] Meghna Das Thakur, Yunfeng Feng, Radhika Jagannathan, Midori J. Seppa, James B. Skeath, and Gregory D. Longmore. Ajuba LIM Proteins Are Negative Regulators of the Hippo Signaling Pathway. *Current Biology*, 20(7):657–662, 2010.

[157] Jinchen Sun, Chao Xiao, Huaping Tan, and Xiaohong Hu. Covalently crosslinked hyaluronic acid-chitosan hydrogel containing dexamethasone as an injectable scaffold for soft tissue engineering. *Journal of Applied Polymer Science*, 129(2):682–688, jul 2013.

[158] Cordelia Rauskolb, Guohui Pan, B. V V G Reddy, Hyangyee Oh, and Kenneth D. Irvine. Zyxin links fat signaling to the hippo pathway. *PLoS Biology*, 9(6), 2011.

[159] Karin Schlegelmilch, Morvarid Mohseni, Oktay Kirak, Jan Pruszak, J. Renato Rodriguez, Dawang Zhou, Bridget T. Kreger, Valera Vasioukhin, Joseph Avruch, Thijn R. Brummelkamp, and Fernando D. Camargo. Yap1 acts downstream of alpha-catenin to control epidermal proliferation. *Cell*, 144(5):782–795, 2011.

[160] Nam-Gyun Kim, Eunjin Koh, Xiao Chen, and Barry M Gumbiner. E-cadherin mediates contact inhibition of proliferation through Hippo signaling-pathway components. *Proceedings of the National Academy of Sciences of the United States of America*, 108(29):11930–11935, 2011.

[161] Elsa R Flores and Georg Halder. Stem cell proliferation in the skin: alpha-catenin takes over the hippo pathway. *Science signaling*, 4(183):pe34, 2011.

[162] Chen Ying Liu, Xianbo Lv, Tingting Li, Yanping Xu, Xin Zhou, Shimin Zhao, Yue Xiong, Qun Ying Lei, and Kun Liang Guan. PP1 cooperates with ASPP2 to dephosphorylate and activate TAZ. *Journal of Biological Chemistry*, 286(7):5558–5566, 2011.

[163] Brian S. Robinson, Juang Huang, Yang Hong, and Kenneth H. Moberg. Crumbs Regulates Salvador/Warts/Hippo Signaling in Drosophila via the FERM-Domain Protein Expanded. *Current Biology*, 20(7):582–590, 2010.

[164] Katie Cockburn, Steffen Biechele, Jodi Garner, and Janet Rossant. The hippo pathway member nf2 is required for inner cell mass specification. *Current Biology*, 23(13):1195–1201, 2013.

[165] Andrew Archibald, Maia Al-Masri, Alyson Liew-Spilger, and Luke McCaffrey. Atypical protein kinase C induces cell transformation by disrupting Hippo/Yap signaling. *Molecular biology of the cell*, pages 1–39, 2015.

[166] Vernadeth B Alarcon. Cell polarity regulator PARD6B is essential for trophectoderm formation in the preimplantation mouse embryo. *Biology of reproduction*, 83(3):347–58, sep 2010.

[167] Ken-Ichi Wada, Kazuyoshi Itoga, Teruo Okano, Shigenobu Yonemura, and Hiroshi Sasaki. Hippo pathway regulation by cell morphology and stress fibers. *Development (Cambridge, England)*, 138(18):3907–14, oct 2011.

[168] Janet Rossant and Patrick P L Tam. Blastocyst lineage formation, early embryonic asymmetries and axis patterning in the mouse. *Development Cambridge England*, 136(5):701–13, 2009.

[169] Hiroaki Nagatomo, Shinjiro Kagawa, Yasunori Kishi, Tetsuya Takuma, Ayari Sada, Ken-Ichi Yamanaka, Yasuyuki Abe, Yasuhiko Wada, Masashi Takahashi, Tomohiro Kono, and Manabu Kawahara. Transcriptional wiring for establishing cell lineage specification at the blastocyst stage in cattle. *Biology of reproduction*, 88(6):158, jun 2013.

[170] Fredrik Lanner. Lineage specification in the early mouse embryo. *Experimental cell research*, 321(1):32–9, feb 2014.

[171] By M Susan Stern. Experimental studies on the organization of the preimplantation mouse embryo. *J. Embryol. exp. Morph.*, 28(1970):255–261, 1972.

[172] Gordon C Douglas, Catherine a VandeVoort, Priyadarsini Kumar, Tien-Cheng Chang, and Thaddeus G Golos. Trophoblast stem cells: models for investigating trophectoderm differentiation and placental development. *Endocrine reviews*, 30(3):228–40, may 2009.

[173] Vernadeth B Alarcón and Yusuke Marikawa. Molecular study of mouse peri-implantation development using the in vitro culture of aggregated inner cell mass. *Molecular reproduction and development*, 67(1):83–90, jan 2004.

[174] Thorsten Boroviak, Remco Loos, Paul Bertone, Austin Smith, and Jennifer Nichols. The ability of inner-cell-mass cells to self-renew as embryonic stem cells is acquired following epiblast specification. *Nature cell biology*, 16(6), 2014.

[175] Kazutoshi Takahashi, Koji Tanabe, Mari Ohnuki, Megumi Narita, Tomoko Ichisaka, Kiichiro Tomoda, and Shinya Yamanaka. Induction of Pluripotent Stem Cells from Adult Human Fibroblasts by Defined Factors. *Cell*, 131(5):861–872, 2007.

[176] Kazutoshi Takahashi and Shinya Yamanaka. Induction of Pluripotent Stem Cells from Mouse Embryonic and Adult Fibroblast Cultures by Defined Factors. *Cell*, 126(4):663–676, 2006.

[177] Qiaolin Deng, Daniel Ramsköld, Björn Reinius, and Rickard Sandberg. Single-cell RNA-seq reveals dynamic, random monoallelic gene expression in mammalian cells. *Science (New York, N.Y.)*, 343(6167):193–6, jan 2014.

[178] Alexei A Sharov, Yulan Piao, Ryo Matoba, Dawood B Dudekula, Yong Qian, Vincent Vanburen, Geppino Falco, Patrick R Martin, Carole A Stagg, Uwem C Bassey, Yuxia Wang, Mark G Carter, Toshio Hamatani, Kazuhiro Aiba, Hidenori Akutsu, Lioudmila Sharova, Tetsuya S Tanaka, Wendy L Kimber, Toshiyuki Yoshikawa, Saied A Jaradat, Serafino Pantano, Ramaiah Nagaraja, Kenneth R Boheler, Dennis Taub, Richard J Hodes, Dan L Longo, David Schlessinger, Jonathan Keller, Emily Klotz, Garnett Kelsoe, Akihiro Umezawa, Angelo L Vescovi, Janet Rossant, Tilo Kunath, Brigid L M Hogan, Anna Curci,

Michele D Urso, Janet Kelso, Winston Hide, and Minoru S H Ko. Transcriptome Analysis of Mouse Stem Cells and Early Embryos. *PLoS Biology*, 1(3), 2003.

[179] Zhigang Xue, Kevin Huang, Chaochao Cai, Lingbo Cai, Chun-yan Jiang, Yun Feng, Zhenshan Liu, Qiao Zeng, Liming Cheng, Yi E Sun, Jia-yin Liu, Steve Horvath, and Guoping Fan. Genetic programs in human and mouse early embryos revealed by single-cell RNA sequencing. *Nature*, 500(7464):593–7, aug 2013.

[180] Yusuke Ohnishi, Wolfgang Huber, Akiko Tsumura, Minjung Kang, Panagiotis Xenopoulos, Kazuki Kurimoto, Andrzej K Oleś, Marcos J Araúzo-Bravo, Mitinori Saitou, Anna-Katerina Hadjantonakis, and Takashi Hiiragi. Cell-to-cell expression variability followed by signal reinforcement progressively segregates early mouse lineages. *Nature cell biology*, 16(1):27–37, jan 2014.

[181] Hitoshi Niwa, Yayoi Toyooka, Daisuke Shimosato, Dan Strumpf, Kadue Takahashi, Rika Yagi, and Janet Rossant. Interaction between Oct3/4 and Cdx2 determines trophectoderm differentiation. *Cell*, 123(5):917–29, dec 2005.

[182] Fernando Biase, Xiaoyi Cao, and Sheng Zhong. Cell fate inclination within 2-cell and 4-cell mouse embryos revealed by single-cell RNA sequencing. *Genome research*, aug 2014.

[183] Maria Skamagki, Krzysztof B. Wicher, Agnieszka Jedrusik, Sujoy Ganguly, and Magdalena Zernicka-Goetz. Asymmetric Localization of Cdx2 mRNA during the First Cell-Fate Decision in Early Mouse Development. *Cell Reports*, 3(2):442–457, 2013.

[184] Alfonso Martinez Arias, Jennifer Nichols, and Christian Schröter. A molecular basis for developmental plasticity in early mammalian embryos. *Development*, 140:3499–3510, 2013.

[185] Tomoko Watanabe, John S Biggins, Neeta Bala Tannan, and Shankar Srinivas. Limited predictive value of blastomere angle of division in trophectoderm and inner cell mass specification. *Development (Cambridge, England)*, 141(11):2279–88, 2014.

[186] Shihadeh Anani, Shivani Bhat, Nobuko Honma-Yamanaka, Dayana Krawchuk, and Yojiro Yamanaka. Initiation of Hippo signaling is linked to polarity rather than to cell position in the pre-implantation mouse embryo. *Development (Cambridge, England)*, 141(14):2813–24, jul 2014.

[187] Jean-Léon Maître, Hervé Turlier, Rukshala Illukkumbura, Björn Eismann, Ritsuya Niwayama, François Nédélec, and Takashi Hiiragi. Asymmetric division of contractile domains couples cell positioning and fate specification. *Nature*, 2016.

[188] Kanako Kono, Dana Ann a Tamashiro, and Vernadeth B Alarcon. Inhibition of RHO-ROCK signaling enhances ICM and suppresses TE characteristics through activation of Hippo signaling in the mouse blastocyst. *Developmental biology*, 394(1):142–55, oct 2014.

[189] María Abad, Lluc Mosteiro, Cristina Pantoja, Marta Cañamero, Teresa Rayon, Inmaculada Ors, Osvaldo Graña, Diego Megías, Orlando Domínguez, Dolores Martínez, Miguel Manzanares, Sagrario Ortega, and Manuel Serrano. Reprogramming in vivo produces teratomas and iPS cells with totipotency features. *Nature*, sep 2013.

[190] Amy Ralston, Brian J Cox, Noriyuki Nishioka, Hiroshi Sasaki, Evelyn Chea, Peter Rugg-Gunn, Guoji Guo, Paul Robson, Jonathan S Draper, and Janet Rossant. Gata3 regulates trophoblast development downstream of Tead4 and in parallel to Cdx2. *Development (Cambridge, England)*, 137(3):395–403, feb 2010.

[191] Ian Lian, Joungmok Kim, Hideki Okazawa, Jiagang Zhao, Bin Zhao, Jindan Yu, Arul Chinnaiyan, Mason a Israel, Lawrence S B Goldstein, Ramzey Abujarour, Sheng Ding, and Kun-Liang Guan. The role of YAP transcription coactivator in regulating stem cell self-renewal and differentiation. *Genes & development*, 24(11):1106–18, jun 2010.

[192] Kathy K Niakan, Nadine Schrode, Lily T Y Cho, and Anna-katerina Hadjantonakis. Derivation of extraembryonic endoderm stem (XEN) cells from mouse embryos and embryonic stem cells. *Nature protocols*, 2013.

[193] Aryeh Warmflash, Benoit Sorre, Fred Etoc, Eric D Siggia, and Ali H Brivanlou. A method to recapitulate early embryonic spatial patterning in human embryonic stem cells. *Nature methods*, jun 2014.

[194] Claire Chazaud, Yojiro Yamanaka, Tony Pawson, and Janet Rossant. Early lineage segregation between epiblast and primitive endoderm in mouse blastocysts through the Grb2-MAPK pathway. *Developmental cell*, 10(5):615–24, may 2006.

[195] Ivan Bedzhov and Magdalena Zernicka-Goetz. Self-organizing properties of mouse pluripotent cells initiate morphogenesis upon implantation. *Cell*, 156(5):1032–1044, 2014.

[196] Yeh-Chuin Poh, Junwei Chen, Ying Hong, Haiying Yi, Shuang Zhang, Junjian Chen, Douglas C Wu, Lili Wang, Qiong Jia, Rishi Singh, Wenting Yao, Youhua

Tan, Arash Tajik, Tetsuya S Tanaka, and Ning Wang. Generation of organized germ layers from a single mouse embryonic stem cell. *Nature communications*, 5(May):4000, jan 2014.

[197] Magdalena Krupa, Ewa Mazur, Katarzyna Szczepańska, Katarzyna Filimonow, Marek Maleszewski, and Aneta Suwińska. Allocation of inner cells to epiblast vs primitive endoderm in the mouse embryo is biased but not determined by the round of asymmetric divisions (8?16- and 16?32-cells). *Developmental biology*, 385(1):136–48, jan 2014.

[198] Nadine Schrode, Néstor Saiz, Stefano Di Talia, and Anna-Katerina Hadjantonakis. GATA6 Levels Modulate Primitive Endoderm Cell Fate Choice and Timing in the Mouse Blastocyst. *Developmental cell*, pages 454–467, may 2014.

[199] Kyle M Loh, Lay Teng Ang, Jingyao Zhang, Vibhor Kumar, Jasmin Ang, Jun Qiang Auyeong, Kian Leong Lee, Siew Hua Choo, Christina Y Y Lim, Massimo Nichane, Junru Tan, Monireh Soroush Noghabi, Lisa Azzola, Elizabeth S Ng, Jens Durruthy-Durruthy, Vittorio Sebastiano, Lorenz Poellinger, Andrew G Elefanty, Edouard G Stanley, Qingfeng Chen, Shyam Prabhakar, Irving L Weissman, and Bing Lim. Efficient endoderm induction from human pluripotent stem cells by logically directing signals controlling lineage bifurcations. *Cell stem cell*, 14(2):237–52, mar 2014.

[200] Madeline A Lancaster, Magdalena Renner, Carol-anne Martin, Daniel Wenzel, Louise S Bicknell, Matthew E Hurles, Tessa Homfray, Josef M Penninger, Andrew P Jackson, and Juergen A Knoblich. Cerebral organoids model human brain development and microcephaly. *Nature*, 501(7467):373–379, 2013.

[201] Karl R Koehler and Eri Hashino. 3D mouse embryonic stem cell culture for generating inner ear organoids. *Nature protocols*, 9(6):1229–44, jun 2014.

[202] Jennifer E. Bruin, Suheda Erener, Javier Vela, Xiaoke Hu, James D. Johnson, Harley T. Kurata, Francis C. Lynn, James M. Piret, Ali Asadi, Alireza Rezania, and Timothy J. Kieffer. Characterization of polyhormonal insulin-producing cells derived in vitro from human embryonic stem cells. *Stem Cell Research*, 12(1):194–208, 2014.

[203] Jens-Erik Dietrich and Takashi Hiiragi. Stochastic patterning in the mouse pre-implantation embryo. *Development (Cambridge, England)*, 134(23):4219–31, dec 2007.

[204] Tianzhi Luo, Krithika Mohan, Pablo a Iglesias, and Douglas N Robinson. Molecular mechanisms of cellular mechanosensing. *Nature materials*, 12(11):1064–71, nov 2013.

[205] Brahatheeswaran Dhandayuthapani, Yasuhiko Yoshida, Toru Maekawa, and D. Sakthi Kumar. Polymeric Scaffolds in Tissue Engineering Application: A Review. *International Journal of Polymer Science*, 2011(ii):1–19, 2011.

[206] Luke MacQueen, Yu Sun, and Craig a Simmons. Mesenchymal stem cell mechanobiology and emerging experimental platforms. *Journal of the Royal Society, Interface / the Royal Society*, 10(84):20130179, jul 2013.

[207] Mehdi Nikkhah, Nouran Eshak, Pinar Zorlutuna, Nasim Annabi, Marco Castello, Keekyoung Kim, Alireza Dolatshahi-Pirouz, Faramarz Edalat, Hojae Bae, Yunzhi Yang, and Ali Khademhosseini. Directed endothelial cell morphogenesis in micropatterned gelatin methacrylate hydrogels. *Biomaterials*, 33(35):9009–18, dec 2012.

[208] Raimon Sunyer, Albert J Jin, Ralph Nossal, and Dan L Sackett. Fabrication of hydrogels with steep stiffness gradients for studying cell mechanical response. *PloS one*, 7(10):e46107, jan 2012.

[209] Yong Doo Park, Nicola Tirelli, and Jeffrey a Hubbell. Photopolymerized hyaluronic acid-based hydrogels and interpenetrating networks. *Biomaterials*, 24(6):893–900, mar 2003.

[210] Michael V Turturro, Megan C Christenson, Jeffery C Larson, Daniel a Young, Eric M Brey, and Georgia Papavasiliou. MMP-sensitive PEG diacrylate hydrogels with spatial variations in matrix properties stimulate directional vascular sprout formation. *PloS one*, 8(3):e58897, jan 2013.

[211] Cailong Li, Toshinobu Sajiki, Yasuhide Nakayama, Masashi Fukui, and Takehisa Matsuda. Novel visible-light-induced photocurable tissue adhesive composed of multiply styrene-derivatized gelatin and poly(ethylene glycol) diacrylate. *Journal of biomedical materials research. Part B, Applied biomaterials*, 66(1):439–46, jul 2003.

[212] Che B. Hutson, Jason W. HIchol, Hug Augbin, Hojae Bae, Seda Yamanlar, Shahed Al-Haque, Sandeep T. Koshy, and Ali Khademhosseini. Synthesis and Characterization of Tunable PEG - Gelatin Methacrylate Hydrogels. *Tissue engineering. Part A*, 0(0):1–10, 2011.

[213] I Levental, K R Levental, E a Klein, R Assoian, R T Miller, R G Wells, and P a Janmey. A simple indentation device for measuring micrometer-scale tissue stiffness. *Journal of physics. Condensed matter : an Institute of Physics journal*, 22(19):194120, may 2010.

[214] Zachary Gautreau, Jeremy Griffin, Todd Peterson, and Ploypan Thongpradit. Characterizing Viscoelastic Properties of Polyacrylamide Gels. *Bachelor thesis*, 2006.

[215] Blayne a. Roeder, Klod Kokini, Jennifer E. Sturgis, J. Paul Robinson, and Sherry L. Voytik-Harbin. Tensile Mechanical Properties of Three-Dimensional

Type I Collagen Extracellular Matrices With Varied Microstructure. *Journal of Biomechanical Engineering*, 124(2):214, 2002.

[216] Cornelis; Storm, Jennifer; Pastore, F. C.; MacKintosh, T. C.; Lubensky, and Paul A.; Janmey. Nonlinear elasticity in biological gels. *Nature*, 435(May):0–3, 2005.

[217] Hideki Mori, Kousuke Shimizu, and Masayuki Hara. Dynamic viscoelastic properties of collagen gels with high mechanical strength. *Materials science & engineering. C, Materials for biological applications*, 33(6):3230–6, aug 2013.

[218] M. S. Hahn, J. S. Miller, and J. L. West. Laser Scanning Lithography for Surface Micropatterning on Hydrogels. *Advanced Materials*, 17(24):2939–2942, dec 2005.

[219] Benjamin D. Fairbanks. Photoinitiated polymerization of PEG-diacrylate with lithium phenyl-2,4,6-trimethylbenzoylphosphinate: polymerization rate and cytocompatibility Benjamin. *Biomaterials*, 30(35):6702–6707, 2009.

[220] L Cheng, X Xia, W Yu, L E Scriven, and W W Gerberich. Flat-Punch Indentation of Viscoelastic Material. *Journal of Polymer Science Part B: Polymer Physics*, 38(August 1999):10–22, 2000.

[221] Peter Mountford, Branko Zevnik, Annette Dowel, Jennifer Nichols, Meng Li, Christian Dani, Morag Robertson, I A N Chambers, and Austin Smith. Dicistronic targeting constructs : Reporters and modifiers of mammalian gene expression. *Proceedings of the National Academy of Sciences*, 91(May):4303–4307, 1994.

[222] Anshul Gupta, Ganesh M Mugundu, Pankaj B Desai, Kenneth E Thummel, and Jashvant D Unadkat. Intestinal Human Colon Adenocarcinoma Cell Line

LS180 Is an Excellent Model to Study Pregnane X Receptor , but Not Constitutive Androstane Receptor , Mediated CYP3A4 and Multidrug Resistance Transporter 1 Induction : Studies with Anti-Human Immunodeficien. *Drug Metabolism and Disposition*, 36(6):1172–1180, 2008.

[223] Philip Thomas and Trevor G Smart. HEK293 cell line: a vehicle for the expression of recombinant proteins. *Journal of pharmacological and toxicological methods*, 51(3):187–200, 2005.

[224] Sara Pedron, Eftalda Becka, and Brendan A C Harley. Biomaterials Regulation of glioma cell phenotype in 3D matrices by hyaluronic acid. *Biomaterials*, 34(30):7408–7417, 2013.

[225] Javier Ramón-Azcón, Samad Ahadian, Raquel Obregón, Gulden Camci-Unal, Serge Ostrovidov, Vahid Hosseini, Hirokazu Kaji, Kosuke Ino, Hitoshi Shiku, Ali Khademhosseini, and Tomokazu Matsue. Gelatin methacrylate as a promising hydrogel for 3D microscale organization and proliferation of dielectrophoretically patterned cells. *Lab on a chip*, 12(16):2959–69, aug 2012.

[226] Ross a. Marklein and Jason a. Burdick. Spatially controlled hydrogel mechanics to modulate stem cell interactions. *Soft Matter*, 6(1):136, 2010.

[227] Dinender Kumar, Timothy J Kamp, and Martin M LeWinter. Embryonic stem cells: differentiation into cardiomyocytes and potential for heart repair and regeneration. *Coronary artery disease*, 16(2):111–6, mar 2005.

[228] Tyler D Ross, Brian G Coon, Sanguk Yun, Nicolas Baeyens, Keiichiro Tanaka, Mingxing Ouyang, and Martin a Schwartz. Integrins in mechanotransduction. *Current opinion in cell biology*, 25(5):613–618, jun 2013.

[229] Xin Liu, Hong Wu, Michael Byrne, John Jeffrey, Stephen Krane, and Rudolf Jaenisch. A targeted mutation at the known collagenase cleavage site in mouse

type I collagen impairs tissue remodeling. *Journal of Cell Biology*, 130(1):227–237, 1995.

[230] Brian Johnstone. Visible light photoinitiation of mesenchymal stem cell-laden bioresponsive hydrogels. 2011.

[231] Jerry M. Rhee, Melinda K. Pirity, Chantal S. Lackan, Jonathan Z. Long, Gen Kondoh, Junji Takeda, and Anna Katerina Hadjantonakis. In vivo imaging and differential localization of lipid-modified GFP-variant fusions in embryonic stem cells and mice. *Genesis*, 44(4):202–218, 2006.

[232] Cheri Y Li, Kelly R Stevens, Robert E Schwartz, Brian S Alejandro, Joanne H Huang, and Sangeeta N Bhatia. Micropatterned cell-cell interactions enable functional encapsulation of primary hepatocytes in hydrogel microtissues. *Tissue engineering. Part A*, 20(15-16):2200–12, aug 2014.

[233] Lina Schukur, Pinar Zorlutuna, Jae Min Cha, Hojae Bae, and Ali Khademhosseini. Directed Differentiation of Size-Controlled Embryoid Bodies Towards Endothelial and Cardiac Lineages in RGD-Modified Poly(Ethylene Glycol) Hydrogels. *Advanced Healthcare Materials*, 2(1):195–205, 2013.

[234] Christiane Fuchs and Waltraud Pasteiner. Self-Organization Phenomena in Embryonic Stem Cell-Derived Embryoid Bodies : Axis Formation and Breaking of Symmetry during Cardiomyogenesis. *Cells Tissues Organs*, pages 377–391, 2012.

[235] Ray Keller, Lance a Davidson, and David R Shook. How we are shaped: the biomechanics of gastrulation. *Differentiation; research in biological diversity*, 71(3):171–205, apr 2003.

[236] Chandrasekhar R Kothapalli and Roger D Kamm. 3D matrix microenvironment for targeted differentiation of embryonic stem cells into neural and glial lineages. *Biomaterials*, 34(25):5995–6007, may 2013.

[237] J F Casella, M D Flanagan, and S Lin. Cytochalasin D inhibits actin polymerization and induces depolymerization of actin filaments formed during platelet shape change. *Nature*, 293(5830):302–305, 1981.

[238] Tam Luan Le, Alpha S. Yap, and Jennifer L. Stow. Recycling of E-cadherin: A potential mechanism for regulating cadherin dynamics. *Journal of Cell Biology*, 146(1):219–232, 1999.

[239] Quanming Shi, Rajarshi P Ghosh, Hanna Engelke, Chris H Rycroft, Luke Cassereau, and James A Sethian. Rapid disorganization of mechanically interacting systems of mammary acini. *Proceedings of the National Academy of Sciences*, 111(2):658–663, 2014.

[240] Andrea Slade, Bede Pittenger, Pascale Milani, Arezki Boudaoud, Olivier Hamant, Petra Kioschis, Leslie M Ponce, and Mathias Hafner. Investigating cell mechanics with atomic force microscopy. *Microscopy & Analysis*, pages 6–9, 2014.

[241] Fernando Calvo, Nil Ege, Araceli Grande-Garcia, Steven Hooper, Robert P Jenkins, Shahid I Chaudhry, Kevin Harrington, Peter Williamson, Emad Moeendarbary, Guillaume Charras, and Erik Sahai. Mechanotransduction and YAP-dependent matrix remodelling is required for the generation and maintenance of cancer-associated fibroblasts. *Nature cell biology*, 15(6):637–46, jun 2013.

[242] Yuexiu Wang, Fanjie Meng, and Frederick Sachs. Genetically encoded force sensors for measuring mechanical forces in proteins. *Communicative and Integrative Biology*, 4(4):385–390, 2011.

[243] H. Hertz. Über die Berührung fester elastischer Körper. *Journal für die reine und angewandte Mathematik*, 171:156–171, 1881.

[244] Valentin L Popov. Contact Mechanics and Friction. *Media*, pages 55–70, 2010.

[245] K.P. Roberts, J.C. Bischof, and B.J. Nelson. Mechanical property characterization of mouse zona pellucida. *IEEE Transactions on Nanobioscience*, 2(4):279–286, 2003.

[246] Yoshinobu Murayama, Christos E. Constantinou, and Sadao Omata. Micromechanical sensing platform for the characterization of the elastic properties of the ovum via uniaxial measurement. *Journal of Biomechanics*, 37(1):67–72, 2004.

[247] Nicolas Dard, Sophie Louvet-Vallée, Angélica Santa-Maria, and Bernard Maro. Phosphorylation of ezrin on threonine T567 plays a crucial role during compaction in the mouse early embryo. *Developmental biology*, 271(1):87–97, jul 2004.

[248] Lynn M. Wiley. Cavitation in the mouse preimplantation embryo: and the origin of nascent blastocoele fluid. *Developmental Biology*, 105(2):330–342, 1984.

[249] L. C. Barcroft, a. E. Moseley, J. B. Lingrel, and a. J. Watson. Deletion of the Na/K-ATPase 1-subunit gene (Atp1a1) does not prevent cavitation of the preimplantation mouse embryo. *Mechanisms of Development*, 121(5):417–426, 2004.

[250] Lisa C Barcroft, Hanne Offenberg, Preben Thomsen, and Andrew J Watson. Aquaporin proteins in murine trophectoderm mediate transepithelial water movements during cavitation. *Developmental Biology*, 256(2):342–354, apr 2003.

[251] Mohamad Eid Hammadeh, Constanze Fischer-Hammadeh, and Khaled Refaat Ali. Assisted hatching in assisted reproduction: A state of the art. *Journal of Assisted Reproduction and Genetics*, 28(2):119–128, 2011.

[252] M Thomas, S Jain, G P Kumar, and M Laloraya. A programmed oxyradical burst causes hatching of mouse blastocysts. *Journal of cell science*, 110 (Pt 1:1597–602, 1997.

[253] Rosario M. Perona and Paul M. Wassarman. Mouse blastocysts hatch in vitro by using a trypsin-like proteinase associated with cells of mural trophectoderm. *Developmental Biology*, 114(1):42–52, 1986.

[254] H. Sawada, K. Yamazaki, and M. Hoshi. Trypsin-like hatching protease from mouse embryos: Evidence for the presence in culture medium and its enzymatic properties. *Journal of Experimental Zoology*, 254(1):83–87, 1990.

[255] Kazumasa Moriwaki, Shoichiro Tsukita, and Mikio Furuse. Tight junctions containing claudin 4 and 6 are essential for blastocyst formation in preimplantation mouse embryos. *Developmental Biology*, 312(2):509–522, 2007.

[256] Richard Budynas and Nisbett J. *Shigley's Mechanical Engineering Design*. New York:McGraw-Hill, 8 edition.

[257] Carlos Felippa. Stress-Strain material laws. *University of Colorado Engineering notes*, page Lecture 5, 2012.

[258] L G Navar, P D Bell, R W White, R L Watts, and R H Williams. Evaluation of the single nephron glomerular filtration coefficient in the dog. *Kidney International*, 12(2):137–149, 1977.

[259] Marshall H. Jacobson, Steven E Levy, Richard M Kaufman, and Wilfred E Gallinek. Urine Osmolality. *Archives of internal medicine*, 110:121–127, 1962.

[260] Ju Hyun Lim, Dong-Hwan Kim, Dong Wook Han, Jong-Young Kwak, and Hae-Rahn Bae. The effect of AQP3 deficiency on fuel selection during a single bout of exhausting exercise. *Pflügers Archiv - European Journal of Physiology*, pages 1283–1293, 2016.

[261] Boardman, L., Lamb, J.F., and D. McCall. UPTAKE OF [3H]OUABAIN AND Na PUMP TURNOVER RATES IN CELLS CULTURED IN OUABAIN. *J. Physiol*, 225:619–635, 1973.

[262] L.R. Pollack, EH Tate, and JS Cook. Turnover and regulation of Na-K-ATPase in HeLa cells. *American Journal of Physiology-Cell Physiology*, 241(5):C173, 1981.

[263] G El Mernissi and a Doucet. Quantitation of [3H]ouabain binding and turnover of Na-K-ATPase along the rabbit nephron. *The American journal of physiology*, 247(1 Pt 2):F158–67, 1984.

[264] Man Liang, Jiang Tian, Lijun Liu, Sandrine Pierre, Jiang Liu, Joseph Shapiro, and Zi Jian Xie. Identification of a pool of non-pumping Na/K-ATPase. *Journal of Biological Chemistry*, 282(14):10585–10593, 2007.

[265] Yoshinobu Murayama, Jinji Mizuno, Hirokazu Kamakura, Yoichi Fueta, Hiroko Nakamura, Kazuyuki Akaishi, Ken Anzai, Akihiko Watanabe, Hiroaki Inui, and Sadao Omata. Mouse zona pellucida dynamically changes its elasticity during

oocyte maturation, fertilization and early embryo development. *Human cell : official journal of Human Cell Research Society*, 19(4):119–125, 2006.

[266] Sunny H. Jun and Amin A. Milki. Assisted hatching is associated with a higher ectopic pregnancy rate. *Fertility and Sterility*, 81(6):1701–1703, 2004.

[267] M Zuccotti, U.A. Urch, and R. Yanagimachi. Collagenase as an agent for dissolving the zona pellucida of hamster and mouse oocytes. *J. Reprod. Fert.*, 93:515–520, 1991.

[268] Kenji Yamatoya, Chizuru Ito, Motoyuki Araki, Ryoji Furuse, and Kiyotaka Toshimori. One-step collagenase method for zona pellucida removal in unfertilized eggs: Easy and gentle method for large-scale preparation. *Reproductive Medicine and Biology*, 10(2):97–103, 2011.

[269] MA Luengo-Oroz, MJ Ledesma-Carbayo, N Peyriéras, and A Santos. Image analysis for understanding embryo development: a bridge from microscopy to biological insights. *Current Opinion in Genetics & Development*, 21(5):630–637, 2011.

[270] Vijay Chickarmane, Adrienne H K Roeder, Paul T Tarr, Alexandre Cunha, Cory Tobin, and Elliot M Meyerowitz. Computational morphodynamics: a modeling framework to understand plant growth. *Annual review of plant biology*, 61:65–87, 2010.

[271] Pierre Barbier de Reuille, Anne-Lise Routier-Kierzkowska, Daniel Kierzkowski, George W Bassel, Thierry Schüpbach, Gerardo Tauriello, Namrata Bajpai, Sören Strauss, Alain Weber, Annamaria Kiss, Agata Burian, Hugo Hofhuis, Aleksandra Sapala, Marcin Lipowczan, Maria B Heimlicher, Sarah Robinson, Emmanuelle M Bayer, Konrad Basler, Petros Koumoutsakos, Adrienne Hk Roeder, Tinri Aegerter-Wilmsen, Naomi Nakayama, Miltos Tsiantis, Angela

Hay, Dorota Kwiatkowska, Ioannis Xenarios, Cris Kuhlemeier, and Richard S Smith. MorphoGraphX: A platform for quantifying morphogenesis in 4D. *eLife*, 4:1–20, 2015.

[272] Hanchuan Peng, Zongcai Ruan, Fuhui Long, Julie H Simpson, and Eugene W Myers. V3D enables real-time 3D visualization and quantitative analysis of large-scale biological image data sets. *Nature Biotechnology*, 28(4):348–353, 2010.

[273] Erlend Hodneland, Tanja Kögel, Dominik Michael Frei, Hans-Hermann Gerdes, and Arvid Lundervold. CellSegm - a MATLAB toolbox for high-throughput 3D cell segmentation. *Source code for biology and medicine*, 8(1):16, 2013.

[274] Georg Halder, Sirio Dupont, and Stefano Piccolo. Transduction of mechanical and cytoskeletal cues by YAP and TAZ, 2012.

[275] Christian Wiwie, Jan Baumbach, and Richard Röttger. Comparing the performance of biomedical clustering methods. *Nature methods*, 12(11):1033–8, 2015.

[276] Adi L. Tarca, Vincent J. Carey, Xue-wen Chen, Roberto Romero, and Sorin Draghici. Machine Learning and Its Applications to Biology. *PLoS Computational Biology*, 3(6):e116, 2007.

[277] Christian Bähnisch, Peer Stelldinger, and Ullrich Köthe. *Fast and Accurate 3D Edge Detection for Surface Reconstruction*, pages 111–120. Springer Berlin Heidelberg, Berlin, Heidelberg, 2009.

[278] Hiroshi Sasaki. Mechanisms of trophectoderm fate specification in preimplantation mouse development. *Development, growth & differentiation*, 52(3):263–73, apr 2010.

[279] Jenny Schlesinger, Markus Schueler, Marcel Grunert, Jenny J. Fischer, Qin Zhang, Tammo Krueger, Martin Lange, Martje Tönjes, Ilona Dunkel, and Silke R. Sperling. The Cardiac Transcription Network Modulated by Gata4, Mef2a, Nkx2.5, Srf, Histone Modifications, and MicroRNAs. *PLoS Genetics*, 7(2):e1001313, 2011.

[280] Mark van der Laan, Katherine Pollard, and Jennifer Bryan. A new partitioning around medoids algorithm. *Journal of Statistical Computation and Simulation*, 73(8):575–584, 2002.

[281] Christine Vogel and Edward M Marcotte. Insights into regulation of protein abundance from proteomics and transcriptomic analyses. *Nature reviews genetics*, 13(4):227–232, 2013.

[282] P. Blakeley, N.M.E. Fogarty, I. Del Valle, S.E. Wamaitha, T.X. Hu, K. Elder, P. Snell, L. Christie, P. Robson, and K.K. Niakan. Defining the three cell lineages of the human blastocyst by single-cell RNA-seq. *Development (Cambridge)*, 142(18):3151–3165, 2015.

[283] Deng Qiaolin, Daniel Ramskold, Björn Reinius, and Rickard Sandberg. Single-Cell RNA-Seq Reveals Dynamic, Random Monoallelic Gene Expression. *Science*, 343:194, 2014.

[284] a Liaw and M Wiener. Classification and Regression by Random Forest. *R news*, 2(December):18–22, 2002.

[285] Yusuke Marikawa and Vernadeth B Alarcón. Establishment of trophectoderm and inner cell mass lineages in the mouse embryo. *Molecular reproduction and development*, 76(11):1019–32, nov 2009.

[286] Sebastian Wennekamp, Sven Mesecke, François Nédélec, and Takashi Hiiragi. A self-organization framework for symmetry breaking in the mammalian embryo. *Nature reviews. Molecular cell biology*, 14(7):452–9, jul 2013.

[287] Henry J. Leese. Metabolism of the preimplantation embryo: 40 Years on. *Reproduction*, 143(4):417–427, 2012.

[288] Tom P. Fleming, Peter M. Cannon, and Susan J. Pickering. The cytoskeleton, endocytosis and cell polarity in the mouse preimplantation embryo. *Developmental Biology*, 113(2):406–419, 1986.

[289] Daniel St Johnston and Christiane Nusslein-Volhard. The origin of pattern and polarity in the Drosophila embryo. *Cell*, 68(2):201–219, 1992.

[290] J. Rossant and W. Tamura Lis. Potential of isolated mouse inner cell masses to form trophectoderm derivatives in vivo. *Developmental Biology*, 70(1):255–261, 1979.

[291] Maria Willecke, Fisun Hamaratoglu, Madhuri Kango-Singh, Ryan Udan, Chiao lin Chen, Chunyao Tao, Xinwei Zhang, and Georg Halder. The Fat Cadherin Acts through the Hippo Tumor-Suppressor Pathway to Regulate Tissue Size. *Current Biology*, 16(21):2090–2100, 2006.

[292] W Bossuyt, C-L Chen, Q Chen, M Sudol, H McNeill, D Pan, a Kopp, and G Halder. An evolutionary shift in the regulation of the Hippo pathway between mice and flies. *Oncogene*, 33(10):1218–28, mar 2014.

[293] Robert Odell Stephenson, Yojiro Yamanaka, and Janet Rossant. Disorganized epithelial polarity and excess trophectoderm cell fate in preimplantation embryos lacking E-cadherin. *Development (Cambridge, England)*, 137(20):3383–91, oct 2010.

[294] Boon Chuan Low, Catherine Qiurong Pan, G. V. Shivashankar, Alexander Bershadsky, Marius Sudol, and Michael Sheetz. YAP/TAZ as mechanosensors and mechanotransducers in regulating organ size and tumor growth. *FEBS Letters*, 588(16):2663–2670, 2014.

[295] M. Susan Stern. Development of Cleaving Mouse Embryos under Pressure. *Differentiation*, 1(6):407–412, dec 1973.

[296] Julia Riedl, Kevin C Flynn, Aurelia Raducanu, Florian Gärtner, Gisela Beck, Michael Bösl, Frank Bradke, Steffen Massberg, Attila Aszodi, Michael Sixt, and Roland Wedlich-Söldner. Lifeact mice for studying F-actin dynamics. *Nature methods*, 7(3):168–9, mar 2010.

[297] Amy Ralston and Janet Rossant. Cdx2 acts downstream of cell polarization to cell-autonomously promote trophectoderm fate in the early mouse embryo. *Developmental Biology*, 313(2):614–629, 2008.

[298] Aneta Suwi, Renata Czo, and Andrzej K Tarkowski. Blastomeres of the mouse embryo lose totipotency after the fifth cleavage division : Expression of Cdx2 and Oct4 and developmental potential of inner and outer blastomeres of 16- and 32-cell embryos. *Developmental Biology*, 322:133–144, 2008.

[299] S Louvet, J Aghion, a Santa-Maria, P Mangeat, and B Maro. Ezrin becomes restricted to outer cells following asymmetrical division in the preimplantation mouse embryo. *Developmental biology*, 177(2):568–79, aug 1996.

[300] N Dard, S Louvet, a Santa-Maria, J Aghion, M Martin, P Mangeat, and B Maro. In vivo functional analysis of ezrin during mouse blastocyst formation. *Developmental biology*, 233(1):161–73, may 2001.

[301] Hongjie Liu, Zhaoting Wu, Xianle Shi, Wenzhi Li, Chang Liu, Dekun Wang, Xiaoying Ye, Lin Liu, Jie Na, Hong Cheng, and Lingyi Chen. Atypical PKC,

regulated by Rho GTPases and Mek/Erk, phosphorylates Ezrin during eight-cell embryocompaction. *Developmental biology*, 375(1):13–22, mar 2013.

[302] Pedro Gaspar and Nicolas Tapon. Sensing the local environment: actin architecture and Hippo signalling. *Current Opinion in Cell Biology*, 31:74–83, dec 2014.

[303] Atsuko Era, Motoki Tominaga, Kazuo Ebine, Chie Awai, Chieko Saito, Kimitsune Ishizaki, Katsuyuki T Yamato, Takayuki Kohchi, Akihiko Nakano, and Takashi Ueda. Application of Lifeact reveals F-actin dynamics in Arabidopsis thaliana and the liverwort, Marchantia polymorpha. *Plant & cell physiology*, 50(6):1041–8, jun 2009.

[304] Marcus Textor and Patrick Meraldi. Effect of Cell Shape and Dimensionality on Spindle Orientation and Mitotic Timing. *PLoS ONE*, 8(6), 2013.

[305] Chantal Roubinet and Clemens Cabernard. Control of asymmetric cell division. *Current opinion in cell biology*, 31C:84–91, sep 2014.

[306] Fa Xing Yu, Bin Zhao, Nattapon Panupinthu, Jenna L. Jewell, Ian Lian, Lloyd H. Wang, Jiagang Zhao, Haixin Yuan, Karen Tumaneng, Hairi Li, Xiang Dong Fu, Gordon B. Mills, and Kun Liang Guan. Regulation of the Hippo-YAP pathway by G-protein-coupled receptor signaling. *Cell*, 150(4):780–791, 2012.

[307] Berenika Plusa, Anna Piliszek, Stephen Frankenberg, Jerome Artus, and Anna-katerina Hadjantonakis. Distinct sequential cell behaviours direct primitive endoderm formation in the mouse blastocyst. *Development*, 135(18):3081–3091, 2009.

[308] Y Yamanaka, F Lanner, and J Rossant. FGF signal-dependent segregation of primitive endoderm and epiblast in the mouse blastocyst. *Development*, 137(5):715–724, 2010.

[309] Sigolène M. Meilhac, Richard J. Adams, Samantha A. Morris, Anne Danckaert, Jean François Le Garrec, and Magdalena Zernicka-Goetz. Active cell movements coupled to positional induction are involved in lineage segregation in the mouse blastocyst. *Developmental Biology*, 331(2):210–221, 2009.

[310] Junji Fujikura and Eiji Yamato. Differentiation of embryonic stem cells is induced by GATA factors. *Genes & Development*, pages 784–789, 2002.

[311] Hideki Yamaguchi, Jeffrey Wyckoff, and John Condeelis. Cell migration in tumors. *Current opinion in cell biology*, 17(5):559–64, oct 2005.

[312] Kohei Ota, Matsui Makoto, Edgar L. Milford, Glenn a. Mackin, Howard L. Weiner, and David a. Hafler. A POU-domain transcription factor in early stem cells and germ cells of the mammalian embryo. *Letters To Nature*, 346(6277):183–187, 1990.

[313] A A Avilion, S K Nicolis, L H Pevny, L Perez, N Vivian, and R Lovell-Badge. Multipotent cell lineages in early mouse development on SOX2 function. *Genes Dev.*, 17:126–140, 2003.

[314] Kathy K. Niakan, Hongkai Ji, Ren?? Maehr, Steven A. Vokes, Kit T. Rodolfa, Richard I. Sherwood, Mariko Yamaki, John T. Dimos, Alice E. Chen, Douglas A. Melton, Andrew P. McMahon, and Kevin Eggan. Sox17 promotes differentiation in mouse embryonic stem cells by directly regulating extraembryonic gene expression and indirectly antagonizing self-renewal. *Genes and Development*, 24(3):312–326, 2010.

[315] Rojas Anabel, Schachterle William, Xu Shan-Mei, Martín Franz, and L Brian Lack. Direct transcriptional regulation of Gata4 during early endoderm specification is controlled by FoxA2 binding to an intronic enhancer. *Developmental Biology*, 2:346–355, 2010.

[316] Robert O. Stephenson, Janet Rossant, and Patrick P L Tam. Intercellular interactions, position, and polarity in establishing blastocyst cell lineages and embryonic axes. *Cold Spring Harbor Perspectives in Biology*, 4:1–15, 2012.

[317] N Saiz, J B Grabarek, N Sabherwal, N Papalopulu, and B Plusa. Atypical protein kinase C couples cell sorting with primitive endoderm maturation in the mouse blastocyst. *Development*, 140(21):4311–4322, 2013.

[318] Fardin Fathi, Taki Altiraihi, Seyed Javad Mowla, and Mansoreh Movahedin. Formation of embryoid bodies from mouse embryonic stem cells cultured on silicon-coated surfaces. *Cytotechnology*, 59(1):11–16, 2009.

[319] Lily T. Y. Cho, Sissy E. Wamaitha, Isheng J. Tsai, Jérôme Artus, Richard I. Sherwood, Roger a. Pedersen, a.-K. Anna-Katerina Hadjantonakis, and Kathy K. Niakan. Conversion from mouse embryonic to extra-embryonic endoderm stem cells reveals distinct differentiation capacities of pluripotent stem cell states. *Development (Cambridge, England)*, 139(16):2866–77, 2012.

[320] Rieko Yagi, Matthew J Kohn, Irina Karavanova, Kotaro J Kaneko, Detlef Vullhorst, Melvin L DePamphilis, and Andres Buonanno. Transcription factor TEAD4 specifies the trophectoderm lineage at the beginning of mammalian development. *Development*, 134(21):3827–3836, 2007.

[321] Aleksandar I Mihajlović, Vasanth Thamodaran, and Alexander W Bruce. The first two cell-fate decisions of preimplantation mouse embryo development are not functionally independent. *Scientific reports*, 5(April):15034, 2015.

[322] Farhan Chowdhury, Yanzhen Li, Yeh-Chuin Poh, Tamaki Yokohama-Tamaki, Ning Wang, and Tetsuya S Tanaka. Soft substrates promote homogeneous self-renewal of embryonic stem cells via downregulating cell-matrix tractions. *PloS one*, 5(12):e15655, jan 2010.

[323] Rowena McBeath, Dana M Pirone, Celeste M Nelson, Kiran Bhadriraju, and Christopher S Chen. Cell shape, cytoskeletal tension, and RhoA regulate stem cell lineage commitment. *Developmental cell*, 6(4):483–95, apr 2004.

[324] Diogo Mosqueira, Stefania Pagliari, Koichiro Uto, Mitsuhiro Ebara, Sara Romanazzo, Carmen Escobedo-Lucea, Jun Nakanishi, Akiyoshi Taniguchi, Ornella Franzese, Paolo Di Nardo, Marie José Goumans, Enrico Traversa, Perpetua Pinto-do Ó, Takao Aoyagi, and Giancarlo Forte. Hippo pathway effectors control cardiac progenitor cell fate by acting as dynamic sensors of substrate mechanics and nanostructure. *ACS nano*, 8(3):2033–47, mar 2014.

[325] D. Axelrod, D.E. Koppel, J. Schelessinger, E. Elson, and W.W. Webb. Mobility Measurement by Analysis of Fluorescence Photobeaching recovery Kinetics. *Biophysical journal*, 16:1055–1069, 1976.

[326] Kouroush Sadegh Zadeh, Hubert J Montas, and Adel Shirmohammadi. Identification of biomolecule mass transport and binding rate parameters in living cells by inverse modeling. *Theoretical biology & medical modelling*, 3:36, 2006.

[327] Yijun Bao, Kentaro Nakagawa, Zeyu Yang, Mitsunobu Ikeda, Kanchanamala Withanage, Mari Ishigami-Yuasa, Yukiko Okuno, Shoji Hata, Hiroshi Nishina, and Yutaka Hata. A cell-based assay to screen stimulators of the Hippo pathway reveals the inhibitory effect of dobutamine on the YAP-dependent gene transcription. *Journal of Biochemistry*, 150(2):199–208, 2011.

[328] Xunbin Wei, Vanessa G Henke, Carsten Strübing, Edward B Brown, and David E Clapham. Real-time imaging of nuclear permeation by EGFP in single intact cells. *Biophysical journal*, 84(2 Pt 1):1317–1327, 2003.

[329] Rg Davies, Da Jans, and Km Wagstaff. Use of fluorescence photobleaching techniques to measure the kinetics of intracellular transport. *Microscopy: Science, Technology, Applications and Education*, pages 756–763, 2010.

[330] Kathryn R. Ayscough, Joel Stryker, Navin Pokala, Miranda Sanders, Phil Crews, and David G. Drubin. High Rates of Actin Filament Turnover in Budding Yeast and Roles for Actin in Establishment and Maintenance of Cell Polarity Revealed Using the Actin Inhibitor Latrunculin-A. *J Cell Biol.*, 139(4):895–905, 1997.

[331] Jérémie Dalous, Emmanuel Burghardt, Annette Müller-Taubenberger, Franz Bruckert, Günther Gerisch, and Till Bretschneider. Reversal of cell polarity and actin-myosin cytoskeleton reorganization under mechanical and chemical stimulation. *Biophysical journal*, 94(February):1063–1074, 2008.

[332] Maria S. Shutova, Antonina Y. Alexandrova, and Jury M. Vasiliev. Regulation of polarity in cells devoid of actin bundle system after treatment with inhibitors of myosin II activity. *Cell Motility and the Cytoskeleton*, 65(9):734–746, 2008.

[333] Mihaly Kovcs, Judit Toth, Csaba Hetenyi, Andras Malnasi-Csizmadia, and James R. Seller. Mechanism of blebbistatin inhibition of myosin II. *Journal of Biological Chemistry*, 279(34):35557–35563, 2004.

[334] Sarmed H Kathem, Ashraf M Mohieldin, and Surya M Nauli. The Roles of Primary cilia in Polycystic Kidney Disease. *AIMS molecular science*, 1(1):27–46, 2015.

[335] Manfred Fliegauf, Thomas Benzing, and Heymut Omran. When cilia go bad: cilia defects and ciliopathies. *Nature reviews. Molecular cell biology*, 8(11):880–93, 2007.

[336] Hiroaki Hirata, Mukund Gupta, Sri Ram Krishna Vedula, Chwee Teck Lim, Benoit Ladoux, and Masahiro Sokabe. Actomyosin bundles serve as a tension sensor and a platform for ERK activation. *EMBO reports*, 16(2):250–7, 2015.

[337] Kimihide Hayakawa, Hitoshi Tatsumi, and Masahiro Sokabe. Actin filaments function as a tension sensor by tension-dependent binding of cofilin to the filament. *Journal of Cell Biology*, 195(5):721–727, 2011.

[338] Sergey V. Plotnikov, Ana M. Pasapera, Benedikt Sabass, and Clare M. Waterman. Force fluctuations within focal adhesions mediate ECM-rigidity sensing to guide directed cell migration. *Cell*, 151(7):1513–1527, 2012.